Electronic Thesis and Dissertation Repository

7-22-2022 3:30 PM

Examining κ, the high frequency spectral decay parameter, in Eastern Canada

Samantha M. Palmer, *The University of Western Ontario*

Supervisor: Atkinson, G. M., *The University of Western Ontario*
Co-Supervisor: Ghofrani, H., *The University of Western Ontario*
A thesis submitted in partial fulfillment of the requirements for the Doctor of Philosophy degree in Geophysics
© Samantha M. Palmer 2022

Follow this and additional works at: https://ir.lib.uwo.ca/etd

Part of the Geophysics and Seismology Commons

Recommended Citation

Abstract

This thesis examines the ground motion modeling parameter kappa (κ) in the stable continental region of eastern Canada. Kappa characterizes the decay of spectral amplitudes at high frequencies due to near-surface material de-amplification and is important in seismic hazard assessments. Kappa has significant economic and seismic safety implications for critical infrastructure such as nuclear power plants and dams.

To examine kappa in eastern Canada, a database of ground motions to analyze near-source ground motion characteristics is developed. The database consists of ground motion records from 3357 earthquakes of moment magnitude (**M**) ≥1.5 recorded within 150 km of 25 seismic stations in eastern Canada. κ, is determined using two different methods: a classical Fourier acceleration spectral technique pioneered by Anderson and Hough [1984], applicable to **M**≥3.5 earthquakes; and Anderson and Humphrey's [1991] broadband method, applicable to **M**≥1.5 earthquakes. Sensitivity and error of κ are examined for each method and used to better understand biases introduced by assumptions. Correlations between κ and physical seismic station characteristics, such as site shear-wave velocity, are examined to better understand what drives kappa.

Kappa as determined using the classical method is on average 7ms on the horizontal component records and 0ms on the vertical for 9 seismic stations along the St. Lawrence River. Using the second method, kappa is determined for all 25 seismic stations and is on average -7ms on the horizontal, and -10ms on the vertical component. Negative kappa values are likely due to an issue inherent in the broadband inversion method where there is a trade-off of κ and corner frequency for small magnitude earthquakes. κ should be viewed as not being significantly different from zero when primary anelastic attenuation effects are modeled through regional whole-path crustal attenuation. Key findings regarding kappa include: (i) on average, kappa is not significantly different from zero on hard rock sites; (ii) kappa has high record-to-record variability both within and between sites; (iii) kappa is smaller on the vertical than the horizontal component; and (iv) kappa on rock sites does not appear to correlate with site-specific characteristic parameters (e.g., V_{S30}, V_{Srock}, and instrument housing).

Keywords

Earthquakes, eastern Canada, western Canada, ground motion database, time series, ground motion, Fourier amplitude spectrum, response spectrum, ground motion modelling, high frequency spectral decay, kappa, broadband inversion, seismology, engineering seismology.

Summary for Lay Audience

Analysis of earthquake ground motions is important for assessment and mitigation of earthquake damage to infrastructure. To examine ground motions in eastern Canada, a ground motion database is created from earthquakes recorded at seismic stations. Using this database, high frequency ground motion characteristics, in particular ground motion amplitude decay at high frequencies is examined using the parameter kappa (κ). Ground motions due to earthquakes are affected by earthquake source, propagation of waves to the surface, and near-surface materials, such as soil or rock, amplification and de-amplification of ground motion. Ground motion is measured as a function of time using a seismometer. Using the time series, the Fourier amplitude spectrum, which displays the ground motion recording as a function of frequency, can be useful to determine earthquake ground motion characteristics. From a near-surface material ground motion perspective, rock sites, in general, are considered beneficial with respect to structures, as they tend to have less amplification of damaging ground motion over most engineering frequencies (<5-10 Hz), when compared to soil sites. However, at higher frequencies (>5-10Hz) ground motion on rock sites tends to exceed that for soil sites for the same magnitude and distance. Thus, ground motion attributes of rock sites are important for the evaluation of infrastructure that is sensitive to high-frequency motions, such as critical equipment in nuclear power plants.

The thesis is divided into three key sections. The first section describes the development of a ground motion database for 3357 earthquakes in eastern Canada for 25 seismic stations. The second section of this thesis measures κ using a common methodology modified to reflect ground motion modeling techniques. The last section of this thesis examines high frequency characteristics using a ground motion modeling approach combined with a broadband method, which uses low frequency ground motions to aid in defining high frequency ground motions. Potential errors that can be introduced when measuring high frequency characteristics of ground motions are discussed in sections two and three.

In summary, this thesis provides a ground motion database, in conjunction with empirically determined high frequency ground motion characteristic parameter, κ, values.

Co-Authorship Statement

The materials presented in Chapters 2, 3, and 4 of this thesis have been previously published or submitted for publication to the peer reviewed journals of Bulletin of Seismological Society of America and Earthquake Spectra. This thesis contains only the original results of research conducted by the candidate under supervision of Dr. Gail Atkinson and Dr. Hadi Ghofrani. Original contribution include:

Compilation of a database in eastern Canada which includes data processed time series for selected earthquakes, determined Fourier amplitude spectrum database and 5%-pseudospectra acceleration response spectrum from time series database, determined horizontal-to-vertical spectral ratios for sites using earthquake records; compilation of a British Columbia database of time series, Fourier amplitude spectrum, horizontal-to vertical spectral ratio for sites using earthquake records; determination of the high frequency spectral decay parameter, kappa, and attenuation, $1/Q$, using $\mathbf{M} \geq 3.5$ earthquakes from a subset of the Fourier amplitude spectrum database in eastern and western Canada; of ground motion modelling parameters kappa, seismic moment, corner frequency, and stress drop using $\mathbf{M} \geq 1.5$ earthquakes in eastern Canada.

Dr. Gail Atkinson is the co-author to all three articles presented in this thesis (Chapters 2, 3, and 4).

Dr. Hadi Ghofrani is a co-author of the first article presented in this thesis (Chapter 2).

Sameer Ladak (M.Sc) and Dr. Sheri Molnar performed the site characterization analysis which was utilized for comparison of ground motion parameters and site characterization parameters. They are co-authors of the first article (Chapter 2) and were recognized for their contribution for the second and third articles (Chapter 3 and 4).

Acknowledgments

First, I would like to thank Dr. Gail Atkinson for her continuous support, guidance, encouragement, and understanding throughout this journey. Gail's passion for engineering seismology is infectious. Her skills to write, orally communicate, and teach via organized workshops, one-on-one time, courses, and encouragement to attend conferences was invaluable to me throughout this work. Thank you for all you have done and currently do for your students and your research field, Gail.

Additionally, I would like to thank my co-supervisor Dr. Hadi Ghofrani who has allowed me full access to his knowledge and experience in seismology which was invaluable. I appreciate his support, guidance, long afternoon discussions, late night chats, and friendship throughout my PhD. Thank you for exploring the restaurant scene in London with Joanna, Soushyant and I. Your compassion and friendship, throughout my PhD, has been a treasure.

I must thank the site characterization field work team who helped me collect data across eastern Canada: Melanie Postman, Alex Bilson Darko, Dr. Sheri Molnar; and the research team at Natural Resources Canada – Ottawa. Thank you to the site characterization analysis team who analyzed the data collected: Dr. Sheri Molnar, Sameer Ladak, and Freddie Jackson. Additionally, thank you to Bernie Dunn for his help with Linux and program set up as well as aid in corrupted SEED file corrections.

I would like to thank my PhD committee Dr. Robert Scherbakov and Dr. Sheri Molnar, as well as Dr. Burns Cheadle for your support and feedback. Additionally, I thank my PhD thesis examiners: Dr. Susan Hough, Dr. Hesham El Naggar, Dr. Sheri Molnar, and Dr. Karen Assatourians for their constructive feedback that has improved this thesis. My thanks to Dr. Debi Kilb, Dr. Adrian Rodriguez-Marek, Dr. David Boore, Dr. Stefano Parolai, Dr. Igor Morozov, and the anonymous paper reviewers for their constructive feedback which improved the manuscripts presented here.

This work would not have been possible without the funding support of the Canadian Nuclear Safety Commission (CNSC) and the enthusiasm of Nebojsa Orbovic, who showed a passion for this project.

Table of Contents

List of Tables

List of Figures

List of Appendices

List of frequently used symbols and acronyms

Common units

cm   centimeters

g   grams

km   kilometers

m   meters

ms   milliseconds

s   seconds

Symbols and acronyms

5%-PSA   5% damped Pseudo-spectral acceleration (response spectrum)

AH   Anderson and Hough kappa determination method

A_{peak} peak amplitude for the horizontal to vertical spectral ratio

BB   Broadband inversion method for kappa determination

β   crustal shear wave velocity

CANSD   Canadian Shield Velocity Profile

CENA   Central and Eastern North America

CNSC   Canadian National Seismic Network

Δσ   Brune stress drop

ε   Damping ratio

EAS	Effective Amplitude Spectrum
eastern Canada	Region bounded by 43°N to 60°N, 95°W to 50°W
eHVSR	earthquake horizontal to vertical spectral ratios
f	frequency
f_0	corner frequency
f_N	Natural frequency of oscillator
f_{peak}	peak frequency for the horizontal to vertical spectral ratio
FAS	Fourier Amplitude Spectrum
FASD	Fourier Amplitude Spectral Density
γ	fall off of the spectrum at high frequencies
GSC	Geological Survey of Canada
H or EAS	horizontal component seismic station recording
high frequency	frequencies > 5 – 10 Hz
HVSR	horizontal to vertical spectral ratio
kappa, κ	high frequency spectral decay parameter
κ_0	site-specific kappa
M	moment magnitude of an earthquake
M_0	seismic moment
MATLAB	Matrix laboratory Programming Software

mHVSR	microtremor horizontal to vertical spectral ratios
NGA-East	Next Generation Attenuation Relationship for the Central and Eastern North American Region
NGA-West	Next Generation Attenuation Relationship for shallow crustal earthquakes in active tectonic regions
NPP	Nuclear Power Plant
ω	Angular frequency
P-wave	compression or primary wave generated by an earthquake
PGV	peak ground velocity
PGA	peak ground acceleration
Q(f)	frequency dependent quality factor
Q_a	frequency independent apparent quality factor
r	circular rupture radius
R	distance metric commonly referred to as hypocentral distance
ρ	crustal density
RotDnn	Orientation-independent response spectrum for a fractile
S-wave	shear or secondary wave generated by an earthquake
SAC	Seismic Analysis Code
SEED	Standard for the Exchange of Earthquake Data

SLg-wave	shear/secondary and crustal guided shear/secondary waves generated by an earthquake
Site_amp	Boore [2003] quarter wavelength site amplification computation program
SNR	signal to noise ratio
$Y(M_0, R, f)$	Stochastic Ground Motion Parameterization
$E(M_0, f)$	Stochastic Source Parameterization
$P(R, f)$	Stochastic Path Parameterization
$G(f)$	Stochastic Site Parameterization
$I(f)$	Stochastic Instrument Parameterization
$A(f)$	Stochastic Amplification function
$D(f)$	Stochastic Diminution function
V or Z	vertical component seismic station recording
V_P	primary wave velocity
V_S	shear or secondary wave velocity
V_{Srock}	shear wave velocity of bedrock
V_{S30}	time averaged shear wave velocity in the upper 30m

Chapter 1

1 Introduction

1.1 Topic and Motivation

This thesis addresses the characterization of high-frequency earthquake ground motions on rock sites in eastern Canada. Earthquake ground motion is generated by the radiation and propagation of earthquake energy outward from its source, along a path to the surface. The ground motion at any point on the surface is the product of source, path, and site effects. At a given location, the near-site subsurface conditions, such as soil layers over rock, act to amplify or diminish the ground motion at the surface. The effect of soil response to ground motion from earthquakes has been widely studied while rock response has not received as much study and is often assumed to be negligible. Rock sites tend to have low amplification over most engineering frequencies (<5-10Hz), when compared to soil sites, and are considered a beneficial site condition for most structural applications. However, at higher frequencies (>10 Hz), ground motions on rock may be larger than those on soil (for the same magnitude and distance), due to lesser damping from impedance contrasts in the near-surface. Thus, site effects on rock are an important topic for structures that are sensitive to high frequencies, such as stiff buildings, or sensitive equipment.

In eastern Canada, there is a wide range of surficial rock conditions which vary from relatively-soft shales to very hard granite [Ladak et al., 2021; Ladak, 2020]. Rock velocity in the near-surface at seismic stations in eastern Canada ranges from 850m/s to 2500m/s [Ladak et al., 2021; Ladak 2020; Stokoe et al., 2021]. The availability of earthquake recordings on a wide variety of rock types and velocities provides an excellent opportunity to study rock response due to earthquakes at high frequencies.

Rock response can be quantified by the parameter kappa (κ) which describes the decay of ground motion at high frequencies; kappa is a key parameter in the estimation of ground motions for engineering applications, through ground motion models [Anderson and Hough, 1984; Atkinson and Boore, 1995; Atkinson and Boore 2006]. Ground motion models are developed using three potential methods: empirical, simulation-based, or a hybrid method which combines the two techniques. Ground motion is modelled considering the effects of three main terms: the source, path, and site terms with an additional term capturing the error [Hanks and McGuire, 1981; Boore, 1983; Boore, 2003]. Each of these terms have physical-based parameters which describe an earthquake's event and the path seismic waves travel. The source term describes the earthquakes size and mechanism, the path term describes the geometric spreading and attenuation over the distance from source to site, and the site term describes the linear and non-linear amplification and de-amplification in the near-surface, which includes the parameter κ.

In eastern Canada there is a paucity of records from larger magnitude earthquakes, which limits the ability to empirically determine ground motion models in a direct manner. Ground motion models rely on seismological modeling to make best use of available data. Ground motion models are an important component of seismic hazard assessment. Within modeling frameworks, kappa is an important parameter representing site effects in the near-surface materials.

Operators of critical infrastructure such as nuclear power plants are required to perform seismic hazard assessment for their sites. Seismic hazard assessment can be performed using a deterministic, probabilistic, or combined approach; the probabilistic approach is a more widely used and accepted method for critical infrastructure [Leblanc and Klimkiewicz, 1994; Alexander et al., 2007; AMEC, 2009; SENES Consultants, 2009; AMEC Geometrix, 2011; Energie NB Power, 2016]. The probabilistic seismic hazard assessment uses four key steps to evaluate seismic hazard: the identification of earthquake sources, the magnitude-recurrence rate of the sources, ground motion models,

and the probability of exceeding the ground motions. Based on a seismic hazard assessment, engineers analyze or construct an earthquake structural design for a given site and building.

High-frequency ground motions from moderate earthquakes can cause an exceedance of earthquake structural design constraints leading to costly outages even if no damage occurs to critical infrastructure (e.g., as in the Perry Nuclear Power Plant (NPP) [Leblanc and Klimkiewicz, 1994]). In eastern Canada, NPPs are located on rock sites. Point Lepreau, in New Brunswick, nuclear plant is founded on a Triassic sandstone conglomerate bedrock [Demerchant and ADI Limited, 1984] which is believed to be a softer rock than that of many Ontario NPP stations, which are founded on Ordovician limestone underlain by Precambrian massive migmatitic gneisses [Lee, 1996]. Although the high frequency decay of ground motions on the macroscopic site condition scale is reasonably understood (e.g., soil vs. rock), the micro-scale site conditions (e.g., within the rock regime) are not as well understood [Ktenidou et al., 2015]. These motions are particularly important for nuclear power plant applications.

This thesis has two main questions it aims to answer:

1. How is high frequency ground motion amplified and/or attenuated at rock sites in eastern Canada?
2. How does the velocity profile of the underlying rock impact these processes in eastern Canada?

To answer these questions, this work developed a ground motion database for eastern Canada from the historic earthquake catalog outlined in Chapter 2. Using this database, ground motions at rock sites were examined to determine ground motion parameters such as the high frequency spectral decay parameter, kappa, and source parameters such as seismic moment and corner frequency, as discussed in Chapter 3 and 4. The interaction between high-frequency site amplification and site characterization conditions were examined to determine the extent of micro-scale site conditions effect on the high

frequency spectral decay. Further, this thesis suggests best practices for defining kappa at specific sites in eastern Canada.

1.2 Study Database

1.2.1 Study Area

Eastern Canada is a part of the North America plate and is characterized as a tectonically stable craton. In this thesis, Eastern Canada is referred to as the area enclosed by the coordinates 43ºN to 60ºN, 95ºW to 50ºW which includes Ontario, Quebec, New Brunswick, Nova Scotia, Prince Edward Island Newfoundland, and Labrador (Figure 1.1).
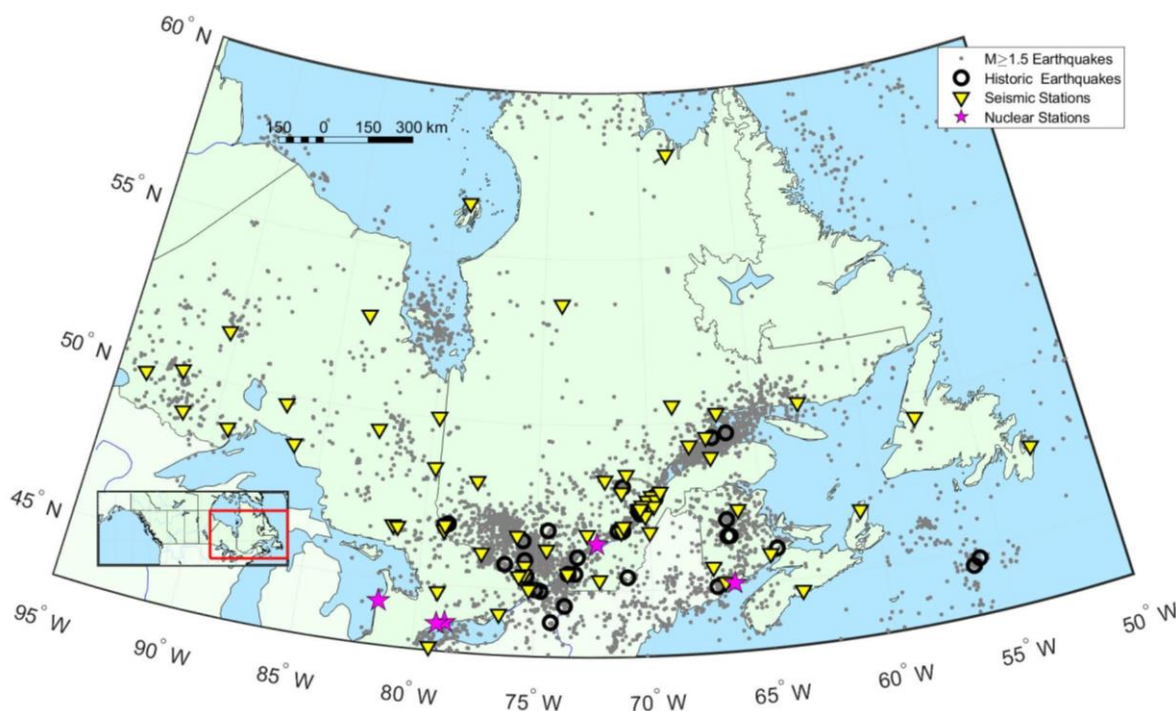
Figure 1.1: Map of eastern Canada seismic stations (yellow triangles), nuclear power plants (magenta stars), earthquakes (grey circles) [Natural Resources Canada's Earthquakes Canada - Geological Survey of Canada (GSC), 2022], and significant historic earthquakes (black open circles), as reported in Lamontagne et al. [2018].

Within this region there are several clusters of seismicity such as: the western Quebec hotspot trace; the Paleozoic Rift System which extends into the Ottawa Valley and St. Lawrence River; Charlevoix impact crater; the Lower St Lawrence River reactivation faults; Appalachian regional seismicity; localized Mirmachi Highlands activity; and the Laurentian Slope southeastern continental margin [Adams and Basham, 1988]. Each of these regions have been known to produce earthquakes of Moment magnitude (**M**) >3. Earthquakes in eastern Canada tend to be located within a 5 to 25 km depth range. The largest earthquakes in eastern Canada are located predominantly in the Paleozoic rift system [Adams and Basham, 1988].

According to Lamontagne et al. [2018] an earthquake is considered significant in eastern Canada if it possesses any of the following properties or conditions: a magnitude 6.0 or greater, had impact on a built or natural environment, felt by a significant number of Canadians, or its occurrence is supported by paleoseismological evidence. The Charlevoix region is one of the most seismically active regions in eastern Canada with 13 significant earthquakes spanning 1663 – 2005. The 1988 Saguenay Earthquake was one of the first significant (**M**>5.5) instrumentally recorded earthquakes in Eastern Canada. Notable historic earthquakes have occurred near cities like Quebec, Montreal, and in the Ottawa Region. Other notable events are those on the Laurentian slope, one of which generated a tsunami; the Miramachi earthquakes in 1982; and those located in Passamaquoddy Bay. Although moderate to large earthquakes are relatively rare in eastern Canada, they constitute a significant hazard, especially for critical infrastructure.

High-frequency ground motions are especially important to nuclear power plants. In eastern Canada there are 5 NPPs, all of which were sited on rock foundations, but the rock conditions vary greatly. These sites are in Ontario (Bruce, Pickering, and Darlington), Quebec (Gentilly; note this plant is no longer operating) and New Brunswick (Point Lepreau). Bruce NPP is founded on 850 meters of limestone, dolostone, shale, and evaporites, which is underlain by Precambrian massive migmatitic gneisses which is also found beneath the other Ontario Nuclear Plants [Intera

Engineering, 2011]. Darlington NPP is underlain by 180 m to 190 m of Paleozoic limestone and shale followed by a siltstone/sandstone bed [SENES Consultants, 2009; AMEC, 2009] and is underlaid by a crystalline basement granite gneiss [Lee, 1996]. Pickering NPP reactor buildings are pile supported on a glacial and engineering till underlaid by bedrock at 18m below the surface [Alexander et al., 2007]. The New Brunswick Point Lepreau NPP has a Triassic sedimentary layer which is a combination of sandstone and conglomerate with 2% content of shale and siltstone layers [Demerchant and ADI Limited, 1984]. The surface of the bedrock is glacial eroded.

1.2.2   Ground motion recordings

Ground motions in Canada are recorded continuously on more than 200 seismographic stations by the Canadian National Seismographic Network (CNSN). In 1897, the first Canadian seismograph, to instrumentally detect an earthquake was operated by McGill University in Montreal, Quebec and over the following 70 years continuously operating seismic stations were introduced in the west, east, and northern areas of Canada [Bent et al., 2019; Cassidy et al., 2010]. In the early 1960s a national seismograph network, the Canadian Seismograph Network (CSN) consisted of 30 seismic stations. In 1991, the CSN was upgrade to a fully digital network called the CNSN with 80 seismic stations which had continuously recorded ground motion transmitted via satellite, phone lines, and UHF radio links [Cassidy et al. 2010].

The CNSN consists of broadband seismographic stations which measure ground motion in either one direction (vertical component) or 3 directions (vertical, East-West, North-South components) as velocity or acceleration. Historically, the CNSN has recorded earthquakes with a sample rate of 40 samples/second and 100 samples/second, producing seismograms that measure velocity or acceleration of the ground versus time. Over the last decade CNSN seismic stations have been upgraded to have consistent sampling, 3-component records, and collocated accelerometer and velocimeter stations. Continuous records are now transmitted via satellite and internet [Bent et al., 2019].

A seismogram is the time series created by an earthquake's radiated energy moving outward from the source location in the form of body waves, compression and shear waves, and surface waves, Love and Rayleigh waves. The Geological Survey of Canada (GSC; Earthquakes Canada) analyzes waveforms from the seismograms to compile a catalogue of earthquake dates, time, location (latitude, longitude, depth) and magnitude (on the local, Nuttli, or moment magnitude scales) [Natural Resources Canada's Earthquakes Canada - Geological Survey of Canada (GSC), 2022]. On average 4000 earthquakes are detected and added to the catalogue yearly in Canada [Cassidy et al., 2010].

Chapter 2, 3, and 4 outline and provide details pertaining to the CNSN seismic stations used in this thesis.

1.3   Ground Motion Modelling

When two masses of rock slide past one another it generates an earthquake which is the release of accumulated energy in the form of seismic waves, as shown in Figure 1.2. The frequency content of the earthquake's energy at the source can be related to the seismic moment and the earthquake stress drop [Brune 1970; Brune 1971; Hanks and McGuire, 1981; Boore 1983; Boore, 2003]. The energy radiated from the source is altered as it travels through crust and dispersed due to geometrical spreading, which is the loss of energy due to the radiation and spreading of the wavefront, and anelastic attenuation, the loss of energy due to friction converted to heat. As the seismic waves approach the surface, they can be altered according to near-surface conditions such as the soil layer thickness (geometry), shear stiffness of soil (shear-wave velocity), impedance ratio, and soil damping. When energy travels across a layer boundary, where physical properties change, conservation of energy states that the energy will be equal in both layers and in general the incoming and outgoing energy are equal. To maintain this balance of energy, the amplitude of the wave is altered; as an example, travelling from a high velocity layer to a low velocity layer will cause an increase in wave amplitude.
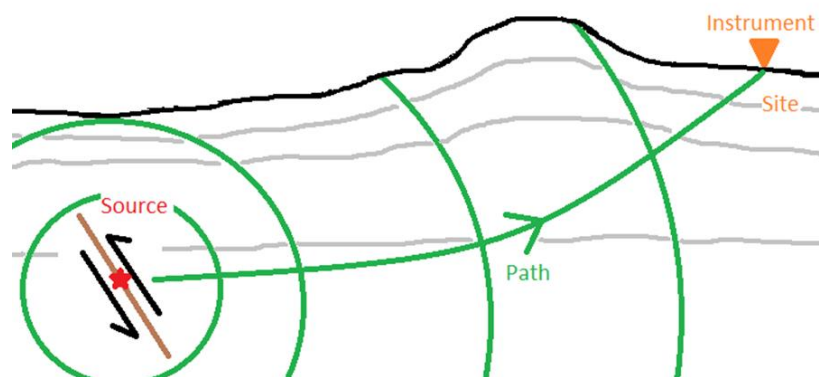
Figure 1.2: Representative earthquake energy travel across the source, path, site, and instrument components of the ground motion measured at the surface. The earthquake nucleation point is represented by the red star with motion of the fault (brown) shown in black arrows. The energy radiated (green) travels through the crustal layers (grey) along a path to the site where the instrument (orange triangle) measures the ground motion.

A classic example of the alteration of ground motions due to site conditions is the 1989 M7.0 Loma Prieta, California earthquake, for which two seismic stations measured ground motions on differing surface conditions [Hanks and Brady, 1991]. Station YBI, on Yerba Buena Island, and TRI, on Treasure Island, were located 96 and 98 km, respectively, from the earthquake epicenter, along the same azimuth. The key difference between the records is attributed to site conditions; YBI resides on a sandstone member of the Franciscan formation and TRI is on a man-made island built within a rock dike on a shallow water sand bar and surrounded by soft bay infilled with gravel, silt, and clay [Hryciw et al., 1991]. The ground motion amplitudes (Peak Ground Acceleration, PGA) differed by a factor of >2, with the largest motions at YBI being 0.069g and TRI being 0.16g [Hanks and Brady, 1991]. There are many such examples, and it is now widely recognized that site conditions play a profound role in shaping ground motion characteristics.

1.3.1 Ground Motion Time Series

The records used in this study are continuous time series recordings on broadband seismometers. The seismometer instrument response is the complex combination of the sensor and digitizer response. The seismometer instrument response must be removed from the signal to provide a measure of ground motion, which can be provided in either the time or frequency domain. In the frequency domain, the Fourier spectrum of the time series is divided by the seismometer instrument response. In general, this division is stabilized using high pass and low pass filters. Between the two filter frequencies, the filter gain is unity, while beyond the filter frequencies the gain tapers smoothly to 0. An example of this smoothed function, which is used in this work, is a quarter cycle of a cosine wave [Goldstein and Snoke, 2014; Goldstein et al., 2003].

It is easy to differentiate or integrate a Fourier spectrum in the frequency domain, via spectral division or multiplication by angular frequency, to obtain the spectral acceleration, velocity, or displacement, as required. To obtain the displacement, velocity, and acceleration time series, the inverse Fourier transform of the appropriate spectral representation is used [Haskov and Ottemoller, 2010]. The resultant time series contains waveforms that represent body and surface waves. Figure 1.3 shows a sample time series of an earthquake with compression (P-waves) and shear (S-waves) wave arrivals marked. In engineering practice time series can be useful as representative ground motion inputs for structural analysis. The time series is also useful in determining source, path, and site parameters.
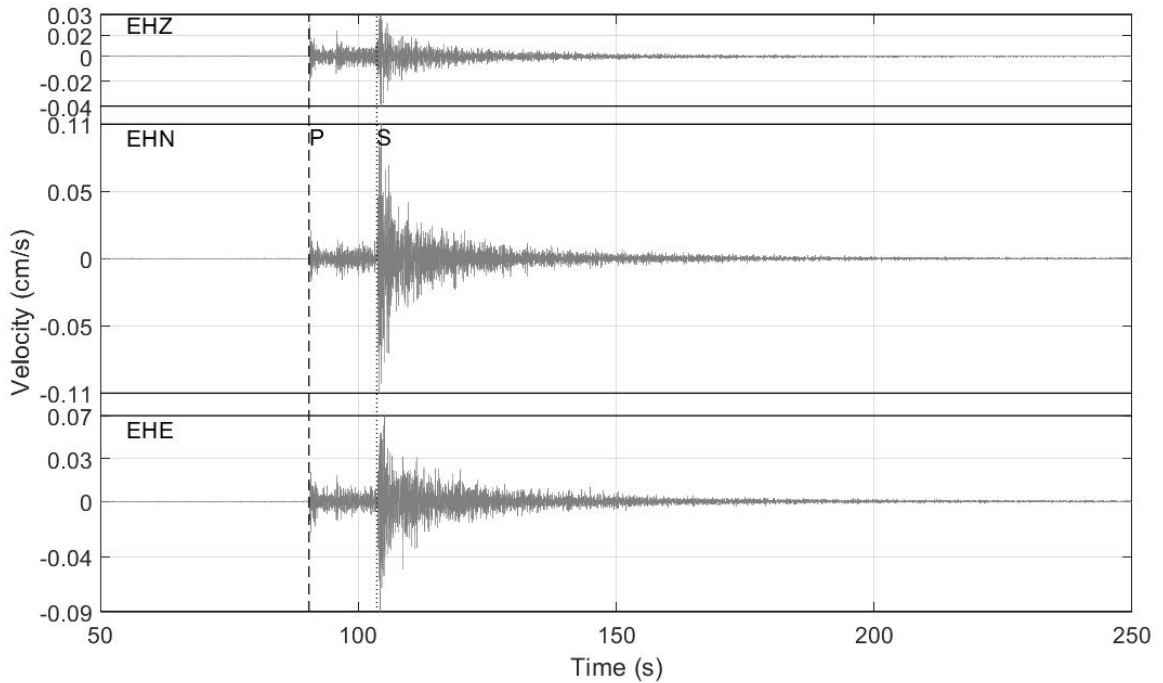
Figure 1.3: Time Series of record 2000/07/12 15:01:49 at station A21 for the vertical (EHZ) and two horizontal components (EHN and EHE). Body waves arrivals: the compressional (P-wave; dashed line) and shear (S-waves; dotted line) wave are marked.

1.3.2 Ground Motion Modelling with the Fourier Spectrum

The Fourier Amplitude Spectrum (FAS) is a useful tool for seismologists as it makes it easy to separate source, path, and site parameters. The FAS ground motion (Y) is the product of source (E), path (P), and site (G):

$$Y(M_0, R, f) = E(M_0, f)P(R, f)G(f) \tag{1.1}$$

where M_0 is the seismic moment, R is a distance parameter such as hypocentral distance, and f is frequency [Hanks and McGuire, 1981; Boore 1983; Boore, 2003]. When a force required to overcome the friction (μ) of a fault area (A) slips a distance (D), an earthquake is generated, having a seismic moment (M_0) (dyne-cm) which is the product of these three parameters [Kanamori, 1977] and a good measure of earthquake size.

Moment magnitude (**M**) [Kanamori, 1977] is a measure of the seismic moment [Hanks and Kanamori, 1979]:

$$M = \frac{2}{3}\log(M_0) - 10.7 \tag{1.2}$$

This magnitude scale has become the preferred magnitude scale for seismological studies as it can be directly related to the physical properties of an earthquake and does not saturate at high magnitudes [Boore, 2003; Sonley and Atkinson, 2005; Bent, 2011; Fereidoni et al., 2012; Goulet et al., 2014].

Aki [1967] developed a source spectrum model termed the ω-squared model. Brune [1970; 1971] extended this model to describe a circular crack shear wave Fourier spectrum of displacement for far-field earthquake sources which Anderson (1986) then extended in the form:

$$E(f, M_0) = \frac{\Re_{\phi\theta}VFM_o}{4\pi\rho\beta^3 R\left[1 + \left(\frac{f}{f_c}\right)^\gamma\right]} \tag{1.3}$$

where $\Re_{\phi\theta}$ is the root-mean squared shear wave displacement radiation pattern coefficient (= 0.6 [Thatcher and Hanks, 1973; Hanks and McGuire, 1981;Anderson and Humphrey, 1991; Baltay and Hanks, 2014]), V is the partitioning of the shear wave onto the two horizontal components ($=\frac{1}{\sqrt{2}}$), F is the free surface amplification of reflected SH-waves (= 2) [Thatcher and Hanks, 1973], M_o is seismic moment (dyne-cm), ρ is the crustal density (gm/cm^3), β is the crustal shear wave velocity (cm/s), R is the source to site distance (cm), f_c is the corner frequency (Hz), γ is the high frequency fall off (= 2 for the ω-squared model). Brune [1970; 1971] related the corner frequency to the source radius ($r\ (cm)$):

$$r = \frac{2.34\beta}{2\pi f_c}. \tag{1.4}$$

and the Brune stress drop parameter, $\Delta\sigma$ (bar), is given by:

$$\Delta\sigma = \frac{7}{16}\frac{M_o}{r^3} \tag{1.5}$$

The path component, $P(R, f)$, is the product of the geometrical spreading function and the anelastic attenuation [Hanks and McGuire, 1981; Boore 1983; Boore, 2003]:

$$P(R, f) = Z(R)e^{-\frac{\pi f R}{\beta Q(f)}} \tag{1.6}$$

where the geometrical spreading function, $Z(R)$, is a piecewise continuous function which reflects the seismic wave energy dispersion with distance and $Q(f)$ is the quality factor as a function of frequency, which represents the inverse of anelastic attenuation.

The last component of ground motion modelling is the site component. The site term, $G(f)$ (in equation 1.1), is the combination of amplification (A) and diminution (D) functions. The amplification function can be described as the linear amplification due to shear-wave profile layers using the quarter wavelength approximation [Joyner et al., 1981; Boore and Joyner, 1997; Boore, 2003; Al Atik and Abrahamson, 2021]. The quarter wavelength approximation computes the linear site amplification at a given frequency ($A(f(z))$) as the square root of acoustic/seismic impedance contrast between the source (Z_S) and surface impedance [Joyner et al., 1981; Boore, 2003],

$$A(f(z)) = \sqrt{\frac{Z_S}{\overline{Z(f)}}} \tag{1.7}$$

where impedance is the density (ρ) times the shear wave velocity (β), $f(z)$ is the quarter wavelength frequency ($\frac{1}{4 \int_0^{z(f)} \frac{1}{\beta(z)} dz}$) and $\overline{Z(f)}$ is the average near-surface impedance:

$$\overline{Z(f)} = \bar{\rho}\bar{\beta} \tag{1.8}$$

Where the average density to depth is $\bar{\rho} = \frac{1}{z(f)} \int_0^{z(f)} \rho(z) dz$ and the average shear wave velocity to depth is $\bar{\beta} = \frac{z(f)}{\int_0^{z(f)} \frac{1}{\beta(z)} dz}$. The average density and shear wave velocity are a function of the frequency corresponding to the depth of the quarter wavelength. A shallow layer, thus in the near-surface, corresponds to a higher frequency and deeper layers to lower frequencies.

Using this approximation, amplification for layered velocity models in the near-surface can be derived for the associated quarter wavelength frequency and stitched together to understand the source to surface amplification over a range of frequencies.

The diminution is described by the path independent high frequency ground motion loss:

$$D(f) = e^{-\pi \kappa_0 f} \tag{1.9}$$

where κ_0 is the site-specific high frequency decay which is an observational parameter that can be related to, with assumptions, physical properties [Anderson and Hough, 1984].

1.3.3   Ground motion modeling with response spectra

Benioff [1934] suggested a method that has been applied to understand how an earthquake's ground motion will impact engineered structures, based on the response of pendulums that have natural frequencies ranging across applicable engineering frequencies. His concept evolved to the modeling of structures with multiple modes of vibration as the summation of a group of pendulums with different natural frequencies, and including the inherent damping of structures [Biot, 1940; Housner and McCann,

1949]. Nigam and Jennings [1969] developed a fast numerical method to compute a response spectrum from an acceleration time series, which is commonly used today. The response spectrum is the maximum response of a single-degree-of-freedom (SDOF) damped oscillator computed at multiple natural frequencies for an input earthquake motion ($a(t)$) where the SDOF equation of motion is represented as:

$$\ddot{x}(t) + 2\varepsilon\omega_N\dot{x}(t) + \omega_N^2 x(t) = -a(t) \qquad (1.10)$$

where $x(t)$ is the displacement of the oscillator, $\dot{x}(t)$ is the velocity of the oscillator, $\ddot{x}(t)$ is the acceleration of the oscillator, ω_N is the natural angular frequency of the oscillator, and ε is the fraction of critical damping. Equation 1.10 can be solved using a numerical integration, like that outlined in Nigam and Jennings [1969], for multiple natural frequencies to determine the maximum displacement response spectrum, which is the maximum displacement versus the natural frequency of the oscillator. The damped psudeo-spectral velocity and acceleration are then computed from the displacement response spectrum by multiplying them by the natural angular frequency or natural angular frequency squared, respectively. The 5% damped pseudo-spectral acceleration (PSA) is the most common response spectral parameter used in ground motion modeling. Chapter 2 outlines the method to compute orientation independent 5% damped PSA, peak ground velocity (PGV) and peak ground acceleration (PGA) using Boore's [2010] RotDnn method. An advantage of the response spectrum is that, unlike the Fourier spectrum, it is not sensitive to record length [Margaris and Boore, 1998]. It is useful for earthquake engineering purposes as it takes into account the natural frequency of a structure [Joyner and Boore 1988; Margaris and Boore, 1998; Baltay and Hanks, 2014].

1.3.4 Ground Motion Modeling Impact to Seismic Hazard Assessment

As discussed in section 1.1, seismic hazard assessment is required for critical infrastructure. Seismic hazard assessment convolves earthquake sources, their magnitude-recurrence rates and ground motion models to obtain the probability of exceeding specified amplitudes of ground motion [Cornell, 1968; McGuire, 2004; Baker et al.

2021]. The probability of exceedance of ground motion is utilized by engineers in seismic design applications. Therefore, the ground motion model impacts the resultant probabilities and the engineering design.

A regional ground motion model (i.e., an ergodic model) is an average representation of ground motion and is assumed to be applicable at all locations in the region. Ground motion models consist of two types of error: epistemic error, which is error introduced by a lack of knowledge of the median model and its parameters, and aleatory error, which is the randomness of ground motions about the median model. By empirically determining components of the ground motion model parameters, such as kappa, the epistemic and aleatory errors can be reduced, thereby avoiding over or underestimation of ground motion hazard [e.g., Atkinson, 2006; Baltay et al., 2017]. Furthermore, for critical infrastructure sites, by determining site-specific ground motion model parameters ergodic ground motion models can be adjusted to a non-ergodic model, which is a model specific to a site [e.g. Atkinson, 2006] that may reduce uncertainty in hazard assessment.

1.4 Kappa

The high frequency spectral decay parameter known as kappa (κ) was defined by Anderson and Hough [1984]. They observed that the acceleration amplitude of the FAS of S-waves decays exponentially at high frequencies (i.e., at frequencies above f_E) and parameterized this decay as:

$$D(f) = A_0 e^{-\pi \kappa f} \quad f > f_E \qquad (1.11)$$

where A_0 depends on source properties and epicentral distance, f is frequency and f_E is the frequency above which the spectral shape decays linearly in a frequency vs logarithmic amplitude.

The physical meaning of kappa is not clearly defined and is debated to have contributions from source, path, and site. Most studies infer that kappa is largely a near-surface site effect driven by high-frequency energy absorption [e.g., Campbell, 2009; Edwards et al.,

2015; Ktenidou et al., 2016]; in this case, stiffer sites should have lower kappa values. The view that kappa is a measure of high-frequency absorption is supported by the well-known effects of path attenuation on high frequencies, as characterized by the Quality factor (or its inverse, the anelastic attenuation coefficient, [e.g., Boore, 2003]); these effects mimic those of kappa in causing a linear decay trend of log FAS vs frequency. However, some studies related kappa to source effects [e.g., Papageorgiou and Aki, 1983; Wen and Chen, 2012; Beresnev, 2019]. To consider all possible contributions, kappa is often expressed as having three components:

$$\kappa = \kappa_0 + \kappa_s + \tilde{\kappa}(R_e) \qquad (1.12)$$

where κ_0 is the site-specific component, κ_s is the source component, and $\tilde{\kappa}(R_e)$ represents the path component, which is a function of epicentral distance [Ktenidou et al., 2014].

Ktenidou et al. [2014] provide a summary of methods that have been developed and used since the 1980s to measure κ. These include: the classical Anderson and Hough acceleration spectrum method (κ_{AS}); the broadband inversion method (κ_{BB}); and methods involving displacement FAS, transfer functions, source spectra determinations, and response spectra. Examples of studies using the various kappa measurement methods are provided in Table 1.1. Note this table is not an exhaustive list of studies using each method.

Table 1.1: Example of studies performed using various kappa measurement methods. Key methodology papers introducing the concept are bolded.

Method	Application Studies
Acceleration Spectral Method (AS)	**Anderson and Hough, 1984**; Hough et al, 1988; Anderson, 1991; Castro et al., 2000; Tsai and Chen, 2000; Dimitriu et al., 2001; Purvance and Anderson, 2003; Bindi et al. 2004; Garcia Garcia et al., 2004; Motazedian, 2006; Motazedian

	and Moinfar, 2006; Fernandez et al., 2010; Douglas et al., 2011; Edwards et al., 2011; Gentili and Franceschina, 2011; Van Houtte et al., 2011; Ktenidou et al, 2013; Sun et al., 2013; Zafarani and Hassani, 2013; Askan et al. 2014; Van Houtte et al., 2014; Dikmen et al., 2016; Huang et al., 2015; Ktenidou et al, 2015; Neighbors et al., 2015; Pavel and Vacareanu, 2015; Fu and Li, 2016; Lai et al., 2016; Zandieh et al., 2016; Cabas et al., 2017; Lermo et al., 2017; Pilz and Fah, 2017; Kumar et al., 2018; Mayor et al., 2018; Saxen et al., 2018; Tanircan and Dikmen, 2018; Yadav et al. 2018; Chang et al., 2019; Fu et al., 2019; Pilz et al., 2019; Sonnemann et al., 2019; Xu et al., 2019; Butcher et al., 2020; Ji et al., 2020; Kumar et al., 2020; Li et al., 2020; Mittal et al., 2020; Palmer and Atkinson, 2020; Park et al., 2020; Sadeghi-Bagherabadi et al., 2020; Stanko et al., 2020; Ji et al., 2021; Sotiriadis et al., 2021; Biro et al., 2022; Castro et al., 2022
Displacement Spectral method (DS)	**Biasi and Smith, 2001**; Brandt, 2017
Broadband Inversion Method (BB)	**Anderson and Humphrey, 1991**; Humphrey and Anderson, 1992; Chapman et al., 2003; Bora et al, 2017; Darragh et al., 2019; Klimasewski et al., 2019
Transfer Function (TF)	**Hough, 1997; Frankel et al., 1999**; Drouet et al, 2010; Kurtulmus and Akyol, 2015
Source Spectral Determination (SS)	Atkinson, 1996; Neighbors et al., 2017; Vandana et al., 2017

Response Spectra (RS)	**Silva and Darragh, 1995**
Ground Motion Prediction Equations (GMPE)	Atkinson and Boore, 2006; Laurendeau et al., 2013; Al Atik et al., 2014; Baltay and Hanks, 2014; Ktenidou and Abrahamson, 2016; Hassani and Atkinson, 2018
Synthetic/Simulation (S)	Parolai and Bindi, 2004; Chopra et al., 2012; Parolai et al., 2015; Parolai, 2018; Beresnev, 2019; Pikoulis et al., 2020
Multimethod (Methods noted in brackets)	**Margaris and Boore, 1998** (AS, **SS**); Biasi and Anderson, 2007 (AS, BB, DS); Oth et al., 2011 (SS, TF); **Kilb et al., 2012** (AS, BB, DS, **Fixed Stress Drop**); Ktenidou et al., 2012 (AS, TF); Kishida et al., 2014 (AS, BB, DS); Castro and Avila-Barrientos, 2015 (AS, TF); Edwards et al., 2015 (AS, BB); Gamage and Venkatesan, 2015 (BB, GMPE); Ktenidou et al., 2016 (AS, BB, DS, RS); Ktenidou et al., 2017 (AS, BB, DS); Perron et al., 2017 (AS, DS); Ktenidou et al., 2018 (AS, BB, DS, RS); Haendel et al., 2020 (AS, Zeta Method); Tsurugi et al, 2020 (AS, fmax); Ktenidou et al., 2021 (AS, BB, DS, RS);

The time series, Fourier spectrum, and response spectrum of a record can all potentially be used to measure kappa. Variations of techniques used for each ground motion representation have varying effects on kappa. For example, the time series or spectrum can be influenced by filtering techniques, such as high and low pass or broadband filtering, or the seismic window selected, such as the S-wave or full event record. Various assumptions in ground motion modelling (Section 1.3.2) can result in bias in the measured kappa; in many cases the error introduced by such assumptions may be larger than the error of the kappa measurement [Ktenidou et al., 2013]. Sample studies in Table 1.2 examine the effect of the selection of wave arrival; seismic wave window selection; smoothing of Fourier spectra; non-linearity of ground motions; use of horizontal and

vertical component records; selection of frequency range; directivity of seismic waves; seismometer housing and environmental conditions; trade off of ground motion parameters such as kappa, corner frequency, stress drop, seismic moment and quality factor; site amplification assumptions; and method variations for resultant kappa using the same data.

Table 1.2: Example studies examining the assumption errors made in the process of measuring kappa.

Assumption	Studies
Directivity of seismic waves	Ji et al., 2020
Method variations	Drouet et al., 2010; Ktenidou et al., 2013; Kishida et al., 2014
Non-linearity of ground motions	Dimitriu et al., 2001; Van Houtte et al., 2014; Ktenidou et al., 2018; Ji et al., 2021
Selection of frequency range	Purvance and Anderson, 2003; Atkinson and Boore, 2006; Kishida et al., 2014; Edwards et al., 2015; Parolai et al., 2015, Perron et al., 2017; Mayor et al., 2018; Chang et al., 2019; Ji et al., 2020; Ji et al, 2021; Castro et al., 2022
Selection of wave arrival	Douglas et al., 2011
Seismic wave window selection	Tsai and Chen, 2000; Douglas et al., 2011; Askan et al., 2014; Parolai et al., 2015; Parolai, 2018; Klimasewski et al., 2019; Pilz et al., 2019; Ji et al., 2020; Ji et al., 2021;
Seismometer housing and environmental	Hollender et al., 2020; Roumelioti et al., 2020

conditions	
Site amplification	Parolai and Bindi, 2004; Drouet et al., 2010; Edwards et al., 2015; Ktenidou et al., 2016; Ktenidou et al., 2017; Perron et al., 2017; Ktenidou and Abrahamson, 2016; Parolai, 2018; Darragh et al., 2019
Smoothing Fourier spectra	Gentili and Franceschina, 2011; Kottke et al. 2018
Trade off of ground motion parameters	Baltay and Hanks, 2014; Edwards et al., 2015; Darragh et al., 2019; Laurendeau et al., 2013
Use of horizontal and vertical component records	Douglas et al., 2011; Ktenidou et al., 2013; Van Houtte et al., 2014; Ji et al., 2020

Kappa has been measured in various locations with varying seismic boundaries and seismicity levels, as summarized in Table 1.3. Locations like Australia, France, eastern US, and eastern Canada are characterized as stable continental regions which are generally aseismic to large magnitude earthquakes.

Table 1.3: Sample kappa computational studies for different locations.

Location	Studies
NORTH AMERICA	
Eastern Canada	Atkinson, 1996; Atkinson and Boore, 2006; Campbell, 2009; Ktenidou and Abrahamson, 2016; Palmer and Atkinson, 2020
Eastern US	Chapman et al., 2003; Atkinson and Boore, 2006; Campbell, 2009; Ktenidou and Abrahamson, 2016; Ktenidou et al., 2018

Western Canada	Atkinson, 1996; Ktenidou and Abrahamson, 2016; Palmer and Atkinson, 2020
Western US	Anderson and Hough, 1984; Hough et al., 1988; Anderson, 1991; Frankel et al., 1999; Biasi and Smith, 2001; Biasi and Anderson, 2007; Van Houtte et al., 2011; Kilb et al., 2012; Kishida et al., 2014; Castro and Avila-Barrientos, 2015; Ktenidou et al., 2017; Hassani and Atkinson, 2018; Ktenidou et al., 2018; Saxen et al., 2018; Darragh et al., 2019; Klimasewski et al., 2019; Sotiriadis et al., 2021
SOUTH AMERICA	
Mexico	Castro et al., 1990; Humphrey and Anderson, 1992; Purvance and Anderson, 2003; Fernandez et al., 2010; Lermo et al., 2017
Chile	Neighbors et al., 2015
EUROPE	
Croatia	Stanko et al., 2020
France	Drouet et al, 2010; Douglas et al, 2011; Perron et al., 2017; Mayor et al., 2018; Hollender et al., 2020
Greece	Margaris and Boore, 1998; Dimitriu et al., 2001; Ktenidou et al., 2012; Ktenidou et al., 2018; Haendel et al., 2020; Hollender et al., 2020; Roumelioti et al., 2020; Sotiriadis et al., 2021
Iceland	Sonneman et al., 2019
Italy	Castro et al., 2000; Bindi et al. 2004; Gentili and Franceschina, 2011; Castro et al., 2022

Romania	Pavel and Vacareanu, 2015
Spain	Garcia Garcia et al., 2004
Switzerland	Edwards et al., 2011; Edwards et al., 2015; Pilz and Fah, 2017
United Kingdom	Butcher et al., 2020
AFRICA	
Africa	Brandt, 2017
ASIA	
China	Wen and Chen, 2012; Sun et al., 2013; Fu and Li, 2016; Fu et al., 2019; Li et al., 2020;
India/Himalaya	Chopra et al., 2012; Vandana et al., 2017; Kumar et al., 2018; Yadav et al., 2018; Kumar et al., 2020; Mittal et al., 2020
Japan	Oth et al., 2011; Van Houtte et al., 2011; Laurendeau et al., 2013; Tsurugi et al., 2020; Xu et al., 2019; Ji et al., 2020; Sotiriadis et al., 2021; Ji et al., 2022;
Taiwan	Tsia and Chen, 2000; Van Houtte et al., 2011; Huang et al., 2015; Lai et al., 2016; Chang et al., 2019
South Korea	Park et al., 2020
Sri Lanka	Gamage and Venkatesan, 2015
MIDDLE EAST	
Iran	Motazedian, 2006; Motazedian and Moinfar, 2006; Sadeghi-

	Bagherabadi et al., 2020; Zafarani and Hassani, 2013
Turkey	Askan et al, 2014; Dikmen et al., 2016; Kurtulmus and Akyol, 2015; Parolai, 2018; Tanircan and Dikmen, 2018; Biro et al., 2022
AUSTRALIA AND OCEANIA	
New Zealand	Van Houtte et al., 2014; Neighbors et al., 2017; Ktenidou et al., 2018
DATABASES	
EIDA (Europe) Database	Pilz et al., 2019
NGA-East	Ktenidou et al., 2016; Ktenidou et al., 2018; Ktenidou et al., 2021
NGA-West	Baltay and Hanks, 2014; Zandieh et al., 2016; Xu et al., 2019
RESORCE Database (Europe, Mediterranean, and Middle East)	Ktenidou and Abrahamson, 2016; Bora et al., 2017

1.4.1   Challenges of measuring kappa in stable continental regions

Each of the methods used to determine kappa have limitations and assumptions that limit their use. The Anderson and Hough method is limited by the corner frequency of the earthquake source. To measure the high frequency decay, the frequency range of measurement must be above the corner frequency (i.e., on the flat part of the acceleration spectrum in the absence of decay) to avoid amplitude contamination from the earthquake source. In general, earthquakes must be above a moment Magnitude (**M**) of 3.5 [Edwards et al. 2011] for the Anderson and Hough method to be applicable.

To avoid such limitations, methods to utilize smaller magnitude earthquakes were developed, such as the displacement spectral method and the broadband inversion method. The use of smaller magnitude earthquakes is vital for regions like eastern Canada which lack larger magnitude earthquakes, as exemplified in Figure 1.4. Figure 1.4 shows records by magnitude versus epicentral distance for 25 stations in eastern Canada. Only 17 of 25 stations have more than 5 earthquakes above **M**3.5 but all stations have many records above **M**1.5. Of the 17 stations only 13 have earthquakes that span the distance range of interest (<150 km).
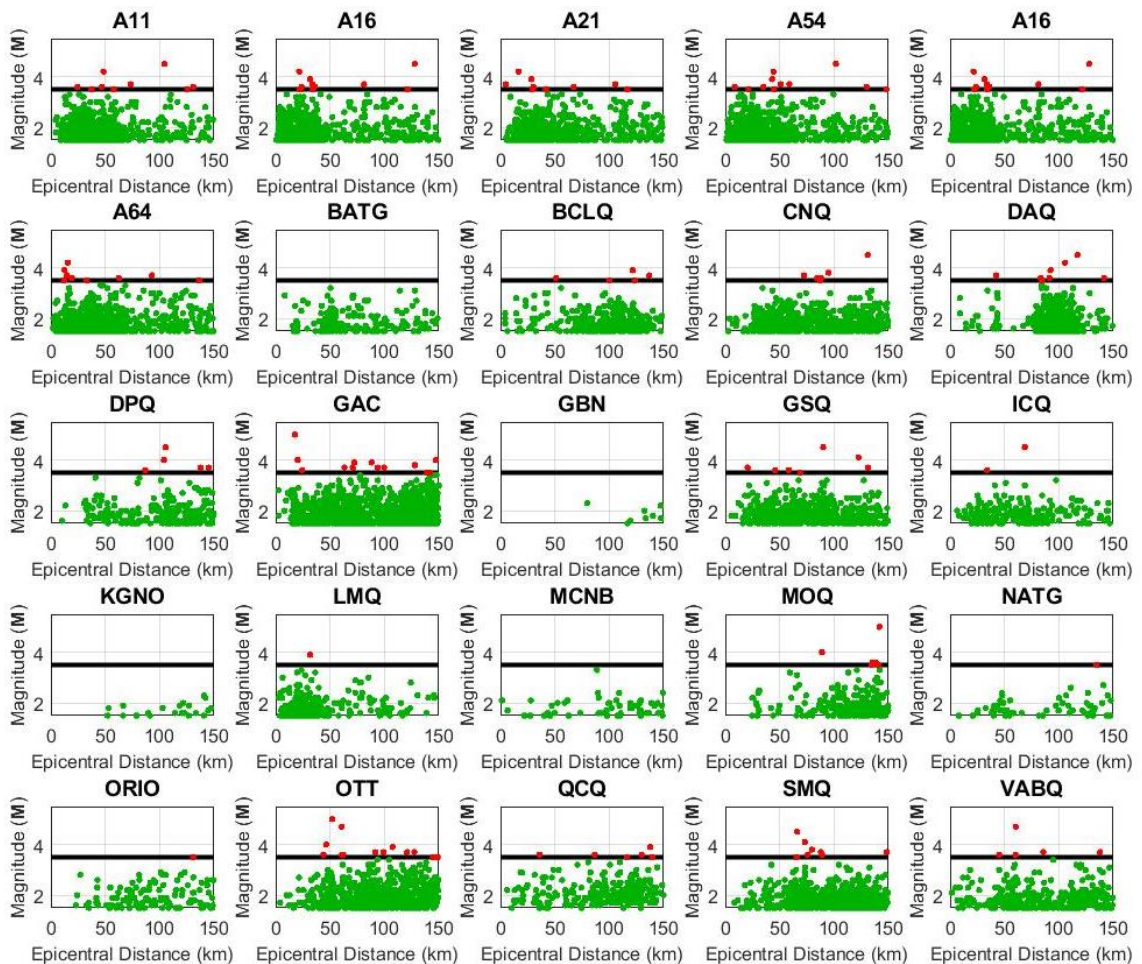
Figure 1.4: Moment magnitude (M) versus epicentral distance for M≥3.5 (red dots) and 1.5≤M≤3.5 (green) earthquakes by station.

1.4.2   Acceleration spectral method (Anderson and Hough method)

The acceleration spectral method measures kappa directly from the FAS of acceleration. κ_{AS} is measured using a linear fit of the log of the FAS of acceleration of the S-wave spectrum versus frequency. The slope of the linear fit is related to κ_{AS} (s):

$$\kappa_{AS} = -\frac{\lambda}{\pi} \tag{1.13}$$

where λ is the slope of the linear fit [Anderson and Hough, 1984]. The linear fit is applied to the FAS in the frequency range that is greater than the corner frequency of the earthquake, but less than the noise limit or the Nyquist frequency (half of the sampling rate of a seismic instrument). Chapter 3 provides a detailed description of this technique.

1.4.3   Broadband inversion method

The broadband inversion method, graphically shown in Figure 1.5, aims to fit a theoretical spectrum to an observed spectrum [Anderson and Humphreys, 1991] and simultaneously determine source and diminution parameters including the seismic moment, corner frequency, and kappa. The technique assumes a source spectral shape and applies site, path, and source characteristic parameters to generate modelled spectra that can be compared to empirical spectra recorded by a station. The source and site parameters are determined by minimizing the misfit between empirical and modelled spectra. A mathematical description of this technique can be found in Chapter 4.
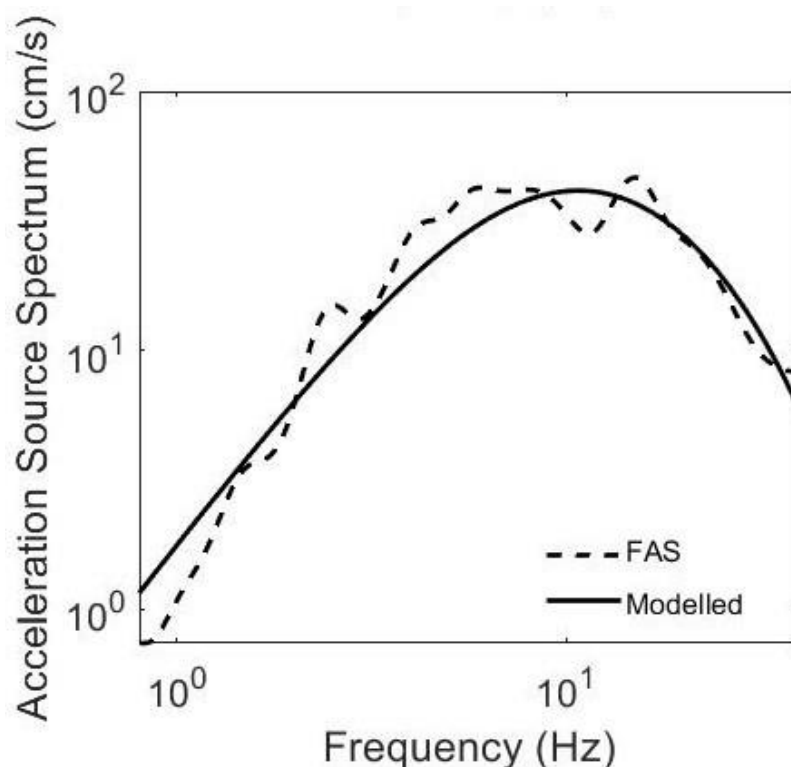
Figure 1.5: An example of the broadband inversion methodology. The empirical FAS is shown in a dashed black line, and the modelled spectrum of the best fit is represented as a solid line.

1.5   Thesis Outline

The research presented in this thesis is organized into five chapters. Chapter 1 introduces the background and motivation for this study.

Chapter 2 presents an earthquake database for eastern Canada which comprises records from 3357 moment magnitude (**M**) $\geq$1.5 earthquakes recorded within 150 km of 25 seismic stations. The database contains instrument-corrected time series for each record; computed Fourier amplitude spectra for the full earthquake time series and multiple windows, the shear wave, the primary wave, a noise window, and the coda window of the earthquake time series; and response spectra with a 5% damping ratio. Station metadata

are also provided, including computed horizontal-to-vertical spectral ratios for each station, geological descriptions, and information on the velocity profile.

Chapter 3 presents kappa measurements at 9 seismic stations in eastern Canada and 8 seismic stations in western Canada for **M** ≥3.5 earthquakes from the database in Chapter 2. This chapter focusses on measuring kappa using a modified version of the classical Fourier acceleration spectral method of Anderson and Hough [1984] and a regional attenuation corrected Fourier amplitude spectral stack method.

Chapter 4 presents kappa measured using Anderson and Humphrey's [1991] record-by-record broadband inversion for 25 seismic stations in eastern Canada using **M** ≥1.5 earthquakes from the database in Chapter 2.

Chapter 5 summarizes the studies performed, provides significant conclusions, and provides suggestions for future studies.

1.6   References

Adams, J. and P. Pasham (1988) Seismicity and seismotectonics of Canada East of the Cordillera, Geoscience Canada 16(1), 3 – 16.

Aki, K. (1967) Scaling law of seismic spectrum, Journal of Geophysical Research 72(4), 1217 – 1231. Doi: 10.1029/JZ072i004p01217

Alexander, C.M., P.D. Baughman, and N.G. Brown (2007) Seismic margin assessment application in Ontario Nuclear Power Plants. Proceedings of SmiRT 19 Conference Toronto Canada, August 12-17. Paper no. M05/4/.

Al Atik, L., A. Kottke, N. Abrahamson, and J. Hollenback (2014) Kappa (k) scaling of ground motion prediction equations using an inverse random vibration theory approach, Bull. Seismol. Soc. Am. 104(1), 336 – 346. Doi: 10.1785/0120120200

AMEC (2009) Site evaluation for the OPG new nuclear at Darlington. Part 6: Evaluation of geotechnical aspects. Report No. P103/RP/006 R04.

AMEC Geomatrix, Inc. (2011) OPG's Deep Geologic Repository for low and intermediate level waste: Seismic hazard assessment. Report No. NWMO DGR-TR-2011-20

Anderson, J. (1986) Implication of Attenuation for Studies of Earthquake Source, Earthquake Source Mechanics (ed. S. Das., j. Boatwrite, C.H. Scholz). Vol. 37, pp. 311-318. doi: 10.1029/GM037

Anderson, J. and S. Hough (1984) A model for the shape of the Fourier amplitude spectrum of acceleration at high frequencies, Bull. Seismol. Soc. Am. 74(5), 1969 – 1993. Doi: 10.1785/BSSA0740051969

Anderson, J.G. and J.R. Humphrey (1991) A least squares method for objective determination of earthquake source parameters, Seism. Res. Lett. 62(3-4), 201 – 209. Doi: 10.1785/gssrl.62.3-4.201

Anderson, J.G. (1991) A preliminary descriptive model for the distance dependence of the spectral decay parameter in Southern California, Bull. Seismol. Soc. Am 81(6), 2186 – 2193. Doi: 10.1785/BSSA0810062186

Askan, A., F.N. Sisman, and O. Peckan (2014) A regional near-surface high frequency spectral attenuation (kappa) model for northwestern Turkey, Soil Dynamics and Earthquake Engineering 65, 113-125. Doi: 10.1016/j.soildyn.2014.06.007

Atkinson, G.M. (1996) The high-frequency shape of the source spectrum for earthquakes in eastern and western Canada, Bull. Seismol. Soc. Am. 86 (1A), 106 – 112. Doi: 10.1785/BSSA08601A0106

Atkinson G.M. (2006) Single Station Sigma, Bull. Seismol. Soc. Am. 96(2), 446-455. doi: 10.1785/0120050137

Atkinson, G.M. and D.M. Boore (2006) Earthquake ground-motion prediction equations for eastern North America, Bull. Seismol. Soc. Am. 96(6), 2181 – 2205. Doi: 10.1785/0120050245

Baker, J.W., B.A. Bradley, and P.J. Stafford (2021) Seismic Hazard and Risk Analysis. Cambridge University Press, Cambridge, England.

Baltay, A.S. and T.C. Hanks (2014) Understanding the magnitude dependence of PGA and PGV in NGA-West 2 data, Bull. Seismol. Soc. Am. 104(6), 2851-2865. Doi: 10.1785/0120130283

Baltay, A.S., T.C. Hanks, and N.A. Abrahamson (2017) Uncertainty, Variability, and earthquake physics in ground-motion prediction equations, Bull. Seismol. Soc. Am. 107(4), 1754-1772. doi: 10.1785/0120160164

Benioff, H. (1934) The physical evaluation of seismic destructiveness, Bull. Seismol. Soc. Am. 24(4), 398 – 403. Doi: 10.1785/BSSA0240040398

Bent, A. (2011) Moment magnitude (M_W) conversion relations for use in hazard assessment in eastern Canada, Seism. Res. Lett. 82, 984 – 990. Doi: 10.1785/gssrl.82.6.984

Bent, A.L., T.J. Cote, H.C.J. Seywerd, D.A. McCormack, and K.A. Coyle. (2019) The Canadian National Seismograph Network: Upgrade and Status, Seismol. Res. Lett. 91(2A), 585-592. Doi: 10.1785/0220190202

Beresnev, I.A. (2019) Short Note: Interpretation of kappa and f_{max} filters as source effect, Bull. Seismol. Soc. Am. 109(2), 822 – 826. Doi: 10.1785/0120180250

Biasi, G. P. and K. D. Smith (2001) Site effects for seismic monitoring stations in the vicinity of Yucca Mountain, Nevada. Report no. MOL20011204.0045 (prepared for the US DOE/University and Community College System of Nevada (UCCSN) Cooperative Agreement).

Biasi, G. and J.G. Anderson (2007) Measurement of the parameter kappa and reevaluation of kappa for small to moderate earthquakes at seismic stations in the vicinity of Yucca Mountain, Nevada. Report no. TR-07-007.

Bindi, D., R.R. Castro, G. Franceschina, L. Luzi, and F. Pacor (2004) The 1997-1998 Umbria-Marche (central Italy): Source, path and site effects estimated from strong ground motion data recorded in the epicentral area, Journal of Geophysical Research 109, doi:10.1029/2003JB002857.

Biot, M.A. (1940) A mechanical analyzer for the prediction of earthquake stresses, Seism. Res. Lett. 74(3), 313-323. Doi: 10.1785/gssrl.74.3.313

Biro, Y., B. Siyah, and B. Akbas (2022) Spectral decay parameter (k) analysis for a single fault source and an automatic selection procedure for spectral flattening frequency (f_x), Soil Dynamics and Earthquake Engineering 153, doi: 10.1016/j.soildyn.2021.107122.

Boore, D.M. (1983) Stochastic simulation of high-frequency ground motions based on seismological models of the radiated spectra, Bull. Seismol. Soc. Am. 73(6), 1865 – 1894. doi: 10.1785/BSSA07306A1865

Boore, D.M. (2003) Simulation of ground motion using the stochastic method, Pure Appl. Geophys. 160, 635 – 676. Doi: 10.1007/PL00012553

Boore, D.M. (2010) Orientation-independent, nongeometric-mean measures of seismic intensity from two horizontal components of motion, Bull. Seismol. Soc. Am. 100(4), 1830–1835. Doi: 10.1785/0120090400

Bora, S.S., F. Cotton, F. Scherbaum, B. Edwards, and P. Traversa (2017) Stochastic source, path and site attenuation parameters and associated variabilities for shallow crustal European earthquakes, Bull. Earthquake Eng. 15, 4531 – 4561. Doi: 10.1007/s10518-017-0167-x

Brandt, M.B.C. (2017) Near surface wave attenuation (kappa) for Far West Rand micro-events, Journal of the Southern Africa Institute of Mining and Metallurgy 117(6), doi: 10.17159/2411-9717/2017/v117n6a1.

Brune, J.N. (1970) Tectonic stress and the spectra of seismic shear waves from earthquakes, J. Geophys. Res. 75, 4997 – 5009. Doi: 10.1029/JB075i026p04997

Brune, J.N. (1971) Correction, J. Geophys. Res. 76, 5002. Doi: 10.1029/JB076i020p05002

Butcher, A., R. Luckett, J.-M. Kendall, and B. Baptie (2020) Seismic magnitude, corner frequencies, and microseismicity Bull. Seismol. Soc. Am 110(3), 1260 – 1275. Doi: 10.1785/0120190032

Cabas, A., A. Rodriguez-Marke, and L.F. Bonilla (2017) Estimation of site-specific kappa (k0)-consistent damping values at KiK-Net sites to assess the discrepancy between laboratory-based damping models and observes attenuation (of seismic waves) in the field, Seism. Res. Lett. 107(5), 2258 – 2271. Doi: 10.1785/0120160370

Campbell, K.W. (2009) Estimates of shear-wave Q and $\kappa 0$ for unconsolidated and semiconsolidated sediments in eastern North America, Bull. Seismol. Soc. Am. 99 (4), 2365 – 2392. Doi: 10.1785/0120080116

Campbell, K.W, Y.M.A. Hashash, B. Kim, A.R. Kottke, E.M. Rathje, W.J. Silva, and J.P. Stewart. (2014) Reference-rock site conditions for Central and Eastern North America: Part II – Attenuation (kappa) definition. PEER Report No. 2014/12.

Cassidy, J.F., G.C. Rogers, M. Lamontagne, S. Halchuk, and J. Adams (2010) Canada's earthquakes: 'The good, the bad, the ugly', Geoscience Canada 37(1), 1-16.

Castro, R.R., J.G. Anderson, and S.K. Singh (1990) Site response, attenuation and source spectra of S waves along the Guerrero, Mexico, subduction zone, Bull. Seismol. Soc. Am. 80(6), 1481-1503. Doi: 10.1785/BSSA08006A1481

Castro, R.R., L. Trojani, G. Monachesi, M. Mucciarelli, and M. Cattaneo (2000) The spectral decay parameter κ in the region of Umbria-Marche, Italy, J. Geophys. Res. 105(B10), 23 811 – 23 823. Doi: 10.1029/2000JB900236

Castro, R.R. and L. Avila-Barrientos (2015) Estimation of the spectral decay parameter kappa in the region of the Gulf of California, Mexico, J. Seismol. 19, 809 – 829. Doi: 10.1007/s10950-015-9496-x

Castro, R. R., L. Colavitti, C. A. Vidales-Basurto, F. Pacor, S. Sgobba, and G. Lanzano (2022) Near-source attenuation and spatial variability of the spectral decay parameter kappa in Central Italy, Seismol. Res. Lett. XX, 1–12. Doi: 10.1785/0220210276

Chang, S.-C., K.-L. Wen, M.-W. Huang, C.-H. Kuo, C.-M. Lin, C.-T Chen, and J.-Y. Huang (2019) The high frequency decay parameter (kappa) in Taiwan, Pure Appl. Geophys. 179, 4861-4879. Doi: 10.1007/s00024-019-02219-y

Chapman, M.C., P. Talwani, and R.C. Cannon (2003) Ground motion attenuation in the Atlantic Coastal Plain near Charleston, South Carolina, Bull. Seismol. Soc. Am. 93(3), 998- 1011. Doi: 10.1785/0120020062

Chopra, S., V. Kumar, A. Suthar, and P. Kumar (2012) Modeling of strong ground motions for 1991 Uttarkashi 1999 Chamoli earthquakes, and a hypothetical great earthquake in Garhwal-Kumaun Himalaya, Nat. Hazards 64, 1141-1159. Doi: 10.1007/s11069-012-0289-z

Cornell, C.A. (1986) Engineering seismic risk analysis, Bull. Seismol. Soc. Am. 58(5), 1583 – 1606. doi: 10.1785/BSSA0580051583

Darragh, R., I. Wong, and W. Silva (2019) Evaluating kappa, Q(f), and stress parameter in Southern Rocky Mountains of Central Colorado, Bull Seism. Soc. Am. 109(2), doi: 10.1785/0120180122.

Demerchant, D.P. and ADI Limited (1984) RE: Site Investigation proposed unit 2 Point Lepreau Generating Station. Project Number: 2193-1/2.3.

Dikmen, S.U., A. Pinar, and A. Edincliler (2016) Near-surface attenuation using traffic-induced seismic noise at a downhole array, J. Seismol. 20, 375-384 Doi: 10.1007/s10950-015-9533-9

Dimitriu, P., N. Theodulidis, P. Hatzidimitriou, and A. Anastasiadis (2001) Sediment non-linearity and attenuation of seismic waves: a study of accelerograms from Lefkas, western Greece, Soil Dynamics and Earthquake Engineering 21, 63-73. Doi: 10.1016/S0267-7261(00)00074-9

Douglas, J., P. Gehl, L.F. Bonilla, and C. Gelis (2011) A kappa model for mainland France, Pure Appl. Geophys. 167 (11), 1303-1315. Doi: 10.1007/s00024-010-0146-5

Drouet, S., F. Cotton, and P. Gueguen (2010) V_{S30}, κ, regional attenuation and MW from accelerograms: application to magnitude 3 – 5 French earthquakes, Geophys. J. Int. 182, 880 – 898. Doi: 10.1111/j.1365-246X.2010.04626.x

Edwards, B., D. Fäh, and D. Giardini (2011) Attenuation of seismic shear wave energy in Switzerland, Geophys. J. Int. 185, 967 – 984. Doi: 10.1111/j.1365-246X.2011.04987.x

Edwards, B., O. J. Ktenidou, F. Cotton, N.A. Abrahamson, C. Van Houtte, and D. Fäh (2015) Epistemic uncertainty and limitations of the κ0 model for near-surface attenuation at hard rock sites, Geophys. J. Int. 202, 1627 – 1645. Doi: 10.1093/gji/ggv222

Energie NB Power (2016) Point Lepreau Nuclear Generation Station: Probabilistic safety assessment. Report No. 0087-03610-0002-001-PSA-A-01.

Fereidoni, A., G. M. Atkinson, M. Macias, and K. Goda (2012) CCSC: A composite seismicity catalog for earthquake hazard assessment in major Canadian cities, Seismol. Res. Lett. 83(1), 179 – 189. Doi: 10.1785/gssrl.83.1.179

Fernandez, A.I., R.R. Castro, and C.I. Huerta (2010) The spectral decay parameter kappa in northeastern Sonora, Mexico, Bull. Seismol. Soc. Am. 100(1), 196 – 206. Doi: 10.1785/0120090049

Frankel, A., D. Carver, E. Cranswick, M. Meremonte, T. Bice, and D. Overturf (1999) Site response for Seattle and source parameters of earthquake in Puget Sound region, Bull Seism. Soc. Am 89(2), 468 – 483. Doi: 10.1785/BSSA0890020468

Fu, L., and X. Li (2016) The characteristics of high-frequency attenuation of shear waves in the Longmen Shan and adjacent regions, Bull. Seismol. Soc. Am. 106(5), 1979-1990. Doi: 10.1785/0120160002

Fu, L., X. Li, F. Wang, and S. Chen (2019) A study of site response and regional attenuation in the Longmen Shan region, eastern Tibetan plateau, SW China, from seismic recordings using the generalized inversion method, Journal of Asian Earth Sciences 181, doi: 10.1016/j.jseaes.2019.103887.

Gamage, P. and S. Venkatesan (2015) Attenuation and apparent source characteristics in the Northern Indian oceanic crust surrounding Sri Lanka, Bull. Seismol. Soc. Am. 105(4), 2041-2057. Doi: 10.1785/0120140120

Garcia Garcia, J.M., M.D. Romacho, and A. Jimenez (2004) Determination of near-surface attenuation, with κ parameter, to obtain the seismic moment, stress drop, source dimensions and seismic energy for microearthquakes in the Granada Basin (Southern Spain), Physics of the Earth and Planetary Interiors 141, 9 – 26. Doi: 10.1016/j.pepi.2003.08.006

Gentili, S. and G. Franceschina (2011) High frequency attenuation of shear waves in the southeastern Alps and northern Dinarides, Geophys. J. Int. 185, 1393 – 1416. Doi: 10.1111/j.1365-246X.2011.05016.x

Goldstein, P., D. Dodge, M. Firpo, and L. Minner (2003) SAC2000: Signal processing and analysis tools for seismologists and engineers, The IASPEI International Handbook of Earthquake and Engineering Seismology, Academic Press, London.

Goldstein, P. and A. Snoke (2005) SAC Availability for the IRIS Community, Incorporated Institutions for Seismology Data Management Center Electronic Newsletter.

Goulet, C.A., T. Kishida, T.D. Ancheta, C.H. Cramer, R.B. Darragh, W.J. Silva, Y.M.A Hashash, J. Harmon, J.P. Stewart, K.E. Wooddell, and R.R. Youngs (2014) PEER NGA-East database. PEER No. Report 2014/17.

Haendel, A., J.G. Anderson, M. Pilz, and F. Cotton (2020) A frequency dependent model for the shape of the Fourier amplitude spectrum of acceleration at high frequencies, Bull. Seismol. Soc. Am. 110(66), 2743 – 2754. doi: 10.1785/0120200118

Hanks, T.C. and H. Kanamori (1979) A moment magnitude scale, Journal of Geophysical Research 85(B5), 2348 – 2350. Doi: 10.1029/JB084iB05p02348

Hanks, T.C. and R.K, McGuire (1981) The Character of high-frequency strong ground motion, Bull. Seismol. Soc. Am. 71(6), 2071 – 2095. doi: 10.1785/BSSA0710062071

Hank, T.C. and A.G. Brady (1991) The Loma Prieta earthquake, ground motion, and damage in Oakland, Treasure Island, and San Francisco, Bull. Seismol. Soc. Am. 81(5), 2019-2047. Doi: 10.1785/BSSA0810052019

Havskov, J. and L. Ottemoller (2010) Routine Data Processing in Earthquake
Seismology. Springer Dordrecht Heidelberg London New York. Doi:
10.1007/978-90-481-8697-6

Hassani, B. and G.M. Atkinson (2018) Adjustable generic ground motion prediction
equation based on equivalent point source simulations: Accounting for kappa
effects, Bull. Seismol. Soc. Am. 108(2), 913-928. Doi: 10.1785/0120170333

Hollender, F., Z. Roumelioti, E. Maufroy, P. Travera, and A. Mariscal (2020) Can we
trust high-frequency content in strong motion database signals? Impact of
housing, coupling, and installation depth of seismic sensors, Seismol. Res. Lett.
91(4), 2192-2205. Doi: 10.1785/0220190163

Hough, S.E., J.G. Anderson, F.V. Brune, J. Berger, J. Fletcher, L. Haar, T. Hanks, and L.
Baker (1988) Attenuation near Anza, California, Bull. Seismol. Soc. Am 78(2),
672 – 691. Doi: 10.1785/BSSA0780020672

Hough, S.E. (1997) Empirical Green's function analysis: Taking the next step, Journal
Geophysical Research 102(B3), 5369 – 5384. doi: 10.1029/96JB03488

Houser, G.W. and G.D. McCann (1949) The analysis of strong motion earthquake
records with the Electric Analog Computor, Bull. Seismol. Soc. Am. 39(1), 47-56.
Doi: 10.1785/BSSA0390010047

Hryciw, R.D., S.E. Shewbridge, K.M. Rollings, M. McHood, and M. Homolka (1991)
Soil amplification at Treasure Island during the Loma Prieta Earthquake.
Proceedings of the International Conference on Recent Advances in Geotechnical
Earthquake and Engineering and Soil Dynamics Missouri United States, March
11 – 15. Paper no. LP20.

Huang, M.-W., K.-L. Wen, S.-C. Chang, C.-L. Chang, S.-Y. Liu, and K.-P. Chen (2017)
The high cut parameter (kappa) for the near-surface geology in and around the

Taipei Basin, Taiwan, Bull. Seismol. Soc. Am. 107(3), 1254-1264. Doi: 10.1785/0120160070

Humphrey, J.R. and J. G. Anderson (1992) Shear Wave Attenuation and Site Response in Guerrero, Mexico, Bull. Seismol. Soc. Am. 81(4), 1622 – 1645. 10.1785/BSSA0820041622

Intera Engineering Ltd. (2011) OPG's Deep Geologic Repository for low and intermediate level waste: Descriptive Geosphere Site Model. Report No. NWMO DGR-TR-2011-24.

Ji, C., A. Cabas, F. Cotton, M. Pilz, and D. Bindi (2020) Within station variability in kappa: Evidence of directionality effect, Bull. Seismol. Soc. Am. 110(3), 1247-1259. Doi: 10.1785/0120190253

Ji, C., A. Cabas, L.F. Bonilla and C. Gelis (2021) Effect of Nonlinear soil behaviour on kappa (k): Observations from the KiK-Net Database, Bull. Seismol. Soc. Am. 111(4), 2138 – 2157. Doi: 10.1785/0120200286

Joyner, W.B., R.E. Warrick, and T.E. Fumal (1981) The effect of quaternary alluvium on strong ground motion in the Coyote Lake, California, earthquake of 1979, Bull. Seismol. Soc. Am. 71(4), 1333-1349. Doi: 10.1785/BSSA0710041333

Joyner, W.B. and D.M. Boore (1988) Measurement, characterization, and prediction of strong ground motion. Proceedings of Earthquake Engineering and Soil Dynamics II-Recent Advances in Ground Motion Evaluation Proceedings of Specially Conference Park City Utah United States, June 27-30.

Kanamori, H. (1977) The energy release in great earthquakes, Journal of Geophysical Research 82(20), 2981-2987. Doi: 10.1029/JB082i020p02981

Kilb, D., G. Biasi, J. Anderson, J. Brune, Z. Peng, and F.L. Vernon (2012) A comparison of spectral parameter kappa from small and moderate earthquakes using Southern

California ANZA Seismic Network data, Bull. Seismol. Soc. Am. 102(1), 284 – 300. Doi: 10.1785/0120100309

Kishida, T., R.E. Kayen, O.-J. Ktenidou, W.J. Silva, R.B. Darragh, J. Watson-Lamprey (2014) PEER Arizona Strong-motion database and GMPEs Evaluation. PEER Report No. 2014/09. Doi: 10.13140/2.1.2188.9289

Klimasewski, A., V. Sahakian, A. Baltay, J. Boatwright, J.B. Fletcher and L.M. Baker (2019) κ0 and broadband site spectra in southern California from source model constrained inversion, Bull. Seismol. Soc. Am. 109(5), 1878-1889. Doi: 10.1785/0120190037

Kottke, A., N.A. Abrahamson, D.M. Boore, Y. Bozorgnia, C. Goulet, J. Hollenback, T. Kishida, A.D. Kiureghian, O.J. Ktenidou, N. Kuehn, E.M. Rathje, W.J. Silva, E. Thompson, and X. Wang. (2018) Selection of random vibration procedures for the NGA-East project. PEER Report No. 2018/05.

Ktenidou, O.-J., F. Cotton, E. Chaljub, S. Drouet, N. Theodoulidis and S. Arnaouti (2012) Estimation of kappa (κ) for a sedimentary basin in Greece (EUROSEISTEST) – Correlation to site characterization parameters. Proceedings of the 15th World Conference Earthquake Engineering Lisbon Portugal, September 24-28.

Ktenidou, O.J., C. Gelis, and L.F. Bonilla (2013) A study on the variability of kappa (κ) in a borehole: Implications of the computation process, Bull. Seismol. Soc. Am. 103(2A), 1048 – 1068. Doi: 10.1785/0120120093

Ktenidou, O., F. Cotton, N.A. Abrahamson, and J. G. Anderson (2014) Taxonomy of κ: A Review of Definitions and Estimation Approached Targeted to Applications, Seismol. Res. Lett. 85, 135 – 146. Doi: 10.1785/0220130027

Ktenidou, O.-J., N.A. Abrahamson, S. Drouet, and F. Cotton (2015) Understanding the physics of kappa (k): insights from a downhole array, Geophys. J. Int. 203, 678-691. Doi: 10.1093/gji/ggv315

Ktenidou, O.-J., and N.A. Abrahamson (2016) Empirical estimation of high-frequency ground motion on hard rock, Seismo. Res. Lett. 87(6), 1465 – 1478. Doi: 10.1785/0220160075

Ktenidou, O.J., N.A. Abrahamson, R.B. Darragh, and W.J. Silva (2016) A Methodology for the Estimation of Kappa (κ) from Large Datasets: Example Application to Rock Sites in the NGA-East Database and Implications on Design Motions. PEER Report No. 2016/01.

Ktenidou, O.-J., W. Silva, R.B. Darragh, N.A. Abrahamson, and T. Kishida (2017) Squeezing kappa (κ) out of the transportable array: A strategy for using bandlimited data in regions of sparse seismicity, Bull. Seismol. Soc. Am. 107(1), 256-275. Doi: 10.1785/0120150301

Ktenidou, O.-J., N.A. Abrahamson, F. Cotton, J.G. Anderson, R.B. Darragh, C. Holden, T. Kishida, T. Larkin, W. Silva, and C. Van Houtte (2018) Some Advances in the understanding and estimation methodology of kappa related to Sigma-1. Proceedings of the 16th European Conference on Earthquake Engineering Thessaloniki Greece, June 18-21.

Ktenidou, O.-J., N.A. Abrahamson, W.J. Silva, R.B. Darragh, and T. Kishida (2021) The search for hard rock kappa (κ) in NGA-East: A semi-automated method for large, challenging datasets in stable continental regions, Earthquake Spectra 37, 1391-1419. Doi: 10.1177/87552930211019763

Kumar, S., D. Kumar, B.K. Rastogi, and A.P. Singh (2018) Kappa model for the Kachchh region of Western India, Natural Hazards and Risk 9(1), 442-455. Doi: 10.1080/19475705.2018.1447025

Kumar, V., S. Chopra, P. Choudhury, and D. Kumar (2020) Estimation of near surface attenuation parameter kappa in Northwest and Northeast Himalaya region, Soil Dynamics and Earthquake Engineering 136, doi: 10.1016/j.soildyn.2020.106237.

Kurtulmus, T.O. and N. Akyol (2015) Separation of source, site and near-surface attenuation effects in western Turkey, Nat. Hazards 77, 1515-1532. Doi: 10.1007/s11069-015-1660-7

Lai, T., H. Mittal, W. Chao, and Y. Wu (2016) A Study on Kappa Value in Taiwan Using Borehole and Surface Seismic Array, Bull. Seismol. Soc. Am. 106(4), 1509 – 1517. Doi: 10.1785/0120160004

Lamontagne, M., S. Halchuk, J.F. Cassidy, and G.C. Rogers (2018) Significant Canadian earthquakes 1600-2017. Geological Survey of Canada Open File 8285. Doi: 10.4095/311183

Laurendeau, A., F. Cotton, O.-J. Ktenidou, L.-F. Bonilla, and F. Hollender (2013) Rock and stiff soil site amplification: dependency on V_{S30} and kappa (κ_0), Bull. Seismol. Soc. Am. 103(6), 3131-3148. Doi: 10.1785/0120130020

Leblanc, G.A. and G.C. Klimkiewicz (1994) Seismological Issues: History and Examples of Earthquake Hazard Assessment for Canadian Nuclear Generating Stations. Geological Survey of Canada Open File No. 2929.

Lee, C.F. (1996) Seismotectonic environment and design basis earthquake for the Darlington nuclear power station, Engineering Geology 43(2), 189 – 200. Doi: 10.1016/0013-7952(96)00060-9

Lermo, J., M.A. Santoyo, M.A. Jaimes, Y. Antayhua, and M. Chavacan (2017) Local earthquakes of the Mexico Basin in Mexico City: k, Q, source spectra, and stress drop, Bull. Seismol. Soc. Am. 107(4), 1423-1437. Doi: 10.1785/0120150189

Li, J., B. Zhou, M. Rong, S. Chen, and Y. Zhou (2020) Estimation of source spectra, attenuation, and site responses from strong motion data recorded in the 2019 Changning earthquake sequence, Bull. Seismol. Soc. Am. 110(2), 410 – 426. Doi: 10.1785/0120190207

Margaris, B.N. and D.M. Boore (1998) Determination of $\Delta\sigma$ and κ_0 from response spectra of large earthquakes in Greece, Bull. Seismol. Soc. Am. 88(1), 170-182. Doi: 10.1785/BSSA0880010170

Mayor, J., S.S. Bora, and F. Cotton (2018) Capturing regional variation of hard rock κ_0 from coda analysis, Bull. Seismol. Soc. Am. 108(1), 399-408. Doi: 10.1785/0120170153

McGuire, R. K. (2004) Seismic Hazard and Risk Analysis, Earthquake Engineering Research Institute, Oakland, California.

Mittal, H., B. Sharma, W.-A. Chao, Y.M. Wu, T.-L. Lin, P. Chingtham (2020) A comprehensive analysis of attenuation characteristics using strong ground motion records for the Central Seismic Gap Himalayan Region, India, Journal of Earthquake Engineering 26, 2599-2624. Doi: 10.1080/13632469.2020.1768969

Motazedian, D. and A. Moinfar (2006) Hybrid stochastic finite fault modeling of 2003, M6.5, Bam earthquake (Iran), Journal of Seismology 10(1), 91-103. Doi: 10.1007/s10950-005-9003-x

Motazedian, D. (2006) Region-specific key seismic parameters for earthquakes in northern Iran, Bull. Seismol. Soc. Am. 96(4A), 1383 – 1395. Doi: 10.1785/0120050162

Natural Resources Canada's Earthquakes Canada – Geological Survey of Canada (GSC) (2022) On-line bulletin earthquake. Available at: http://www.earthquakescanada.nrcan.gc.ca/stndon/NEDB-BNDS/bulletin-en.php (accessed 2022 April).

Neighbors, C., E.J. Liao, E.S. Cochran, G.J. Funning, A.I. Chung, J.F. Lawrence, C. Christensen, M. Miller, A. Belmonte, and H.H. Andres Sepulveda (2015) Investigation of the high frequency attenuation parameter, κ (kappa), from aftershock of the 2010 Mw 8.8 Maule, Chile earthquake, Geophys. J. Int. 200, 200-215. Doi: 10.1093/gji/ggu390

Neighbors, C., E.S. Cochran, K.J. Ryan, and A.E. Kaiser (2017) Solving for source parameters using nested array data: a case study from the Canterbury New Zealand earthquake sequence, Pure Appl. Geophys. 174, 875-893. Doi: 10.1007/s00024-016-1445-2

Nigam, N.C. and P.C. Jennings (1969) Calculation of response spectrum from strong motion earthquake records, Bull. Seismol. Soc. Am. 59(2), 909-922. Doi: 10.1785/BSSA0590020909

Oth, A., D. Bindi, S. Parolai, and D. Di Giacomo (2011) Spectral analysis of K-NET and KiK-net data in Japan part II: On attenuation characteristic, source spectra, and site response of borehole and surface stations, Bull. Seismo. Soc. Am. 101(2), 667-687. Doi: 10.1785/0120100135

Palmer, S.M. and G.M. Atkinson (2020) High frequency decay slope of spectra (kappa) for M≥3.5 earthquakes on rock sites in eastern and western Canada, Bull. Seism. Am. 110(2), 471-488. Doi: 10.1785/0120190206

Papageorgiou, A.S. and K. Aki (1983) A specific barrier model for the quantitative description of inhomogeneous faulting and the prediction of strong ground motion. I. Description of model, Bull. Seismol. Soc. Am. 73(3), 693 – 722. Doi: 10.1785/BSSA0730030693

Park, S.J., J.M. Lee, and C.-E. Baag (2020) Estimation of high frequency spectral decay (κ) for the Gyeongju area in South Korea, Bull. Seismol. Soc. Am. 110(1), 295-311. Doi: 10.1785/0120180345

Parolai, S. and D. Bindi (2004) Influence of soil layer properties on κ evaluation, Bull. Seismol. Soc. Am. 94(1), 349-356. Doi: 10.1785/0120030022

Parolai, S., D. Bindi, and M. Pilz (2015) Short Note κ_0: The role of intrinsic and scattering attenuation, Bull. Seismol. Soc. Am. 105(2A), 1049-1052. Doi: 10.1785/0120140305

Parolai, S. (2018). K0: Origin and usability, Bull. Seismol. Soc. Am. 108(6), 3446 – 3456. Doi: 10.1785/0120180135

Pavel, F., and R. Vacareanu (2015) Kappa and regional attenuation for Vrancea (Romania) earthquakes, J. Seismol. 19, 791 – 799. Doi: 10.1007/s10950-015-9490-3

Perron, V., F. Hollender, P. Bard, C. Gélis, C. Guyonnet-Benaize, B. Hernandez, and O.-J. Ktenidou (2017) Robustness of kappa (κ) measurement in low-to-moderate seismicity areas: Insight from a site-specific study in Provence, France, Bull. Seismol. Soc. Am. 107(5), 2272 – 2292. Doi: 10.1785/0120160374

Pikoulis, E.V., O.-J. Ktenidou, E.Z. Psarakis, and N.A. Abrahamson (2020) Stochastic modeling as a method of arriving at higher frequencies: An application to κ estimation, Journal of Geophysical Research: Solid Earth 125, doi: 10.1029/2019JB018768.

Pilz, M. and D. Fah (2017) The contribution of scattering to near-surface attenuation, J. Seismol. 21, 837 – 855. Doi: 10.1007/s10950-017-9638-4

Pilz, M., F. Cotton, R. Zaccarelli, and D. Bindi (2019) Capturing regional variations of hard-rock attenuation in Europe, Bull. Seismol. Soc. Am. 109(4), 1401-1418. Doi: 10.1785/0120190023

Purvance, M.D. and J.G. Anderson (2003) A comprehensive study of the observed spectral decay in strong motion accelerations recorded in Guerrero, Mexico, Bull. Seismol. Soc. Am. 93(2), 600-611. Doi: 10.1785/0120020065

Roumelioti, Z., Hollender F., and Gueguen P. (2020) Rainfall Induced Variation of Seismic Waves Velocity in Soil and Implication for Soil response: What the ARGONEST (Cephalonia, Greece) vertical array data reveal, Bull. Seism. Soc. Am. 110(2), 441-451. Doi: 10.1785/0120190183

Sadeghi-Bagherabadi, A., F. Sobouti, S. Pachhai, and A. Aoudia (2020) Estimation of geometrical spreading, quality factor and kappa in the Zagros Region, Soil Dynamics and Earthquake Engineering 133, 10.1016/j.soildyn.2020.106110.

Saxen, S., J. Anderson, and R. Motamed (2018) Incorporation of site-specific attenuation model using kappa in broadband simulations. Proceedings of the 11th US National Conference on Earthquake Engineering Los Angeles United States, June 25-29.

SENES Consultants Limited (2009) Environmental Impact Statement New Nuclear Darlington Environmental Assessment. Report No. NK054-REP-07730-00029.

Silva, W. and R.B. Darragh (1995) Engineering Characterization of Strong Motion Recorded at Rock Sites. Electric Power Research Institute Report No. TR-1022632.

Sonley, E. and G.M. Atkinson (2005) Empirical relationship between moment magnitude and Nuttli magnitude for small-magnitude earthquakes in southeastern Canada, Seism. Res. Lett. 76(6), 752 – 755. Doi: 10.1785/gssrl.76.6.752

Sonnemann, T., B. Halldorsson, and S. Jonsson (2019) Automatic estimation of earthquake high frequency strong motion spectral decay in south Iceland, Soil Dynamics and Earthquake Engineering 125, doi: 10.1016/j.soildyn.2019.05.015.

Sotiriadis, D., B. Margaris, N. Klimis, A. Sextos (2021) Implication of high frequency decay parameter, κ-kappa, in the estimation of kinematic soil structure interaction effects, Soil Dynamics and Earthquake Engineering 144, doi: 10.1016/j.soildyn.2021.106665.

Stanko, D., S. Markusic, T. Korbar, and J. Ivancic (2020) Estimation of the high frequency attenuation parameter kappa for the Zagreb (Croatia) seismic stations, Applied Sciences 10, doi: 10.3390/app10248974.

Tanircan, G. and S.U. Dikmen (2018) Variation of high frequency spectral attenuation (kappa) in vertical arrays, Soil Dynamics and Earthquake Engineering 113, doi: 10.1016/j.soildyn.2018.06.016

Thatcher, W. and T.C. Hanks (1973) Source parameters of Southern California earthquakes, Journal of Geophysical Research 78(35), 8547 – 8576. doi: 10.1029/JB078i035p08547

Tsai, C.-C.P. and K.-C. Chen (2000) A model for the high cut process of strong motion accelerations in terms of distance, magnitude, and site condition: an example from the SMART 1 array, Lotung Taiwan, Bull. Seismol. Soc. Am. 90(6), 1535-1542. Doi: 10.1785/0120000010

Tsurugi, M., R. Tanaka, T. Kagawa, K. Irikura (2020) High-frequency spectral decay characteristics of seismic records of inland crustal earthquakes in Japan: evaluation of the f_{max} and κ models, Bull. Seismol. Soc. Am. 110(2), 452-470. Doi: 10.1785/0120180342

Van Houtte, C., S. Drouet, and F. Cotton (2011) Analysis of the origins of κ (kappa) to compute hard rock to rock adjustment factors for GMPE's, Bull. Seismol. Soc. Am. 101(6), 2926 – 2941. Doi: 10.1785/0120100345

Van Houtte, C., O.-J. Ktenidou, T. Larkin, and C. Holden (2014) Hard-site $κ_0$ (kappa) calculations for Christchurch, New Zealand, and comparison with local ground-

motion prediction models, Bull. Seismol. Soc. Am. 104(4), 1899 – 1913. Doi: 10.1785/0120130271

Vandana, A. Kumar, S.C. Gupta, O.P. Mishra, A. Kumar, and Sandeep (2017) Source parameters and high frequency characteristics of local events (0.5<ML<2.9) around Bilaspur region of the Himachal Himalaya, Pure Appl. Geophys. 174, 1643-1658. Doi: 10.1007/s00024-017-1493-2

Wen, J. and X. Chen (2012) Variation in f_{max} along the ruptured fault during the Mw 7.9 Wenchuan earthquake of 12 May 2008, Bull. Seismol. Soc. Am. 102(3), 991-998. Doi: 10.1785/0120110105

Sun, X., X. Tao, S. Duan and C. Liu (2013) Kappa derived from accelerograms recorded in the 2008 Wenchuan mainshock, Journal of Asian Earth Sciences 73, 306-316. Doi: 10.1016/j.jseaes.2013.05.008

Xu, B., E.M. Rathje, Y. Hashash, J. Stewart, K. Campbell, and W.J. Silva (2019) κ_0 for soil sites: observations from KiK-net sites and their use in constraining small strain damping profiles for site response analysis, Earthquake Spectra 36, 111-137. Doi: 10.1177/8755293019878188

Yadav, R., D. Kumar, and S. Chopra (2018) The high frequency decay parameter κ (kappa) in the region of North East India, Open Journal of Earthquake Research 7, 141-159. Doi: 10.4236/ojer.2018.72009

Zafarani, H. and B. Hassani (2013) Site response and source spectra of S waves in the Zagros region, Iran, J. Seismol. 17, 645-666. Doi: 10.1007/s10950-012-9344-1

Zandieh, A., K.W. Campbell, and S. Pezeshk (2016) Estimation of κ_0 implied by high frequency shape of NGA-West2 ground motion prediction equations, Bull. Seismol. Soc. Am. 106(3), 1342-1256. Doi: 10.1785/0120150356

<div align="center">Chapter 2</div>

2 Earthquake Ground Motion and Site Characterization Database for Earthquakes in Eastern Canada[1]

2.1 Introduction

Compiled ground motion databases, including event and site metadata, are required for studies that characterize earthquake source, path, and site effects on ground shaking. Eastern Canada is a stable continental region, for which there are relatively abundant ground motion recordings for small to moderate earthquakes (moment magnitude ($\mathbf{M}$)<5) but few records for larger events. Nevertheless, larger potentially-damaging earthquakes such as the 1925 Charlevoix-Kamouraska ($\mathbf{M}$6.2), 1929 Laurentian slope Newfoundland and Nova Scotia ($\mathbf{M}$7.2), 1935 Timiskaming ($\mathbf{M}$6.1), 1982 Miramachi ($\mathbf{M}$5.7) and 1988 Saguenay ($\mathbf{M}$5.9) earthquakes do occur [Lamontagne et al., 2018]. Thus, understanding ground motions is vital to the assessment of seismic hazard in the region.

Ground motion databases that have been compiled for other regions have been referenced widely in seismological and engineering studies. Examples of such databases include the PEER NGA-West database [Ancheta et al., 2013], and PEER NGA-East database [Goulet et al, 2014; 2021] – both of which have been useful in the development of ground motion models used in hazard assessments. The NGA-East database compiled ground motions in the central and eastern regions of north America (CENA) for magnitudes greater than 2.5;

---

[1] A version of this chapter has been submitted for publication to Earthquake Spectra: Palmer S.M., Atkinson G.M., Ladak, S., Molnar, S. and Ghofrani H. (XXXX) Earthquake Ground Motion and Site Characterization Database for Earthquakes in Eastern Canada. Earthquake Spectra. The database has been published: Palmer, S.M.., G.M. Atkinson, S. Ladak, S. Molnar, and H. Ghofrani (2022) Eastern Canada Earthquake Ground Motion and Site Characterization Database. DesignSafe, doi: 10.17603/ds2-3b7s-yw72.

it comprises records from 96 candidate earthquakes, of which ~ 1/3 are from eastern Canada. Thus, the NGA-East database has some overlap with the database compiled in this study.

This report aims to provide a high-quality database of Fourier Spectra and Response Spectra from earthquake records in eastern Canada having **M**≥1.5 at epicentral distances ≤150 km. The distance range is selected to focus on records for which path effects on high frequency amplitudes are not severe. For this purpose, Ktenidou et al. [2016] suggest restricting studies of high frequency ground motions to records within 100 – 150 km in central and eastern North America. Similarly, Palmer and Atkinson [2020] found that high frequency path effects in eastern Canada become most significant at distances beyond 50 – 150km, dependent on the location.

The Canadian National Seismic Network (CNSN) has 67 active seismic stations (as of September 2020) in eastern Canada. These stations record earthquakes continuously on a single component (vertical) or on 3 components (vertical and two orthogonal horizontal), at sampling rates of 40 or 100 samples per second. The continuous records are stored and made available through Earthquakes Canada – Canadian National Data Center waveform archive (see Data and Resources). Our compiled database draws from these resources to provide data resources for events of **M**≥1.5 in eastern Canada recorded at distances ≤150 km.

The compiled database provides the following products:

1) an event table that summarizes earthquake event metadata including date, time, location, magnitudes, number of records, and record stations;

2) station metadata includes station names, locations, geological and mounting conditions, and p- and s-wave velocity profiles;

3) instrument-corrected time series;

4)   Fourier amplitude spectra for the vertical and horizontal components, for several window choices; the horizontal component is represented by the Effective Amplitude Spectra (EAS) [Kottke et al., 2018, 2021]; and

5)   5%-damped psueudo-spectral acceleration (PSA) response spectra.

This article describes the database generation criteria, compilation process and record processing approach. All databases can be freely accessed via: https://doi.org/10.17603/ds2-3b7s-yw72 [Palmer et al., 2022].

2.2   Data Selection: Earthquake Events and Stations

We considered earthquakes recorded within the region 43ºN to 60ºN, 95ºW to 50ºW from 1989/01/01 to 2020/09/01. For each event we adopted the epicenter location provided by Earthquakes Canada. Moment magnitude, if not available from Earthquakes Canada (see Data and Resources), was estimated using the conversion equations of Fereidoni et al. [2012].

We considered only those stations having a minimum sampling rate of 100 Hz (to maximize the useable bandwidth), and recording at least 10 events of any magnitude type (M) >2 within 100 km. We further limited our study to stations having some site characterization information and several recordings of events of **M** ≥3.5 earthquakes. These criteria resulted in the selection of 25 seismic stations, as listed in Table 2.1. Station GBN in Nova Scotia was included due to its unique location and geology, even though it did not strictly meet the criteria for number of events. Earthquakes within 150 km of each selected seismic station were considered. Figure 2.1 shows the epicentral distribution of 3357 earthquakes and the location of 25 seismic stations included in the database.
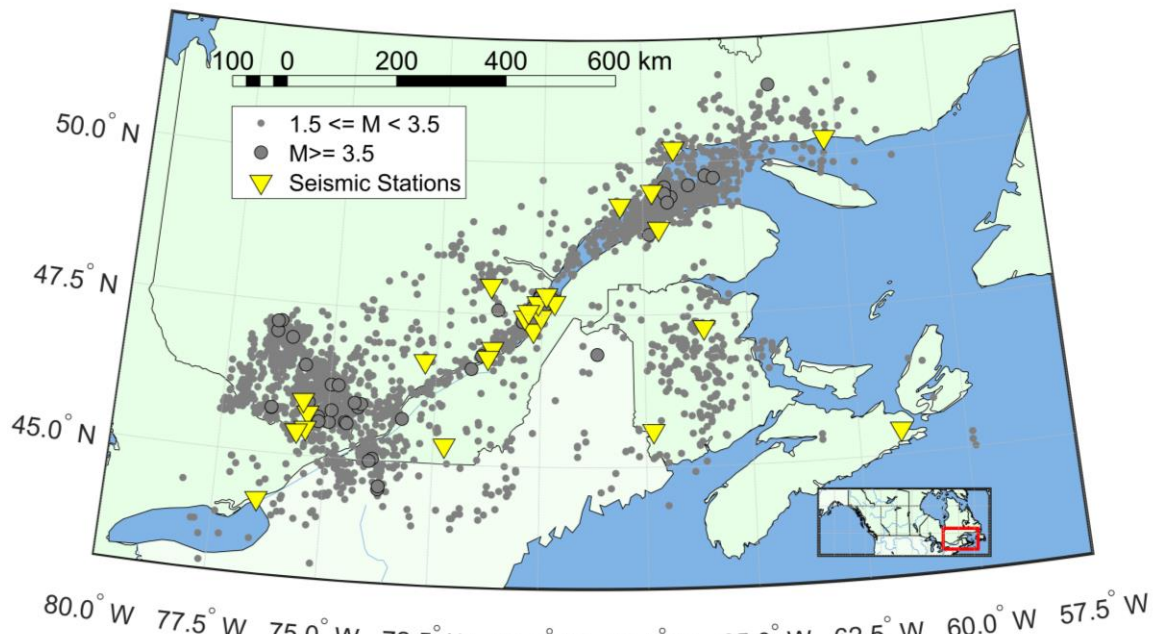
Figure 2.1: Earthquake locations (grey circles) for M≥3.5 (large with black ring) and M<3.5 (small) and the seismic stations (yellow triangles) in this database.

Table 2.1: Location, data channels (band code, instrument code, and orientation code), and operational status of seismic station in Eastern Canada included in the database. The data channels consist of 3 letters: the first letter represents a short-period (E) or broadband (H) seismometer, the second represents a high gain (H) broadband seismometer, and the last letter is the orientation of the instrument in either east-west(E), north-south (N) or the vertical (Z) direction [Incorporated Research Institutions for Seismology, 2012]. The recording time provides two date ranges and if the seismometer is still active, we represent the second date with the word active.

Station Name	Location	Data Channels	Recording Time Frame YYYY/MM/DD
A11	47.2431° N, 70.1969° W	EHE/N/Z and HHE/N/Z	1994/10/16 – active
A16	47.4680° N, 70.0096° W	EHE/N/Z and HHE/N/Z	1994/10/15 – active
A21	47.7045° N, 69.6892°W	EHE/N/Z and HHE/N/Z	1994/10/17 – active

A54	47.4568° N, 70.4134° W	EHE/N/Z and HHE/N/Z	1994/10/02 – active
A61	47.6936° N, 70.0914° W	EHE/N/Z and HHE/N/Z	1987/10/30 – active
A64	47.8264° N, 69.8914° W	EHE/N/Z and HHE/N/Z	1987/10/30 – active
BATG	47.2767° N, 66.0599° W	HHE/N/Z	2005/10/22 – 2017/09/26
BCLQ	46.9264° N, 71.1727° W	HHE/N/Z	2007/11/02 – active
CNQ	49.3020° N, 68.0746° W	EHZ	1996/02/01 – active
DAQ	47.9627° N, 71.2437° W	EHZ	1995/11/08 – 2017/08/30
DPQ	46.6803° N, 72.7771° W	EHZ AND HHE/N/Z	1996/09/20 – active
GAC	45.7032° N, 75.4776° W	EHZ AND HHE/N/Z	1993/04/27 – active
GBN	45.4079° N, 61.5128° W	HHE/N/Z	2005/10/17 – active
GSQ	48.9142° N, 67.1106° W	EHZ	1996/01/09 – 2019/01/31
ICQ	49.5223° N, 67.2715° W	EHZ and HHE/N/Z	1996/02/15 – active
KGNO	44.2272° N, 76.4934° W	HHE/N/Z	2015/05/13 – active
LMQ	47.5485° N, 70.3258° W	EHZ and HHE/N/Z	2012/05/01 – active
MCNB	45.5958° N, 67.3198° W	HHE/N/Z	2016/05/21 – active
MOQ	45.3115° N, 72.2409° W	EHZ	1996/02/01 – active
NATG	50.2872° N, 62.8102° W	HHE/N/Z	2005/11/26 – 2017/09/22
ORIO	45.4515° N, 75.5110° W	HHE/N/Z	2016/12/02 – active
OTT	45.3942° N, 75.7167° W	EHZ and HHE/N/Z	1992/06/01 – active
QCQ	46.7792° N, 71.2756° W	EHZ and HHE/N/Z	1997/11/01 – active
SMQ	50.2225° N, 66.7025° W	EHZ	1996/02/02 – active
VABQ	45.9047° N, 75.6079° W	HHE/N/Z	2010/11/29 – 2018/05/18

2.3   Site Metadata Database

In situ non-invasive site characterization field work was completed by Samantha Palmer with two field assistants: Melanie Postman and Alex Bilson Darko in summer and fall 2017 to obtain a multi-method site characterization at the 25 seismic station sites. Field

techniques involved active surveys such as a refraction survey, and a multi-channel analysis of surface waves and passive surveys which included ambient vibration array surveys and single station horizontal-to-vertical spectral ratio (HVSR). In addition, rock samples were collected at as many stations as possible. Processing of the field data was primarily completed by Sameer Ladak with a preliminary analysis done by Frederick Jackson. The survey techniques and computation of site characteristics are described in Ladak et al [2021] and Ladak [2020].

The field data were processed to determine the microtremor HVSR, Vs Profile, P-wave velocity (V_P) of lithological units, and the Poisson ratio of the subsurface beneath the station [Ladak, 2020; Ladak et al., 2021]. Earthquake HVSR were computed for all 3-component seismic stations. Earthquake HVSR were computed using the Konno Ohmachi [1998] (b-value 20) smoothed Fourier amplitude spectrum (FAS) where the horizontal, effective amplitude spectrum [Kotkke et al., 2018; 2021], was divided by the vertical spectrum. This database contains flatfiles for each station which show the resultant station site characterizations which include V_S profiles inferred for each station, which vary from shallow (<100 m) profiles to deeper profiles (>1km) [Cassidy, 1995; Kao et al., 2014; Kuponiyi et al., 2016; Bent et al., 2019; Ladak, 2020; Bent personal communication, 2021; Ladak et al. 2021; Stokoe, 2021].

The metadata for each site includes: i) Station Name; ii) Station Location; iii) Recording type; iv) Surficial Geology [Geological Survey of Canada, 2014]; v) Bedrock Geology [Energie et Ressources Naturelle Quebec, 2012; Keppie, 2000; Ontario Geological Survey, 2011; Department of Natural Resources Minerals, Policy and Planning Division., 2008]; vi) rock sample identification; vii) seismic instrument mounting and housing types; viii) average Poisson Ratio [Ladak, 2020; Ladak et al. 2021]; ix) microtremor HVSR [Ladak, 2020; Ladak et al. 2021]; x) earthquake HVSR; x) Vs Profiles (DINVER and PWSP from Ladak [2020; Ladak et al., 2021]); xi) Vp of lithological units [Ladak, 2020; Ladak et al., 2021]; and xii) curated velocity profiles from literature [Cassidy,

1995; Kao et al., 2014; Kuponiyi et al., 2016; Bent et al., 2019; Bent personal communication, 2021; Stokoe, 2021].

2.4   Record Database: Signal Processing

Velocity time series for all selected records were obtained from the AutoDRM system from Natural Resources Canada in SEED format (Data and Resources). The requested time series begin 70 seconds prior to the reported event time and contained a signal duration of 360 seconds. Many of the archived SEED files carry incorrect station response information in their header files. Dataless SEED files with the correct information for each station were obtained from Earthquakes Canada and the station response attributes were corrected accordingly.

Data processing was performed using a combination of the Seismic Analysis Code (SAC) program [Goldstein et al., 2003; Goldstien and Snoke, 2005] and Matlab. Using standard SAC procedures, the full time series was processed to obtain the instrument-corrected signal between 0.8 Hz and 0.8*Nyquist frequency (i.e., 40 Hz for 100 samples per second instruments); these procedures include removal of the mean and trends, tapering, and removal of the instrument response in the Fourier domain.

A Matlab script was used to update SAC earthquake event files to contain all reported event data, such as location of event, magnitude, etc., and the predicted P and S wave arrivals. The predicted P- and S-wave arrivals are computed by adding the expected travel times (as computed from a regional P- (6.0 km/s) and S-wave (3.7 km/s) velocity value and the hypocentral distance for the earthquake) to the reported origin time for the earthquake. A single analyst utilized SAC to manually select the P- and S-wave arrivals. As a primary check on the arrival picks, a MATLAB script was used to flag the manually selected arrivals which differed from the predicted arrivals by >2%. The flagged arrivals were reexamined to confirm or correct the P- and S-wave arrival times.

From the processed full time-series seismograms, windowed signals were generated. The time series were windowed using the Goulet et al. [2014; 2021] windowing technique to

produce a full signal, noise, P-wave, S-wave, and Coda wave signal. In this study, the "S-window" includes the S and Lg phases. Figure 2.2 shows a sample time series with the marked windows. Time series were cut, a 5% Hanning taper applied, and the time series were zero-padded to 400 seconds. Having a consistent time window ensures consistent frequency steps for all Fourier spectra. The Fast Fourier Transform was computed from the processed signals using SAC and then differentiated in the frequency domain to obtain the FAS of acceleration. From here on the FAS will refer to the FAS of acceleration.
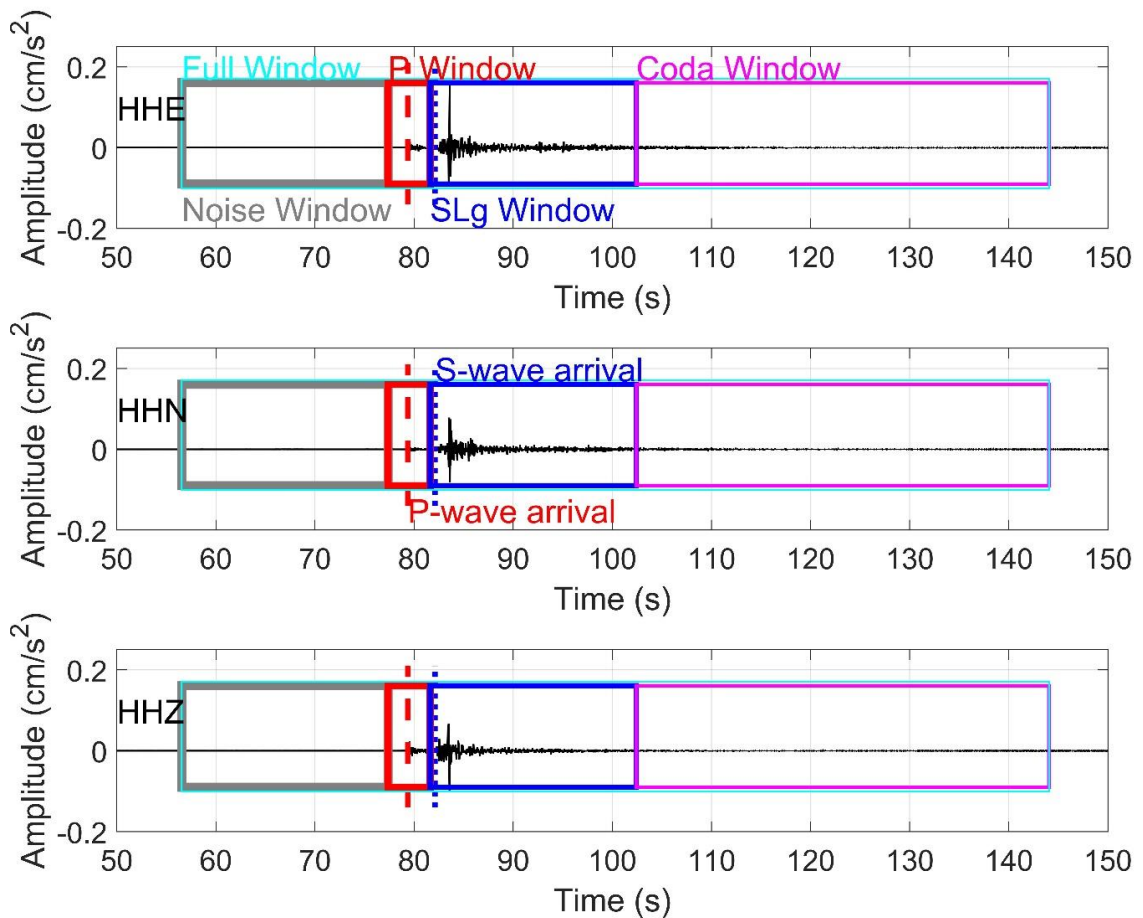
Figure 2.2: Sample time series of earthquake 2013/07/11 20:16:07 for station A21 showing the Goulet et al. [2014;2021] windowing method. The full window (cyan box), pre-event noise window (grey box), P-wave window (red box), S-wave window

(blue box), and Coda window (magenta box) are shown in each of the three components time series. The P wave arrival manual pick is shown by a vertical dashed red line and the S-wave arrival manual pick in dotted blue line.

FAS are generated for all records from a station – this can include the vertical, east-west, and north-south components. If a record has an east-west and north-south component then the effective amplitude spectra (EAS) [Kottke et al., 2018, 2021] was computed. We provide the Vertical and EAS Fourier spectra in our database. The resultant FAS were smoothed using a Konno and Ohmachi [1998] smoothing filter with a bandwidth coefficient b-value of 20; the smoothed FAS contains 400 log10-spaced frequency steps from 0.8 Hz to 40 Hz. Figure 2.3 shows a sample FAS before and after smoothing for the vertical and horizontal (EAS) components for the SLg and Noise windows. The smoothed FAS database contains a unique record name (data, time, and station); earthquake latitude, longitude, and depth; catalog magnitude and type [NRCan, 2020]; moment magnitude; the recorded station name, latitude, longitude, and elevation; component; the epicentral and hypocentral distances; the azimuth and back azimuth, origin time of the earthquake, the P and S-wave arrival times, the upper and lower frequencies for a signal-to-noise ratio (SNR)>3, and the smoothed FAS. The SNR is computed for all wave types using the Fourier amplitude spectral density (FASD) as outlined in Perron et al. [2018]. The FASD is the length-independent Fourier spectrum computed by dividing the FAS by the square root of the duration of the time window.
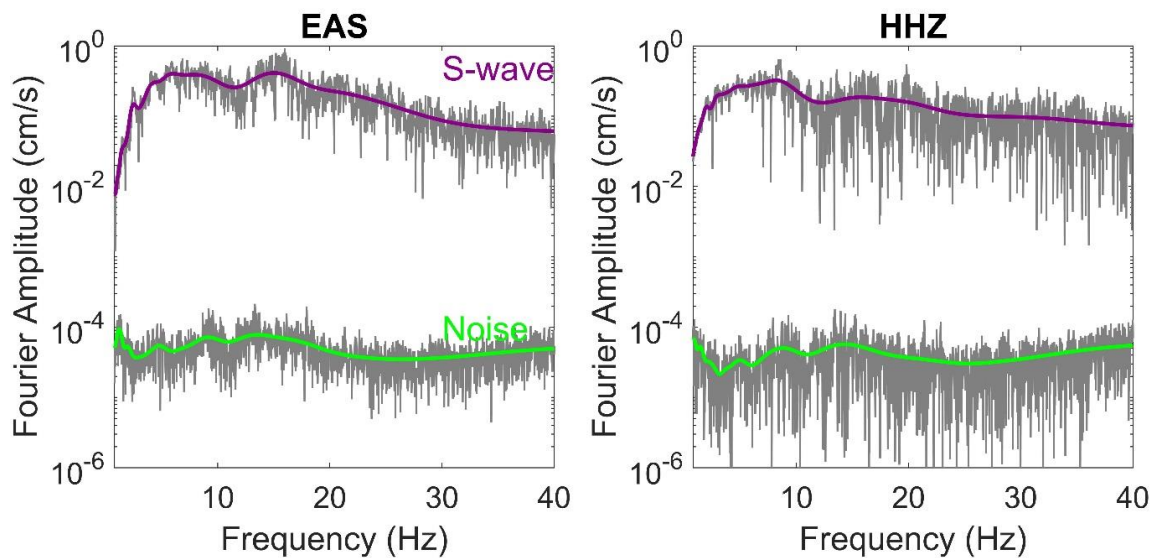
Figure 2.3: Sample Fourier amplitude spectrum of acceleration for earthquake 2013/07/11 20:16:07 recorded at station A21. The S-wave and noise window uncorrected (grey) are shown beneath the respective smoothed S-wave (purple) and noise window (green) Fourier amplitude spectrum of acceleration for the EAS (left) and the vertical spectrum (right).

5%-damped response spectra are computed for all records from a station using the full signal window of the processed time series [Goulet et al., 2014; 2021]. We utilized Boore's [2010] RotDnn method to compute response spectra for period-dependent rotation angles (D) for 3 fractiles (nn): 0 (minimum), 50 (median), and 100 (maximum). When a record has two orthogonal horizontal velocity time series, we converted the time series to acceleration and then computed the rotated acceleration time series from 0 to 180 degrees in steps of 1 degree. We compute response spectrum at 30 frequencies log10-spaced from 0.8 to 40 Hz. The response spectrum was computed at each angle and the resultant pseudo-spectral acceleration (PSA) is the fractile spectral amplitude at all angles for a given frequency. The response spectrum database contains a unique record name (data, time, and station); earthquake latitude, longitude, depth; catalog magnitude and type [NRCan, 2020]; moment magnitude; recorded station name; station latitude and

longitude; epicentral distance; hypocentral distance; the 5%-PSA at 30 frequencies; the peak ground velocity (PGV); and the peak ground acceleration (PGA).

The record database comprises: i) processed time series; ii) unsmoothed Fourier amplitude spectrum for the vertical and horizontal (EAS) components for each Goulet et al. [2014; 2021] window; iii) smoothed Fourier amplitude spectrum for the vertical and horizontal (EAS) components for each Goulet et al. [2014; 2021] window; and iv) the 5% damped response spectrum for the orientation-independent horizontal component using the Goulet et al. [2014; 2021] full signal time series.

2.5   Summary/Conclusions

This report describes a compiled earthquake record database for eastern Canada that includes processed time series, Fourier amplitude spectra (unsmoothed and smoothed) for horizontal and vertical components for Goulet et al.'s [2014, 2021] windows, and station metadata describing site conditions for each station. The database includes 39,424 records from 3357 events of $\mathbf{M} \geq 1.5$ recorded at hypocentral distances from 5 to 150 km. The database has been used by Palmer and Atkinson [2020] to better understand high-frequency ground motions on rock sites, but may have many other potential uses.

We caution that the data from the smaller earthquakes may have a limited bandwidth for which SNR>3. Moreover, arrival pick error has not been estimated.

The database records are publicly available at: https://doi.org/10.17603/ds2-3b7s-yw72 [Palmer et al., 2022].

2.6   Data and Resources

The earthquake database was provided from Natural Resources Canada's Earthquakes Canada - Geological Survey of Canada (GSC) on-line bulletin earthquake search at http://www.earthquakescanada.nrcan.gc.ca/stndon/NEDB-BNDS/bulletin-en.php (last accessed September 2020). The seismograms for the earthquakes used in this study were provided by Earthquakes Canada – GSC email data service at

AutoDRM@seismo.NRCan.gc.ca (last accessed September 2020). rdSEED is available from https://ds.iris.edu/ds/nodes/dmc/software/downloads/rdseed/. Seismic Analysis Code (SAC) program used for processing is available at https://ds.iris.edu/ds/nodes/dmc/software/downloads/sac/ [Goldstein et al. 2003; Goldstein and Snoke, 2005].

2.7   References

Ancheta, T.D., R.B. Darragh, J.P. Stewart, E. Seyhan, W.J. Silva, B.S.J. Chiou, K.E. Wooddell, R.W. Graves, A.R. Kottke, D.M. Boore, T. Kishida, and J.L. Donahue (2013) PEER NGA-West2 Database. PEER Report No. 2013/03.

Bent, A. (2011) Moment magnitude (MW) conversion relations for use in hazard assessment in eastern Canada, Seism. Res. Lett. 82, 984 – 990. doi: 10.1785/gssrl.82.6.984

Bent, A., H. Kao, and D. Darbyshire (2019) Structure and anisotropy of the crust and upper mantle along the St. Lawrence Corridor, eastern Canada, from the Charlevoix Seismic Zone to the Gulf of St. Lawrence, Seism. Res. Lett. 90, 950.

Boore, D.M. (2010) Orientation-independent, nongeometric-mean measures of seismic intensity from two horizontal components of motion, Bull. Seismol. Soc. Am. 100(4), 1830–1835. doi: 10.1785/0120090400

Cassidy, J.F. (1995) A comparison of the receiver structure beneath stations of the Canadian National Seismograph Network, Can. J. Earth Sci. 32(7): 938–951. doi: 10.1139/e95-079

Department of Natural Resources Minerals, Policy and Planning Division (2008) Map NR-1 Bedrock Geology of New Brunswick. Available at: https://www2.gnb.ca/content/gnb/en/departments/erd/energy/content/minerals/content/bedrock_mapping.html (accessed 2021 November)

Energie et Ressources Naturelle Quebec (2012) Geology of Quebec DV2012-07 1:2,000,000 map. Available at: https://mern.gouv.qc.ca/english/mines/publications/publications-maps.jsp (accessed 2021 November).

Fereidoni, A., G. M. Atkinson, M. Macias, and K. Goda (2012) CCSC: A composite seismicity catalog for earthquake hazard assessment in major Canadian cities, Seismol. Res. Lett. 83(1), 179 – 189. doi: 10.1785/gssrl.83.1.179

Geological Survey of Canada (2014) Canadian Geoscience Map 195 Surficial Geology of Canada. Catalogue No. M183-1/195-2014E-PDF. doi: 10.4095/295462.

Goldstein, P., D. Dodge, M. Firpo, and L. Minner (2003) SAC2000: Signal processing and analysis tools for seismologists and engineers, The IASPEI International Handbook of Earthquake and Engineering Seismology, Academic Press, London.

Goldstein, P. and A. Snoke (2005) SAC Availability for the IRIS Community, Incorporated Institutions for Seismology Data Management Center Electronic Newsletter.

Goulet, C.A., T. Kishida, T.D. Ancheta, C.H. Cramer, R.B. Darragh, W.J. Silva, Y.M.A Hashash, J. Harmon, J.P. Stewart, K.E. Wooddell, and R.R. Youngs (2014) PEER NGA-East database. PEER No. Report 2014/17.

Goulet, C.A., T. Kishida, T.D. Ancheta, C.H. Cramer, R.B. Darragh, W.J. Silva, Y.M.A Hashash, J. Harmon, G.A. Parker, J.P. Stewart, and R.R. Youngs (2021) PEER NGA-East database, Earthquake Spectra 37, 1331-1353. doi: 10.1177/87552930211015695

Incorporated Research Institutions for Seismology (2012) SEED Reference Manual: Appendix A. SEED Format Version 2.4, 133 – 140.

Kao, H., S.J. Shan, J.F. Cassidy, and S.A Dehler (2014) Crustal structure in the Gulf of the St. Lawrence Region, Eastern Canada: Preliminary results from receiver function analysis. Geological Survey of Canada Open File 7456. doi:10.4095/293724.

Keppie, J.D. (2000) Geological map of the province of Nova Scotia: Nova Scotia Department of Natural Resources, Minerals and Energy Branch, Map ME 2000-1, scale 1:500 000. Available at: https://novascotia.ca/natr/meb/download/mg/map/htm/map_2000-001.asp (accessed 2021 November).

Konno K. and T. Ohmachi (1998) Ground motion characteristics estimated from spectral ratio between horizontal and vertical components of microtremor, Bull. Seism. Soc. Am. 88, 228–241.

Kottke, A., N.A. Abrahamson, D.M. Boore, Y. Bozorgnia, C. Goulet, J. Hollenback, T. Kishida, A.D. Kiureghian, O.J. Ktenidou, N. Kuehn, E.M. Rathje, W.J. Silva, E. Thompson, and X. Wang. (2018) Selection of random vibration procedures for the NGA-East project. PEER Report No. 2018/05.

Kottke, A., N.A. Abrahamson, D.M. Boore, Y. Bozorgnia, C. Goulet, J. Hollenback, T. Kishida, O.J. Ktenidou, E.M. Rathje, W.J. Silva, E. Thompson, and X. Wang (2021) Selection of random vibration theory procedures for the NGA-East project and ground-motion modeling, Earthquake Spectra 37, 1420-1439. doi: 10.1177/87552930211019052

Ktenidou, O.J., N.A. Abrahamson, R.B. Darragh, and W.J. Silva (2016) A Methodology for the Estimation of Kappa (κ) from Large Datasets: Example Application to Rock Sites in the NGA-East Database and Implications on Design Motions. PEER Report No. 2016/01.

Kuponiyi, A.P., H. Kao, C.R. van Staal, S.E. Dosso, J.F. Cassidy, and G.D. Spence (2016) Upper crustal investigation of the Gulf of Saint Lawrence region, eastern Canada using ambient noise tomography, Jour. Geo. Res. Solid Earth 122, 5208–5227. doi: 10.1002/2016JB013865

Ladak, S. (2020) Earthquake site characterization of rock site in eastern Canada and stiff ground sites in Vancouver, British Columbia. MSc Thesis, University of Western Ontario, https://ir.lib.uwo.ca/etd/6972.

Ladak, S., S. Molnar, and S.M. Palmer (2021) Multimethod site characterization to verify the hard rock (site class A) assumption at 25 seismograph stations across eastern Canada, Earthquake Spectra 37, 1487–1515. doi: 10.1177/87552930211001076

Lamontagne, M., S. Halchuk, J.F. Cassidy, and G.C. Rogers (2018) Significant Canadian earthquakes 1600-2017. Geological Survey of Canada Open File 8285. doi: 10.4095/311183

Natural Resources Canada's Earthquakes Canada - Geological Survey of Canada (GSC) (2020) On-line bulletin earthquake. Available at: http://www.earthquakescanada.nrcan.gc.ca/stndon/NEDB-BNDS/bulletin-en.php (accessed 2020 September).

Ontario Geological Survey (2011) Bedrock Geology map for the Province of Ontario scale 1:250000 MRD126. Available at: https://www.geologyontario.mndm.gov.on.ca/ogsearth.html#bedrock-geology (accessed 2021 November).

Palmer, S.M. and G.M. Atkinson (2020) The high-frequency decay slope of spectra (kappa) for $\mathbf{M} \geq 3.5$ earthquakes on rock sites in eastern and western Canada, Bull. Seismol. Soc. Am. 110(2), 471–488. doi: 10.1785/0120190206

Palmer, S.M., G.M. Atkinson, S. Ladak, S. Molnar, and H. Ghofrani (2022) Eastern Canada earthquake ground motion and site characterization database. DesignSafe, doi: 10.17603/ds2-3b7s-yw72.

Perron, V., F. Hollender, P. Bard, C. Gélis, C. Guyonnet-Benaize, B. Hernandez, and O.-J. Ktenidou (2017) Robustness of kappa (κ) Measurement in low-to-moderate seismicity areas: Insight from a site-specific study in Provence, France, Bull. Seismol. Soc. Am. 107(5), 2272 – 2292. doi: 10.1785/0120160374

Sonley, E. and G.M. Atkinson (2005) Empirical relationship between moment magnitude and Nuttli magnitude for small-magnitude earthquakes in southeastern Canada, Seism. Res. Lett. 76(6),– 752 - 755. doi: 10.1785/gssrl.76.6.752

Stokoe, K.H., G. Kim, and S. Hwang (2021) Shear wave velocity profiling using the SAWS method with "Raptor" as the active seismic source in Quebec, Canada: Data Summary. Report GIRS-2021-10. doi: 10.34948/G44W29.

Chapter 3

3 The high-frequency decay slope of spectra (kappa) for **M**≥3.5 earthquakes on rock sites in eastern and western Canada[2]

3.1 Introduction

The high-frequency characteristics of ground motions and how they depend on site conditions is consequential for seismic design and safety reviews for many structures, particularly nuclear plants and dams founded on very hard rock, which can effectively transmit high-frequency motion [e.g., Leblanc and Klimkiewicz, 1994]. This work examines the high-frequency decay slope, kappa (κ), and its interaction with the Quality factor (Q) on rock sites in eastern and western Canada, based on the Fourier spectra of earthquakes of **M**≥3.5 (where **M** is moment magnitude).

Ground motions (Y) recorded at a site are modelled in the Fourier domain as the product of the source (E), path (P), site (G), and instrument (I) responses:

$$Y(M_0, R, f) = E(M_0, f)P(R, f)G(f)I(f) \qquad (3.1)$$

where M_0 is the seismic moment, R is a distance parameter such as hypocentral distance, and f is frequency [Hanks and McGuire, 1981; Boore 1983; Boore, 2003]. To characterize the influence of site conditions on ground motions, we need to separate the effects of the site from those of source and path. Path effects are usually described by the

---

combination of geometric spreading, which is frequency-independent, and anelastic attenuation, which is an increasing function of frequency:

$$P(R,f) = Z(R)e^{-\frac{\pi f R}{Q(f)\beta}} \tag{3.2}$$

where β is the average mid-crustal shear wave velocity, and $Z(R)$ represent geometrical spreading [Boore, 2003]. In Equation (3.2), we have represented anelastic attenuation using the regional Quality factor, Q, to which it is inversely proportional. Atkinson and Mereu [1992] studied attenuation in southeastern Canada and determined the relationship Q=670$f^{0.33}$. Mereu et al. [2013] determined a similar relation for Q in southeastern Canada, $526f^{0.51}$, applicable for frequencies of 1Hz to 43 Hz. Moreover, they show that there is a trade-off between the constant and the exponent in Q models, such that many models proposed for eastern North America are roughly equivalent to Q ~ $500f^{0.5}$. In western Canada, Atkinson [1995] determined that Q=380$f^{0.39}$ from 1 to 15 Hz; in a later study [Atkinson, 2005], a model given by Q=229$f^{0.6}$ from 0.5 Hz to 15 Hz was determined, using records beyond 250 km. Farahbod et al. [2016] suggest Q=72$f^{0.91}$ across a frequency range of 2 Hz to 16Hz. Studies from California suggest similar Q models, such as Raoof et al.'s [1999] Q=180$f^{0.45}$ and Yenier and Atkinson's [2015] Q=max(100, 170$f^{0.45}$). Considering the trade-off issue between the constant and the exponent, as raised by Mereu et al. [2013], these western Q models could be generalized as Q ~ $200f^{0.5}$.

The site component of ground motions (G) is a combination of amplification and de-amplification effects, both of which are frequency-dependent. The amplification effects depend on the velocity gradient and layering beneath the site [e.g., Boore and Joyner, 1991]. The de-amplification effects can be described by a steady linear decay of the log of spectral amplitude with increasing frequency, resulting in a site-based attenuation of high-frequency ground motion. The slope of the decay trend is characterized by the parameter kappa (κ), originally introduced by Anderson and Hough [1984]:

$$A(f) = A_0 e^{-\pi \kappa f} \tag{3.3}$$

where A is the Fourier amplitude of acceleration for the S-wave window, A_0 is the amplitude level, and κ is the spectral decay parameter. κ can be considered to comprise several components [Ktenidou et al., 2014]:

$$\kappa = \kappa_0 + \kappa_s + \tilde{\kappa}(R_e) \tag{3.4}$$

including a site-specific portion (κ_0), a source-dependent portion (κ_S) and a distance-dependent path component, which is attributed to the anelastic attenuation along the path ($\tilde{\kappa}(R_e)$). The path component of κ is inversely proportional to the Quality factor [Hough and Anderson, 1988]. Due to its significant engineering impact, kappa has become a topic of renewed interest in the last decade. Kappa has been measured in many regions, for example: eastern and western Canada [e.g., Atkinson, 1996; Ktenidou et al., 2016], Central and Eastern North America [e.g., Campbell, 2009; Campbell et al., 2014], United States [e.g., Anderson and Hough, 1984; Kilb et al., 2012], France [e.g., Drouet et al., 2010], Greece [e.g., Ktenidou et al., 2013], Italy [e.g., Castro et al., 2000], Europe [e.g., Pilz et al., 2019], Switzerland [e.g., Edwards et al., 2011], New Zealand [e.g., Van Houtte et al., 2014], Japan [e.g., Van Houtte et al., 2011], and Taiwan [e.g., Lai et al., 2016]. Studies use a variety of methods to measure kappa, as outlined in Ktenidou et al. [2014]. Despite the plethora of studies that have measured kappa, scientific consensus on the physical parameters driving kappa is elusive. It is widely viewed that kappa is mainly driven by near-surface attenuation and is thus, primarily a site parameter. However, there are studies relating kappa to each of the ground-motion components: source [e.g., Papageorgiou and Aki, 1983; Wen and Chen, 2012; Beresnev, 2019], path [e.g., Anderson, 1991; Humphrey and Anderson, 1992], and site [e.g., Anderson and Hough, 1984; Campbell, 2009; Drouet et al., 2010; Edwards et al., 2015; Pilz and Fah, 2017; Parolai, 2018]. Other studies have suggested seasonal fluctuations in kappa values and its dependence on the installation design of the seismic instrument [Hollender, 2019] as other potential factors that obscure kappa's physical meaning. We do not attempt to

define the physical parameters that influence kappa in this study. Our aim is to measure kappa empirically within the framework for which it is used in ground motion models.

A few older studies have estimated kappa on rock sites in eastern and western Canada. Atkinson [1996] examined kappa values in Ontario, Quebec and New Brunswick and determined that there was no resolved kappa effect on vertical-component spectra for hard-rock sites in most parts of eastern Canada (horizontal components were not widely available at the time). Atkinson suggested an upper bound kappa value of 0.004 s (i.e., 4ms) for hard-rock sites using the Hanks [1982] f_{max} method of estimating kappa. However, she reported higher kappa values, of 20 to 40ms, for sites within the fractured rocks of the Sudbury and Charlevoix meteor impact craters. In Western Canada (British Columbia), Atkinson [1996] determined a regional kappa value of 11 ± 2ms (also from the vertical component). Campbell et al. [2014] reviewed existing studies for Central and Eastern North America to suggest an overall regional kappa value of 6ms for rock (horizontal component). Ktenidou et al. [2016] determined a kappa value of 7ms for rock sites, using the NGA-East Database [Goulet et al., 2014]. Thus, previous studies suggest a range of possible kappa values from <4 to 40ms for rock sites in Canada and point to the potential for variability due to rock conditions such as the degree of deep-seated fracturing.

 To understand the variability of kappa in eastern and western Canada we compile a database of earthquake ground motions on rock sites and a few soil sites and examine high-frequency site effects on both the vertical and horizontal component. The study is motivated both by the renewed interest in kappa and the availability of richer datasets than have been used in previous studies for rock sites.

3.2   Database and Methods

3.2.1   Database Compilation

We compiled three-component ground motions recorded at 100 samples/second on broadband seismographic stations of the Canadian National Seismographic Network

(CNSN) (see Data and Resources Section). Records were selected based on magnitude-distance criteria. Natural Resources Canada reports earthquake magnitudes on several scales, including the local magnitude, body wave magnitude, and Nuttli magnitude scales. To better reflect the earthquake size and provide one consistent magnitude type, we convert all magnitudes to moment magnitude (**M**) using the reported **M** (i.e., from global or regional moment tensor solutions) or applying the conversion equations of the Fereidoni et al. [2012] Composite Canadian Seismicity Catalogue. We consider records for earthquakes of **M**≥3.5 within an epicentral distance of 150 km in eastern Canada and 100 km in western Canada.

Figure 3.1 illustrates the expected shape of the Fourier amplitude spectrum of acceleration and its dependence on magnitude, distance, and kappa. The figure assumes a simple Brune source spectrum (Equation 3.1, with Brune-model spectrum as given by Boore [2003]) modified to account for frequency-dependent regional anelastic attenuation effects and kappa. The figure shows that regional anelastic attenuation effects will exert a significant effect on the high-frequency slope at distances of >100 km. The rationale for restricting the distance range for kappa studies is to ensure that the site component of kappa is not overwhelmed by the path component. Moreover, by restricting the distance we avoid ray paths of distant earthquakes that are affected by multiple regional attenuation parameters. This facilitates a simple approximation for the path and site components of kappa. Ktenidou et al. [2016] suggest that in Central and Eastern North America, measured values of kappa are dominated by the site component for distances out to 50 – 100 km. In this study, we initially consider observations out to 150 km in eastern Canada and to 100 km in western Canada. The expanded distance range for eastern Canada, 50 – 100 km beyond the range suggested by Ktenidou et al. [2016], allows us to empirically examine the trend in kappa with distance. For western Canada, where data are more abundant, we examine data only to 100 km to avoid additional path complications. We explicitly examine the effects of anelastic attenuation of the measured values of kappa within these distance ranges both jointly by determining a site-specific kappa and apparent Quality factor and using a fixed regional anelastic attenuation and

determine site-specific kappa. We include only stations that have recorded a minimum of 5 earthquakes.
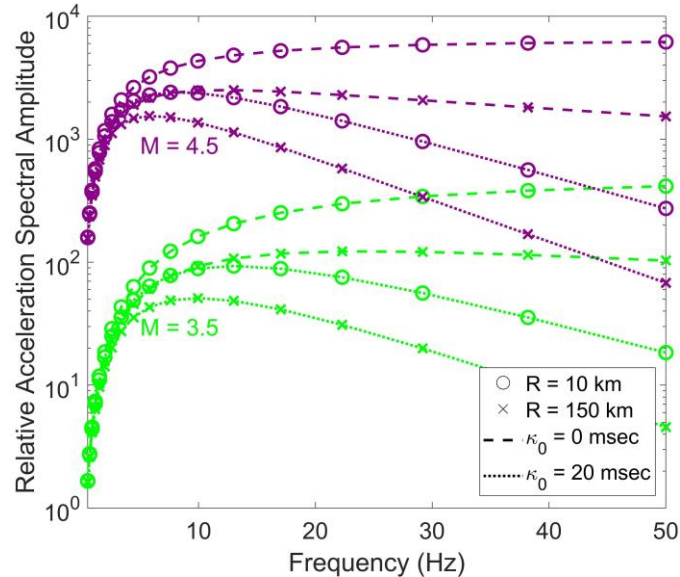
Figure 3.1: Ideal Brune spectral shape for M3.5 (lower 4 lines) and M4.5 (upper 4 lines) at epicentral distance 10 km (circle) and 150 km (cross), for Q = 526f$^{0.51}$, κ$_0$ of 0 (dashed) and 20ms (dotted), and a stress drop of 300 bars. Amplitudes have been normalized to a value of 1 at 1 Hz for M3.5, 100 at 1 Hz for M4.5; thus, only the shape is relevant.

The magnitude-distance and minimum-record-number criteria resulted in the selection of 9 seismic stations in eastern Canada: these included stations A11, A16, A21, A54, A61, A64 and DAQ in the Charlevoix, Quebec region, plus stations GSQ and CNQ at the mouth of the St. Lawrence River (see Table 3.1). The compiled eastern Canada database includes 187 velocity time series from 9 stations and 20 earthquakes, recorded from August 1989 to May 2019; their distribution in magnitude and distance is shown in Figure 3.2 and on a map in Figure 3.3. All selected eastern Canadian stations are either directly in contact with rock or sit on a concrete platform in contact with the rock. This was confirmed by a site visit to each station. Estimated shear wave velocities for the rock range from 1200 m/s to 3300 m/s at the 9 sites [Ladak et al., 2019b].
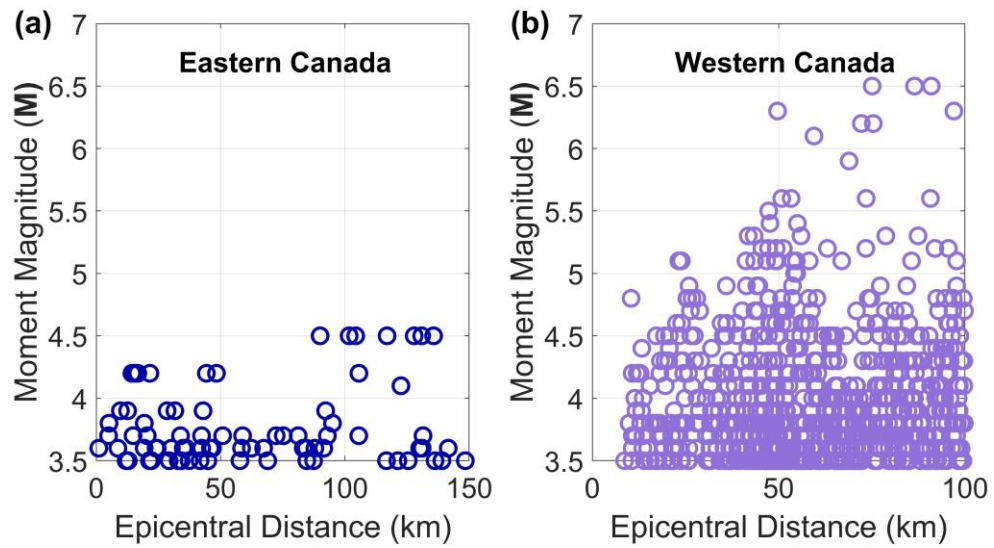
Figure 3.2: Data Distribution in moment magnitude and epicentral distance for (a) Eastern Canada (20 earthquakes, 9 stations) and (b) Western Canada (404 earthquakes, 8 stations).

Table 3.1: Eastern Canada Station Information and characteristics of H/V spectra.

Station	Location	Fpeak[*] (Hz)	Apeak[†]	Site Class[‡]	Surface Geology[§]	Bedrock Geology (~ age)[‖]
A11	47.2431°N 70.1968°W (Charlevoix)	7.5	2.0	CL-V (flat, low A)	Veneer (sand, gravel, and pockets of finer sediment) includes washed till and bedrock	Cambrian to Ordovician Inferior Mudrock, Green and Red Slate, Sandstone, and Limestone (443 to 541 Ma)
A16	47.4706°N 70.0064°W (Charlevoix)	3.9[(flat)]	1.6	CL-V (flat, low A)	Offshore Sediments (dominant silt and clay)	Cambrian to Ordovician Inferior Mudrock, Green and Red Slate, Sandstone, and Limestone (443 to 541 Ma)
A21	47.7036°N 69.6897°W (Charlevoix)	0.3[(flat)]	2.2	CL-V (flat, low A)	Offshore Sediments (dominant silt and clay)	Cambrian to Ordovician Inferior Mudrock, Sandstone, Conglomerate, and Limestone (443 to 541 Ma)
A54	47.4567°N 70.4125°W (Charlevoix)	0.5[(flat)]	1.2	CL-V (flat, low A)	Till Veneer (may include rock outcrop)	Precambrian Orthopyroxene granitoid, Charnockite, Mangerite, Jotunite, and Hypersthen Syenite (1600 to 2500 Ma)
A61	47.6936°N 70.0913°W (Charlevoix)	20.9	3.4	CL-I (Tg<0.2s)	Till Blanket	Precambrian Paragneiss Pelitic Gneiss, Marble, Quartzite and Iron Formation, Mafic Intrusive Rock Common (1600 to 2500 Ma)
A64	47.8264°N 69.8922°W (Charlevoix)	22.8[(flat)]	2.1	CL-I (Tg<0.2s)	Till Veneer (may include rock outcrop)	Precambrian Migmatite (1600 to 2500 Ma)

CNQ	49.302°N 68.0746°W (Mouth of St. Lawrence)	N/A	N/A	N/A	Bedrock, undifferentiated (75% rock outcrop) may include minor colluvial	Precambrian Granitoid Orthogneiss (1600 to 2500 Ma)
DAQ	47.9627°N 71.2437°W (Northeast of Charlevoix)	N/A	N/A	N/A	Till Veneer (may include rock outcrop) or Till Blanket	Precambrian Orthopyroxene granitoid, Charnockite, Mangerite, Jotunite, and Hypersthene Syenite (1600 to 2500 Ma)
GSQ	48.9142°N 67.1106°W (Mouth of St. Lawrence)	N/A	N/A	N/A	Bedrock, undifferentiated (75% rock outcrop) may include minor colluvial	Cambrian to Ordovician Inferior Mudrock, Sandstone, Conglomerate, and Limestone (443 to 541 Ma)

[*]Fpeak is the peak frequency

[†]Apeak is the amplitude of the earthquake H/V (N/A if station is vertical component only) at the peak frequency.

[‡]Site Class is according to the method of Di Alessandro et al. [2012]. Site Class CL-I is classified as a rock/stiff soil with a sites natural period below 0.2 s and V_{S30} >600 m/s, and CL-V is classified a generic rock site due to an almost average HVSR with no clear peak and a small HVSR (<2) [Zhoa et al., 2006; Di Alessandro et al., 2012]. Flat infers there is no significant peak amplitude in the H/V spectrum and low A infers amplitude is below 2.

[§]Surficial geology from the Geological Survey of Canada [2014].

[Ɩ]Bedrock Geology is inferred from Energie et Ressources Naturelles Quebec, ages estimate from Era (Ma – Millions years ago) (see Data and Resources).
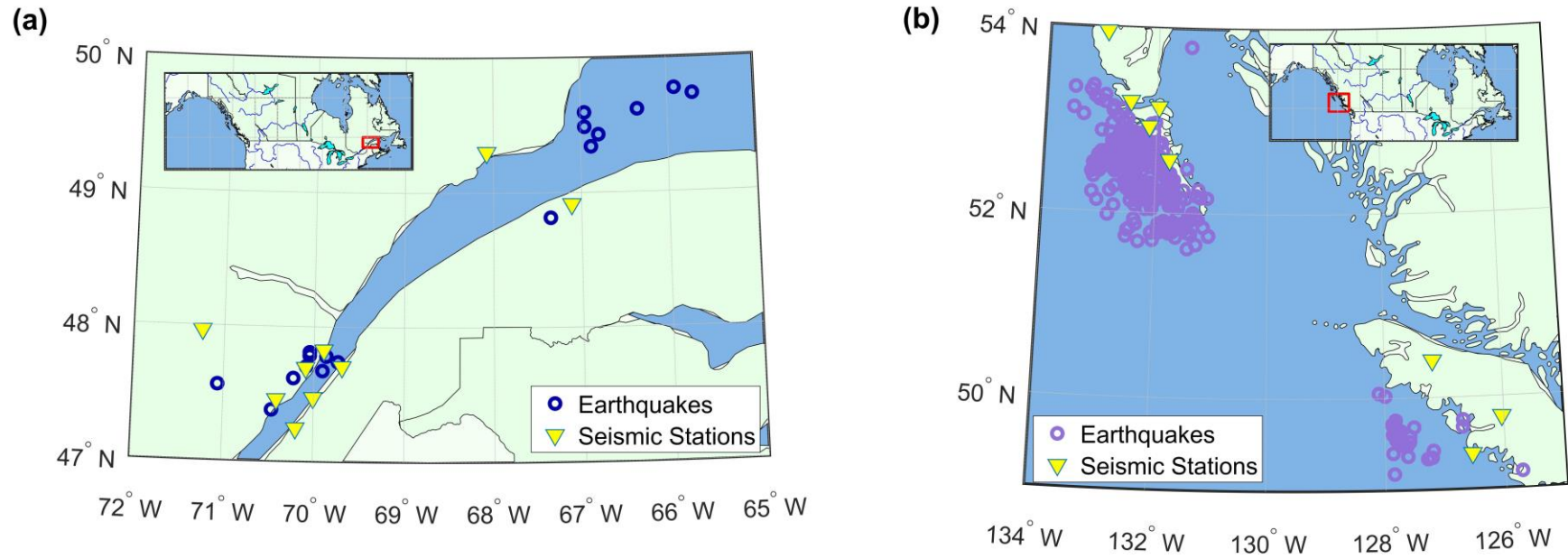
Figure 3.3: Map of earthquakes (circles) and stations (triangles) for (a) eastern Canada and (b) western Canada. The inset maps show Canada and a box shows the region of study.

Eight seismic stations were analysed in western Canada: these include stations BNB, DIB, HG1B, MOBC, and NDB in the Haida Gwaii region and ETB, GDR, and MAYB on Vancouver Island (see Table 3.2). The compiled western Canada database includes 1515 velocity time series from 8 stations and 404 earthquakes, recorded from January 2008 to May 2019, as shown in Figure 3.2 and on a map in Figure 3.3. Bedrock shear wave velocity measurements at seismograph stations in western Canada are not available. Previous studies have suggested that a typical shear wave velocity for Tertiary rock sites in western Canada is ~1500 m/s [Hunter et al., 1997]. On Vancouver Island, three BC Hydro Dam sites located on basaltic volcanic rock have measured bedrock shear wave velocities that range from 800 m/s to 3300 m/s [Catchings et al., 2019]. Thus, bedrock velocities may vary significantly from site to site, in both eastern and western Canada, over a range from <1000 m/s to >3000 m/s.

We calculated the Fourier amplitude spectrum of the S-wave portion of the signals (for a 15-second window) using files obtained from Natural Resources Canada (see Data and Resources Section) for the vertical and the horizontal component records. The horizontal component record is defined as the geometric mean of the East-West and North-South horizontal Fourier acceleration spectrum for the record. We calculated both raw and smoothed spectra, where the smoothing used the Konno Ohmachi smoothing method [Konno and Ohmachi, 1998] with a b value of 20. Smoothed spectra are useful to visualize the decay trend of the spectra, and to compute the horizontal to vertical spectral ratios. The compiled database comprises the time series for both S-wave and noise, the instrument-corrected unsmoothed Fourier amplitude spectra for both S-wave (vertical and geometric mean horizontal components) and noise, the instrument response spectrum for the record, smoothed Fourier amplitude spectra for both S-wave (vertical and geometric mean horizontal components) and noise, and the horizontal to vertical spectral ratios for the S-wave window. The example spectra plotted on Figure 3.4 show the classic shape expected for a simple Brune source model [Brune, 1970; Brune, 1971; Anderson, 1986; Boore, 2003], in which the acceleration rises as the square of frequency to a corner

frequency which depends on earthquake magnitude; large earthquakes are rich in low-frequency energy and thus have low corner frequencies, in comparison to small earthquakes. Above the corner frequency, the acceleration spectrum is approximately constant in amplitude, except for the effects of anelastic attenuation (path) and kappa (site), which cause a gradual decay trend with increasing frequency.
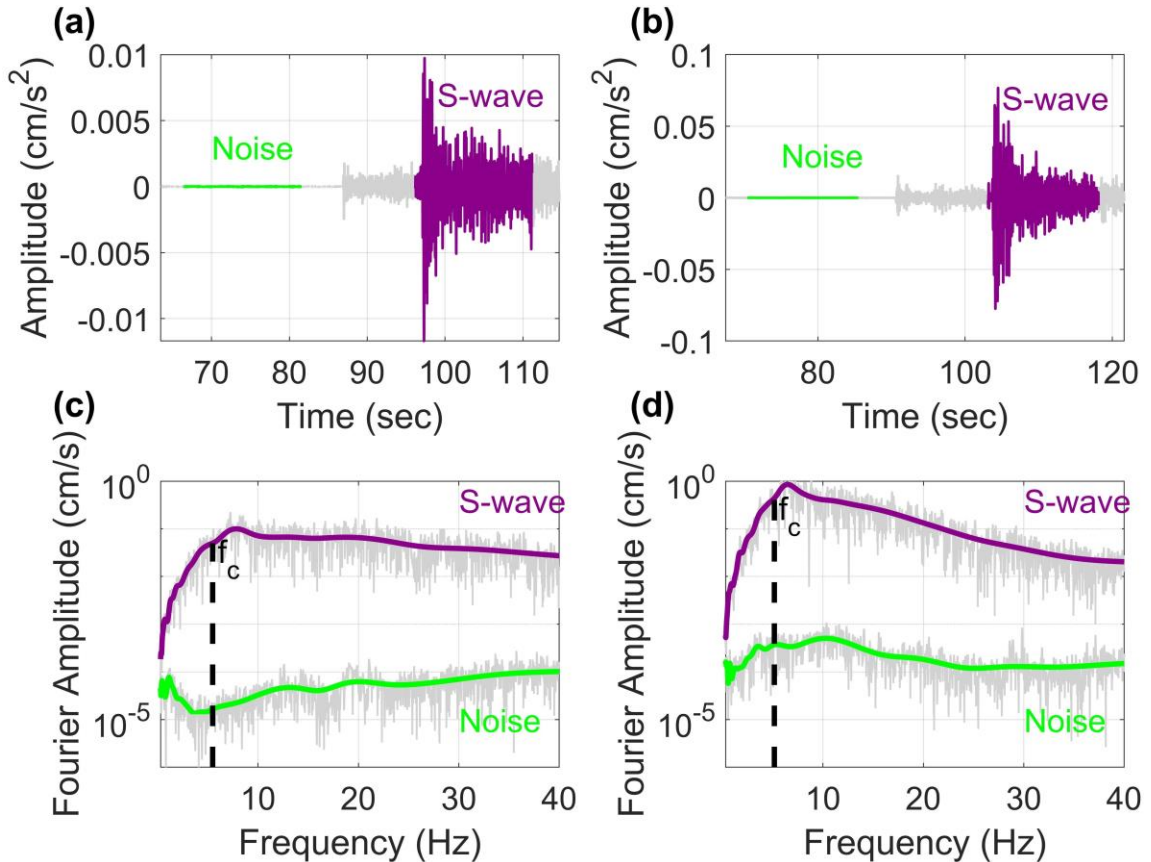
Figure 3.4: Data from an M 3.7 on 2000/07/12 at 15:01:49. Time series and spectral data from stations A16 (a and c), and A21 (b and d). S-wave and Noise signal are highlighted and labelled in the time series plot (a and b). Fourier amplitude spectrum of the signal before smoothing (jagged line) and after smoothing (smooth line; Konno Ohmachi b = 20) are labelled (c and d). Dashed vertical line shows the approximate corner frequency ($f_0 \sim 5Hz$) of the spectra, at which half the maximum amplitude is attained (c and d).

Table 3.2: Western Canada Station Information and characteristics of H/V spectra

Station	Location	Fpeak (Hz)[*]	Apeak[†]	Site Class[‡]	Surface Geology[§]	Bedrock Geology (~age)[‖]
BNB	52.5758°N 131.7522°W (Haida Gwaii)	N/A	N/A	N/A	Bedrock Undifferentiated	Middle Jurassic quartz dioritic intrusive (166 to 174 Ma)
DIB	53.20247°N 132.47666°W (Haida Gwaii)	12.9 (flat)	1.6	CL-V (flat, low A)	Bedrock Undifferentiated	Oligocene granodioritic (23 to 57 Ma)
ETB	49.3834°N 126.5423°W (Vancouver Island)	N/A	N/A	N/A	Veneer	Upper Eocene to Oligocene undivided sedimentary (23 to 39 Ma)
GDR	49.781°N 126.0319°W (Vancouver Island)	N/A	N/A	N/A	Bedrock Undifferentiated	Middle Jurassic quartz dioritic intrusive (170 to 185 Ma)
HG1B	52.93449°N 132.12071°W (Haida Gwaii)	3.9	7.6	CL-II (Peak at 0.26s)	Bedrock Undifferentiated	Upper Triassic basaltic volcanic (223 to 235 Ma)
MAYB	50.40251°N 127.173646°W (Vancouver Island)	N/A	N/A	N/A	Till Veneer or Till Blanket	Middle Triassic to Upper Triassic basaltic volcanic (208 to 241 Ma)
MOBC	53.1437°N 131.9663°W (Haida Gwaii)	4.8	3.2	CL-I (Peak at 0.2s – Broad 0.12s to 0.21s)	Colluvial Veneer	Upper Cretaceous conglomerate, coarse clastic sedimentary (87 to 89 Ma)
NDB	53.955°N 132.9417°W (Haida Gwaii)	N/A	N/A	N/A	Bedrock Undifferentiated or Till Veneer	Upper Oligocene to Lower Pliocene basaltic volcanic (3 to 29 Ma)

*Fpeak is the peak frequency

†Apeak is the amplitude of the earthquake H/V (N/A if station is vertical component only) at the peak frequency.

‡Site Class is according to the method of Di Alessandro et al. [2012]. Site Class CL-I is classified as a rock/stiff soil with a sites natural period below 0.2 s and VS30 >600 m/s, CL-II is classified as a hard soil, with a sites natural period between 0.2 s and 0.4 s and 300 m/s< VS30 ≤600 m/s, and CL-V is classified a generic rock site due to an almost average HVSR with no clear peak and a small HVSR (<2) [Zhoa et al., 2006; Di Alessandro et al., 2012]. Flat infers there is no significant peak amplitude in the H/V spectrum and low A infers amplitude is below 2.

§Surficial geology from the Geological Survey of Canada [2014].

‖Bedrock Geology from BC Geological Survey, ages provided by BC Geological Survey (Ma – Millions years ago) (see Data and Resources).

3.2.2   Kappa determination

We determine kappa utilizing a variant of Anderson and Hough's [1984] classical method, in which we consider a fixed frequency range over which to take the measurement. To isolate high-frequency site effects from source effects, we wish to ensure that we are measuring kappa at frequencies greater than 1.5 times the earthquake's corner frequency. An initial estimate of the apparent corner frequency was obtained for each record as the lowest frequency at which ½ of the maximum amplitude of the Fourier amplitude spectra is attained, as shown in Figure 3.5 [Boore, 2003]. We note that 90% of the records have an estimated apparent corner frequency below 14 Hz for eastern Canada, or 10 Hz for western Canada (Figure 3.5). It is important to be well above the corner frequency to avoid kappa and corner frequency trade-off as small magnitude events are utilized [Anderson, 1986]. Anderson [1986] show that the apparent corner frequency can be lower than the true corner frequency of the event when attenuation is considered on smaller magnitude events ($\mathbf{M}$<3). Accordingly, we selected a minimum frequency of 21 Hz for eastern Canada and 15 Hz for western Canada (e.g., 21 Hz (=1.5 * 14 Hz)) for the frequency range over which to measure kappa. To choose the maximum frequency, we note that most records have good signal-to-noise ratio up to 40 Hz. We selected a maximum frequency of 36 Hz; choosing a high-frequency limit slightly less than the largest possible value allows evaluation of the sensitivity of kappa estimates to the selected frequency range, as will be discussed later. In eastern Canada we measure κ from 21 Hz to 36 Hz, on each record having a lowest useable frequency ≤ 21 Hz and a highest useable frequency ≥ 36 Hz. In western Canada we measure κ from 15 Hz to 36 Hz, on each record having a lowest useable frequency ≤ 15 Hz and a highest useable frequency ≥ 36 Hz. The lowest useable frequency (LUF) is defined by Ktenidou et al. [2016] as the maximum value of: the lowest resolvable frequency of the spectrum (<<1 Hz in this study); the low-frequency limit imposed by the instrument response (<< 1 Hz in this study); the lowest frequency imposed by the signal to noise criterion; and the half-maximum corner frequency*1.5. The highest useable frequency (HUF), also defined by Ktenidou et al. [2016], is the minimum value of: the upper frequency imposed by the

instrument response; and the upper frequency imposed by the signal to noise criterion. Records that have a LUF ≥ 21 Hz (eastern Canada) or LUF ≥ 15 Hz (western Canada) and/or a HUF ≤ 36 Hz are not included in the computation of κ, allowing the use of a single frequency range within each region for consistency of kappa determinations. Based on these criteria, 105 Fourier acceleration spectra are available to measure kappa in eastern Canada, whereas 865 spectra are available in western Canada.
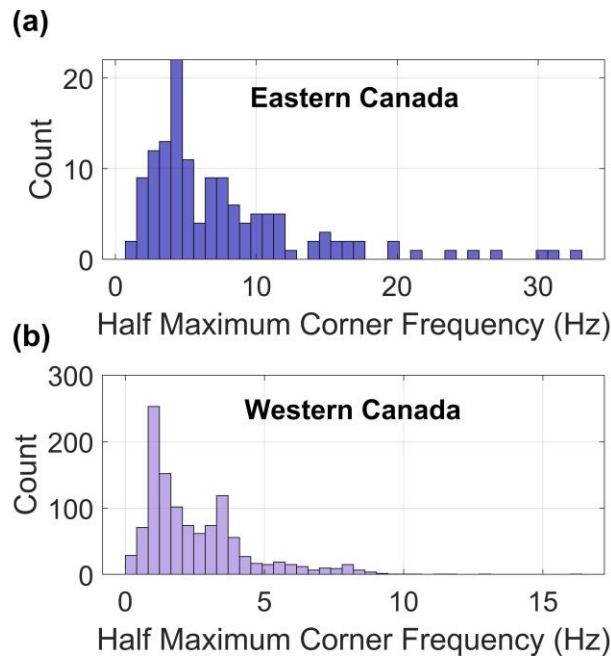
Figure 3.5: Histogram depicting the half-maximum estimate of corner frequency for (a) eastern Canada (187 records) and (b) western Canada (1515 records).

We use the approach of Perron et al. [2017] to check the sensitivity of measured kappa to the selected frequency range. In this method, f_1 (the lower bound from which to measure κ) and f_2 (the upper bound from which to measure κ) are varied by an increment of δf; κ is determined by applying a linear regression to Eqn. (3) over all frequency ranges given by $f_1 \pm \varepsilon_1 \delta f$ and $f_2 \pm \varepsilon_2 \delta f$ where ε_1 and ε_2 are random numbers between 0 and 1. We simplified Perron's approach by assigning fixed values for f_1, f_2, ε_1, ε_2, and δf (rather than taking many random samples). We vary the upper and lower frequency limits by the increment $\delta f = 2$ Hz, which was selected to avoid encroaching on the corner frequency of

most records, and fix ε_1 and ε_2 at 1. We measure kappa over all nine combinations of the frequency ranges given by $f_1\pm\delta f$ to $f_2\pm\delta f$. Using the linear regression slope of the unsmoothed spectrum we determine κ by dividing by $-\pi$ (see Equation 3.3). Figures 3.6 and 3.7 show sample Fourier amplitude spectra and the measurement process for κ for eastern Canada and western Canada respectively. From the nine perturbations of the frequency ranges over which we measure κ, we determine the mean and median κ. The mean and median κ values are similar, with the median value lying within the standard error of the mean. In measuring κ there are two significant sources of uncertainty: (i) the choice of frequency range leads to variability in the computed values; and (ii) amplitude variability of the spectra leads to measurement uncertainty on the slope (for a single selected frequency range). We report the error as the maximum value of: (i) the standard error of the nine measured κ values (i.e., from $f_1\pm\delta f$ to $f_2\pm\delta f$); and (ii) the value obtained by propagation of standard error of the slope from the nine linear regressions. The second error value is within the standard error of the nine measured kappa values over the various frequency perturbations. In other words, the amplitude variability of the spectrum contributes less to measurement uncertainty than does the frequency range over which κ is measured.
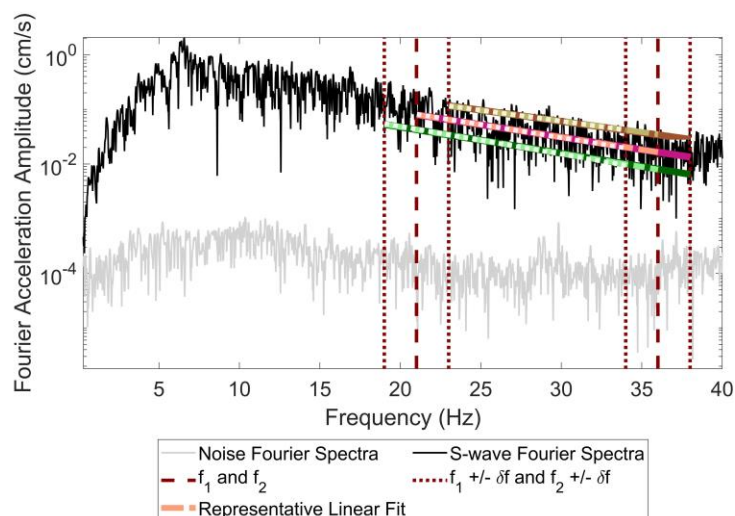
Figure 3.6: Example of measuring kappa and its associated variability for earthquake 2000/07/12 15:01:49 M 3.7 recorded at station A21. The vertical dashed

lines represent f₁, the lower bound for the κ measurement, and f₂, the upper bound for the κ measurement. The vertical dotted lines show the frequency increment, δf, applied to evaluate variability (i.e., ±2 Hz about f₁ and f₂). The S-wave Fourier amplitude acceleration spectrum is shown as the upper jagged line, and the noise Fourier amplitude acceleration spectrum is the lower jagged line. Solid, dashed and dotted lines going between the dashed and dotted vertical lines represent the 9-slope determinations for the S-wave spectra. Note: the upper 3 lines, beginning at f₁ – δf, and lower 3 lines, beginning at f₁ + δf, have been shifted in amplitude for clearer visualization of the slopes.

Figure 3.7: Example of measuring kappa and its associated variability for earthquake 2009/11/17 19:04:11 M 4.7 recorded at station BNB. The vertical dashed lines represent f₁, the lower bound for the κ measurement, and f₂, the upper bound for the κ measurement. The vertical dotted lines show the frequency increment, δf, applied to evaluate variability (i.e., ±2 Hz about f₁ and f₂). The S-wave Fourier amplitude acceleration spectrum is shown as the upper jagged line, and the noise Fourier amplitude acceleration spectrum is the lower jagged line. Solid, dashed and dotted lines going between the dashed and dotted vertical lines represent the 9-slope determinations for the S-wave spectra. Note: the upper 3 lines, beginning at f₁ – δf,

and lower 3 lines, beginning at $f_1 + \delta f$, have been shifted in amplitude for clearer visualization of the slopes.

3.2.3   Determination of apparent quality factor

It is well known that measured values of kappa increase with increasing distance from the source due to regional anelastic attenuation [Anderson and Hough, 1984]. Both kappa and regional anelastic attenuation have the same overall effect on spectral shape (Figure 3.1), but the regional anelastic component can be isolated by examining observed kappa values as a function of distance. The site-specific component of kappa, κ_0, is its observed value at close distances. The increase in measured kappa with distance is driven by the effects of regional anelastic attenuation, which reduce spectral amplitudes according to $e^{-\pi f R/Q\beta}$ (from Eqn 3.2). If we know the value of Q, then we can correct for the regional anelastic effects to obtain κ_0. Alternatively, we can use the increase in measured kappa with distance to infer Q in the area surrounding each station. To do this, we neglect any frequency-dependence in Q over the limited frequency range considered (eg. from 21 to 36 Hz). Based on previous studies [e.g., Atkinson, 2005; Mereu et al., 2013], we assume that Q should lie between 1000 and 6000 in this frequency range. We assume a typical regional mid-crustal velocity of $\beta = 3.7$ km/s [Atkinson, 1995; Atkinson, 2005; Atkinson and Boore, 2006] and use a grid search approach to find the apparent value of Q for each station, searching over the range from 1000 to 6000 in increments of 100. For each trial Q value, we apply the corresponding attenuation correction to the spectra before computing kappa. The Q value that produces a zero-distance trend, using a weighted linear regression, is taken as the apparent Quality factor (Q_a) in the region surrounding that station. The value of κ_0 at each station is the weighted mean of the attenuation-corrected kappa values; note that this is approximately equal to the intercept of the trend-corrected kappa values versus distance. The weights are provided by the inverse variance of the measured kappa values. The error for the associated station κ_0 is reported as the standard error obtained from a weighted bootstrap, iterated 1000 times, to find the weighted means associated error of the trend-corrected kappa values; we note that this error measure is always greater than that obtained by propagation of the standard errors of the individual

kappa measurements uncertainties (i.e., as determined from the square root of the sum of the standard errors squared) . In some cases, Q_a is >6000 because there is little apparent distance trend; in such cases the reported κ_0 is defined as the weighted mean κ for epicentral distances < 100 km and no Q correction is made.

3.3 Results

3.3.1 Eastern Canada

Figure 3.8 shows the relationship between κ and epicentral distance before and after attenuation corrections (i.e., Q-corrections) for two of nine stations in eastern Canada. In general, κ values are relatively insensitive to distance within 50 to 100 km, which is as expected based on the exponential effects of distance on anelastic attenuation, and in agreement with the findings of Ktenidou et al. [2016]. As a result, κ_0 could be determined either by correcting for attenuation and obtaining the mean, or by simply averaging the measured κ values for stations within 50 to 100 km. Due to the paucity of earthquakes recorded at close distances, particularly on some stations (DAQ, GSQ, and CNQ), we prefer the approach of estimating κ_0 based on the attenuation-corrected values of κ. Table 3.3 provides the values of κ_0 and the associated values of Q_a, for eastern Canada, determined for each station that recorded at least five **M**$\geq$3.5 events within 150 km**.**
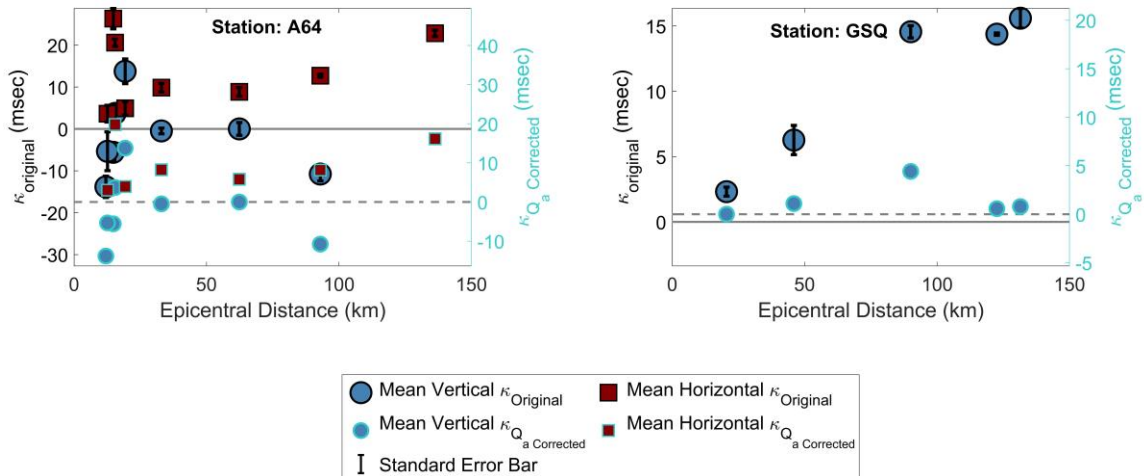
Figure 3.8: Kappa derived from recordings at stations A64 and GSQ in eastern Canada. Horizontal component (large squares) κ and vertical component (large circles) κ values show κ measured from spectra prior to corrections for attenuation using the left axis for scale. Standard error is represented by error bars. Q-corrected κ values are shown as small squares (horizontal component) or small circles (vertical component) using the right axis for scale; Values of Q_a to obtain zero distance trend are given in Table 3.3. Zero-kappa lines are shown for each axis, solid for left axis, and dashed for right axis.

Table 3.3: Comparison of site-specific kappa and apparent Quality factor derived from the stacked and classical method (Anderson and Hough, 1984; Perron et al., 2017) for horizontal (H) and vertical (V) components.

Region	Station	# Records		Stacked Method				Classical Method					
		V	H	κ_0^* (V) (ms)	SE[†] (V) (ms)	κ_0^* (H) (ms)	SE[†] (H) (ms)	κ_0^* (V) (ms)	SE[†] (V) (ms)	Q_a (V)	κ_0^* (H) (ms)	SE[†] (H) (ms)	Q_a (H)
rn Canada	A11	7	7	-4	0.6	8	0.6	-4	1	>6000	1	2	1600
	A16	4	9	-2	0.6	3	0.2	-5	2	>6000	2	1	2300

	Station												
	A21	7	8	12	0.5	23	0.7	10	3	2500	20	2	2700
	A54	5	8	-3	0.9	-3	0.4	2	1	>6000	-4	1	2400
	A61‡	7	9	5	0.4	5	0.4	5	3	>6000	0	2	1700
	A64‡	8	8	-7	0.5	8	0.9	-2	2	>6000	10	2	5500
	CNQ‡	5		0	1.3			-24	2	1100			
	DAQ	8		2	0.3			-2	1	2400			
	GSQ‡	5		-2	1.4			0.7	0.3	2400			
	Regional Average κ_0 and standard error			**0**	**0.3**	**7**	**0.2**	**-2**	**1**		**5**	**1**	
Western Canada	**BNB‡**	262		16	0.2			14	0.4	>6000			
	DIB	183	196	12	0.1	10	0.4	15	0.5	>6000	15	0.4	>6000
	ETB‡	10		-2	1.1			-2	0.2	>6000			
	GDR‡	6		12	1.1			6	4	>6000			
	HG1B‡	75	85	2	0.6	14	0.8	9	0.7	4300	15	0.9	2200
	MAYB‡	16		15	0.5			17	2	>6000			
	MOBC‡	11	12	23	1.3	32	0.3	14	1	1000	20	0.8	1200
	NDB‡	9		37	1.0			28	3	>6000			
	Regional Average κ_0 and standard error			**14**	**0.3**	**19**	**0.3**	**13**	**0.7**		**17**	**0.4**	

*For stations, using the Classical Method with Q_a >6000, κ_0 values are computed as weighted mean of κ values at < 100km (no Q correction); other values of κ are Q-corrected. Negative values of κ_0 imply increasing spectral amplitudes with frequency, after Q corrections, and should be considered equivalent to κ_0 ~0.
†Standard Error
‡Stations with potential site amplification contributing to the kappa computation.

The values of κ_0 and Q_a vary considerably from site to site, but the values of κ measured on the horizontal component tend to be consistently larger than those on the vertical component, whilst the apparent Q values are larger on the vertical than on the horizontal. Both observations are consistent with lesser attenuation of high-frequency energy on the vertical component.

To evaluate whether the values of κ might be significantly influenced by near-surface site amplification effects, we examine horizontal to vertical spectral ratios (HVSR). The HVSR is a well-known proxy for site response [e.g., Nakamura, 1989; Lermo and Chavez-Garcia, 1993]. The idea is that site amplification effects are stronger on the horizontal than on the vertical component, and thus, HVSR is a rough estimate of site amplification, which should at least identify the predominant frequency, although it may

not capture complications such as higher-mode effects. On stations with both horizontal and vertical component records we can measure the HVSR directly from the records compiled in this study. At stations where there are only vertical component records (DAQ, CNQ, and GSQ), we rely on the measurements of Ladak et al. [2019a] who used active and passive methods to determine the microtremor HVSR at seismographic stations in eastern Canada. Earthquake HVSR for stations A11, A16, A21, A54, A61, and A64, shown in Figure 3.9, are examined to evaluate the likely site amplification effects; typical spectra for the H and V components are also shown, to check for evidence of features (e.g., vertical-component resonances) that could complicate interpretation of H/V as a first-order site amplification model. Based on the earthquake records, stations A11, A16, A21, and A54 are characterized by relatively flat HVSR with amplitudes < 2 at all frequencies and are thus, believed to be relatively free of significant site amplifications. Station A61 and A64 have a frequency peak near 20 Hz, which is expected to bias the measured values of κ. CNQ has a peak frequency near 5 Hz, which should not affect the κ measurement between 21 to 36 Hz [Ladak et al., 2019a]. DAQ has a HVSR that is relatively flat from 2 Hz to 40 Hz, but has a high amplitude [Ladak et al., 2019a]. GSQ has a flat HVSR with low amplitude [Ladak et al., 2019a]. Examination of the sample H component spectra in comparison to the V spectra generally supports this interpretation, although stations CNQ and GSQ's vertical component spectra appear to have amplification at ~40 Hz and ~20Hz respectively (see Figure 3.9 b) and c)). Thus, based on the HVSR, the kappa values at most stations, except A61, A64, CNQ, and GSQ are likely to be relatively unaffected by site amplification effects. Sites A11, A16, and A54 all have HVSR <2 in the frequency range of interest but this value decreases below HVSR = 1, suggesting that site amplification may be causing high frequency diminution. This could be the result of highly fractured rock in the near-surface [Steidel et al., 1996]. Table 3.1 summarizes the stations analysed, the locations, number of components the instrument records on, the peak frequency and amplitude of the HVSR, estimated site class based on Di Alessandro et al. [2012] classification scheme, the listed surface geology based on the Canadian Geoscience Map 195 [Geological Survey of Canada,

2014: see Data and Resources], and the inferred bedrock geology and age estimated from Energies et Ressources Naturelles Quebec (see Data and Resources).
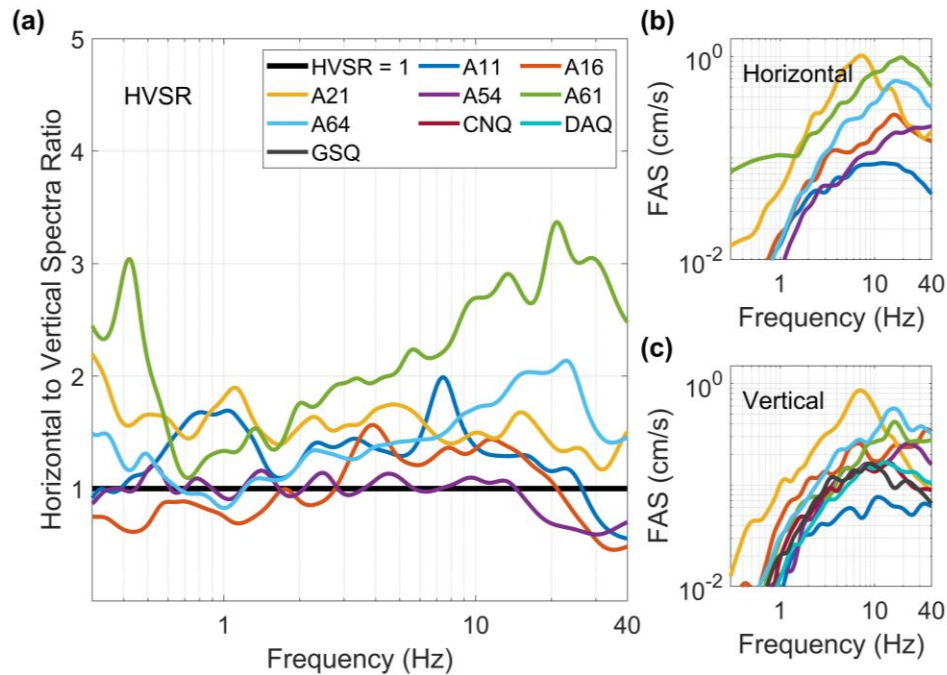
Figure 3.9: (a) Horizontal to Vertical Spectral Ratios (HVSR) from earthquake records for stations in eastern Canada. Representative smoothed (using Konno Ohmachi Method, b = 20) Fourier amplitude spectrum of S-wave Acceleration (Mean FAS) of each station are shown for the horizontal (b) and vertical (c) components.

In Table 3.3, it is interesting to note that in some cases we report negative values for κ_0, implying a slight positive trend in amplitudes with increasing frequency; sometimes a positive slope is seen even before any attenuation corrections. This is not considered meaningful in view of measurement uncertainties, and we assume that negative κ should be interpreted as near-zero κ_0.

From the results shown in Table 3.3, Station A21 has a much higher kappa value than the rest of the stations. This station is on the top of a cliffside ~20 m above the regional

elevation and may have significant topographic effects. The remaining stations in eastern Canada have kappa values that range from -4 ms ± 1 ms to 10 ms ± 2 ms for the horizontal component and -24 ms ± 2 ms to 5 ± 3 ms for the vertical component.

3.3.2   Western Canada

We measure kappa on eight stations located on Haida Gwaii and Vancouver Island, all of which are believed to be sited on rock, using earthquakes from crustal, in-slab, and offshore sources at distances < 100 km. Figure 3.10 shows two sample relationships between κ and epicentral distance before and after attenuation corrections. Although earthquake depths varied from 0 km to 58 km, there is no sensitivity to distance metric (epicentral versus hypocentral) because of the large distances involved (i.e., the distance measures are essentially equal). The trends of kappa values with distance were not significant at many of the western stations, within the 100 km distance range, leading to large values for the apparent Q, as shown in Table 3.3. As a result, often the linear trend obtained is not statistically significant (i.e., the slope is within a standard error of zero). In such cases we use the weighted mean kappa value for all stations within 100 km and do not apply any attenuation correction. Of the 8 stations, 2 stations: HG1B and MOBC exhibit significant slopes that warrant Q-correction before measuring kappa. It is interesting to note that the apparent Q values are significantly higher than would be expected, relative to regional Q models for British Columbia and California. Also, the kappa values for vertical and horizontal components do not differ much for western Canada, in contrast to the observations for eastern Canada.
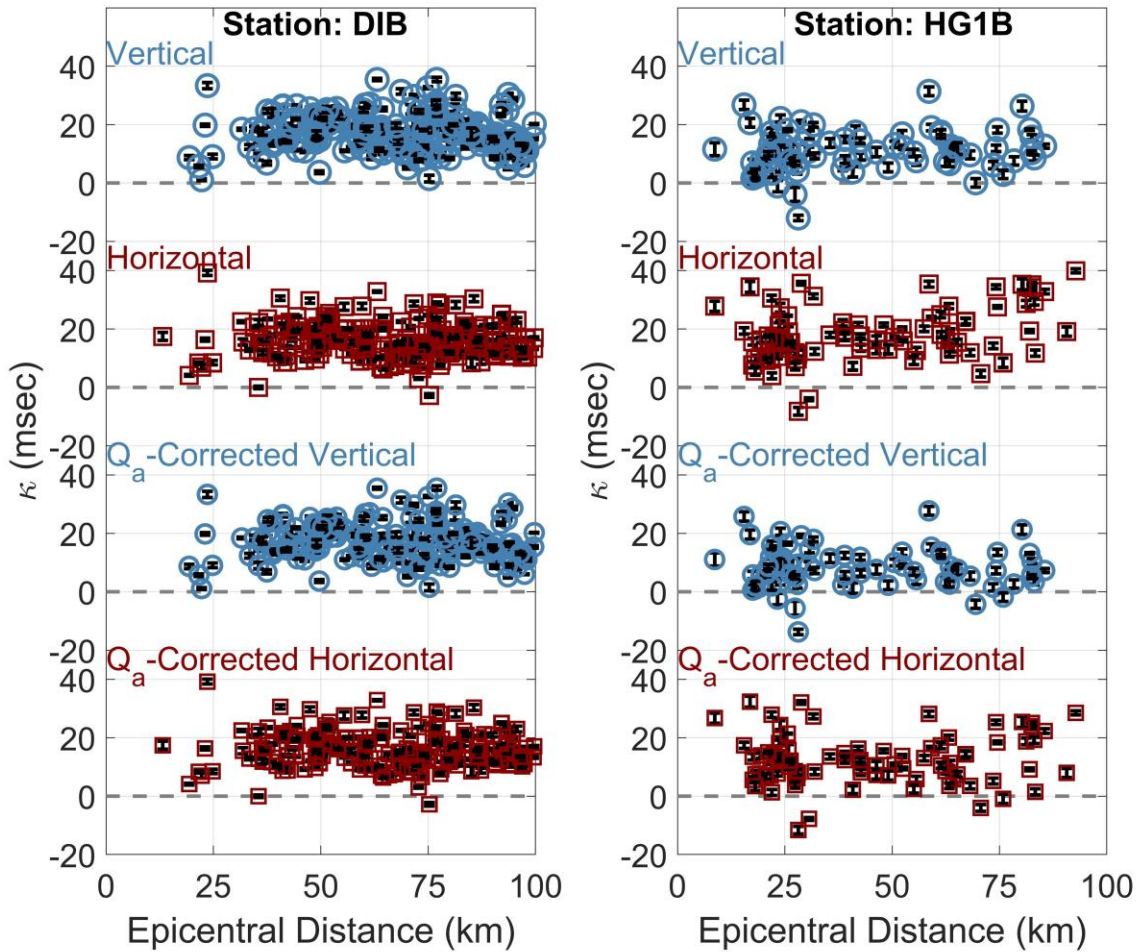
Figure 3.10: Kappa for stations DIB, and HG1B in western Canada. Horizontal component κ (squares) and vertical component κ (circles) derived using spectra before (upper two panels) and after Q-corrections (lower two). Standard error is represented by error bars. Zero lines are denoted by dashed lines. Values of Q_a to obtain zero distance trend are given in Table 3.3.

We checked whether the kappa values are sensitive to event type (crustal, in-slab, offshore). Contributing events for the three stations on Vancouver Island, MAYB, GDR and ETB, come entirely from in-slab events; thus, the high apparent Q values for these stations may not be representative of crustal paths. On Haida Gwaii, there is a

complicated mix of event types and travel paths, with most travel paths crossing the Queen Charlotte Fault. There are 2 stations, BNB and DIB, that have at least 5 contributing values from paths that are entirely within the shallow continental crust (east of the Queen Charlotte Fault, onshore Haida Gwaii, with focal depth < 20 km). We calculated the kappa values from just these crustal events at each of these stations and confirmed that the crustal-only kappa values do not differ significantly from those reported in Table 3.3. This is consistent with the interpretation of kappa as predominantly a site and path effect.

Earthquake horizontal to vertical spectral ratios for DIB, HG1B, and MOBC are shown in Figure 3.11, along with sample H and V component spectra. As indicated in Table 3.2, station DIB has a low amplitude, and reasonably flat spectrum. Station HG1B has a peak HVSR amplitude of ~8 near 4 Hz but this decays rapidly to a relatively flat amplitude (~ 2) beyond 7 Hz. MOBC has a broad amplification peak that spans the range from 3 Hz to 12 Hz, then attains an amplitude of <2 at higher frequencies. The plotted representative spectra suggest that these trends are influenced primarily by amplification effects on the horizontal component.
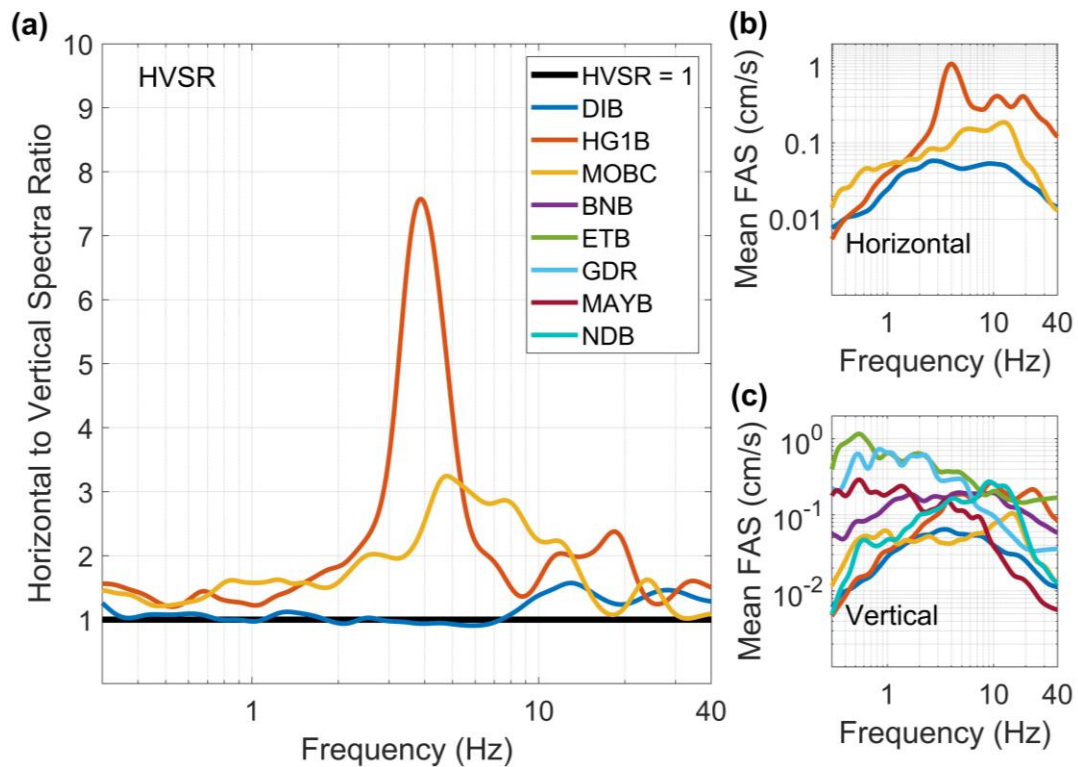
Figure 3.11: (a) Horizontal to Vertical Spectral Ratios (HVSR) from earthquake records for stations in western Canada. Representative smoothed (using Konno Ohmachi Method, b = 20) Fourier amplitude spectrum of S-wave Acceleration (Mean FAS) of each station are shown for the horizontal (b) and vertical (c) components.

As a check on possible site amplification effects that may impact kappa, we examined the horizontal- and vertical-component spectra, sample characteristic spectra are shown in Figure 3.11 b) and c), for each station to identify any notable deviations from expected spectral shapes (Figure 3.1). Seven stations show potential site amplification as evidenced by peaks in component spectra. These are stations HG1B and MOBC, which have peaks consistent with site amplification effects inferred from the horizontal to vertical spectral ratios, stations ETB and NDB, which show elevated amplitudes relative to expected shapes across the frequency range 15 – 25 Hz, and stations ETB, GDR, HG1B, NDB, and MOBC all appear to have a narrow amplification on the vertical

component ranging from 20 Hz to 35 Hz dependent on the station. In Table 3.3, we denote stations that could be impacted by site amplification based on visual inspection of HVSR or stacked spectra with a double dagger symbol.

3.4   Discussion

3.4.1   Sensitivity to methodology

We used the classical approach as introduced by Anderson and Hough [1984] to measure kappa on rock sites, using records from events of $\mathbf{M} \geq 3.5$ within 150 km in eastern Canada and within 100 km in western Canada. We interpret any distance-dependent trends in terms of an apparent Quality factor for the region surrounding the station. The use of Q-corrected kappa values is considered preferable to the alternative of fitting a trend-line to the (uncorrected) kappa values to infer the value at zero distance, because it does not require extrapolation to distances closer than those observed. The application of both kappa and anelastic attenuation corrections in the manner we employ is consistent with the way these parameters are used in the development of ground motion models [e.g., Boore, 2003]. The values that we infer for attenuation, based on the limited records in this study, are consistent with expectations based on more comprehensive attenuation studies. For example, Atkinson and Mereu [1992] and Mereu et al. [2013] infer that Q is in the range from 1800 to 3300 for frequencies from 21 to 36 Hz. Our results suggest an apparent Q between 1100 and >6000, which is generally consistent with this range. The high values of Q_a obtained for the vertical component on a few stations suggests that high-frequency attenuation is often minimal for rock sites for distances within 100 km; an alternative interpretation could be that higher resonant modes and vertical P-wave resonances may be biasing the apparent attenuation.

 We can take our Q-correction approach further by using it to determine kappa values that are consistent with ground-motion spectra, considering regional source and path effects assumed in ground motion modeling. This provides an alternative methodology for determining kappa. In this alternative method, we assume that the spectra follow a simple Brune model, which can be corrected for regional attenuation using equations 3.1 and

3.2, with $Q = 526f^{0.51}$ in eastern Canada [Mereu et al., 2013] and $Q = 229f^{0.6}$ [Atkinson, 2005] in western Canada. Each spectrum is Q-corrected to obtain a Brune spectrum that can be characterized by its amplitude, corner frequency, and kappa. We stack the Q-corrected spectra to normalize for amplitude and corner frequency as follows and illustrated in Figure 3.12a. For each station, we select the Fourier amplitude spectrum with the largest corner frequency and define it as the reference spectrum. The reference spectrum is normalized to a maximum amplitude of 1. We then shift all other spectra for that station, in the frequency direction, so that their corner frequencies align at the reference spectrum's corner frequency. Note that all other spectra are shifted up in frequency (i.e., to the right along the frequency axis) to meet the reference spectrum. The shifted spectra are then amplitude-scaled to the normalized reference spectrum across the frequency band in which they overlap. Finally, a mean and standard deviation of the stacked normalized spectra is computed (at each frequency having at least 3 contributions to the stack). A linear fit of the high-frequency decay trend is computed for the mean of the stacked spectra, using the same approach that was applied to individual spectra; thus, nine slope values contribute to the mean and standard error of a site-specific kappa value. We note that the frequency range over which this kappa value is measured varies within the spectra contributing to the stack, but is always above the corner frequency, because the spectrum with the highest corner is used as the reference. The included frequencies in the stacked spectrum are as low as 9 Hz in eastern Canada and 11 Hz in western Canada. Figure 3.12b shows a sample stacked spectrum, the mean and standard deviation of the stack, and a sample linear fit.
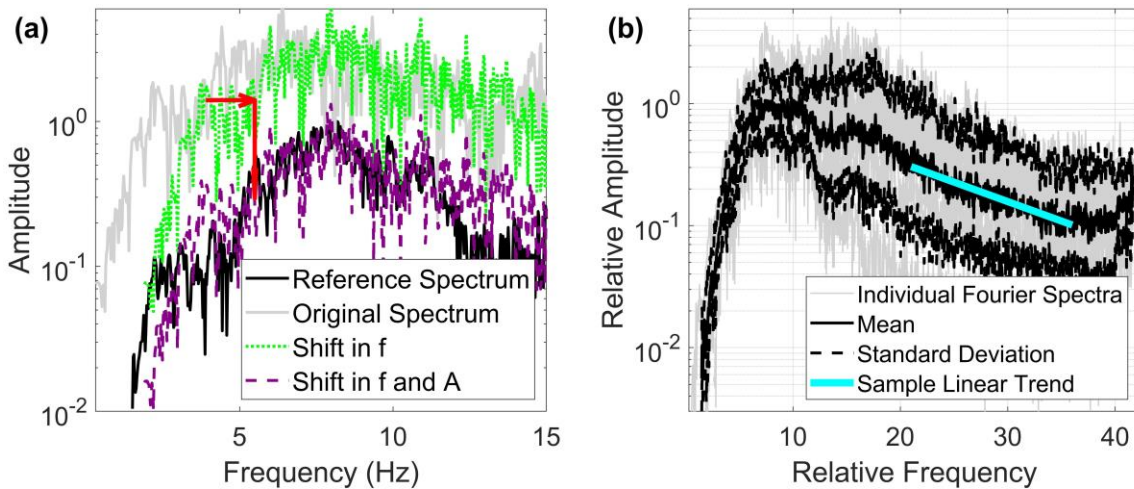
Figure 3.12: (a) Illustration of how a spectrum (light solid line) is shifted in frequency (dotted line) and then in frequency and amplitude (dashed line) to the reference spectrum (black solid line). Arrows show the shift in the frequency direction and amplitude direction. (b) Sample stack of the Fourier amplitude spectra for station A21 (eastern Canada), horizontal component. Individual spectra are shown as jagged thin light lines, the mean spectrum is solid black, the standard deviation of the mean is shown in dashed black lines and a sample linear trend over the range in which kappa is taken is shown as a thick straight line.

Utilizing the approach described in the foregoing, stacking the spectra and measuring kappa on the stacked spectra, we obtain values for kappa that are generally consistent with those obtained with the classical approach, but the standard error of kappa decreases. Table 3.3 and Figure 3.13 compares the results from the stacked method and the classical method for eastern and western Canada. For some stations (about half of the eastern and ¼ of the western stations), the stacked site-specific kappa values agree with those from the classical method within the standard error bounds; this generally occurs for stations that have good distance distributions of measured kappa and do not have significant outliers. For other stations, the difference in values between methods significantly exceeds the standard error bounds. This suggests that the true uncertainty in measuring kappa, due to factors such as attenuation and site response, is not captured by

the statistical uncertainty. Thus, statistical measures of error on site-specific kappa should be treated with caution. However, when considering average regional values of kappa, the results are robust regardless of which approach is used. The average site-specific kappa using the stacked method for the sampled rock sites in eastern Canada is 7ms (horizontal) and 0ms (vertical) in comparison to the classical methods κ_0 of 5ms (horizontal) and -2ms (vertical) (see Table 3.3). In western Canada the average κ_0, using the stacked method is 19ms (horizontal) and 14ms (vertical) compared to the classical methods average κ_0 of 17ms (horizontal) and 13ms (vertical) (see Table 3.3). (Note: The standard error on the regional kappa values is based on the propagation of uncertainties of the individual site-specific kappa measurements.)
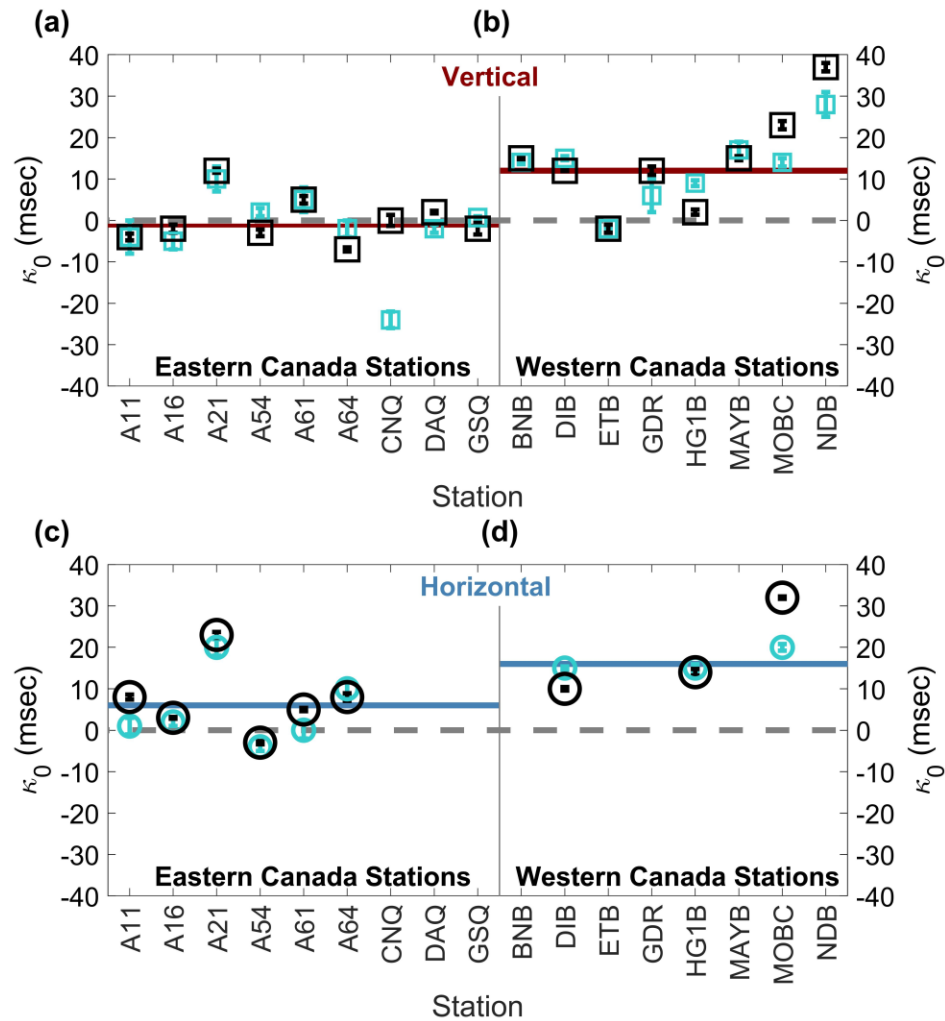
Figure 3.13: Site-specific kappa values for rock sites for the stacked method (dark edges) and classical method (light edges) for eastern Canada (a and c) and western Canada (b and d). Squares show vertical values (a and b); circles show horizontal (c and d), with standard error bars (dark: stacked method; light: classical method). Solid heavy lines show average regional kappa values (using kappa from both methods) determined for the vertical and horizontal for each region. Dashed lines show the zero line.

Analyzing kappa using the classical approach has significant limitations due to the interplay between kappa and corner frequency for small-to-moderate events, and due

to the possibility of significant amplification effects at higher frequencies as discussed previously. The impact of these effects may be muted by using the stacked method, because the frequency shifting will spread such effects over frequency. However, κ_0 values from both the classical and stacked approaches may still contain some contamination from site amplification effects. Site velocity profiles would be useful to calculate expected site amplification effects in the near-surface, which could potentially be removed in the computation of kappa.

The uncertainty in the determination of κ_0 and Q_a using the classical approach is particularly large when there are few stations at close distances. In such cases, the value obtained for κ_0 can vary significantly depending on the data distribution and fitting methodology. When fitting kappa versus distance, we utilize a weighted linear regression to account for the measurement error on kappa. We compare kappa from the weighted linear regression to that from a standard linear regression; this choice does not affect kappa by more than 3ms on average (which is approximately the error contribution from measurement), but the difference can be larger in some cases (e.g., station CNQ). We performed some sensitivity tests on the effects of the distance distribution of data, using the data from station HG1B, which are well distributed across the entire distance range from 0 to 100km. We find that to obtain stable values for both κ_0 and Q_a, we should have data that span most of the distance range (i.e., a difference of 70 to 85km between lowest and highest distances), and have minimal gaps (i.e., no more than 5 to 25km across) between data clusters.

We note that the classical approach for kappa determination normally uses the intercept of the linear fit of values versus distance to define κ_0. Our variation is similar, in that we use the slope of the linear fit to determine the path effect and correct for it, enabling κ_0 to be taken as a mean of the Q-corrected values. Our rationale for this variation is that it is more stable than taking the intercept of the fit line, particularly when data are lacking at short distances. Additionally, site-specific kappa using the Q_a correction result in smaller error of the κ_0 compared to the intercept approach. In practice, the two variations on the

classical method produce similar values in most cases. However, in cases where there is a poor distance distribution, such as CNQ, the determined kappa value can be very sensitive to methodology. An example of significant differences from the classical κ_0 mean from the intercept method can be observed at station GDR on the vertical component (where distance distribution is poor, < 50km wide); the Q_a is >6000 and the interpreted mean κ_0 (6 ms) differs from the corresponding intercept value (60 ms) by 54 ms. In cases where $Q_a<6000$ the mean κ_0 differ from the intercept value by 0 to 1 ms for both vertical and horizontal components. A potential shortcoming of our Q-correction approach is that we assume constant Q over the high frequency range, whereas it may have significant frequency dependence. This simplification may be a cause of discrepancies between κ_0 from the stacked versus Q-corrected approaches, such as at station CNQ for example. For the stacked approach there are two limitations in estimating the kappa values: i) amplification features in the records may bias the average record shape; and ii) Q models are generally not well characterized for high frequencies. Moreover, most Q models were derived from data at large distances (>100 km) and their applicability at shorter distances is uncertain.

3.4.2   Sensitivity to other factors

We restricted our analysis to stations with a minimum of five **M**$\geq$3.5 records. We test the sensitivity of kappa to the number of records using data from three stations having plentiful data: BNB, DIB, and HG1B. We use a bootstrap method, randomly selecting 5, 10, 15, 20, 25, 30, 35, 40, 60, and 70 records from the dataset for each station, over 1000 trials. As the number of records was reduced the average κ_0 values (over 1000 trials) remained remarkably stable, deviating from the value obtained for the full record set by no more than 0.1ms, even when only 5 records were drawn. However, the standard deviation of the average increases with decreasing record size, and thus, the uncertainty in the obtained value is increasing. For example, for station BNB, the standard deviation of the average value of $\kappa_0 = 16$ms (vertical) is 1ms for 30 records, 2ms for 10 records, and 3ms for 5 records.

In our study we utilize the geometric mean Fourier amplitude spectrum of the two horizontal components to determine a horizontal kappa. We examined the sensitivity of results to using just the east-west or north-south component. Interestingly, at some stations (A21, A54, MOBC) the two components appear to differ significantly from each other in their kappa values, possibly reflecting trade-offs between kappa and apparent Q that may be traced to path or site-specific alignments in attenuation structure. Further study of such site-specific features is required.

3.4.3   Comparisons with other studies

A curious feature of the results we obtained is the high values for apparent Q in western Canada, much higher than expected based on regional Q models from other studies. From examination of the ray paths from events to stations, we note that many of the paths travelled by the waves cross from offshore or in-slab to continental crust and thus, the crustal Q models may not be appropriate. Moreover, the complexity of the geology could be resulting in complex path effects which are not a simple function of distance. In eastern Canada, the apparent Q values agree with our expectations for horizontal components but are higher than expected for the vertical components. This could also reflect complexities in path effects. For example, for the direct wave (distances to ~60 km), the high-frequency components may attenuate as expected, then as the direct wave is joined by post critical reflections and refractions there may be a bump in high frequency content that is most pronounced on the vertical. An amplification at high frequencies on the vertical component could also explain its negative kappa values.

In previous studies, κ_0 on the vertical component has been estimated to be <4ms in eastern Canada, with the Charlevoix region featuring much higher κ_0, 20 – 40ms [Atkinson, 1996]. We find a consistently low regional value for the vertical component on average, $\kappa_0 = 0$ms. However, in Charlevoix we find only one station having a significantly higher κ_0 (12ms), whilst the Charlevoix average κ_0 is 0.2ms (vertical). In western Canada, Atkinson [1996] reported a κ of 11ms for the vertical component which is in good agreement with our κ_0 of 14ms (vertical).

For the horizontal component, Campbell et al. [2014] suggest a κ_0 of 6ms for rock sites in CENA while Ktenidou et al. [2016] suggest a value of 7ms. Our regional average for eastern Canada of $\kappa_0 = 7$ms is consistent with these findings. Ktenidou et al. [2016] examined stations in Charlevoix using the NGA-East Database for M>2.4 earthquakes recorded within 100km. They applied a crustal amplification correction to their dataset but found that the κ were not affected significantly (<5%), because the frequency range over which kappa is measured did not overlap with the frequency range affected by crustal amplification. Other differences between the studies include the selected data. Ktenidou et al. [2016] use a larger data set which includes smaller earthquakes, and also includes the 1988 Saguenay earthquakes. Methodology differs in that we include a Q-correction whereas Ktenidou et al. [2016] does not. There are also some differences in the frequency range over which kappa is measured. Table 3.4 compares our results with those of Ktenidou et al. [2016] for stations in common. Kappa is represented in Table 3.4 as: $\kappa_r = \kappa_0 + \tilde{\kappa}(R_e)$, where κ_r is not path corrected and κ_0 is the site-specific kappa regionally corrected for anelastic attenuation related to path. In general, the difference in the values appears to be dominated by the database selection and the Q correction. Overall, we conclude that the standard errors reported for kappa measurements (including ours) are not a realistic measure of uncertainty in the value, because of sensitivity to data selection, methodology, and other factors such as amplification that may affect spectral shape.

Table 3.4: Comparison of horizontal component kappa measured for our stacking method and Ktenidou et al.'s (2016) stacking method.

Station	SSN*	No. Records: This Study	No. Records: Ktenidou et al. 2016	κ_0 (ms) this study†	κ_r (ms) this study‡	$\kappa_{r[21 - 36Hz]}$ (ms)§	$\kappa_{r[15 - 30 Hz]}$ (ms)‖	$\kappa_{r\_AS[15 - 30 Hz]}$ (ms) Ktenidou et al. 2016#
A11	8	7	12	8	11	12	9	9
A16	9	9	13	3	6	7	7	4
A21	10	8	11	23	25	23	34	38
A54	11	8	17	-3	1	4	-0.1	9
A61	12	9	15	5	8	9	8	13

A64	13	8	15	8	10	14	7	7

*NGA-East station code, Station Sequence Number (SSN)

[†] Site-specific kappa (κ_0), with Q correction, utilizing our database, method, and measured using a relative frequency range of $21 \pm 2Hz$ to $36Hz \pm 2Hz$.

[‡] Kappa (κ_r), without Q-corrections, utilizing our database, method, and measured using a relative frequency range of $21 \pm 2Hz$ to $36Hz \pm 2Hz$.

[§] Kappa ($\kappa_{r[21 - 36\,Hz]}$), without Q-corrections, utilizing our database, Ktenidou et al.'s (2016) stacking method, and measured using the frequency range: 21 to 36 Hz.

[‖] Kappa ($\kappa_{r[15 - 30\,Hz]}$), without Q-corrections, utilizing our database, Ktenidou et al.'s (2016) stacking method, and their frequency range: 15 to 30 Hz.

[#] Ktenidou et al. (2016) reported kappa ($\kappa_{r\_AS[15 - 30\,Hz]}$) which used their data and method which measured kappa on the frequency range: 15 to 30 Hz.

3.4.4   Relationship between kappa and bedrock velocity

We examine the correlation, or lack thereof, between site-specific kappa and bedrock velocity for the stations in the east, see Table 3.5 and Figure 3.14. Figure 3.14 suggests that there is no apparent correlation between kappa and bedrock velocity in eastern Canada. Due to a lack of knowledge of bedrock velocities for stations in the west, we compare the bedrock type [BC Geological Survey, See Data and Resources] to the site-specific kappa values and observe there is no obvious correlation between kappa and rock type in western Canada (Figure 3.14, Table 3.5). Assuming that harder rock has a faster velocity, if there was a correlation between bedrock velocity and kappa we might expect kappa values on granitic or basaltic sites to be smaller than those on sedimentary rock. However, this does not appear to be the case with the limited number of stations sampled in this study (see Figure 3.14). This suggests that kappa at hard rock sites may be driven by factors other than the near-surface bedrock velocity. Such factors could include the velocity profile over the top few kilometers, if kappa is sampling a significant volume beneath the site. This may also explain the higher kappa values for western sites relative to those in the east: the older and more competent eastern crust would be expected to have lower kappa than the more recently reworked western crust. Additionally, we examine estimated bedrock age and find no apparent correlation with site-specific kappa (Table 3.5). Further geophysical investigation of the seismographic sites and their environs is needed to provide a better understanding of the relationship between kappa and rock properties, in both the east and the west.

Table 3.5: Comparison of kappa from the stacked method for horizontal (H) and vertical (V) components to bedrock velocity and age. Approximate geographic locations are provided as well.

Region	Geographic Location	Station	Bedrock Velocity (m/s)	Bedrock Age Range (Millions years ago)[*]	κ_0 (V) (ms)	κ_0 (H) (ms)
Eastern Canada	Charlevoix	A11	1500 ± 500[†]	443 – 541	-4	8
		A16	2925 ± 285[‡]	443 – 541	-2	3
		A21	1500 ± 500[†]	443 – 541	12	23
		A54	1357 ± 95[‡]	1600 – 2500	-3	-3
		A61[§]	2000 ± 300[‡]	1600 – 2500	5	5
		A64[§]	2553 ± 686[‡]	1600 – 2500	-7	8
	North Charlevoix	DAQ	1573 ± 260[∥]	1600 – 2500	2	
	Mouth of St. Lawrence	CNQ[§]	2500 ± 700[†]	1600 – 2500	0	
		GSQ[§]	1500 ± 500[†]	443 – 541	-2	
Western Canada	Haida Gwaii	BNB[§]	Quartz Dioritic Intrusive[*]	166 – 174	16	
		DIB	Granodioritic[*]	23 – 57	12	10
		HG1B[§]	Basaltic Volcanic[*]	223 – 235	2	14
		MOBC[§]	Sedimentary[*]	87 – 89	23	32
		NDB[§]	Basaltic Volcanic[*]	3 – 29	37	
	Vancouver Island	ETB[§]	Sedimentary[*]	23 – 39	-2	
		GDR[§]	Quartz Dioritic Intrusive[*]	170 – 185	12	
		MAYB[§]	Basaltic Volcanic[*]	208 – 241	15	

[*]Estimated bedrock age ranges, for eastern Canada, are provided by Energie et Ressources Naturelles Quebec (see Data and Resources). Estimated bedrock age ranges and bedrock type are from Bedrock Geology from BC Geological Survey (see Data and Resources) for western Canada.

[†]Estimates or regional shear wave bedrock velocities are shown for stations where direct measurements were not available, velocities from Nastev et al. [2016].

[‡]Shear-wave bedrock velocities from Ladak et al. [2019b]

[§]Stations with potential site amplification contributing to the kappa computation.

[∥]Shear wave bedrock velocities from Ladak [2020].
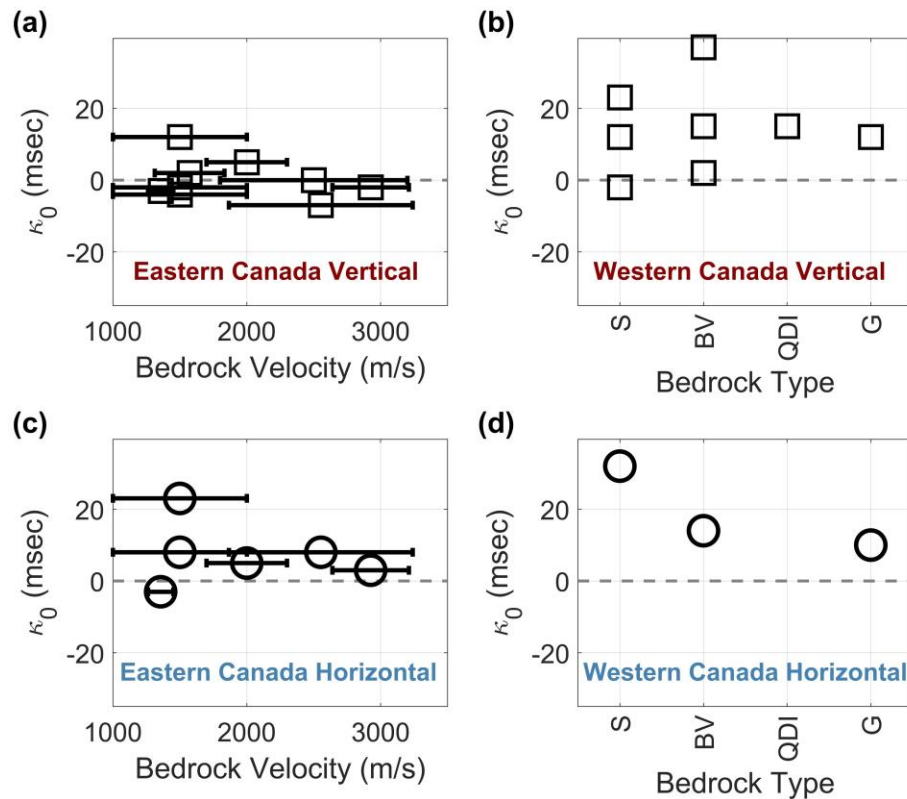
Figure 3.14: Kappa, κ0, values compared to shear wave bedrock velocities for rock sites in eastern Canada (a and c) and western Canada (b and d) for vertical (a and b) and horizontal (c and d) components, see Table 3.5. Kappa values are from the stacked method and errors are not shown for them (as they are much smaller than the velocity error). Bedrock types include Sedimentary (S), Basaltic Volcanic (BV), QDI (Quartz Dioritic Intrusive) and G (Granodiorite). Standard deviation of bedrock velocity is shown with black horizontal bars. Based on Ladak et al. (2019b) and Nastev et al. (2016) Paleozoic rock exhibits V_S ~1500 m/s and Precambrian rock have V_S ~2100 – 2500 m/s in eastern Canada. Dashed line shows zero line.

Future empirical work will expand the database by including smaller earthquakes, which can be used in conjunction with broadband analysis methods as described by Ktenidou et al. (2014). Further examination will also be made of the interplay between Q effects and kappa in western Canada, to explore the observation that anelastic path effects on the spectra appear to be negligible within 100 km. Additionally, examining site amplification

effects beyond a predominant peak frequency will be of value in determining if site amplification is affecting reported κ_0 values.

3.5   Conclusions

We applied two methods to determine site-specific kappa values for rock sites in eastern and western Canada. The methods produce consistent results when data are well behaved with respect to their distance distribution and have few outliers. A method based on stacking spectral shapes results in lower statistical uncertainty than does the classical approach of Anderson and Hough [1984] and is consistent with the use of kappa in ground motion modeling, which includes an empirically-determined regional path attenuation correction. We conclude, from the stacked method, that site-specific kappa for rock sites in eastern Canada ranges from -7ms to 23ms, with a typical measurement uncertainty of 0.7ms. In western Canada, site-specific kappa ranges from -2ms to 37ms, with a typical uncertainty of 0.7ms. However, we note that the measurement error of kappa does not reflect its true uncertainty, as measurements can vary significantly depending on data selection and methodology. Moreover, spectral shape at some sites may be significantly influenced by high-frequency site amplification effects. The analysis of site-specific high-frequency ground motion should simultaneously consider the effects of amplification, kappa, and regional Q.

We examined whether there is any obvious correlation between kappa and rock velocities and/or types. In eastern Canada, there does not appear to be a correlation between bedrock shear-wave velocity and site kappa, for sites with bedrock velocities from 1200m/s to 3000m/s. In western Canada, no measurements of bedrock velocity at seismograph stations have been made. Bedrock velocities likely range from 1000m/s to 3000m/s depending on rock type. There is no apparent correlation between rock type and site kappa.

Measuring a site-specific kappa at each site location may not always be feasible. Based on the results of this study, average regional kappa values for eastern and western Canada

can be summarized as follows. In eastern Canada, the average value of kappa over all rock sites, from the stacked method, is $\kappa_0 = 7$ms (horizontal) and 0ms (vertical). In western Canada, the average value of kappa over all rock sites is $\kappa_0 = 19$ms (horizontal) and 14ms (vertical). We caution that there may be large site-to-site variability in these values.

3.6   Data and Resources

The earthquake database used in this study was provided from Natural Resources Canada's Earthquake's Canada - Geological Survey of Canada (GSC) on-line bulletin earthquake search at http://www.earthquakescanada.nrcan.gc.ca/stndon/NEDB-BNDS/bulletin-en.php (last accessed May 2019). The seismograms for the earthquakes used in this study were provided by Earthquakes Canada – GSC email data service at AutoDRM@seismo.NRCan.gc.ca (last accessed May 2019). Waveforms were initially processed with rdSEED from https://ds.iris.edu/ds/nodes/dmc/software/downloads/rdseed/. Data analysis was completed in part using the Seismic Analysis Code (SAC) which is a seismological processing software available at https://ds.iris.edu/ds/nodes/dmc/software/downloads/sac/ [Goldstein et al. 2003; Goldstein and Snoke, 2005]. Signals are 360 seconds long, starting 70 seconds prior to the earthquake time. rdSEED is used to convert files into SAC and RESP (response) files. Standard SAC procedures are used to remove the mean, detrend, taper, remove instrument response from the full time series in the Fourier domain, select the S and P-wave arrivals, cut the time series 0.5 seconds prior to the S-wave arrival and 14.5 seconds after to obtain the 15 second S-window, cut the time series 20 seconds prior to the P-wave arrival and 5 seconds prior to obtain a 15 second noise window, applying the FFT (fast Fourier transform) to the cut time series, and finally differentiate using mulomega function to obtain the Fourier amplitude spectrum of acceleration. We take the geometric mean of the two horizontal component Fourier amplitude spectra to obtain one horizontal component. Bedrock types for British Columbia seismometer sites were found at https://catalogue.data.gov.bc.ca/dataset/bedrock-geology (Accessed July 26th, 2019), provided by the BC Geological Survey Bedrock Geology: Ministry of Energy, Mines and

Petroleum Resource – BC Geological Survey. Bedrock types for Eastern Canada seismometer sites were found at https://mern.gouv.qc.ca/english/mines/publications/publications-maps.jsp (Accessed November 15th, 2019), provided by the Energie et Ressources Naturelles Quebec: Ministere des Resource Naturelles (2012).

3.7   References

Anderson, J. and S. Hough (1984) A model for the shape of the Fourier amplitude spectrum of acceleration at high frequencies, Bull. Seismol. Soc. Am. 74(5), 1969 – 1993. doi: 10.1785/BSSA0740051969

Anderson, J.G. (1991) A preliminary descriptive model for the distance dependence of the spectral decay parameter in Southern California, Bull. Seismol. Soc. Am 81(6), 2186 – 2193. doi: 10.1785/BSSA0810062186

Anderson, J. (1986) Implication of Attenuation for Studies of Earthquake Source, Earthquake Source Mechanics (ed. S. Das., J. Boatwright, C.H. Scholz). Vol. 37, pp. 311-318. doi: 10.1029/GM037Atkinson, G.M., and R.F. Mereu (1992) The shape of ground motion attenuation curves in southeastern Canada, Bull. Seismol. Soc. Am. 82(5), 2014 – 2031. doi: 10.1785/BSSA0820052014

Atkinson, G.M. (1995) Attenuation and source parameters of earthquakes in the Cascadia Region, Bull. Seismol. Soc. Am. 85(5), 1327 – 1342. doi: 10.1785/BSSA0850051327

Atkinson, G.M. (1996) The high-frequency shape of the source spectrum for earthquakes in eastern and western Canada, Bull. Seismol. Soc. Am. 86(1A), 106 – 112. doi: 10.1785/BSSA08601A0106

Atkinson, G.M. (2005) Ground motions for earthquakes in southwestern British Columbia and northwestern Washington: Crustal, in-slab and offshore events, Bull. Seismol. Soc. Am. 95(3), 1027 – 1044. doi: 10.1785/0120040182

Atkinson, G.M. and D.M. Boore (2006) Earthquake ground-motion prediction equations for eastern North America, Bull. Seismol. Soc. Am. 96(6), 2181 – 2205. doi: 10.1785/0120050245

Beresnev, I.A. (2019) Short Note: Interpretation of kappa and f_{max} filters as source effect, Bull. Seismol. Soc. Am. 109(2), 822 – 826. doi: 10.1785/0120180250

Boore, D. M. and W. B. Joyner (1991) Estimation of ground motion at deep-soil sites in eastern North America, Bull. Seismol. Soc. Am. 81(6), 2167-2185. doi: 10.1785/BSSA0810062167

Boore, D.M. (1983) Stochastic simulation of high-frequency ground motions based on seismological models of the radiated spectra, Bull. Seismol. Soc. Am. 73(6), 1865 – 1894. doi: 10.1785/BSSA07306A1865

Boore, D.M. (2003) Simulation of ground motion using the stochastic method, Pure Appl. Geophys. 160, 635 - 676. doi: 10.1007/PL00012553

Brune, J.N. (1970) Tectonic stress and the spectra of seismic shear waves from earthquakes, J. Geophys. Res. 75, 4997 – 5009. doi: 10.1029/JB075i026p04997

Brune, J.N. (1971) Correction, J. Geophys. Res. 76, 5002. doi: 10.1029/JB076i020p05002Campbell, K.W. (2009) Estimates of Shear-Wave Q and κ0 for unconsolidated and semiconsolidated sediments in eastern North America, Bull. Seismol. Soc. Am. 99 (4), 2365 – 2392. doi: 10.1785/0120080116

Campbell, K.W, Y.M.A. Hashash, B. Kim, A.R. Kottke, E.M. Rathje, W.J. Silva, and J.P. Stewart. (2014) Reference-rock site conditions for Central and Eastern North America: Part II – Attenuation (kappa) definition. PEER Report No. 2014/12.

Castro, R.R., L. Trojani, G. Monachesi, M. Mucciarelli, and M. Cattaneo (2000) The spectral decay parameter κ in the region of Umbria-Marche, Italy, J. Geophys. Res. 105(B10), 23 811 – 23 823. doi: 10.1029/2000JB900236

Catchings, R.D., K.O. Addo, M.R. Goldman, J.H. Chan, R.R. Sickler, and C.J. Criley (2019) Two-dimensional seismic velocities and structure variation at three British Columbia Hydro and Power Authority (BC Hydro) dam sites, Vancouver Island, British Columbia, Canada. USGS Open File Report No. 2019-1015.

Di Alessandro, C., L.F. Bonilla, D.M. Boore, A. Rovelli, and O. Scotti (2012) Predominant-period site classification for response spectra prediction equations in Italy, Bull. Seismol. Soc. Am. 102(2), 680–695. doi: 10.1785/0120110084

Drouet, S., F. Cotton, and P. Gueguen (2010) V_{S30}, κ, regional attenuation and M_w from accelerograms: application to magnitude 3 – 5 French earthquakes, Geophys. J. Int. 182, 880 – 898. doi: 10.1111/j.1365-246X.2010.04626.x

Edwards, B., D. Fäh, and D. Giardini (2011) Attenuation of seismic shear wave energy in Switzerland, Geophys. J. Int. 185, 967 – 984. doi: 10.1111/j.1365-246X.2011.04987.x

Edwards, B., O. J. Ktenidou, F. Cotton, N.A. Abrahamson, C. Van Houtte, and D. Fäh (2015) Epistemic uncertainty and limitations of the κ_0 model for near-surface attenuation at hard rock sites, Geophys. J. Int. 202, 1627 – 1645. doi: 10.1093/gji/ggv222

Farahbod, A.M., A. J. Calvert, J. F. Cassidy, C. Brillon (2016) Coda Q in Northern Cascadia Subduction Zone, Bull. Seismol. Soc. Am. 106(5), 1939 – 1947. doi: 10.1785/0120160058

Fereidoni, A., G. M. Atkinson, M. Macias, and K. Goda (2012) CCSC: A composite seismicity catalog for earthquake hazard assessment in major Canadian cities, Seismol. Res. Lett. 83(1), 179 – 189. doi: 10.1785/gssrl.83.1.179

Geological Survey of Canada (2014) Canadian Geoscience Map 195 Surficial Geology of Canada. Catalogue No. M183-1/195-2014E-PDF. doi: 10.4095/295462

Goldstein, P., D. Dodge, M. Firpo, and L. Minner (2003) SAC2000: Signal processing and analysis tools for seismologists and engineers, The IASPEI International Handbook of Earthquake and Engineering Seismology, Academic Press, London.

Goldstein, P. and A. Snoke (2005) SAC Availability for the IRIS Community, Incorporated Institutions for Seismology Data Management Center Electronic Newsletter.

Goulet, C.A., T. Kishida, T.D. Ancheta, C.H. Cramer, R.B. Darragh, W.J. Silva, Y.M.A Hashash, J. Harmon, J.P. Stewart, K.E. Wooddell, and R.R. Youngs (2014) PEER NGA-East database. PEER No. Report 2014/17.

Hanks, T.C. (1982) f_{max}, Bull. Seismol. Soc. Am. 72(6A), 1867 – 1879. doi: 10.1785/BSSA07206A1867

Hanks, T.C. and R.K, McGuire (1981) The Character of high-frequency strong ground motion, Bull. Seismol. Soc. Am. 71(6), 2071 – 2095. doi: 10.1785/BSSA0710062071

Hollender, F. (2019) Improvement of Practices for a More Robust Site-Specific Seismic Hazard Assessment, Habilitation a Diriger des Recherches: Universite Grenoble Alps.

Hough, S.E. and J.G. Anderson (1988) High-frequency spectra observed at Anza, California: Implications for Q Structure, Bull. Seismol. Soc. Am. 78(2), 692-707. doi: 10.1785/BSSA0780020692

Humphrey, J.R. and J. G. Anderson (1992) Shear Wave Attenuation and Site Response in Guerrero, Mexico, Bull. Seismol. Soc. Am. 81(4), 1622 – 1645. 10.1785/BSSA0820041622

Hunter, J., J. Harris, and J. Britton (1997) Compressional and shear wave interval velocity data for Quaternary sediments in the Fraser River delta from

multichannel seismic reflection surveys. Geological Survey of Canada Open-File Report No. 97-3325.

Kilb, D., G. Biasi, J. Anderson, J. Brune, Z. Peng, and F.L. Vernon (2012) A comparison of spectral parameter kappa from small and moderate earthquakes using Southern California ANZA Seismic Network data, Bull. Seismol. Soc. Am. 102(1), 284 – 300. doi: 10.1785/0120100309

Konno, K. and T., Ohmachi (1998) Ground motion characteristics estimated from spectral ratio between horizontal and vertical components of microtremor, Bull. Seism. Soc. Am. 88(1), 228 – 241. doi: 10.1785/BSSA0880010228

Ktenidou, O.J., C. Gelis, and L.F. Bonilla (2013) A study on the variability of kappa (κ) in a borehole: Implications of the computation process, Bull. Seismol. Soc. Am. 103(2A), 1048 – 1068. doi: 10.1785/0120120093

Ktenidou, O., F. Cotton, N.A. Abrahamson, and J. G. Anderson (2014) Taxonomy of κ: A Review of Definitions and Estimation Approached Targeted to Applications, Seismol. Res. Lett. 85, 135 – 146. doi: 10.1785/0220130027

Ktenidou, O.J., N.A. Abrahamson, R.B. Darragh, and W.J. Silva (2016) A Methodology for the Estimation of Kappa (κ) from Large Datasets: Example Application to Rock Sites in the NGA-East Database and Implications on Design Motions. PEER Report No. 2016/01.

Ladak, S., S. Molnar, S.M. Palmer, and G.M. Atkinson (2019a) Application of active and passive seismic methods for determining the shear wave velocity profile at hard rock sites in eastern Canada. Proceedings of the 12th Canadian Conference on Earthquake Engineering Quebec City Quebec Canada, June 17-20.

Ladak, S., S. Molnar, S.M. Palmer, and G.M. Atkinson (2019b) Earthquake site characterization at seismograph stations in eastern Canada, Proceedings of the

12th Canadian Conference on Earthquake Engineering Quebec City Quebec Canada, June 17-20.

Ladak, S. (2020) Earthquake site characterization of rock site in eastern Canada and stiff ground sites in Vancouver, British Columbia. MSc Thesis, University of Western Ontario, https://ir.lib.uwo.ca/etd/6972

Lai, T., H. Mittal, W. Chao, and Y. Wu (2016) A Study on Kappa Value in Taiwan Using Borehole and Surface Seismic Array, Bull. Seismol. Soc. Am. 106(4), 1509 – 1517. doi: 10.1785/0120160004

Leblanc, G.A. and G.C. Klimkiewicz (1994) Seismological Issues: History and Examples of Earthquake Hazard Assessment for Canadian Nuclear Generating Stations. Geological Survey of Canada Open File No. 2929.

Lermo, J., M.A. Santoyo, M.A. Jaimes, Y. Antayhua, and M. Chavacan (2017) Local earthquakes of the Mexico Basin in Mexico City: κ, Q, source spectra, and stress drop, Bull. Seismol. Soc. Am. 107(4), 1423-1437. doi: 10.1785/0120150189

Mereu, R. F., S. Diveva, and G.M. Atkinson (2013) The application of velocity spectral stacking to extract information on source and path effects for small-to-moderate earthquakes in southern Ontario with evidence for constant-width faulting, Seismol. Res. Lett. 84, 899 – 916. doi: 10.1785/0220130009

Nakamura, Y. (1989) A method for dynamic characteristics estimation of subsurface using microtremor on the ground surface. Quarterly Report of Railway Technical Research 30, 25-33.

Nastev, M., M. Parent, N. Benoit, M. Ross, D. Howlett (2016) Regional V_{S30} model for the St. Lawrence Lowlands, Eastern Canada, Georisk: Assessment and Management of Risk for Engineered Systems and Geohazards 10, 200-212. doi: 10.1080/17499518.2016.1149869

Papageorgiou, A.S. and K. Aki (1983) A specific barrier model for the quantitative description of inhomogeneous faulting and the prediction of strong ground motion. I. Description of model, Bull. Seismol. Soc. Am. 73(3), 693 – 722. doi: 10.1785/BSSA0730030693

Parolai, S. (2018). κ0: Origin and usability, Bull. Seismol. Soc. Am. 108(6), 3446 – 3456. doi: 10.1785/0120180135

Perron, V., F. Hollender, P. Bard, C. Gélis, C. Guyonnet-Benaize, B. Hernandez, and O.-J. Ktenidou (2017) Robustness of kappa (κ) measurement in low-to-moderate seismicity areas: Insight from a site-specific study in Provence, France, Bull. Seismol. Soc. Am. 107(5), 2272 – 2292. doi: 10.1785/0120160374

Pilz, M. and D. Fah (2017) The contribution of scattering to near-surface attenuation, J. Seimol. 21, 837 – 855. doi: 10.1007/s10950-017-9638-4

Pilz, M., F. Cotton, R. Zaccarelli, and D. Bindi (2019) Capturing regional variations of hard-rock attenuation in Europe, Bull. Seismol. Soc. Am. 109(4), 1401-1418. doi: 10.1785/0120190023

Raoof, M., R.B. Hermann, and L. Malagnini (1999) Attenuation and excitation of three-component ground motion in southern California, Bull. Seism. Soc. Am. 89, 888 – 902. doi: 10.1785/BSSA0890040888

Steidl, J.H., A. G. Tumarkin, and R.J. Archuleta (1996) What is a reference site?, Bull. Seismol. Soc. Am. 86(6), 1733 – 1748. doi: 10.1785/BSSA0860061733

Van Houtte, C., S. Drouet, and F. Cotton (2011) Analysis of the origins of κ (kappa) to compute hard rock to rock adjustment factors for GMPE's, Bull. Seismol. Soc. Am. 101(6), 2926 – 2941. doi: 10.1785/0120100345

Van Houtte, C., O.-J. Ktenidou, T. Larkin, and C. Holden (2014) Hard-site κ0 (kappa) calculations for Christchurch, New Zealand, and comparison with local ground-

motion prediction models, Bull. Seismol. Soc. Am. 104(4), 1899 – 1913. doi: 10.1785/0120130271

Wen, J. and X. Chen (2012) Variation in fmax along the ruptured fault during the Mw 7.9 Wenchuan earthquake of 12 May 2008, Bull. Seismol. Soc. Am. 102(3), 991-998. doi: 10.1785/0120110105

Yenier, E. and G.M. Atkinson (2015) An equivalent point-source model for stochastic simulation of earthquake ground motions in California, Bull. Seismol. Soc. Am. 105(3), 1435 – 1455. doi: 10.1785/0120140254

Zhao, J.X., K. Irikura, J. Zhang, Y. Fukashima, P.G. Somerville, A. Asano, Y. Ohno, T. Oouchi, T. Takahashi, and H. Ogawa (2006) An empirical site-classification method for strong-motion stations in Japan using H/V response spectral ratio, Bull. Seismol. Soc. Am. 96(3), 914-925. doi: 10.1785/0120050124

Chapter 4

4 The high frequency spectral decay, kappa, in eastern Canada determined with a broadband inversion approach[3]

4.1 Introduction

There has been recent interest in site response attributes for hard-rock sites, due to their importance for seismic hazard assessment for critical infrastructure such as nuclear power plants and dams [e.g., Campbell, 2009; Campbell et al., 2014; Douglas et al., 2011; Drouet et al. 2010; Ktenidou et al., 2016]. Characterization of earthquake ground motion at high frequencies requires parameterization of amplification effects due to the crustal velocity profile and diminution effects due to energy absorption in the near-surface materials (kappa). A classical approach measures the slope of the high frequency spectral decay versus frequency (kappa) for earthquakes recorded at near-source distances, for frequencies above the corner frequency [Anderson and Hough, 1984]. A limitation to this approach is that it is applicable only to earthquakes with moment magnitude (**M**) >~3.5, to ensure sufficient frequency bandwidth above the corner frequency. To overcome this limitation, broadband inversion techniques that make use of the entire spectral bandwidth [e.g., Anderson and Humphrey, 1991] are useful in low-to-moderate seismicity regions, such as those in eastern North America.

The broadband inversion approach aims to separate site effects (amplification and kappa) from the influences of variable source effects and the distance-dependent influence of path attenuation (inverse of regional Quality factor). In ground motion modelling, for a

---

[3] A version of this chapter has been submitted for publication: Palmer, S.M. and G.M. Atkinson (XXXX) The high frequency spectral decay, kappa, in eastern Canada determined with a broadband inversion approach, Bull. Seismol. Soc. Am.

generic site such as rock or soil, the amplification (G(f)) can be described as the combination of amplification (A(f)) due to shear wave velocity versus depth and diminution (D(f)) from a path independent loss of high frequency content in the Fourier domain (Boore, 2003). Previous studies have reported kappa ranging from <4ms to 40ms for rock sites in Canada [Atkinson, 1996; Campbell, 2009; Campbell et al., 2014; Ktenidou et al., 2016]. These reported kappa values often contain the net effect of both amplification and diminution; alternatively, they may have removed the amplification effects by assuming an underlying generic rock amplification model. The wide range of reported kappa for rock sites, coupled with an apparent lack of correlation between kappa and estimated rock velocity [Palmer and Atkinson, 2020], suggests that a site-specific ground motion modelling approach is vital in understanding kappa and its interaction with amplification. In this study, we examine high frequency (f>10Hz) ground motion in eastern Canada and the relationship between ground motions and the conditions of the site, with a focus on rock sites. Our database comprises >39,000 recordings from 25 seismic stations, sampling 3318 earthquakes with moment magnitudes (**M**) ranging from 1.5 to 5.0 occurred from 1989 to 2020.

Ktenidou et al. [2014] summarize multiple methods that can be used to measure kappa. An approach that is suitable for application over the magnitude range of our study events is based on using broadband spectral inversion. We estimate kappa using a variation of the broadband technique of Anderson and Humphrey [1991], in which a theoretical spectrum is fit to an observed spectrum using a least squares minimization procedure. This method fits the S-wave observed spectrum, $Y(f_i)$, to a modelled spectrum, $E(f_i)$, which is characterized by seismic moment (M_0), corner frequency (f_0), and the spectral decay parameter (κ), using the least square's solution:

$$\chi(f_o') = \frac{1}{NF} \sum_{i=1}^{NF} [\ln Y(f_i) - \ln E(f_i)]^2 \qquad (4.1)$$

where the smallest misfit (χ) over a number of spectral frequencies (NF) is calculated from the observed spectrum and the predicted model spectrum, which is described in the next section. For a given trial value of f_0, the inversion to determine the corresponding values of M_0 and κ is straightforward. Thus, as a practical matter, the solution is found by performing the inversion for a range of trial values for the corner frequency of the spectrum (f_o').

The trial corner frequency value which results in the lowest misfit defines the resultant seismic moment, corner frequency and spectral decay parameter for each spectrum. The key advantage of the broadband spectral inversion method is that the frequency range that can be used to determine kappa is not limited by the corner frequency of the earthquake and thus, the method can be applied over a broad magnitude range. However, the inversion becomes non-unique at small **M** due to trade-off between kappa and the corner frequency.

To isolate the effects of kappa on the spectrum at high frequencies, we need to remove the effects of site amplification. The amplification effects can be predicted if we know the velocity profile beneath the station. Site-specific velocity profiles are sparse and tend to describe deep structure (i.e., >0.5 km) in eastern Canada [e.g., Brune and Dorman, 1963; Cassidy, 1995; Kao et al., 2014; Bent and Kao, 2015; Kuponiyi et al., 2016; Bent et al., 2019; personal communication Bent, 2021]. Consequently, amplification functions often assume generic values of velocity near the surface (such as 2000 m/s) [e.g., Ktenidou et al., 2016]. In this study, by contrast, we make use of recent measurements of shear wave velocity at seismic stations in eastern Canada [Ladak, 2020; Ladak et al. 2021; Stokoe et al., 2021]. The near-surface rock shear wave velocity at stations ranges from 847 m/s to 2409 m/s, with the average shear wave velocity in the upper 30 m ranging from 887 to 2936 m/s [Ladak et al., 2021]. This significant variability in velocity, and its impact on near-surface amplification, needs to be considered in the determination of kappa from recordings at the stations. Utilizing a combination of the near-surface and deeper structure profiles, we can estimate site amplification at each site and thereby

isolate the diminution term. Thus, we use a combination of site amplification modelling and the broadband approach to determine kappa for seismic stations on rock in eastern Canada. We also examine the relationship between site characteristics and kappa.

4.2 Database

The dataset for this study was curated from the Canadian National Seismic Network (CNSN) earthquake database for eastern Canada (longitude 82.5ºW to 52.5ºW, latitude 44ºN to 52ºN) from 1989/01/01 – 2020/09/01 for earthquakes with a **M** ≥1.5 with a station-earthquake distance ≤ 150 km at 25 seismic stations (See Data and Resources). The CNSN reports magnitudes on several scales; magnitudes are converted to moment magnitude where required by applying conversion equations from the Composite Canadian Seismicity Catalog [Fereidoni et al., 2012]. The compiled database includes all useable records from 3318 earthquakes of **M**1.5 to 5.0, where the criteria for useable records are described further in the following.

The initial database, as shown in Figure 4.1, was processed using standard processing procedures (see Data and Resources). Windowing of the time series follows the methodology of Goulet et al. [2014; 2021], in which the P wave window is defined from 2 seconds(s) to 0.5 s prior to the P- and S-wave picks, respectively. The S-Lg wave window begins 0.5 seconds prior to the S wave pick; the end is defined from the combination of the expected Lg arrival time (origin time subtracted from the hypocentral distance divided by 3.53), the expected duration of the Lg wave (17.4 plus 0.052 multiplied by the hypocentral distance), and a magnitude dependent source duration (1 second for M<5 and 3 seconds for M≥5). The pre-event window, also known as the noise window, ends 2 seconds prior to the P wave pick, and has the same duration as the S-Lg window. From the windowed time series, a Fourier Amplitude Spectrum (FAS) database was generated for all three components, and the mean of the horizontal components was obtained using the Effective Amplitude Spectrum (EAS) as defined by Kottke et al. [2018; 2020]. Records were smoothed using the Konno Ohmachi [1998] smoothing function with a b value of 20. The resultant 25,546 records for 25 stations in eastern

Canada are used to generate spectra for: signal to noise ratio; horizontal-component EAS; vertical FAS. For a minimum signal-to-noise ratio of 3, and requiring a frequency band at least 10Hz in width, we retain 17,595 of the 18,590 (EAS and Vertical) records for spectral inversion.
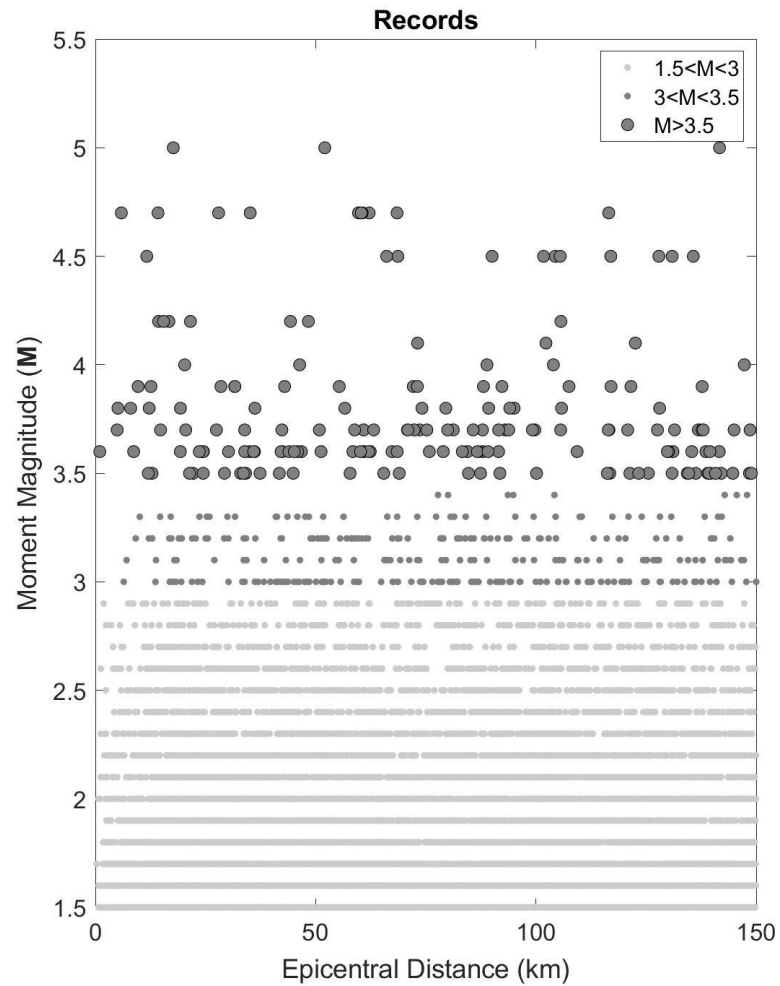
Figure 4.1: Earthquake records from 1987/01/01 to 2020/09/01 used in this study. Small grey circles represent moment magnitude (M) from 1.5 to 3, darker grey small circles represent M from 3 to 3.5 and larger circles with a dark ring represent M >3.

4.3 Methods

We implement a broadband inversion approach based on the basic principles and assumptions illustrated in Figure 4.2. The first assumption is that the Fourier spectrum of the ground motion at near-source distances follows a Brune [1970; Boore, 2003] model, in which the spectrum is characterized by seismic moment and corner frequency. Frequency-dependent spectral amplification occurs during transit through the velocity gradients beneath the station and can be modeled utilizing the quarter-wavelength of Boore [2003] (with his site_amp function; see Data and Resources). Spectral amplitudes are attenuated at high frequencies due to: (i) anelastic attenuation with distance (where the anelastic attenuation is inversely proportional to regional Quality factor); and (ii) near-surface site effects, as modeled by kappa (κ_0 parameter of Anderson and Hough [1984], denoted more simply here by κ). The overall amplitude level of the spectrum will decay with distance due to geometrical spreading, but this does not impact spectral shape; it impacts only the amplitude of the spectrum.
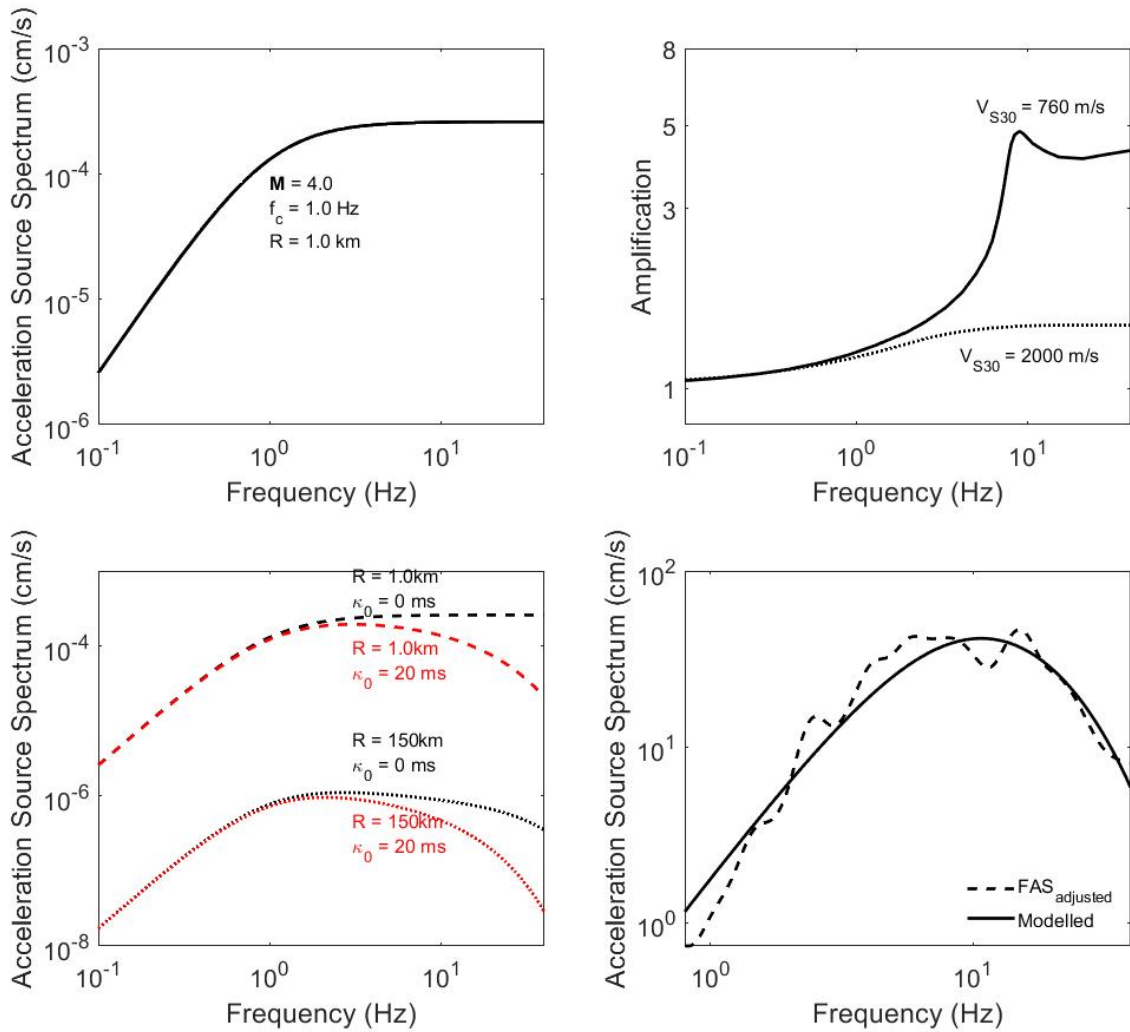
Figure 4.2: Assumptions and basic principles of the broadband inversion. Earthquakes are assumed to follow a Brune spectral shape (upper left panel); amplification is due to velocity gradients that can be calculated from the velocity profile using the quarter-wavelength approximation (upper right panel); diminution of high-frequency amplitudes is attributed to anelastic attenuation with distance and near-surface kappa (lower left panel); and observed Fourier spectra is adjusted to remove the effects of geometrical spreading, regional anelastic attenuation, and crustal amplification to obtain a FAS adjusted (dashed black line) which then has a broadband inversion implemented to obtain the modelled spectrum (black solid line) (lower right panel).

 The recorded spectra are first adjusted to remove the frequency-dependent effects of regional anelastic attenuation and crustal amplifications, as described in detail in the next section. From each resultant adjusted spectrum (E(f)), we then implement the Anderson and Humphrey [1991] broadband inversion method to determine the three controlling parameters of the Fourier amplitude spectra: seismic moment (M_0), corner frequency (f_0), and the spectral decay parameter kappa (κ_0). The only constraint applied to the measurement of the three parameters is that the corner frequency ranges from 0.8Hz to 40Hz. We keep the approach as simple as possible to better understand the biases introduced by our assumptions regarding site amplification due to velocity profile and data selection. In addition, by not applying a constraint to kappa, for example a non-negativity constraint, we can then understand if we have captured a site's amplification well or if we have over- or under-estimated it Using the Brune model [1970; 1971] the apparent earthquake source spectrum (i.e., at a distance of 1 km, after removal of regional anelastic attenuation and crustal amplification, but including the effects of kappa) as described by Anderson (1986) can be expressed as:

$$E(f_i) = \frac{0.85 M_o (2\pi f_i)^2}{4\pi\rho\beta^3 R' \left[1 + \left(\frac{f_i}{f_0}\right)^\gamma\right]} e^{-\pi\kappa_0 f_i} \tag{4.2}$$

where f_i are the frequency steps, γ is the fall off of the spectrum at high frequencies (=2), ρ is the density, β is the shear wave velocity (=3.7 km/s in eastern Canada), and R' represents the geometrical spreading function. The partitioning of energy on the two horizontal components, amplification due to free surface, and the shear wave radiation pattern is captured in the constant 0.85. The geometrical spreading function, R', is represented by a piecewise trilinear form [e.g., Atkinson and Mereu, 1992; Atkinson, 2004]:

$$R' = \begin{cases} R^{1.3}, R \leq 70 \\ [70^{1.3}](\frac{R}{70})^{-0.2}, 70 \leq R \leq 140 \\ [70^{1.3}][(\frac{140}{70})^{-0.2}]\left(\frac{R}{140}\right)^{0.5}, R \geq 140 \end{cases} \tag{4.3}$$

where R is the source to station distance (hypocentral distance). To ensure the assumed geometrical spreading and anelastic attenuation is reasonable for this dataset we plotted residuals of the observed spectra with respect to the model spectra (i.e., the difference between observed and predicted Fourier amplitudes in log space) versus distance to verify that there are no significant trends (see Figure 4.3 below).

We invert Equation 4.2 at trial corner frequencies that range from the lowest frequency to the highest frequency for which the signal-to-noise ratio >3. One-hundred corner frequencies (NF=100), log10 spaced across the valid SNR>3 frequency range, are used as trial corner frequencies. The trial corner frequencies are inserted into equation 4.2, then the equation is simplified to invert for M_0 and κ_0. The combination that minimizes the misfit of Equation 4.1 is taken as the resultant f_0, κ_0, and M_0 for that individual record. The inversion is performed for each recording on the effective amplitude spectrum (EAS) and the vertical FAS.

We note that the value of f_0 can be used to infer the source radius and stress drop using [Brune, 1970; 1971]:

$$r = \frac{2.34\beta}{2\pi f_0} \tag{4.4}$$

where r is the source radius, β is the shear wave velocity, and f_0 is the corner frequency. The Brune stress drop parameter, $\Delta\sigma$, is given by:

$$\Delta\sigma = \frac{7}{16}\frac{M_0}{r^3} \tag{4.5}$$

4.4   Analysis and Results

In the following, we provide details on how kappa values were obtained for each station, for each available component, using the inversion methodology described above. Table 4.1 outlines the stations examined and their properties. Note that most stations are located at rock outcrops or on bedrock, usually within an insulated vault, or within a basement building or underground vault.

Table 4.1: Station locations, region, instrument record type, and geology

Station	Record Type	Surficial Geology[1]	Bedrock Geology [2] (Unless noted otherwise)
A11 47.2431° N 70.1968° W (Charlevoix)	EHE/N/Z HHE/N/Z	Veneer (sand, gravel, and pockets of finer sediment) includes washed till and bedrock	Cambrian to Ordovician inferior mudrock, green and red slate, sandstone, and limestone
A16 47.4706° N, 70.0064° W (Charlevoix)	EHE/N/Z HHE/N/Z	Offshore Sediments (dominant silt and clay)	same as A11
A21 47.7036° N, 69.6897°W (Charlevoix)	EHE/N/Z HHE/N/Z	Offshore Sediments (dominant silt and clay)	same as A11
A54 47.4567° N, 70.4125° W (Charlevoix)	EHE/N/Z HHE/N/Z	Till veneer (may include rock outcrop)	Precambrian orthopyroxene granitoid, charnockite, mangerite, jotunite, and hypersthene syenite
A61 47.6936° N, 70.0913° W (Charlevoix)	EHE/N/Z HHE/N/Z	Till blanket	Precambrian paragneiss pelitic gneiss, marble, quartzite and iron formation, mafic intrusive rock common

A64 47.8264° N, 69.8922° W (Charlevoix)	EHE/N/Z HHE/N/Z	Till veneer (may include rock outcrop)	Precambrian migmatite
BATG 47.2767° N, 66.0599° W (north New Brunswick)	HHE/N/Z	Till veneer (may include rock outcrop)	Ordovician felsic volcanic rock [5.]
BCLQ 46.9263° N, 71.1728° W (Quebec)	HHE/N/Z	Offshore Sediments (dominant silt and clay)	Mesoproterozoic pink banded quartzofeldspathic gneiss
CNQ 49.302° N, 68.0746° W (mouth of St. Lawrence)	EHZ	Bedrock, undifferentiated (75% rock outcrop) may include minor colluvial	Precambrian granitoid orthogneiss
DAQ 47.9627° N, 71.2437° W (northeast of Charlevoix)	EHZ	Till veneer (may include rock outcrop) or till blanket	same as A54
DPQ 46.6804° N, 72.7774° W (Quebec)	EHZ HHE/N/Z	Till veneer (may include rock outcrop)	Mesoproterozoic dominant felsic granulites
GAC	EHZ	Till veneer (may include rock outcrop)	Archean to Proterozoic quartzite

45.7033° N, 75.4786° W (Quebec)	HHE/N/Z		
GBN 45.4077° N, 61.5128° W (Nova Scotia)	HHE/N/Z	Till veneer (may include rock outcrop)	Devonian siltstone, sandstone, wacke, conglomerate, dolostone [3.]
GSQ 48.9142° N, 67.1106° W (mouth of St. Lawrence)	EHZ	Bedrock, undifferentiated (75% rock outcrop) may include minor colluvial	Same as A11
ICQ 49.5217° N, 67.2719° W (mouth of St. Lawrence)	EHZ HHE/N/Z	Till veneer (may include rock outcrop)	Mesoproterozoic monzodiorite, quartz, monzonite, mangerite containing diorite enclaves
KGNO 44.2272° N, 76.4934° W (Kingston)	HHE/N/Z	Offshore Sediment, variable thicknesses	Ordovician Limestone, dolostone, shale, arkose, and sandstone [4.]
LMQ 47.5485° N, 70.3258° W (Charlevoix)	EHZ HHE/N/Z	Till blanket	Mesoproterozoic undifferentiated migmatite, charnockite, mangerite and enderbite
MCNB 45.59582° N, 67.3198° W	HHE/N/Z	Bedrock, undifferentiated (75% rock outcrop) may include minor colluvial	Silurian sedimentary deep water marine clastics[5.]

(south New Brunswick)			
MOQ 45.312° N, 72.2541° W (Quebec)	EHZ	Till veneer (may include rock outcrop) of Till Blanket	Cambrian to Lower Ordovician mafic to ultramafic intrusive gabbro and tonalite
NATG 50.2872° N, 62.8102° W (mouth of St. Lawrence)	HHE/N/Z	Bedrock, undifferentiated (75% rock outcrop) may include minor colluvial	Neoproterozoic biotite granite coarse to medium grained
ORIO 45.4515° N, 75.511° W (Ottawa)	HHE/N/Z	Till Veneer (may include rock outcrop) or Offshore Sediments (dominant silt and clay)	Same as KGNO
OTT 45.3942° N, 75.7167° W (Ottawa)	EHZ HHE/N/Z	Till veneer (may include rock outcrop) or Offshore Sediments (dominant silt and clay)	Same as KGNO
QCQ 46.7791° N, 71.276° W (Quebec)	EHZ HHE/N/Z	Offshore Sediments (dominant silt and clay)	Mesoproterozoic tonalitic and trondhjemite gneiss
SMQ 50.2225° N, 66.7025° W (mouth of St. Lawrence)	EHZ	Bedrock, undifferentiated (75% rock outcrop) may include minor colluvial	Precambrian granite gneiss orthogneiss granitoid

VABQ 45.6047° N, 75.6079° W (Ottawa)	HHE/N/Z	Till veneer (may include rock outcrop)	Archean to Proterozoic paragneiss, garnet, quartzite

[1.] Geological Survey of Canada [2014]

[2.] Energie et Ressources Naturelles Quebec [2012] (Ma, Millions years ago)

[3.] Keppie, J.D. [2000]

[4.] Ontario Geological Survey [2011]

[5.] Department of Natural Resources Minerals, Policy and Planning Division. [2008]

4.4.1   Anelastic Attenuation

The anelastic attenuation can be described as the inverse of the regional quality factor, Q, which is frequency dependent. To establish the regional anelastic attenuation model, we use Equation (4.3) to correct all spectra for geometrical spreading to a hypocentral distance (R) = 1 km, considering events that were recorded on 3 or more stations to allow an average apparent source spectrum to be computed. We then examine the remaining attenuation trends with distance (which are attributed to anelastic attenuation), assuming that the spectral decay can be expressed by one of the alternative models for eastern Canada from the literature [e.g., Mereu et al., 2013; Atkinson, 2004]. A regional anelastic attenuation model, consistent with the geometrical spreading function, which effectively minimizes the residuals (i.e., the difference between the logs of the observed record spectra and the average event source spectrum) and was determined in conjunction with the geometrical spreading function is Atkinson's [2004] function:

$$logQ = 3.052 - 0.393 \log_{10} f_i + 0.945(\log_{10} f_i)^2 - 0.327(\log_{10} f_i)^3 \qquad (4.6)$$

Figure 4.3 shows the residuals versus distance for two selected frequencies (2 and 20 Hz), for the assumed geometric and anelastic attenuation model.
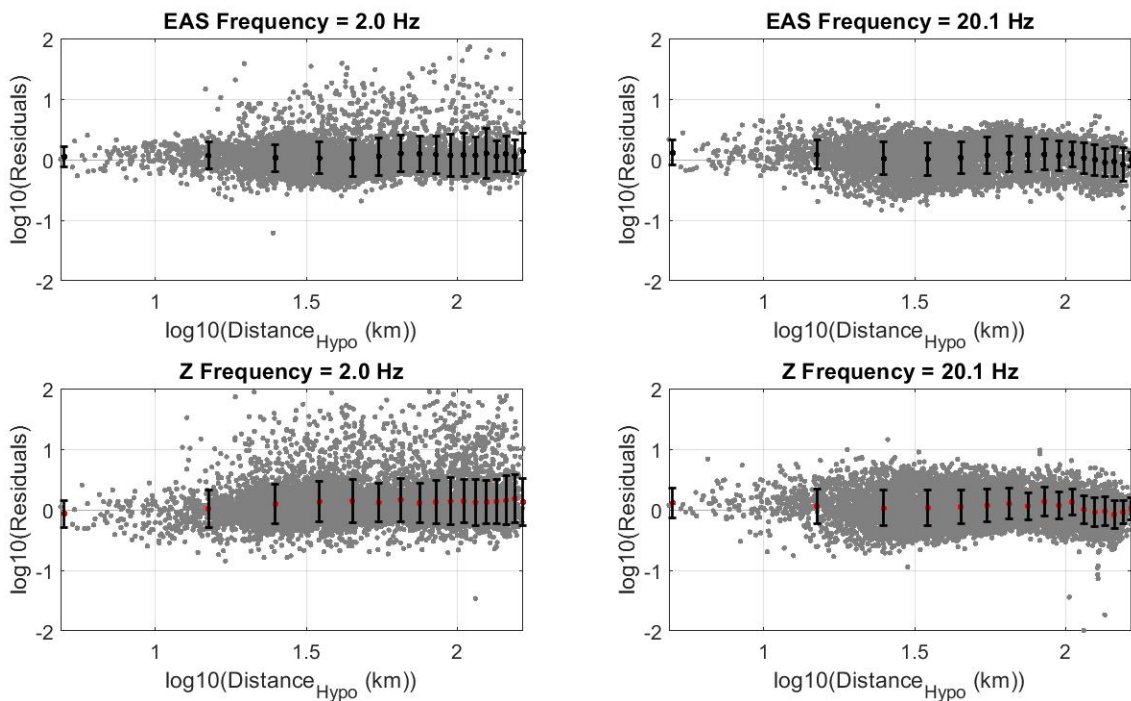
Figure 4.3: Horizontal-component residuals (top) and vertical-component residuals (bottom) for all records (grey) for frequencies of 2 Hz (left) and 20 Hz (right). Black symbols show mean binned distance residual (black circle) with standard deviation bars (black whiskers).

4.4.2   Apparent Source Spectra

It is useful to examine the general trends of the source spectrum as a guide to further analysis. After removing anelastic attenuation and geometric spreading effects from the spectra as described in the foregoing, we obtain an apparent source spectrum for each record; this spectrum contains both the effects of the average regional crustal amplification and the average regional kappa for the sites. We can remove the average crustal amplification effects for a generic velocity profile from the horizontal component by adopting the amplification model of Boore and Campbell [2017], which corresponds to a rock site in eastern North America having a time-average shear wave velocity over the top 30m (V_{S30}) of 2000m/s. This amplification function is unity at low frequencies and increases to a factor of 1.4 at frequencies of 10 to 20Hz. For the vertical component,

we assume (initially) that the amplification is negligible and equals unity. After dividing out the crustal amplification function, the remaining Fourier amplitude spectrum should be the product of the source spectrum and the near-surface kappa effects. We visualize these spectra by binning them by magnitude, and log-averaging their amplitudes. Figure 4.4 displays these spectra in both acceleration and displacement, in comparison to the corresponding Brune model spectra for an assumed average kappa of 2ms, for a stress parameter that approximately models the shape at each magnitude level. Overall, the spectral trends we observe in the binned apparent source spectra are consistent with a Brune model in which the stress drop parameter increases with magnitude (as observed in previous studies such as Yenier and Atkinson [2015]). The observed deviations from the Brune model at low frequencies and small magnitudes are likely due to noise contamination. We observe that the inferred average value of kappa is low (~2ms), while cautioning that a larger value of kappa could be accommodated if the crustal amplification was assumed to have a greater frequency dependence. In the next section, we look at the implications of the crustal amplification function and its implications for kappa values on a more site-specific basis.
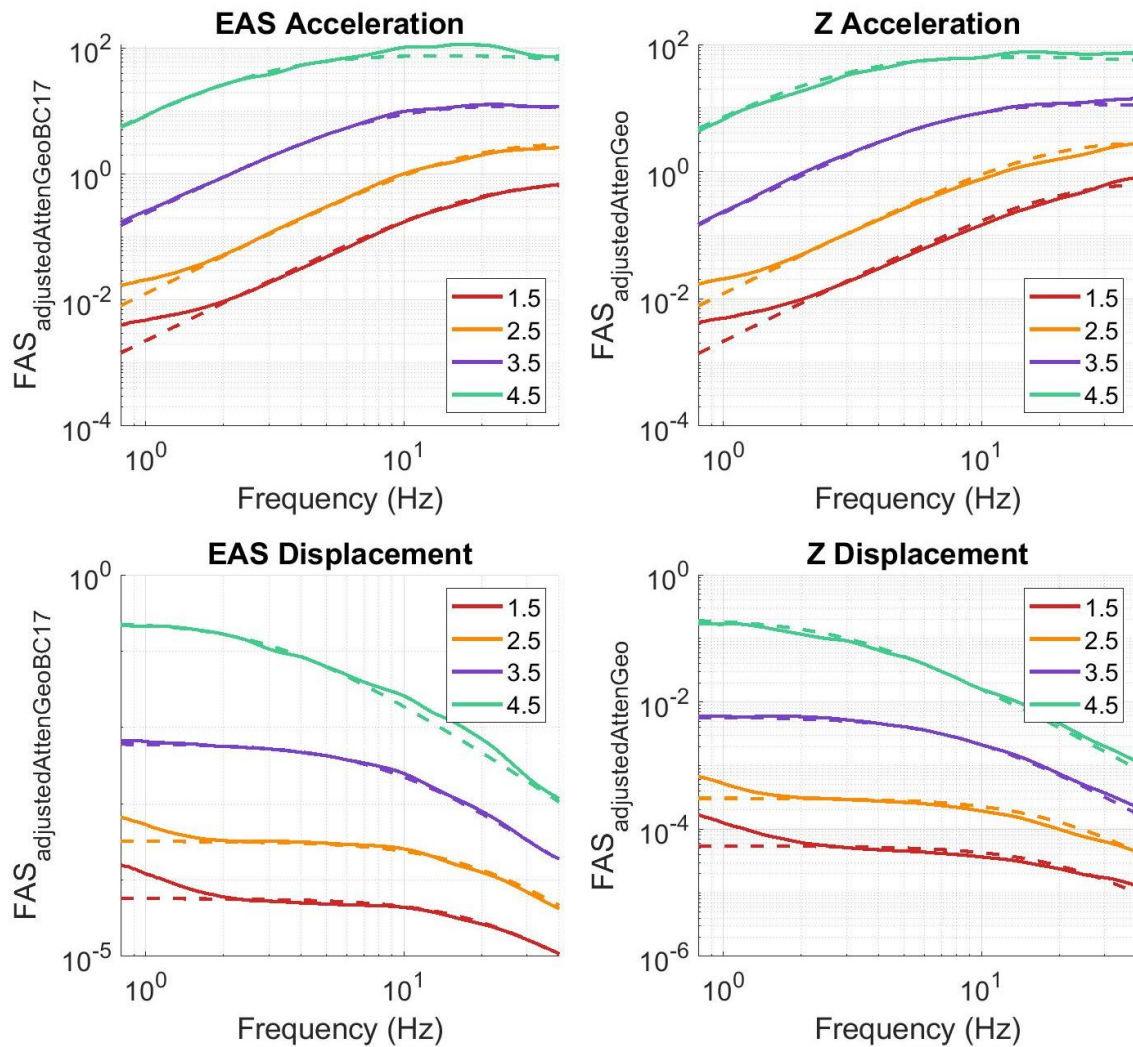
Figure 4.4: Mean source spectra for the horizontal (left) and vertical (right) component in acceleration (top) and displacement (bottom), for magnitude bins 1.5, 2.5, 3.5, and 4.5. Dashed lines show the corresponding Brune model spectra for stress parameters values of 20, 70, 100, and 210 bar respectively.

4.4.3 Crustal Amplifications and their Impact on Kappa

Crustal amplification are frequency dependent and in general, rock sites amplification acts to increase amplitudes with increasing frequency, and counteracts kappa, which has the opposite effect on high-frequency amplitudes. Therefore, it is important to explore the robustness and sensitivity of kappa estimates to the assumed crustal amplification and its

uncertainty. The ratio of the horizontal to vertical component spectrum (HVSR) is a well-known proxy for first order amplification effects [e.g., Borcherdt, 1970; Nakamura, 1989; Field and Jacob, 1993] and thus, examining HVSR at each station provides a good initial guide to these effects. Figure 4.5 shows HVSR for 4 example stations (for signal-to-noise ratio ≥3) from earthquake records (eHVSR) and microtremor HVSR (mHVSR) (from Ladak et al. [2021]), along with the amplification functions computed from the corresponding site-specific velocity profiles, which will be discussed later. We show HVSR and amplification functions to examine if first order estimations of amplification (HVSR) at the site are consistent with functions derived from the assumed velocity profile. From Figure 4.5 we can observe both stations A11 and GAC do not have similar amplification functions to the HVSR which suggests that the velocity profile may not capture the amplification of the site well. Stations A64 and ORIO have similar HVSR and velocity driven amplification profiles suggesting the velocity profile may be capturing site amplification well. The appendix, Figures and Tables A1-A25, contains similar information for all stations. Based on the HVSR, stations can be characterized by four types of HVSR shapes: (i) flat (A16, A54, A61, BCLQ, ICQ, NATG, VABQ); (ii) increasing with frequency (DPQ, KGNO, MCNB, ORIO); (iii) decreasing with frequency (A11, GBN, QCQ); or (iv) displaying a dominant peak frequency (A21, A64, BATG, GAC, LMQ, OTT). Stations CNQ, DAQ, GSQ, MOQ and SMQ do not have eHVSR as they only record ground motion on the vertical component. Based on the mHVSR it is likely that stations DAQ and GSQ have a flat HVSR, station SMQ may be flat or have a decreasing HVSR, and station CNQ and MOQ likely have a dominant peak frequency.
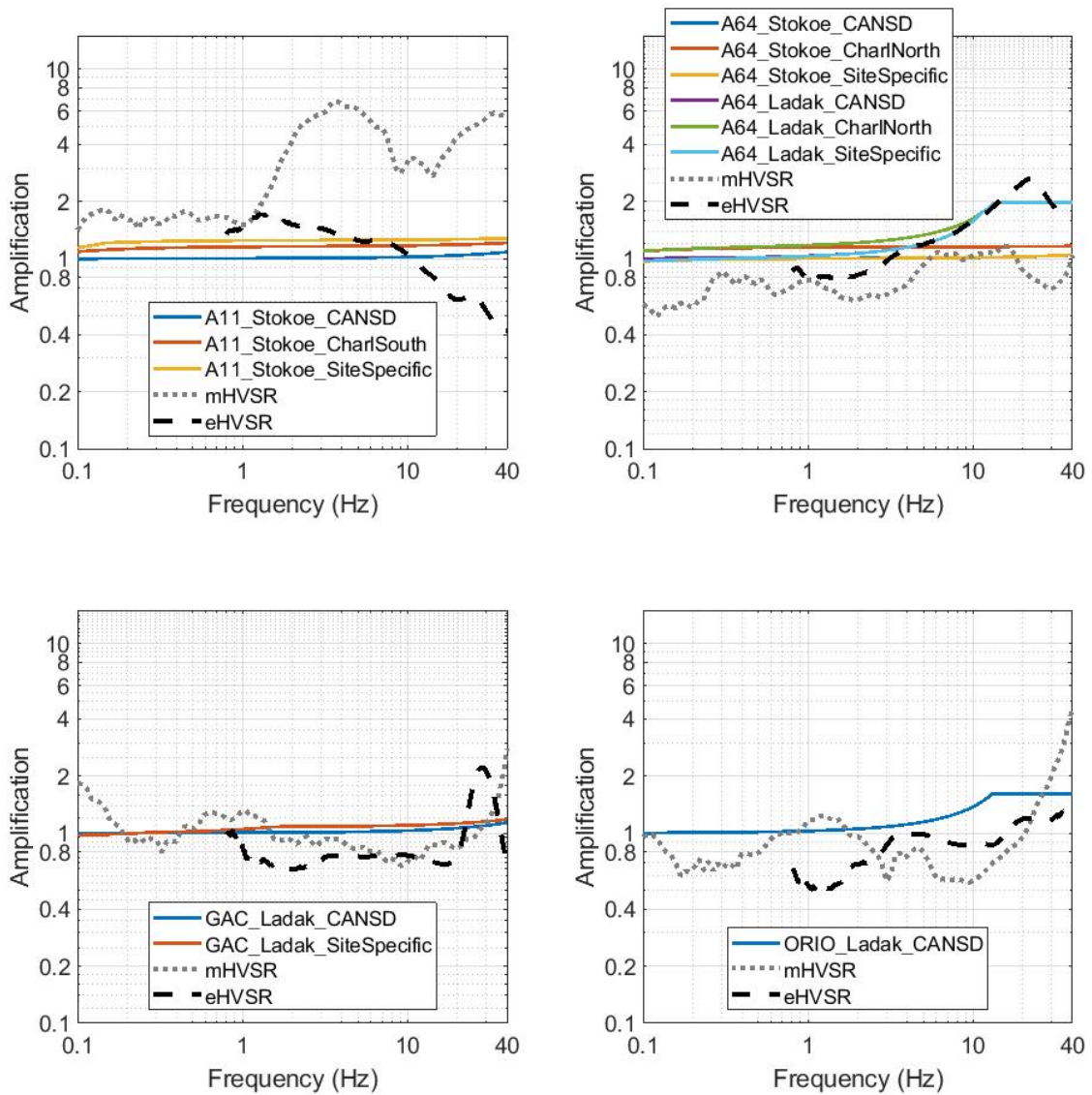
Figure 4.5: Sample seismic station mean horizontal to vertical spectral ratio from earthquake records (dashed black) and microtremor data (dotted grey; Ladak, 2020; Ladak et al. 2021) and amplification functions (solid colour lines) for a stations assumed velocity profiles (see the electronic supplement Figures A1-A25 for all stations amplifications and HVSR).

The HVSR, from Figure 4.5 and Figures A1- A25 (see appendix), show that high frequencies can affected by site amplification effects which need to be considered when

assessing kappa. A common assumption is that amplification on the vertical component is negligible compared to that on the horizontal component [e.g., Nakamura, 1989; Lermo and Chavez Garcia, 1993] which has been shown to be an inaccurate assumption [Edwards et al., 2013], for example, in cases such as topography amplification [Sanchez-Sesma, 1985]. By comparing the HVSR to the modelled amplification for a site we can assess whether this assumption is reasonable. Figure 4.5 shows that in some cases the HVSR agrees well with the computed amplification based on the velocity profile (e.g., A64), and in other cases (e.g., A11) it does not. We infer that the vertical component will not necessarily be free of amplification (and/or the amplification effects are not always predicted well from the velocity profile based on visual comparison of HVSR and site amplification from velocity profiling). It is expected that vertical component amplification effects will result in differences in the determined values of kappa from the vertical and horizontal components, if we assume that the amplification on the vertical component is unity, whereas that of the horizontal amplification is captured by the computed amplification effects due to the velocity profile.

We can compute the expected crustal amplification from the velocity profile, which may vary from station to station based on its geology (e.g., Table 4.1). The generic crustal profile of Ktenidou et al. [2016] provides a good starting point. It is characterized by an average Vs of 2000 m/s in the upper 30m, then extended to greater depth using eastern Canada's Canadian Shield (CANSD) profile [Brune and Dorman, 1963]. As shown on Figure 4.6, we perturb this profile to express variability in near-surface velocity, depth and number of layers, considering the impact of both shallow and deep velocity perturbations. For each of the velocity profiles we compute the corresponding frequency-dependent amplification according to the classic quarter-wavelength approach using Boore's [2003] site_amp function (see Data and Resources), in each case varying only the velocity. We remove each computed amplification from the Fourier amplitude spectra (i.e., by spectral division) in the inversion process, allowing us to determine the sensitivity of kappa to the velocity profile.
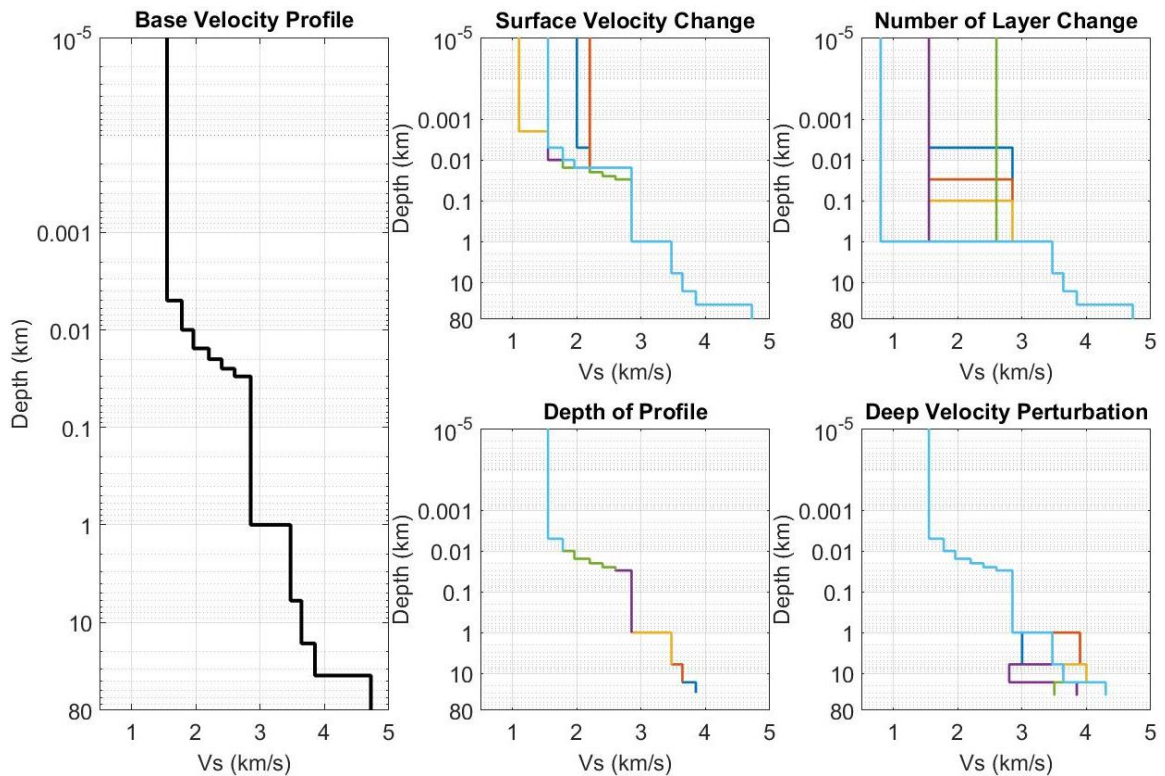
Figure 4.6: Generic velocity profile to test velocity perturbation effects on kappa: the generic base profile (left panel), surface velocity changes (upper middle panel), change in the number of layer perturbations (upper right panel), changing depth of profile (lower middle panel), and deep velocity perturbations (lower right panel).

The sensitivity of kappa to velocity perturbations affecting crustal amplification is shown in Figure 4.7. A key initial observation is that kappa does not deviate significantly from zero, within our ability to measure it, considering the factors involved. From a ground-motion modeling point of view, for generic hard rock sites there is no sound empirical basis for imposing any additional high-frequency damping beyond that already included via the anelastic attenuation coefficient. This is consistent with the inference from Figure 4.4 that kappa is ~2 ms (i.e., a very low value). Uncertainty in the velocity profile and, as a result, the crustal amplification function results in corresponding uncertainty in the inferred value of kappa by ~1 to 6ms, which can move kappa either above or below the value of 0. Another way to think of this is that the net effect of the near-surface rock

profile could result in either amplification or de-amplification of high-frequency motions. For example, a near-surface velocity perturbation of ~500 m/s can modify the inferred kappa by ~1 to 2 ms. The alteration of the depth and resolution (number of layers) of the profile also modifies inferred kappa by ~ 1 – 2ms. To consider the effects of deeper structure, we combine the near-surface profiles with a deeper profile drawn from receiver function analysis [Cassidy, 1995; Kao et al., 2014; Bent and Kao, 2015; Bent et al., 2019; personal communication Bent] and surface wave analysis [Brune and Dorman, 1963; Kuponiyi et al., 2014]. Kappa is not significantly impacted by changes in the assumed velocity structure at depths >1 km, as the deep structure only impacts amplification at frequencies <0.1 Hz. However, it is important to consider the profile to seismogenic depths in order to capture the full amplification due to the crustal gradient; if the profile is truncated as shallow depths (<1km), the inferred kappa is impacted by as much as 6ms.
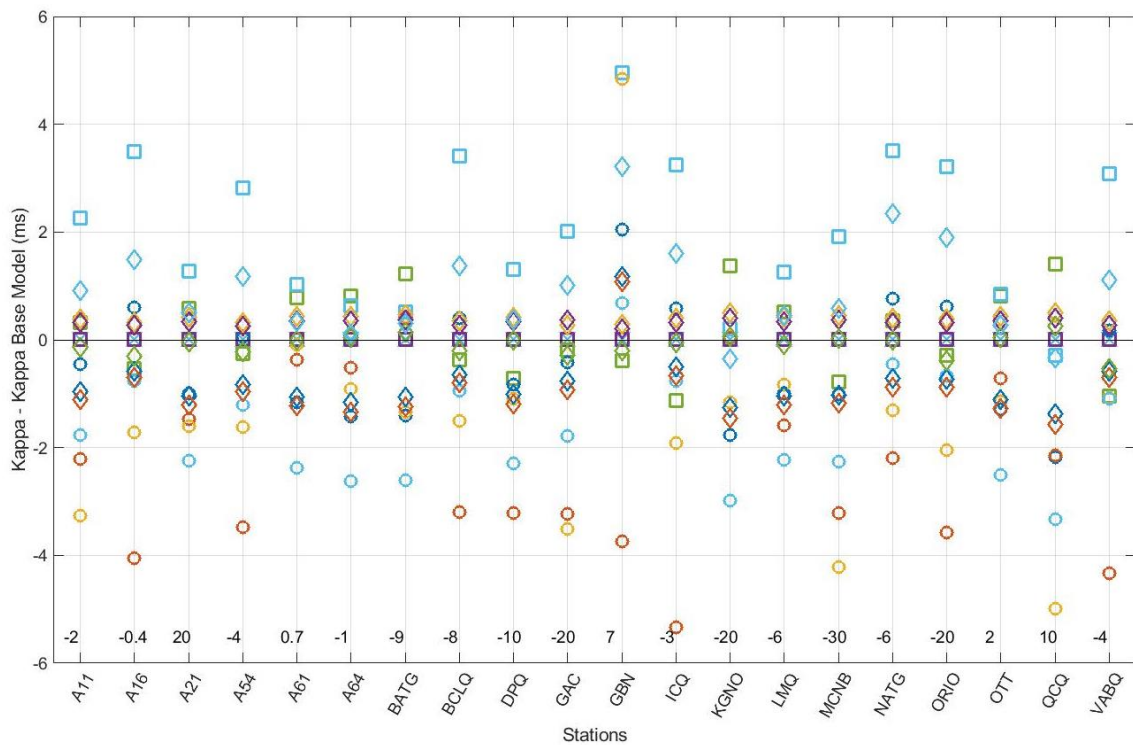
Figure 4.7: Impact of velocity profile perturbations on calculated EAS kappa. The vertical axis represents the difference of the specific model from the base model

shown in Figure 4.6. Testing profiles for each type of velocity profile change (Number of Layers = □, Depth of Profile = •, Deep Velocity Perturbation = x, Surface Velocity Perturbation = ◊) are shown by coloured symbols which correspond to the colours in Figure 4.6. Base velocity profile kappa values are shown above the respective station on the x-axis.

The recent measurements of Ladak [2020], Ladak et al. [2021], and Stokoe et al. [2021] of near-surface (upper 100m) shear wave velocity profiles in eastern Canada allow for site-specific velocity profiles and thus, site-specific amplification profiles. These near-surface velocity profiles have maximum depths from 7m to 62m [Ladak et al., 2021] and 3m to 129m [Stokoe et al., 2021]. At a given station, 1 to 6 velocity profiles were created to estimate the uncertainty in kappa due to uncertainty in crustal amplification. Figure 4.8 shows the 6 velocity profiles and the associated amplification functions generated for station A54. In cases where a station had multiple estimated near-surface velocity profiles, such as those in Charlevoix (e.g., A11), the deeper profiles were fixed while the near-surface velocities were perturbed (see the appendix Figures and Tables A1 – A27). Each station has a near-surface profile extended with the CANSD [Brune and Dorman, 1963] profile; for stations having a deeper site-specific velocity profile, this deeper information was used to generate an alternative profile. In Charlevoix, a third profile was generated for each station. The third profile features a different deep velocity profile that is specific to the Paleozoic stations (A11, A16, and A21) or the Precambrian stations (A54, A61, A64, LMQ); this allowed us to test whether differences in deep structure may impact kappa in the two different types of geology.
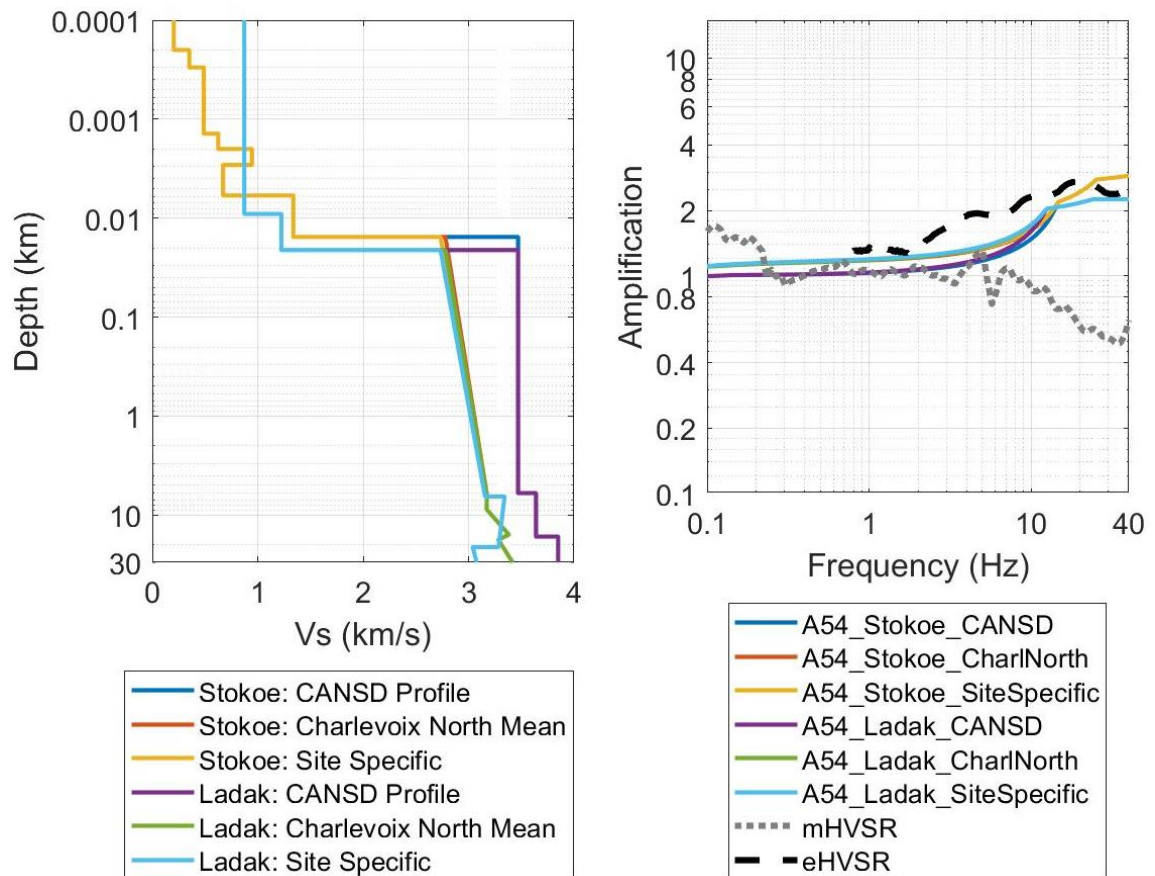
Figure 4.8: Station A54 velocity profile, on the left, and resultant amplification profiles, on the right, for 3 different types of profiles – a region wide (CANSD), a local profile (Charlevoix North), and a site-specific profile (Site-specific) with two near-surface velocity profiles (Ladak and Stokoe) (solid lines) (Bent et al., 2019; personal communication Bent; Brune and Dorman, 1963; Ladak, 2020; Ladak et al. 2021; Stokoe et al, 2021) and the horizontal to vertical spectral ratio from earthquake (black dashed) and microtremor (grey dotted) (Ladak, 2020; Ladak et al., 2021) data.

At stations CNQ, GSQ, NATG, MOQ, SMQ, and VABQ there were no near-surface velocity profiles available. At these stations we utilize bedrock geology, shown in Table 4.1, and the average shear wave velocity for each region. We consider the bedrock to be subdivided into two generic types: Paleozoic rock south of the St. Lawrence River, or

Precambrian rock north of the river, with average shear wave velocities of 1671 m/s and 1935 m/s respectively [Ladak, 2020; Ladak et al., 2021]. These average shear wave velocities are used to construct a generic shallow profile to attach to the CANSD model and, if available, a deeper structure profile. The velocity and amplification profiles and mean kappa for each station are provided in Appendices.

Many of the amplification functions exhibit similar slope at higher frequency; this is expected because their near-surface profiles are similar. An exception is the Charlevoix region, within which the near-surface conditions are highly variable. In general, adopting a site-specific velocity profile (in place of a generic regional profile) may result in changes in computed kappa of 1 to 3ms.

Figure 4.9 shows how the mean site-specific kappa is impacted by the velocity profile, by comparing site-specific kappa values obtained assuming either the Ladak [Ladak, 2020; Ladak et al., 2021] or Stokoe [Stokoe et al., 2021] near-surface profiles for the Charlevoix stations; in both cases the deeper profile is that of CANSD [Brune and Dorman, 1963]. This demonstrates that the mean site-specific kappa is affected only marginally by uncertainty in the near-surface profile. Sampling across alternative velocity models for all stations, the kappa values obtained vary from 0 to 6ms, with an average sensitivity to the assumed profile of 1ms. The largest impact of the assumed velocity model for a single component (i.e., the horizontal component results) is observed for the three stations in Charlevoix – A16, A54, and LMQ. The sensitivity of kappa to the profiles at these stations reflects the influence of the very soft upper layers of Stokoe et al.'s [2021] profiles. These profiles were obtained at a distance offset of 1m, 20m, and 30m on softer material/deposits than that of the seismic stations; thus, those profiles may not reflect the actual conditions beneath the seismometers.
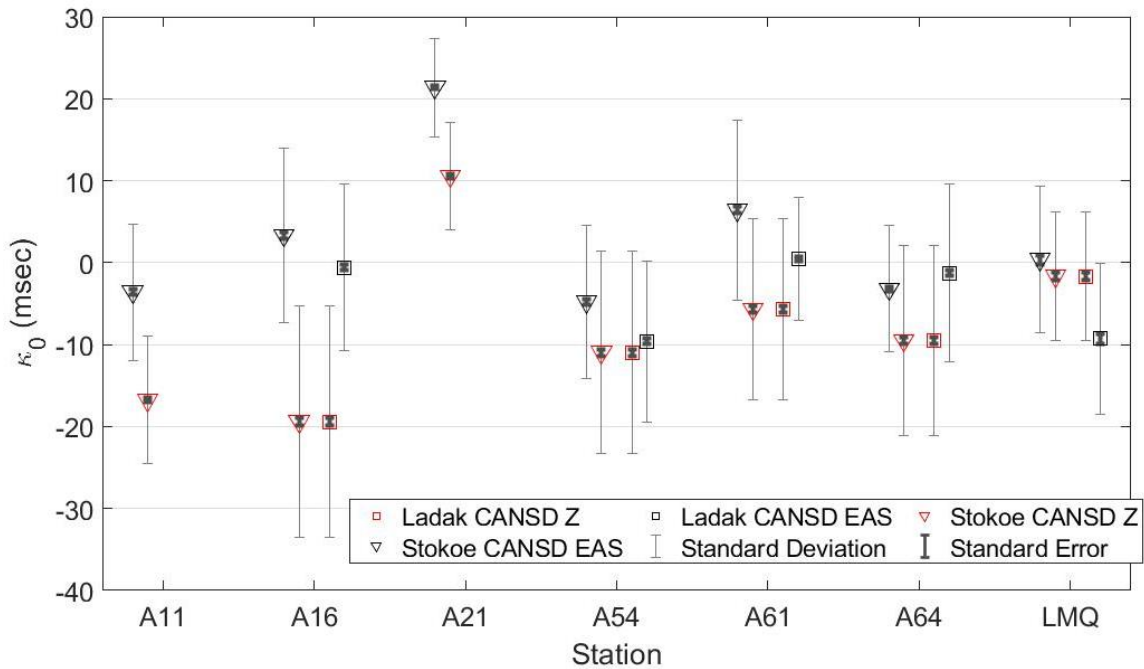
Figure 4.9: Mean site-specific kappa determined using Ladak (squares) and Stokoe (triangles) near-surface velocity profiles coupled with CANSD (red) deeper profile for the vertical (red) and effective amplitude spectrum (black) components.

4.4.4   Other Kappa Sensitivities

Kappa may be sensitive to factors other than those involving crustal amplification. For example, we determined kappa in the foregoing by taking the average values obtained for each station from individual records (corrected for geometrical spreading, regional attenuation, and site-specific amplification). Many (but not all) earthquakes, such as those recorded in Charlevoix and near the mouth of the Saint Lawrence River, had several useable records. For earthquakes with more than one record, it is logical to constrain the seismic moment and corner frequency to be the same for all records of the same event. To test the impact of this constraint, we adopt the log-average moment and log-average corner frequency for each event where 3 or more records exist. For these fixed source parameters, we can recalculate site-specific kappa values for the records of that event. Figure 4.10 shows how this iterative step to constrain the source parameters impacts determined site-specific kappa values (assuming the Ladak-CANSD velocity model).

Appendix Tables A28 and A29, provide site-specific kappa results for the unconstrained and constrained kappa for all velocity model perturbations. In general, we find that changes in computed site-specific kappa fall within the same uncertainty bounds as those attributable to the influence of crustal amplification (i.e., a few ms).
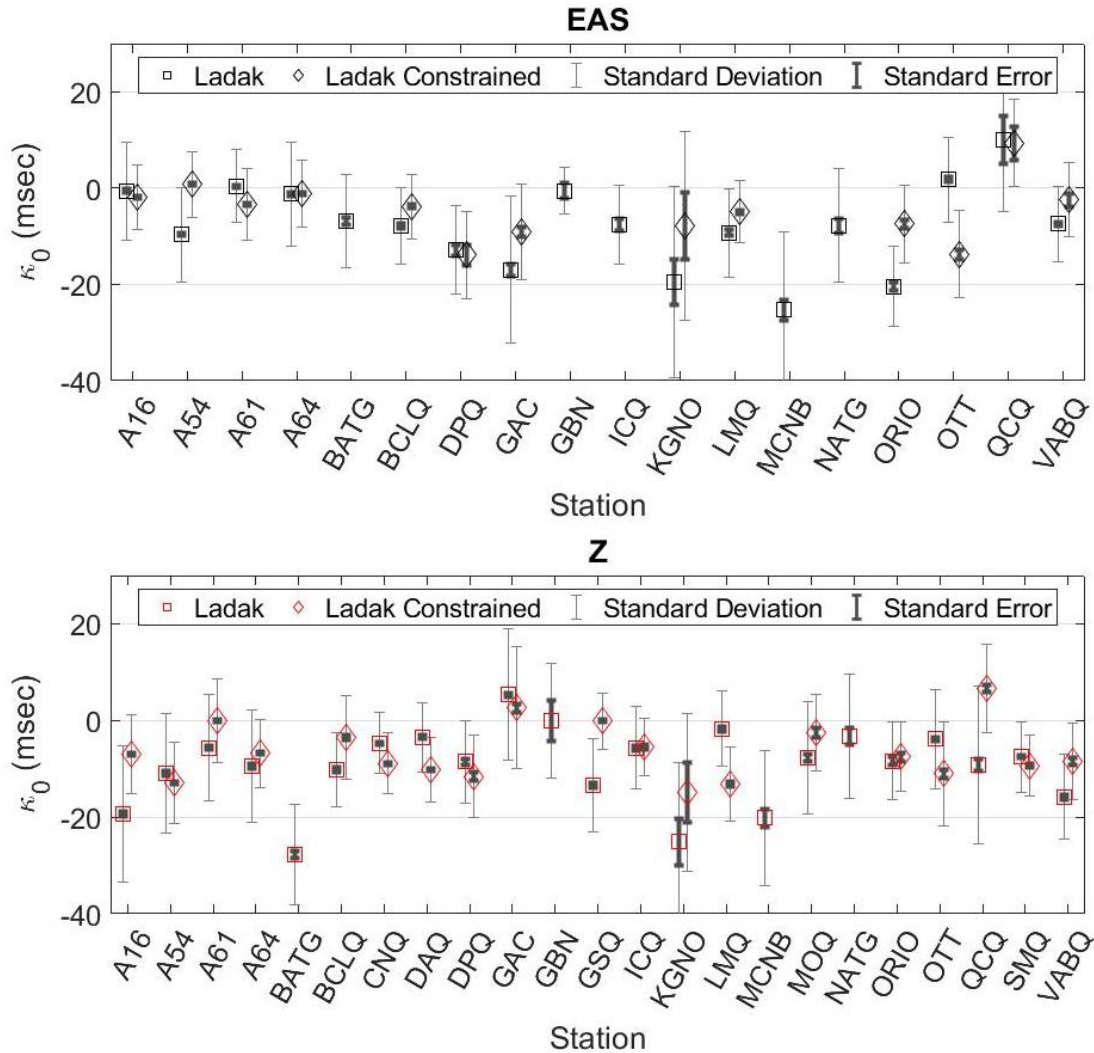
Figure 4.10: Mean site-specific kappa (up to 150km) using the Ladak and CANSD velocity profiles for stations in eastern Canada. Horizontal kappa (black) without constraint on the source parameters (square) and with constraint (diamond) are shown in the upper panel while vertical kappa (red) are in the lower panel.

Standard deviation (thin grey whisker) and standard error (thick grey whisker) are shown for each kappa.

Kappa may also be sensitive to the assumed anelastic attenuation model. We selected an anelastic attenuation model that results in no distance trends on average. However, if we plot the Fourier amplitude spectrum of acceleration after anelastic attenuation correction, residuals (difference of logarithm mean event spectrum, for events with 3 or more records, from the logarithm of the individual record spectrum) for individual stations do not all follow the average trend equally well, as shown in Figure 4.11. For example, there are some attenuation trends at higher frequencies at A54, A64, DAQ, CNQ, LMQ, and SMQ. The attenuation sensitivity can also be examined by looking at how computed kappa varies with the choice of cut-off distance, as shown in Figure 4.12. We fit a simple linear trend to kappa versus distance, to distance cut-offs incremented in steps of 25km (i.e., 0-25km, 0-50km, 0-75km, etc.). If the slope is not statistically significant (i.e., within a standard error of 0), then the site-specific kappa can be determined by the mean of kappa values to this distance, which is the approach that we have implicitly assumed. Station-specific kappa values, reported in Table 4.2, were determined with data up to 150km excluding stations NATG, and ORIO where the site-specific kappa was determined with data up to 75km. Station GBN and KGNO had very few records close to the station and the linear fit(s) tend to be very steep as a result. We have reported site-specific kappa using the mean of values to 150km for these stations but caution the reader in their use as they may be overestimating the site-specific kappa. Table 4.2 summarizes site-specific kappa values by station, taking means to the applicable distance cut-off, and using the applicable velocity model. The selected velocity model follows a preferred order. For deeper structure we prefer the site-specific model; if not available we use the CANSD model. For shallower structure we prefer the Ladak-directly measured model; if not available we use the Stokoe model, or if neither is available, we use the Ladak average model based on regional velocity values.
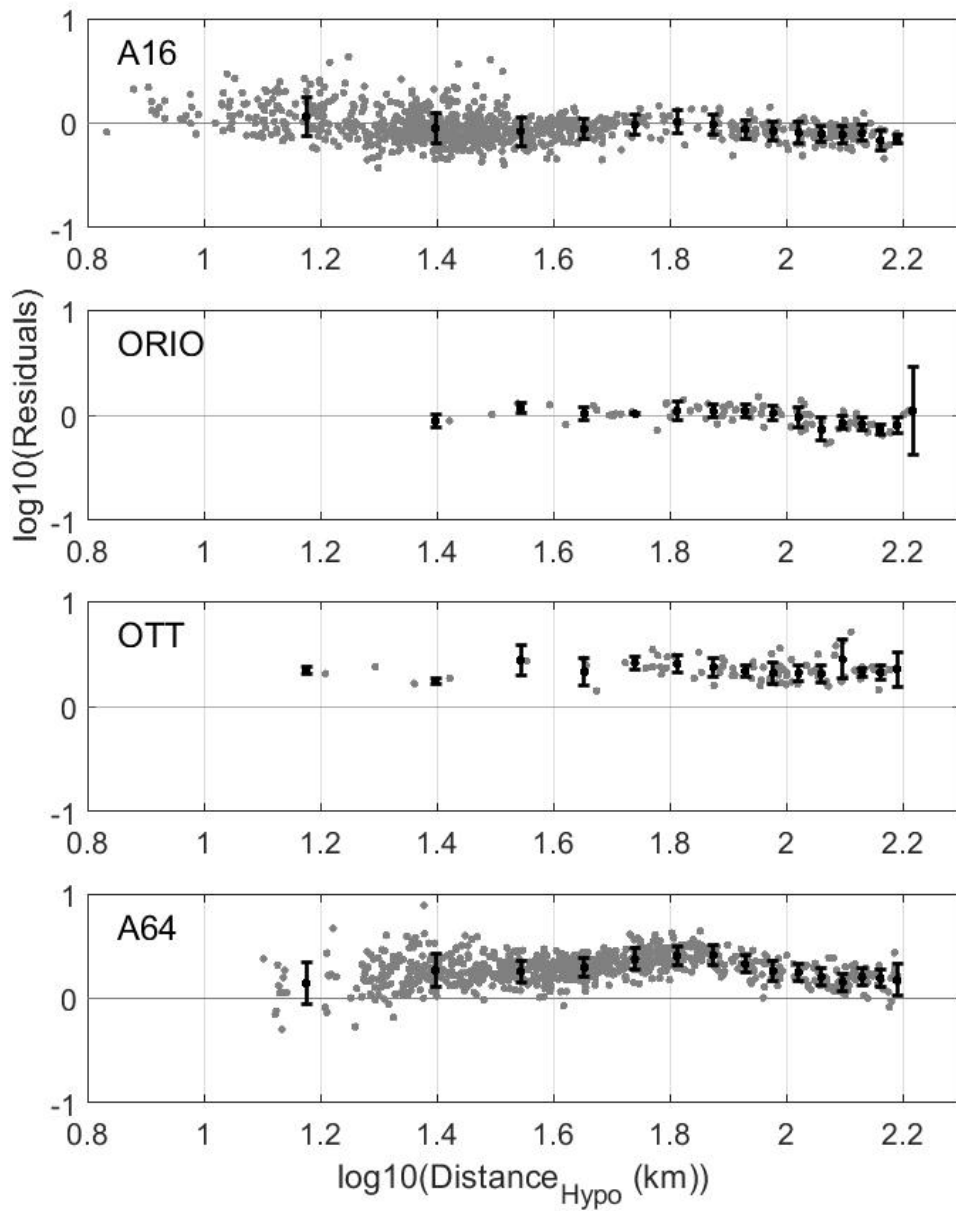
Figure 4.11: Residuals (with anelastic attenuation and geometrical spreading corrections) for the horizontal component at 20.1Hz for stations A16, ORIO, OTT and A64 respectively. Black symbols show mean binned distance residual (black circle) with standard deviation bars (black whiskers).

Table 4.2: Kappa and Site Parameters by Station

Station	κ_{0EAS} (ms)	κ_{0EAS} stdev (ms)	κ_{0V} (ms)	κ_{0V} stdev (ms)	Velocity Profile Used[†]	Distance cut-off (km)	V_{Srock}[1.] (m/s)	V_{S30}[1.] (m/s)	Number of Records	Rock Type [2., 3., 4., 5.]	Rock Age [2., 3., 4., 5.]	Instrument Housing[1.]
A11	-4	8	-17	8	S21SS	150	N/A	N/A	717 (EAS) 717 (V)	Paleozoic	443-541	Concrete insulated vault
A16	-0.7	10	-19	14	L20SS	150	1336	1530	816 (EAS) 815 (V)	Paleozoic	443-541	Concrete insulated vault
A21	21	6	11	7	S21SS	150	N/A	N/A	721 (EAS) 724 (V)	Paleozoic	443-541	Concrete insulated vault
A54	-9	10	-11	12	L20SS	150	850 over 1357	1232	821 (EAS) 827 (V)	Precambrian	1600-2500	Concrete insulated vault
A61	0.03	7	-6	11	L20SS	150	2424	1915	809 (EAS) 811 (V)	Precambrian	1600-2500	Concrete insulated vault
A64	-1	11	-10	12	L20SS	150	1020 over 2553	1352	785 (EAS) 783 (V)	Precambrian	1600-2500	Concrete insulated vault
BATG	-6	10	-28	11	L20SS	150	1441	1480	171 (EAS)	Paleozoic	460-471	Rock outcrop

145

									173 (V)			
BCLQ	-9	8	-10	8	L20SS	150	1612	1530	300 (EAS) 297 (V)	Precambrian	1000-1600	Rock outcrop
CNQ	N/A	N/A	-5	6	L20SS	150	N/A	N/A	583 (V)	Precambrian	1600-2500	Reinforced concrete on bedrock
DAQ	N/A	N/A	-3	7	L20CS	150	N/A	N/A	583 (V)	Precambrian	1600-2500	Reinforced concrete on bedrock
DPQ	-13	9	-9	9	L20SS	150	1574	1711	62 (EAS) 230 (V)	Precambrian	1000-1600	Reinforced concrete on bedrock
GAC	-18	15	5	14	L20SS	150	1080 over 2780	2405	148 (EAS) 947 (V)	Precambrian	541-4000	Underground Vault
GBN	-0.6*	5*	-0.1*	12*	L20SS	150	1237 over 1976	1364	8 (EAS) 8 (V)	Paleozoic	140-353	Rock outcrop

GSQ	N/A	N/A	-13	10	L20SS	150	N/A	N/A	552 (V)	Paleozoic	443-541	Reinforced concrete on bedrock
ICQ	-6	9	-6	8	L20SS	150	1959	1954	43 (EAS) 218(V)	Precambrian	1000-1600	Rock outcrop
KGNO	-23*	19*	-27*	17*	L20CS	150	1553	1860	15 (EAS) 10 (V)	Paleozoic	443-485	Building Basement
LMQ	-7	8	-2	8	L20SS	150	889 over 2717	887	257 (EAS) 257 (V)	Precambrian	1000-1600	Underground Vault
MCNB	-29	16	-20	14	L20SS	150	2409	1991	52 (EAS) 55 (V)	Paleozoic	416-422	Underground Vault
MOQ	N/A	N/A	-7	11	L20SS	150	N/A	N/A	232 (V)	Paleozoic	443-541	Reinforced concrete on bedrock
NATG	-14	12	-9	14	L20SS	75	N/A	N/A	25 (EAS) 25 (V)	Precambrian	541-1000	Rock outcrop
ORIO	-25	6	-13	6	L20CS	75	1708	1570	29 (EAS) 29 (V)	Paleozoic	443-485	Rock outcrop

OTT	2	9	-4	10	L20CS	150	1612	1539	432 (EAS) 527 (V)	Paleozoic	443-485	Underground Vault
QCQ	-10	16	-9	15	L20SS	150	1503	1523	9 (EAS) 165 (V)	Paleozoic	1000-1600	Building Basement
SMQ	N/A	N/A	-8	7	L20SS	150	N/A	N/A	638 (V)	Precambrian	1600-2500	Reinforced concrete on bedrock
VABQ	-8	8	-16*	9*	L20CS	150	N/A	N/A	278 (EAS) 278 (V)	Precambrian	541-4000	Rock outcrop

1. Geological Survey of Canada (2014)

2. Energie et Ressources Naturelles Quebec (2012) (Ma, Millions years ago)

3. Keppie, J.D. (2000)

4. Ontario Geological Survey (2011)

5. Department of Natural Resources Minerals, Policy and Planning Division. (2008)
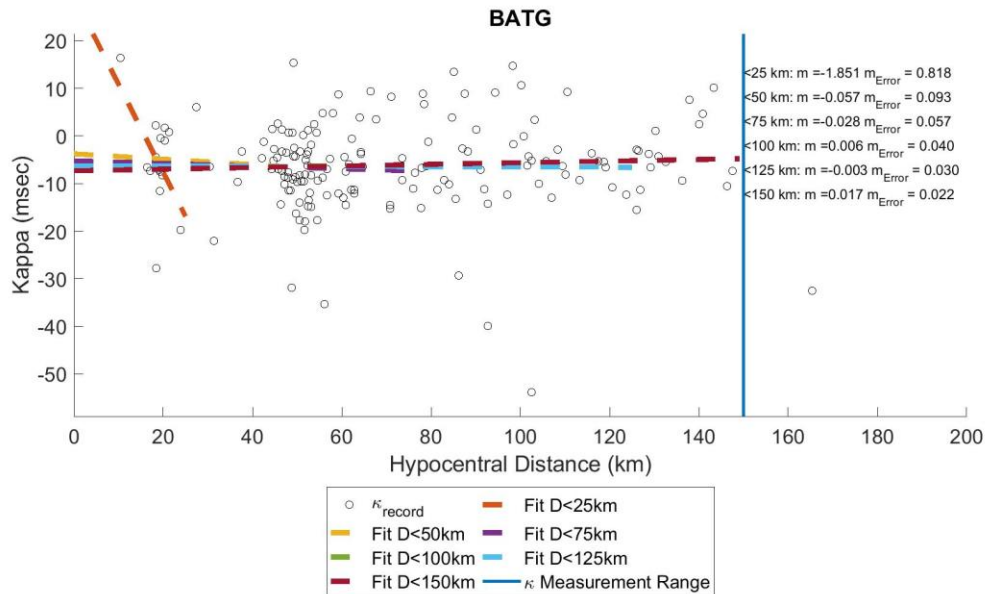
Figure 4.12: BATG horizontal (EAS) component record kappa versus distance with linear fits to cut off distances 25, 50, 75, 100, 125, and 150 km.

Figures 4.13 (EAS) and 4.14 (vertical) show the sensitivity of mean kappa values to the cut-off distance. At many stations, like those in Charlevoix, which have more than 50 records regardless of cut-off distance, the mean kappa are reasonably stable suggesting minimal path attenuation effects. Station KGNO's increase in kappa as the cut off distance increases is believed to be the result of a lack of data and may not be significant. For most stations, it appears that using data to 150 km in the calculation of mean kappa results in a stable and unbiased estimate.
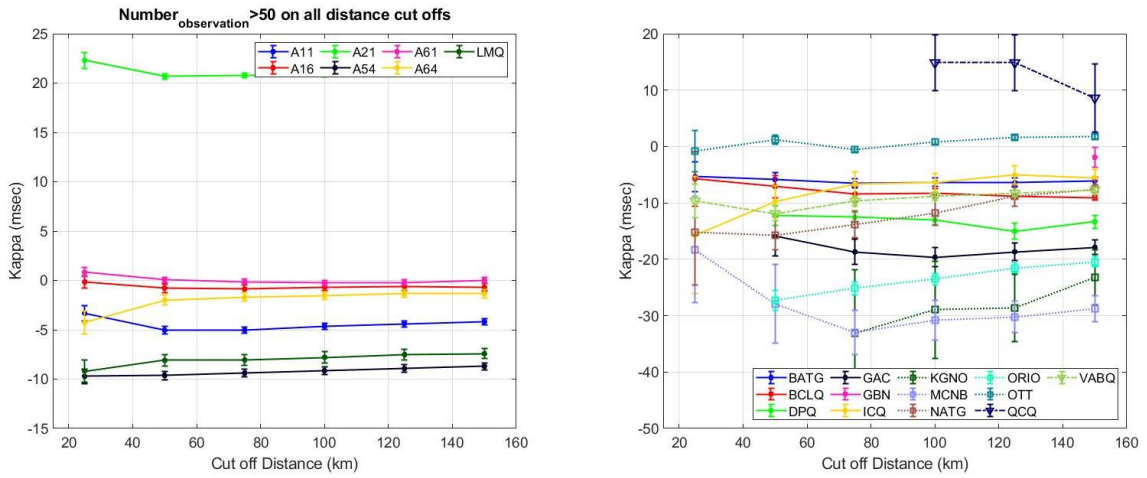
Figure 4.13: Horizontal (EAS) mean kappa and the standard error at specific cut off distances for stations with more than 50 individually measured kappa (left panel) and the remainder stations (right panel).
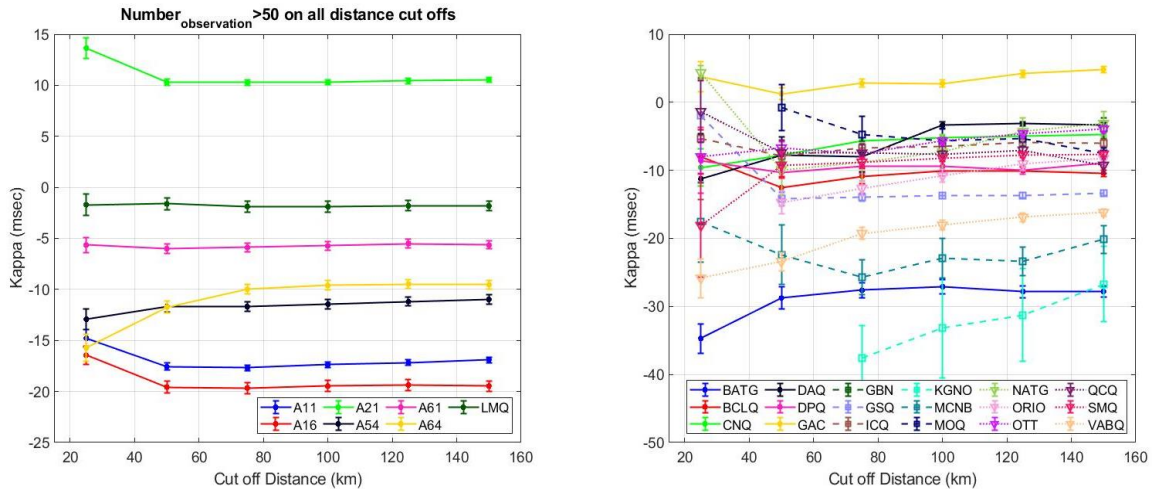
Figure 4.14: Vertical mean kappa and the standard error at specific cut off distances for stations with more than 50 individually measured kappa (left panel) and the remainder stations (right panel).

As we show on Figure 4.10, there are significant differences in kappa values between the horizontal and vertical components. Kappa on the horizontal component is greater than that on the vertical, by 2 to 23ms, reflecting the greater impact of near-surface attenuation

on horizontal components and due to the negative nature of the values show the amplification on the vertical has not been captured.

4.4.5 Relationship of Kappa Values to Site Characteristics

In engineering seismology practice, kappa values are sometimes estimated from proxies that express the stiffness of a site, such as V_{S30}. Figure 4.15 compares the site-specific kappa values obtained in this study, listed in Table 4.2, to the several site characteristics: V_{Srock}, V_{S30}, V_P, Site Class, rock type, rock age, and instrument housing types to observe correlations. Each kappa value has an error based on the variability of all records for a given station after geometric, anelastic attenuation, and site-specific corrections, which are shown as vertical bars on Figure 4.15. Some of the site characteristics also have error, which are shown in Figure 4.15 as horizontal error bars. In addition, for site characteristics with multiple kappa which includes Rock type, Site Class, and Instrument Housing we provide an average kappa and the standard deviation for that characteristic to examine average kappa trends with these characteristics.
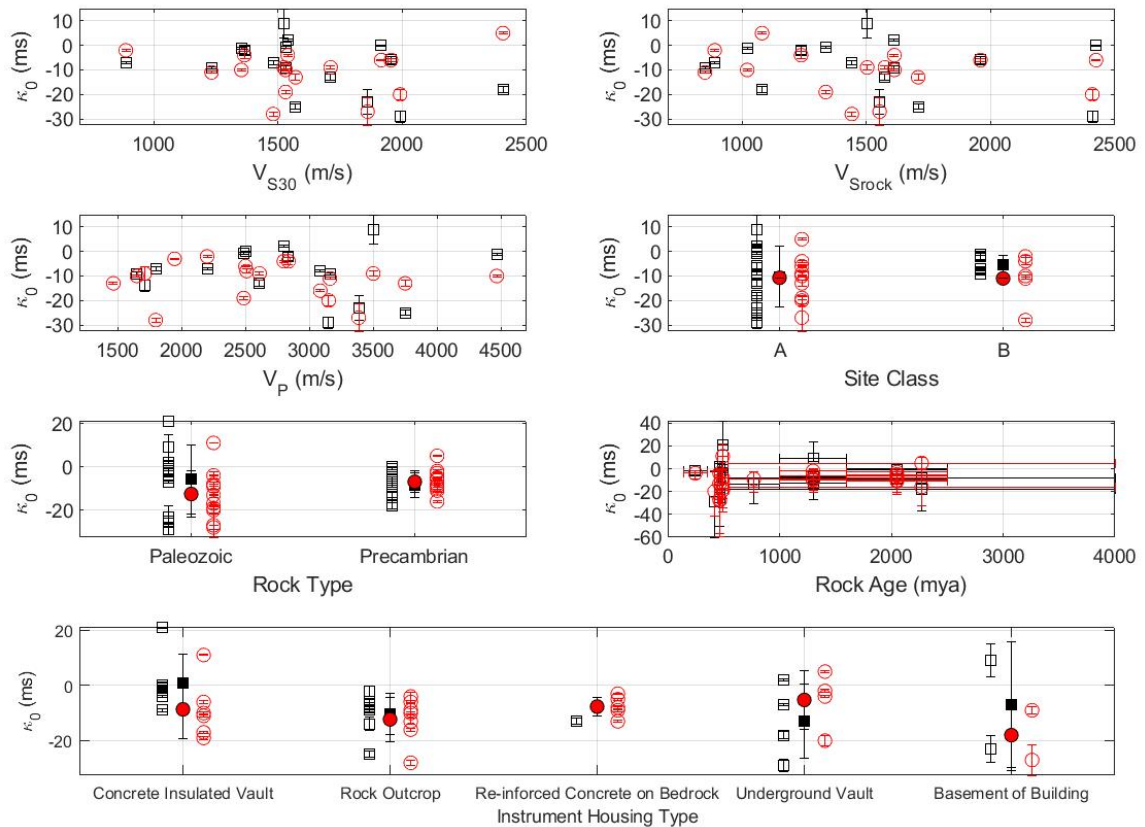
Figure 4.15: Comparison of seismic station properties (V_{S30}, V_{Srock}, V_P, Site Class, Rock Type, Rock Age, Instrument Housing) and site-specific kappa for the vertical (red circles) and horizontal (black squares) where error bars show standard error of kappa. Mean kappa values for vertical (red filled circle) and horizontal (black filled squares) are shown for each site class, rock type, and instrument housing where error bars show the standard deviation. The age range for rock types is shown as horizontal bars.

Kappa is not significantly correlated with bedrock velocity, V_{S30} or P-wave velocity. When general characteristics such as the National Building Code of Canada's site classification and general rock type are examined, there is no distinction between kappa for Class A and B sites. Rock age at a given site has a broad range and as a result meaningful relation between kappa and rock age are difficult to discern. Lastly, we

compared the kappa to the type of seismic instrument housing and observe that the instrument housing does not appear to influence kappa in a systematic way.

4.4.6   Broadband Inversion compared to Acceleration Spectral Kappa

Palmer and Atkinson [2020] computed the vertical and horizontal (geometric mean) site-specific kappa for $\mathbf{M} \geq 3.5$ earthquakes in eastern Canada for 9 stations. Using the smoothed geometric spreading, regional attenuation, and site-specific amplification profile corrected FAS kappa was determined with the broadband method and using the Anderson and Hough method for all records at any station with a $\mathbf{M} \geq 3.5$ earthquakes in eastern Canada. The Anderson and Hough (1984) method utilized here measured kappa using the corrected smoothed vertical and horizontal (EAS) FAS across a frequency band of 1.5 times the estimated half maximum corner frequency to the maximum useable frequency. Figure 4.16 shows kappa and estimated corner frequencies determined for each record using the simple Anderson and Hough (AH) and the broadband (BB) method. We also compare (Figure 4.16) site-specific kappa, computed using the mean of individual records per station, from Palmer and Atkinson [2020] (PA20), the Anderson and Hough method (AH), and the broadband method (BB) for $\mathbf{M} \geq 3.5$ and $\mathbf{M} \geq 1.5$.
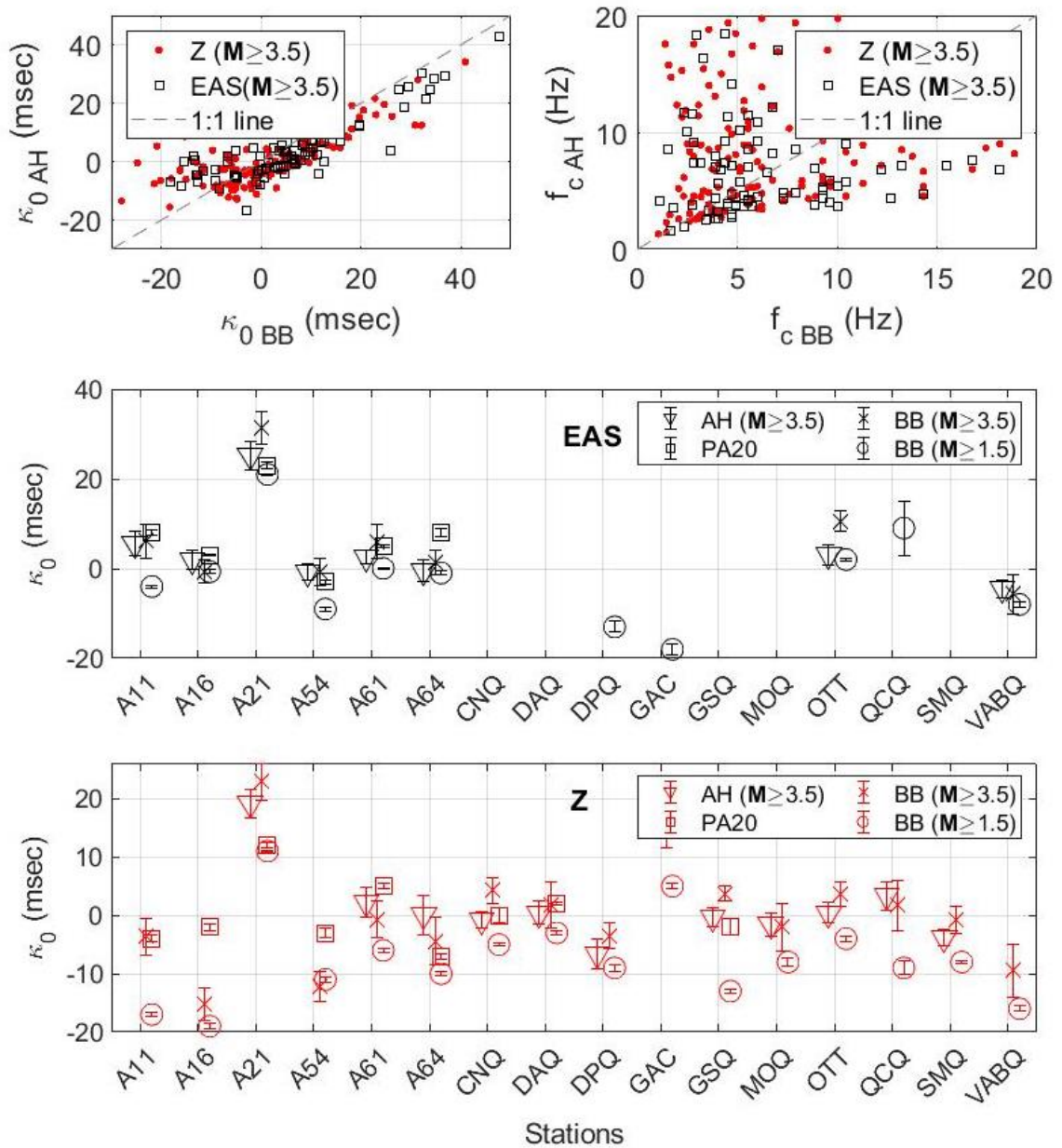
Figure 4.16: Site-specific Kappa comparison for the Acceleration Spectral Method (PA20) (from Palmer and Atkinson (2020)), the Broadband Inversion Method (BB) and the Anderson and Hough Method (AH). Individual record kappa and corner frequency are compared in the upper panels for the vertical (red) and horizontal (black) components with a 1:1 line (dashed grey) for M≥3.5 earthquakes. The station-determined kappa are compared in the lower two panels for the Anderson

and Hough Method M≥3.5 (triangle), Broadband Inversion Method M≥3.5 (crosses), Acceleration Spectral Method from Palmer and Atkinson (square), and the Broadband Inversion Method M≥1.5 (circle) for the vertical (bottom panel) (red) and horizontal (middle panel) (black) components with standard error bars. Note the horizontal components computed in Palmer and Atkinson (2020) were Geometrical Mean spectra (GM) while those computed in this paper are the Effective Amplitude Spectra (EAS).

The upper two panels show individual record, **M**≥3.5 earthquakes, Anderson and Hough kappa measurements and corner frequency estimates compared to the broadband values using the same corrected FAS. If both measurement methods resulted in the same kappa and corner frequencies, Figure 4.16's upper panels would align on the 1:1 ratio line. In the case of the individual record kappa, although there is random variability about the 1:1 line the trend follows the 1:1 line with a shift favouring somewhat larger kappa values measured by the broadband method, in comparison to that of Anderson and Hough. The corner frequencies measured in the two methods appear to have significant scatter beyond 5Hz, diverging from the 1:1 line symmetrically. This divergence is likely the result non-uniqueness in the broadband inversion, combined with poor corner frequency estimation from the Anderson and Hough method, where we used a simple approach of estimating the corner frequency by finding the frequency at which the spectral amplitude is half that of the maximum. In the lower panel of Figure 4.16, we compare site-specific kappa values for **M**≥3.5 from the Anderson and Hough method, broadband method, and the Palmer and Atkinson [2020] results. The results are generally consistent with each other across methodologies for **M**≥3.5 earthquakes. The horizontal site-specific kappa values are consistently larger than the vertical, as previously noted. When examining broadband site-specific kappa values for **M**<3.5 earthquakes the site-specific kappa are consistently less than those for **M**≥3.5 earthquakes, for both the horizontal and the vertical, when compared using either the acceleration spectral or broadband method results.

To examine the potential impact of kappa and corner frequency trade-off we compute the Brune stress drop parameter using Equations 4.4 and 4.5 and compare it and the corner frequency to seismic moment for each record (Figure 4.17). Anderson [1986] shows that in the presence of attenuation, as magnitude decreases towards **M**<3, the corner frequency begins to overlap with the high frequency measurement range for kappa. As a result of this trade-off the inferred stress drop will decrease at small magnitudes. Figure 4.17 shows that as seismic moment decreases the stress drop also decreases, which could suggest that the corner frequency is being impacted by the attenuation (i.e., kappa). Atkinson (1993) also observed this high frequency spectral decay dependence, for earthquakes with **M**<3.5 which have corner frequencies that approach 10 Hz. Figure 4.17 shows that the corner frequencies estimated from the broadband inversion can reach up to 40Hz, which is the upper limit of useable data; therefore the Brune stress parameter will be systematically underestimated as magnitude decreases. Considering this trade-off the high frequency attenuation parameter kappa may be poorly estimated for lower magnitude events.
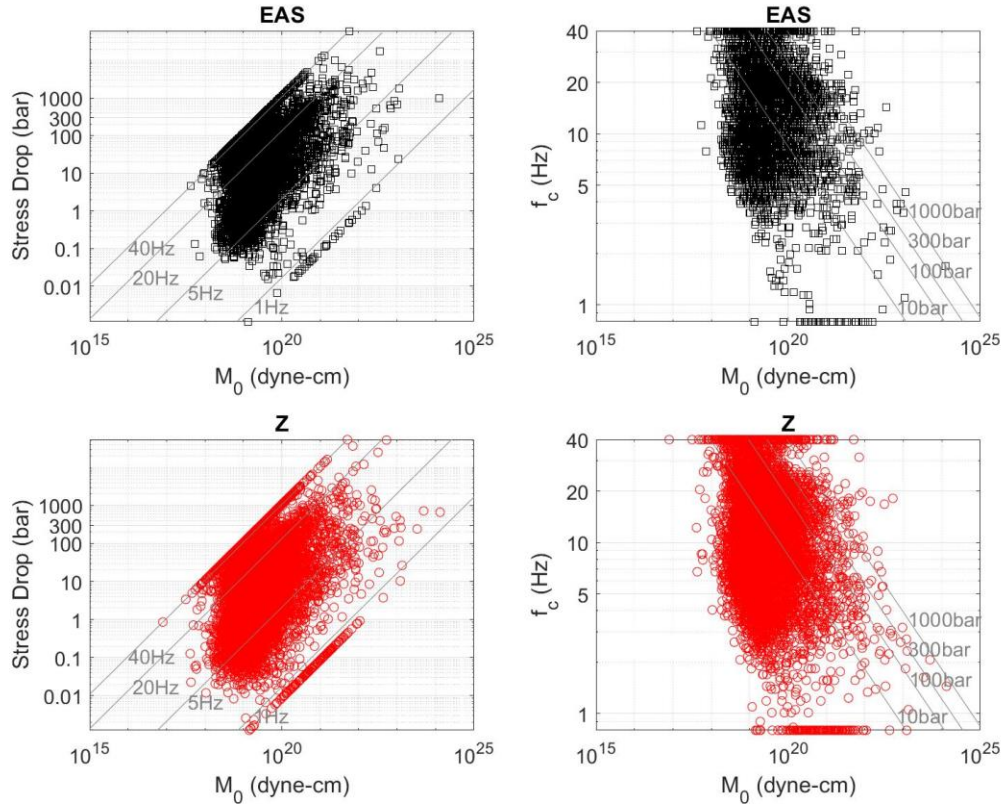
Figure 4.17: Record seismic moment, corner frequency, and computed stress drop for the horizontal (upper panels) and the vertical (lower panels) FAS. Grey lines are shown on each plot which correspond to either the theoretical corner frequency (1Hz, 5Hz, 20Hz, or 40Hz) or stress drop (10bar, 100bar, 300bar, or 1000 bar).

Figure 4.18 examines the impact on broadband site-specific kappa by decreasing the minimum earthquake moment magnitude considered. Recall that Figures 4.13 and 4.14 showed that, regardless of number of records or cut-off distance, 23 of 25 stations had robust site-specific kappa. With this in mind, the decrease of site-specific kappa when the **M** is reduced from 3.5 to 1.5 is most likely attributable to the trade-off between kappa and corner frequency and the consequent non-uniqueness of the broadband method. Reducing the minimum magnitude from 3.5 to 1.5, the kappa reduces, on average, by 6ms on the horizontal and 8ms on the vertical. The broadband site-specific kappa

(**M**≥1.5) are lower than those from the Palmer and Atkinson [2020] acceleration spectral method by an average of 2ms for the horizontal component or 4ms for the vertical component, which is well within the error introduced by a velocity profile amplification model.
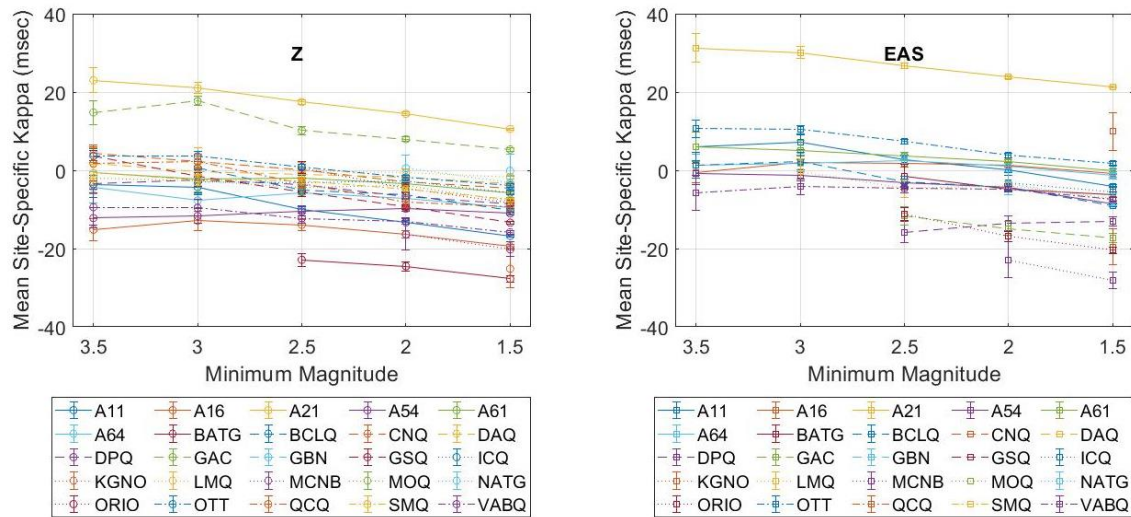
Figure 4.18: Mean Site-Specific Kappa with varying minimum moment magnitude values from M≥3.5 to M≥1.5 for 25 stations in eastern Canada on the vertical (Z) (left panel) and horizontal (EAS) (right panel) components. Symbols and line type are shown in the legend for each station.

4.5   Conclusions

Site-specific kappa values were computed at 25 seismograph stations in eastern Canada using the broadband inversion method of Anderson and Humphrey [1991], based on the horizontal (EAS) and vertical Fourier Amplitude spectra adjusted using Atkinson's [2004] geometrical spreading and regional attenuation model, and amplification from the site-specific velocity profile. The sites have shear wave velocities ranging from ~850m/s to 2400m/s [Ladak et al., 2021; Ladak 2020; Stokoe et al., 2021]. It is noteworthy that this range of velocities is lower than the range of 2000 – 3000 m/s that has generally been assumed in ground-motion modeling for eastern Canada. This means that near-surface

crustal amplifications are a significant factor in the interpretation of recorded ground motions. Average kappa values at rock sites are near zero and range from -29ms ± 16ms to +21ms ± 6ms on the horizontal component and -28ms ± 11ms to +11ms ± 7ms on the vertical component.

For rock sites of NEHRP Class A and B, kappa does not deviate significantly from zero on average, within our ability to measure it, after accounting for the effects of the velocity profile and regional anelastic attenuation. From a ground-motion modeling point of view, for generic hard rock sites there is no empirical basis for imposing additional high-frequency damping beyond that already included via the anelastic attenuation coefficient. The net effect of the near-surface rock profile could result in either amplification or de-amplification of high-frequency motions. An estimate of the amplification or de-amplification was removed on a site-by-site basis using velocity profiles determined from fieldwork, literature-based profiles and earthquake recording measurements. The negative kappa values could be the result of not capturing this amplification or de-amplification in its' entirety and/or could be the result of the limitation of the broadband spectral method and use of small, low magnitude, earthquakes where there exists a corner frequency-kappa trade-off.

Kappa values obtained from the broadband method, for earthquakes $M \geq 1.5$, tend to be lower than those obtained from the acceleration spectral method which uses $M \geq 3.5$ earthquakes. When the same dataset ($M \geq 3.5$ earthquakes) is utilized the broadband method kappa tend to be slightly larger than those determined by the acceleration spectral method. This could be due to the simplistic approach taken to define corner frequency in the acceleration spectral method and the trade-off between kappa and corner frequency in the broadband method. This is emphasized as the corner frequencies differ between the two methods. The broadband method, while being applicable to a broader range of event magnitudes, may be less precise in its ability to measure kappa because it needs to jointly determine seismic moment and corner frequency, and fit all parameters to a pre-defined spectral shape.

Rock amplifications and kappa effects are highly variable from one rock site to another and are not significantly correlated with $V_{S30,}$ V_{Srock}, V_P, Rock type, Rock age, Site Class, or Instrument Housing. Therefore, site-specific determination of kappa requires site-specific observations. In the absence of site-specific observations, it should be assumed, for the purpose of ground-motion modeling, that rock sites of Class A or B have only nominal high-frequency damping (i.e., kappa = 0 to 2ms), beyond that attributable to regional anelastic attenuation.

4.6   Data and Resources

Supplemental material can be found in the appendix. Appendix A provides velocity profiles, amplification function, and horizontal-to-vertical spectral ratios for each station. Using various velocity profiles, we also provide station-specific kappa values in the appendix material. The earthquake database used in this study was obtained using Natural Resources Canada's Earthquakes Canada - Geological Survey of Canada (GSC) on-line bulletin earthquake search at http://www.earthquakescanada.nrcan.gc.ca/stndon/NEDB-BNDS/bulletin-en.php (last accessed September 2020) to identify records candidate events and stations. The seismograms were obtained from Earthquakes Canada – GSC email data service at AutoDRM@seismo.NRCan.gc.ca (last accessed September 2020). Waveforms were initially processed with rdSEED from https://ds.iris.edu/ds/nodes/dmc/software/downloads/rdseed/. Data analysis was completed in part using the Seismic Analysis Code (SAC) which is a seismological processing software available at https://ds.iris.edu/ds/nodes/dmc/software/downloads/sac/ [Goldstein et al. 2003; Goldstein and Snoke, 2005]. Signals are 360 seconds long, starting 70 seconds prior to the earthquake time. rdSEED is used to convert files into SAC files. Standard SAC procedures are used to remove the mean, detrend, taper, remove instrument response from the full time series in the Fourier domain, select the S and P-wave arrivals, cut the time series dependent on the windowing technique implemented for defining the S-wave, cut the time series prior to the P-wave arrival the length of the S-wave window to obtain the noise window, apply the FFT (fast Fourier transform) to the cut time series, and finally differentiate using the mulomega function to obtain the

Fourier amplitude spectrum of acceleration. We use the Boore [2003] site_amp function to determine the site amplification given a velocity profile (assuming the standard Poisson ratio).

4.7 References

Anderson, J. (1986) Implication of Attenuation for Studies of Earthquake Source, Earthquake Source Mechanics (ed. S. Das., J. Boatwright, C.H. Scholz). Vol. 37, pp. 311-318. doi: 10.1029/GM037

Anderson, J. and S. Hough (1984) A model for the shape of the Fourier amplitude spectrum of acceleration at high frequencies, Bull. Seismol. Soc. Am. 74(5), 1969 – 1993. doi: 10.1785/BSSA0740051969

Anderson, J.G. and J.R. Humphrey (1991) A least squares method for objective determination of earthquake source parameters, Seism. Res. Lett. 62(3-4), 201 – 209. doi: 10.1785/gssrl.62.3-4.201

Atkinson, G.M., and R.F. Mereu (1992) The shape of ground motion attenuation curves in southeastern Canada, Bull. Seismol. Soc. Am. 82(5), 2014 – 2031. doi: 10.1785/BSSA0820052014

Atkinson, G.M. (1993) Earthquake source spectra in eastern North America, Bull. Seismol. Soc. Am. 83(6), 1778-1789. doi: 10.1785/BSSA0830061778

Atkinson, G.M. (1996) The high-frequency shape of the source spectrum for earthquakes in eastern and western Canada, Bull. Seismol. Soc. Am. 86(1A), 106 – 112. doi: 10.1785/BSSA08601A0106

Atkinson, G.M. (2004) Empirical attenuation of ground-motion spectra amplitudes in southeastern Canada and northeastern United States, Bull. Seismol. Soc. Am. 94(3), 1079 – 1095. doi: 10.1785/0120030175

Bent, A. and H. Kao (2015) Crustal Structure of Eastern and Central Canada from a Neighborhood Algorithm Inversion. Geological Survey of Canada Open File No. 7833. doi:10.4095/296797.

Bent, A., H. Kao, and F. Darbyshire (2019) Structure and anisotropy of the crust and upper mantle along the St. Lawrence Corridor, eastern Canada, from the Charlevoix Seismic Zone to the Gulf of St. Lawrence, Seism. Res. Lett. 90(2B), 950. doi: 10.1785/0220190061

Boore, D.M. (2003) Simulation of ground motion using the stochastic method, Pure Appl. Geophys. 160, 635 - 676. doi: 10.1007/PL00012553

Boore, D.M. and K.W. Campbell (2017). Adjusting Central and Eastern North America ground-motion intensity measures between sites with different reference-rock site conditions, Bull. Seism. Soc. Am. 107(1), 132-148. doi: 10.1785/0120160208

Borcherdt, R. D. (1970) Effects of local geology on ground motion near San Francisco Bay. Bull. Seismol. Soc. Am. 60(1), 29-61. doi: 10.1785/BSSA0600010029

Brune, J.N. and J. Dorman (1963) Seismic waves and earth structure in the Canadian Shield, Bull. Seismol. Soc. Am. 53(1), 167-210. doi: 10.1785/BSSA0530010167

Brune, J.N. (1970) Tectonic stress and the spectra of seismic shear waves from earthquakes, J. Geophys. Res. 75, 4997 – 5009. doi: 10.1029/JB075i026p04997

Brune, J.N. (1971) Correction, J. Geophys. Res. 76, 5002. doi: 10.1029/JB076i020p05002

Campbell, K.W. (2009) Estimates of Shear-Wave Q and $\kappa 0$ for unconsolidated and semiconsolidated sediments in eastern North America, Bull. Seismol. Soc. Am. 99 (4), 2365 – 2392. doi: 10.1785/0120080116

Campbell, K.W, Y.M.A. Hashash, B. Kim, A.R. Kottke, E.M. Rathje, W.J. Silva, and J.P. Stewart. (2014) Reference-rock site conditions for Central and Eastern North America: Part II – Attenuation (kappa) definition. PEER Report No. 2014/12.

Cassidy, J.F. (1995) A comparison of the receiver structure beneath stations of the Canadian National Seismograph Network, Can. J. Earth Sci. 32(7): 938–951. doi: 10.1139/e95-079

Department of Natural Resources Minerals, Policy and Planning Division (2008) Map NR-1 Bedrock Geology of New Brunswick. Available at: https://www2.gnb.ca/content/gnb/en/departments/erd/energy/content/minerals/content/bedrock_mapping.html (accessed 2021 November)

Douglas, J., P. Gehl, L.F. Bonilla, and C. Gelis (2011) A kappa model for mainland France, Pure Appl. Geophys. 167 (11), 1303-1315. doi: 10.1007/s00024-010-0146-5

Drouet, S., F. Cotton, and P. Gueguen (2010) V_{S30}, κ, regional attenuation and M_W from accelerograms: application to magnitude 3 – 5 French earthquakes, Geophys. J. Int. 182, 880 – 898. doi: 10.1111/j.1365-246X.2010.04626.x

Edwards, B., C. Michel, V. Poggi, and D. Fah (2013) Determination of Site Amplification from Regional Seismicity: Application to the Swiss National Seismic Networks, Seismol. Res. Lett. 84(4), 611 – 621. doi: 10.1785/0220120176

Energie et Ressources Naturelle Quebec (2012) Geology of Quebec DV2012-07 1:2,000,000 map. Available at: https://mern.gouv.qc.ca/english/mines/publications/publications-maps.jsp (accessed 2021 November).

Fereidoni, A., G. M. Atkinson, M. Macias, and K. Goda (2012) CCSC: A composite seismicity catalog for earthquake hazard assessment in major Canadian cities, Seismol. Res. Lett. 83(1), 179 – 189. doi: 10.1785/gssrl.83.1.179

Field, E. and K. Jacob (1993) The theoretical response of sedimentary layers to ambient seismic noise, Geophys. Res. Lett. 20(24), 2925-2928. doi: 10.1029/93GL03054

Geological Survey of Canada (2014) Canadian Geoscience Map 195 Surficial Geology of Canada. Catalogue No. M183-1/195-2014E-PDF. doi: 10.4095/295462

Goldstein, P., D. Dodge, M. Firpo, and L. Minner (2003) SAC2000: Signal processing and analysis tools for seismologists and engineers, The IASPEI International Handbook of Earthquake and Engineering Seismology, Academic Press, London.

Goldstein, P. and A. Snoke (2005) SAC Availability for the IRIS Community, Incorporated Institutions for Seismology Data Management Center Electronic Newsletter.

Goulet, C.A., T. Kishida, T.D. Ancheta, C.H. Cramer, R.B. Darragh, W.J. Silva, Y.M.A Hashash, J. Harmon, J.P. Stewart, K.E. Wooddell, and R.R. Youngs (2014) PEER NGA-East database. PEER No. Report 2014/17.

Goulet, C.A., T. Kishida, T.D. Ancheta, C.H. Cramer, R.B. Darragh, W.J. Silva, Y.M.A Hashash, J. Harmon, G.A. Parker, J.P. Stewart, and R.R. Youngs (2021) PEER NGA-East database, Earthquake Spectra 37, 1331-1353. doi: 10.1177/87552930211015695

Kao, H., S.J. Shan, J.F. Cassidy, and S.A Dehler (2014) Crustal structure in the Gulf of the St. Lawrence Region, Eastern Canada: Preliminary results from receiver function analysis. Geological Survey of Canada Open File 7456. doi:10.4095/293724.

Keppie, J.D. (2000) Geological map of the province of Nova Scotia: Nova Scotia
     Department of Natural Resources, Minerals and Energy Branch, Map ME 2000-1,
     scale 1:500 000. Available at:
     https://novascotia.ca/natr/meb/download/mg/map/htm/map_2000-001.asp
     (accessed 2021 November).

Konno, K. and T., Ohmachi (1998) Ground motion characteristics estimated from
     spectral ratio between horizontal and vertical components of microtremor, Bull.
     Seism. Soc. Am. 88(1), 228 – 241. doi: 10.1785/BSSA0880010228

Kottke, A., N.A. Abrahamson, D.M. Boore, Y. Bozorgnia, C. Goulet, J. Hollenback, T.
     Kishida, A.D. Kiureghian, O.J. Ktenidou, N. Kuehn, E.M. Rathje, W.J. Silva, E.
     Thompson, and X. Wang. (2018) Selection of random vibration procedures for the
     NGA-East project. PEER Report No. 2018/05.

Kottke, A., N.A. Abrahamson, D.M. Boore, Y. Bozorgnia, C. Goulet, J. Hollenback, T.
     Kishida, O.J. Ktenidou, E.M. Rathje, W.J. Silva, E. Thompson, and X. Wang
     (2021) Selection of random vibration theory procedures for the NGA-East project
     and ground-motion modeling, Earthquake Spectra 37, 1420-1439. doi:
     10.1177/87552930211019052

Ktenidou, O., F. Cotton, N.A. Abrahamson, and J. G. Anderson (2014) Taxonomy of κ:
     A Review of Definitions and Estimation Approached Targeted to Applications,
     Seismol. Res. Lett. 85, 135 – 146. doi: 10.1785/0220130027

Ktenidou, O.J., N.A. Abrahamson, R.B. Darragh, and W.J. Silva (2016) A Methodology
     for the Estimation of Kappa (κ) from Large Datasets: Example Application to
     Rock Sites in the NGA-East Database and Implications on Design Motions. PEER
     Report No. 2016/01.

Kuponiyi, A.P., H. Kao, C.R. van Staal, S.E. Dosso, J.F. Cassidy, and G.D. Spence
     (2016) Upper crustal investigation of the Gulf of Saint Lawrence region, eastern

Canada using ambient noise tomography, Jour. Geo. Res. Solid Earth 122, 5208–5227. doi: 10.1002/2016JB013865

Ladak, S. (2020) Earthquake site characterization of rock site in eastern Canada and stiff ground sites in Vancouver, British Columbia. MSc Thesis, University of Western Ontario, https://ir.lib.uwo.ca/etd/6972

Ladak, S., S. Molnar, and S.M. Palmer (2021) Multimethod site characterization to verify the hard rock (site class A) assumption at 25 seismograph stations across eastern Canada, Earthquake Spectra 37, 1487–1515. doi: 10.1177/87552930211001076

Lermo, J. and F.J. Chavez Garcia (1993) Site effect evaluation using spectral ratios with only one station, Bull. Seismol. Soc. Am. 83(5), 1574 – 1594. doi: 10.1785/BSSA0830051574

Mereu, R. F., S. Diveva, and G.M. Atkinson (2013) The application of velocity spectral stacking to extract information on source and path effects for small-to-moderate earthquakes in southern Ontario with evidence for constant-width faulting, Seismol. Res. Lett. 84, 899 – 916. doi: 10.1785/0220130009

Nakamura, Y. (1989) A method for dynamic characteristics estimation of subsurface using microtremor on the ground surface. Quarterly Report of Railway Technical Research 30, 25-33.

Ontario Geological Survey (2011) Bedrock Geology map for the Province of Ontario scale 1:250000 MRD126. Available at: https://www.geologyontario.mndm.gov.on.ca/ogsearth.html#bedrock-geology (accessed 2021 November).

Palmer, S.M. and G.M. Atkinson (2020) The high-frequency decay slope of spectra (kappa) for $\mathbf{M} \geq 3.5$ earthquakes on rock sites in eastern and western Canada, Bull. Seismol. Soc. Am. 110(2), 471–488. doi: 10.1785/0120190206

Stokoe, K.H., G. Kim, and S. Hwang (2021) Shear wave velocity profiling using the SAWS method with "Raptor" as the active seismic source in Quebec, Canada: Data Summary. Report GIRS-2021-10. doi: 10.34948/G44W29.

Yenier, E. and G.M. Atkinson (2015) An equivalent point-source model for stochastic simulation of earthquake ground motions in California, Bull. Seismol. Soc. Am. 105(3), 1435 – 1455. doi: 10.1785/0120140254

Chapter 5

5   Summary, Conclusions, and Future Work

In this thesis a ground motion database consisting of processed time series, Fourier amplitude spectra (FAS) of acceleration, 5% damped pseudo-spectral acceleration (response spectra, PSA), and seismic station metadata is presented. Using this database, ground motion modelling parameters are empirically determined with a particular focus on the high frequency spectral shape parameter, kappa. Two approaches are used to measure kappa: the Anderson and Hough [1984] and Anderson and Humphrey [1991] methods. The assumptions and impacts on resultant kappa are explored.

Chapter 1 presented an introduction to eastern Canada earthquakes and seismic stations which measure ground motion and reviewed the significance of ground motion studies to seismic hazard assessment for critical infrastructure.

In Chapter 2, a ground motion database for eastern Canada was developed. The database consists of processed time series for 3357 earthquakes with a moment magnitude ($\mathbf{M}$) $\geq$1.5. Using the time series and Goulet et al.'s [2013; 2021] methodology for windowing particular seismic waves and signals, Fourier amplitude spectra (FAS) are computed for the noise signal, P-wave, SLg-wave, Coda wave, and the full event signal of acceleration. Konno-Ohmachi [1998] (b=20) smoothed FAS are computed for each of the windowed FAS. The 5%-PSA, peak ground velocity (PGV), and peak ground acceleration (PGA) are computed using the full event signal for the horizontal component records. In addition, site metadata, including physical station descriptions, the horizontal-to-vertical spectral ratio of earthquakes and microtremors for a given station, geological descriptions, and velocity profiles from literature, are provided for each station. The database presents a semi-automated uniformly processed ground motion repository for earthquake ground motions measured for 3357 events of $\mathbf{M}$$\geq$1.5 at $\leq$150km, for 25

seismic stations sited on rock, with shear-wave velocity ranging from 850m/s to 2400m/s, in eastern Canada.

In Chapter 3, the most widely used method to determine kappa [Anderson and Hough, 1984] was executed for nine seismic stations in eastern Canada and eight seismic stations in western Canada. For **M**≥3.5 earthquakes, the high-frequency FAS of acceleration decays due to site-related kappa and the regional Quality factor (**Q**). After correcting for Q, site-specific values of kappa for rock sites in eastern and western Canada ranged from -24ms ± 2ms to 28ms ± 3ms across the seventeen stations on the vertical component. On the horizontal component, kappa ranges from -4ms ± 1ms to 20ms ± 0.8ms. As in Motazedian [2006], Ktendiou et al. [2013] and Douglas et al. [2011], the reported site-specific kappa is larger for the horizontal than the vertical component. Motazedian [2006] relates this difference to the vertical component being less sensitive to near-surface shear-wave velocity variations. Ktendiou et al. [2013] observe that at bedrock depth, there is a 1:1 ratio of horizontal-to-vertical kappa, while at the surface, there is a 1.4:1 ratio. Seismic stations in eastern Canada are predominately located on rock. Steidel et al. [1996] suggest differences between the horizontal and vertical kappa could be related to highly fractured or eroded rock in the near-surface causing amplifications.

A limitation of the study presented in Chapter 3 is that the Anderson and Hough method [1984], as applied, does not correct for site amplification. The diminution of high-frequency FAS is coupled with any amplification present. Horizontal-to-vertical spectral ratios were examined to inform which station's site-specific kappa were potentially affected by site amplifications. In addition to measuring kappa using the classical approach with a frequency-independent Q, an approach was developed which removed a frequency-dependent Q, stacked the spectra by corner frequency and amplitude, then determined the site-specific kappa directly from the slope of the stacked spectral decay; the stacked method produced similar kappa values compared to the classical method. This method produced kappa values that represent the coupled effects of amplification and diminution. On average, the site-specific kappa determined for rock stations in

eastern Canada was 7ms (horizontal) and 0ms (vertical) which is consistent with other studies [e.g., Ktendiou et al., 2016; Campbell et al., 2014]. In western Canada, a much higher site-specific kappa was determined: 19ms (horizontal) and 14ms (vertical).

Chapter 4 extended the magnitude range of earthquakes used to measure kappa, using a broadband inversion method combined with a ground motion modelling approach to examine all earthquakes of $M \geq 1.5$ at 25 seismic stations from the database outlined in Chapter 2. The method first adjusted the FAS to account for the effects of a regional Q-model and various crustal amplifications, before computing site-specific kappa using Anderson and Humphrey's [1991] broadband inversion procedure, which captures the source spectrum, geometrical spreading, and kappa effects.

An initial analysis of source spectra for eastern Canada was also carried out by stacking the adjusted spectra in magnitude bins. A Brune spectrum with a kappa of 2ms and stress drop values of 20, 70, 100, and 210 bars, are a good representation of the binned: $M1.5$, $M2.5$, $M3.5$, and $M4.5$, source spectra, respectively.

Chapter 4 also examined the effect of the underlying velocity profile on crustal amplification and the inferred kappa. Perturbing the assumed velocity profile by a reasonable amount resulted in a 1-6ms change in the computed site-specific kappa values. Different velocity profiles, obtained from literature, were created for each station; such profiles varied site-specific kappa values on average by 1ms, with the range being 0 to 6ms. Sensitivity of kappa to the assumed source parameters and anelastic attenuation model (inverse Q) was also examined. This suggested that the assumed source parameters have minimal effect on resultant kappa, while the regional Q-model was not ideal for all seismic stations.

Our study supports the findings of Ktenidou et al. [2016], that the distance range where kappa is dominated by only site, after correction for regional path attenuation, is 75-150 km. Thus, observations at <150 km can be used to determine site-specific kappa, using the broadband method applied. The resultant site-specific kappa values determined were,

on average, -7ms (horizontal) and -10ms (vertical) with ranges of -29ms ± 16ms to 21ms ± 6ms and -28ms ± 11ms to 11ms ± 7ms on the respective components. In both Chapters 3 and 4, we showed that site-specific kappa values do not correlate well with known seismic station site characteristics such as shear-wave velocity.

The most significant conclusions of this thesis are:

- A ground motion database for 3357 earthquakes of **M**≥1.5 within 150 km of 25 seismic stations in eastern Canada was generated for use in ground motion studies.

- Kappa values measured in eastern Canada are on average 7ms on the horizontal component and 0ms on the vertical component when using a modified classical approach of Anderson and Hough [1984], that does not explicitly consider the frequency-dependent effects of amplification on rock spectra.

- Using ground motion modelling theory in combination with the Anderson and Humphrey [1991] method, kappa was determined on average to be -7ms on the horizontal component and -10ms on the vertical component, with a wide site variability; in this method, the frequency-dependent amplification effects were removed.

- When we compute kappa with **M**≥3.5 earthquakes, the Anderson and Hough method produces similar site-specific kappa as the broadband inversion method when the same ground motion modelling assumptions are implemented.

- When kappa values determined by broadband inversion for lower magnitude earthquakes are included, it results in lower kappa values (i.e., less high-frequency attenuation), which is likely the result of trade-offs between kappa and stress drop (corner frequency).

- Eastern Canada kappa values are significantly lower than western Canada kappa values.

- In eastern Canada, kappa effects on rock sites do not appear to be significant within ~150 km, if path attenuation effects are first removed, with few exceptions.

- Horizontal component site-specific kappa values tend to be larger than the vertical component kappa.
- Kappa exhibits large scatter for an individual site.
- Unless site amplification is unity across the frequency band of interest, or has been accounted for, the kappa measured represents the combined effects of amplification and diminution in the near-surface of the site (as corroborated by Ktenidou et al. [2021]).
- The assumptions made in the process in determining kappa play a large role in the uncertainty or use of a determined kappa.
- Crustal amplification model assumptions introduce errors on the same order or larger than the standard error of the mean kappa for a given station.
- Site characterization parameters such as V_{S30}, V_{Srock}, V_P, site class, rock type, rock age, and instrument housing do not appear to correlate with kappa.
- Kappa is highly variable from station to station and as such should be determined from ground motion recorded at a specific site, if intended to be used in site-specific hazard assessment for critical sites.
- If kappa is determined empirically for use in a ground motion model, to avoid doubly accounting for source, path, or site components when computing kappa, assumptions made in the ground motion model should be accounted for with corrections prior to measuring kappa.
- On average, for both the horizontal and vertical component on rock sites in eastern Canada, kappa is not significantly different from zero, if the effects of average regional anelastic attenuation, as captured in most ground motion models, are removed from the observed spectra.

Kappa is highly variable on rock sites in eastern Canada. Ktenidou et al. [2015; 2021] show how kappa for rock sites with high values of V_{S30} tend to exhibit asymptotic kappa values while kappa values for softer rocks, and sites with sediment over rock, correlate reasonably well with V_{S30}. Understanding the correlation is important to providing site-specific assessments of reasonable kappa values when ground motions are unavailable,

especially in the case of critical infrastructure sited on rock. The examination of biases introduced when measuring kappa have been outlined in Table 2.3. These studies are important to understanding the physical meaning of kappa as well as the uncertainties introduced into kappa. Further understanding of how the empirically determined kappa can be utilized in ground motion models is an important bridge between earthquake seismology and engineering seismology. Further investigation is recommended in the following areas:

- Systematic evaluation of errors introduced by methodology in measuring kappa, such as attenuation models, source spectral shape models, and processing techniques such as wave windowing, selection of seismic waves, and measurement frequency band to better understand aleatory (random) and epistemic (model) errors introduced when using an empirically determined kappa value.

- Determine kappa in eastern Canada using other techniques such as the response spectral technique, displacement spectral analysis, transfer function analysis, and a broadband inversion which simultaneously determines source and site parameters using multiple earthquakes recorded on multiple stations. This would be limited to regions like Charlevoix and the mouth of the St. Lawrence where high station and earthquake density exists.

- Examine ground motion spectra for lower magnitude earthquakes, which can be potentially contaminated by poor signal to noise ratios, using Pikolous et al.'s [2020] stochastic modeling method to enable the use of the higher frequency poor signal to noise ratio records.

- Improve site characterization at the 25 seismic stations using horizontal geophones and a S-wave refraction survey and revisit 17 of the 25 stations as suggested by Ladak (2020) to improve velocity profiles.

- Determine kappa for other regions in Canada, such as Alberta or BC, where varying rock conditions exist to establish kappa-rock relationships, if they exist, outside of eastern Canada's rock environment.

This thesis presented a database of ground motions from 3357 earthquakes of **M**≥1.5 within 150 km of 25 seismic stations. The high frequency spectral decay parameter, kappa, was computed using 2 well-known methods and a corner frequency stacked method. Kappa was compared to site characterization properties of the 25 seismic stations which have bedrock shear-wave velocities ranging from 850m/s to 2400m/s covering soft and hard rock ranges and the kappa was found to be highly variable. This suggests that in rock environments, kappa should not be determined via proxy methods and instead should be determined via ground motion records at a given location. There is little evidence for kappa effects on rock sites in eastern Canada that are not already accounted for in ground motion modeling through the average regional anelastic attenuation parameter.

This work corroborates kappa results for eastern Canada from previous studies. The work enhances the study of high frequency ground motion characteristics by measuring kappa, demonstrating the impact different measurement techniques have, and how ground motion modelling assumptions in turn effect the high frequency parameter, kappa, in eastern Canada. Determination of site-specific kappa and its uncertainty helps to reduce epistemic and aleatory uncertainty in ground motion models and aids in moving towards a non-ergodic ground motion model, which can be used for critical infrastructure hazard assessment and design.

5.1   References

Anderson, J. and S. Hough (1984) A model for the shape of the Fourier amplitude spectrum of acceleration at high frequencies, Bull. Seismol. Soc. Am. 74(5), 1969 – 1993. doi: 10.1785/BSSA0740051969

Anderson, J. G. and J. R. Humphrey (1991) A least squares method for objective determination of earthquake source parameters, Seism. Res. Lett. 62(3-4), 201 – 209. doi: 10.1785/gssrl.62.3-4.201

Atkinson, G.M., and R.F. Mereu (1992) The shape of ground motion attenuation curves in southeastern Canada, Bull. Seismol. Soc. Am. 82(5), 2014 – 2031. doi: 10.1785/BSSA0820052014

Atkinson, G.M. (2004) Empirical attenuation of ground-motion spectra amplitudes in southeastern Canada and northeastern United States, Bull. Seismol. Soc. Am. 94(3), 1079 – 1095. doi: 10.1785/0120030175

Boore, D.M. (2003) Simulation of ground motion using the stochastic method, Pure Appl. Geophys. 160, 635 - 676. doi: 10.1007/PL00012553

Boore, D.M. and K.W. Campbell (2017). Adjusting Central and Eastern North America ground-motion intensity measures between sites with different reference-rock site conditions, Bull. Seism. Soc. Am. 107(1), 132-148. doi: 10.1785/0120160208

Brune, J.N. (1970) Tectonic stress and the spectra of seismic shear waves from earthquakes, J. Geophys. Res. 75, 4997 – 5009. doi: 10.1029/JB075i026p04997

Brune, J.N. (1971) Correction, J. Geophys. Res. 76, 5002. doi: 10.1029/JB076i020p05002

Campbell, K.W, Y.M.A. Hashash, B. Kim, A.R. Kottke, E.M. Rathje, W.J. Silva, and J.P. Stewart. (2014) Reference-rock site conditions for Central and Eastern North America: Part II – Attenuation (kappa) definition. PEER Report No. 2014/12.

Douglas, J., P. Gehl, L.F. Bonilla, and C. Gelis (2011) A kappa model for mainland France, Pure Appl. Geophys. 167 (11), 1303-1315. doi: 10.1007/s00024-010-0146-5

Goulet, C.A., T. Kishida, T.D. Ancheta, C.H. Cramer, R.B. Darragh, W.J. Silva, Y.M.A Hashash, J. Harmon, J.P. Stewart, K.E. Wooddell, and R.R. Youngs (2014) PEER NGA-East database. PEER No. Report 2014/17.

Goulet, C.A., T. Kishida, T.D. Ancheta, C.H. Cramer, R.B. Darragh, W.J. Silva, Y.M.A Hashash, J. Harmon, G.A. Parker, J.P. Stewart, and R.R. Youngs (2021) PEER NGA-East database, Earthquake Spectra 37, 1331-1353. doi: 10.1177/87552930211015695

Konno, K. and T., Ohmachi (1998) Ground motion characteristics estimated from spectral ratio between horizontal and vertical components of microtremor, Bull. Seism. Soc. Am. 88(1), 228 – 241. doi: 10.1785/BSSA0880010228

Ktenidou, O.J., C. Gelis, and L.F. Bonilla (2013) A study on the variability of kappa (κ) in a borehole: Implications of the computation process, Bull. Seismol. Soc. Am. 103(2A), 1048 – 1068. doi: 10.1785/0120120093

Ktenidou, O.-J., N.A. Abrahamson, S. Drouet, and F. Cotton (2015) Understanding the physics of kappa (k): insights from a downhole array, Geophys. J. Int. 203, 678-691. doi: 10.1093/gji/ggv315

Ktenidou, O.J., N.A. Abrahamson, R.B. Darragh, and W.J. Silva (2016) A Methodology for the Estimation of Kappa (κ) from Large Datasets: Example Application to Rock Sites in the NGA-East Database and Implications on Design Motions. PEER Report No. 2016/01.

Ktenidou, O.J., R. Darragh, P. Traversa, Y. Bozorgnia, and W. Silva (2021) Kappa estimates at hard rock sites. OECD NEA Kappa Workshop Videoconference via Zoom, May 25-28. Oral Presentation.

Motazedian, D. (2006) Region-specific key seismic parameters for earthquakes in northern Iran, Bull. Seismol. Soc. Am. 96(4A), 1383 – 1395. doi: 10.1785/0120050162

Pikoulis, E.V., O.-J. Ktenidou, E.Z. Psarakis, and N.A. Abrahamson (2020) Stochastic modeling as a method of arriving at higher frequencies: An application to κ

estimation, Journal of Geophysical Research: Solid Earth 125, doi: 10.1029/2019JB018768.

Steidl, J.H., A. G. Tumarkin, and R.J. Archuleta (1996) What is a reference site?, Bull. Seismol. Soc. Am. 86(6), 1733 – 1748. doi: 10.1785/BSSA0860061733

Appendices

Appendix A: The high frequency spectral decay, kappa, in eastern Canada determined with a broadband inversion approach

All velocity profiles used in this study and their associated amplification functions are presented in Figures A1-A25. Velocity profiles are provided in Tables A1-A25. Sources for the velocity profiles are listed in the caption. Figures and Tables A26 and A27 show an average regional velocity profile for north Charlevoix and south Charlevoix. Tables A28 and 29 show kappa results for all different velocity profiles at the various stations for the vertical and EAS component respectively.
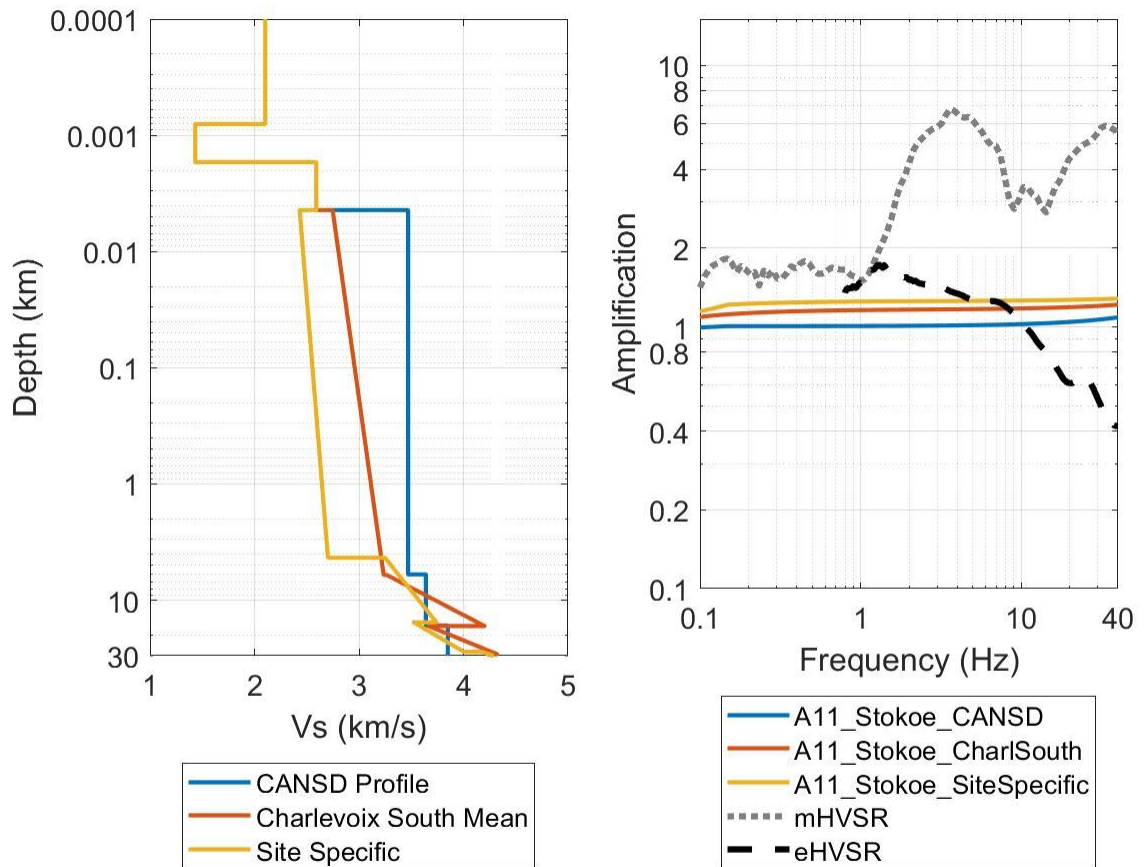
Figure A1: Station A11 velocity profile, on the left, and resultant amplification profile on the right for 3 different types of profiles – a region wide, a local profile, and a site-specific profile (solid lines) (Bent et al., 2019; personal communication Bent; Brune and Dorman, 1963; Stokoe et al, 2021) and the horizontal to vertical spectral ratio from earthquake (black dashed) and microtremor (grey dotted) (Ladak, 2020; Ladak et al., 2021) data.

Table A1: Station A11 combined velocity profiles (Bent et al., 2019; personal communication Bent; Brune and Dorman, 1963; Stokoe et al, 2021).

CANSD Profile		Charlevoix South Mean		Site-specific	
Vs (km/s)	*Depth (km)*	*Vs (km/s)*	*Depth (km)*	*Vs (km/s)*	*Depth (km)*
2.103	0	2.103	0	2.103	0
2.103	0.0001	2.103	0.0001	2.103	0.0001
2.103	0.0008	2.103	0.0008	2.103	0.0008
1.433	0.0008	1.433	0.0008	1.433	0.0008
1.433	0.0017	1.433	0.0017	1.433	0.0017
2.591	0.0017	2.591	0.0017	2.591	0.0017
2.591	0.0044	2.591	0.0044	2.591	0.0044
3.47	0.0044	2.748	0.0044	2.432	0.0044
3.47	6	3.236	6.056667	2.703	4.31
3.64	6	3.264667	6.056667	3.249	4.31
3.64	16.5	4.202333	16.67667	3.741	15.49
3.85	16.5	3.666667	16.67667	3.523	15.49
3.85	35.2	4.322	29.13333	4.002	27.77
		4.231333	29.13333	4.177	27.77
		5.064333	47.66	4.884	46.19
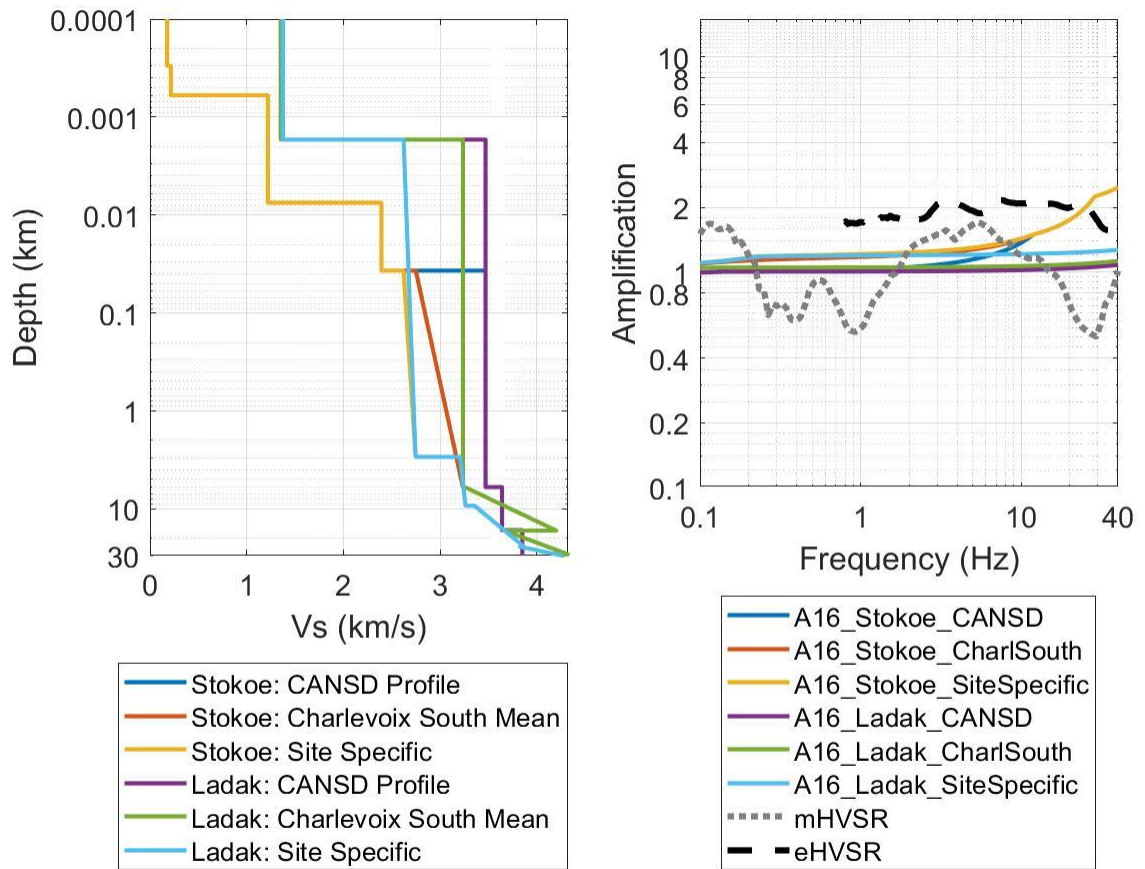
Figure A2: Station A16 velocity profile, on the left, and resultant amplification profile on the right for 3 different types of profiles – a region wide, a local profile, and a site-specific profile with two near-surface velocity profiles (solid lines) (Bent et al., 2019; personal communication Bent; Brune and Dorman, 1963; Ladak, 2020; Ladak et al., 2021; Stokoe et al, 2021) and the horizontal to vertical spectral ratio from earthquake (black dashed) and microtremor (grey dotted) (Ladak, 2020; Ladak et al., 2021) data.

Table A2: Station A16 combined velocity profiles (Bent et al., 2019; personal communication Bent; Brune and Dorman, 1963; Ladak, 2020; Ladak et al. 2021; Stokoe et al, 2021).

Stokoe: CANSD Profile		Stokoe: Charlevoix South Mean		Stokoe: Site-specific		Ladak: CANSD Profile		Ladak: Charlevoix South Mean		Ladak: Site-specific	
Vs (km/s)	Depth (km)	Vs (km/s)	Depth (km)	Vs (km/s)	Depth (km)	Vs (km/s)	Depth (km)	Vs (km/s)	Depth (km)	Vs (km/s)	Depth (km)
0.177	0	0.177	0	0.177	0	1.352	0	1.352	0	1.374	0
0.177	0.0001	0.177	0.0001	0.177	0.0001	1.352	0.001	1.352	0.0001	1.374	0.0001
0.177	0.0003	0.177	0.0003	0.177	0.0003	1.352	0.0017	1.352	0.0017	1.374	0.0017
0.216	0.0003	0.216	0.0003	0.216	0.0003	3.47	0.0017	3.236	0.0017	2.622	0.0017
0.216	0.0006	0.216	0.0006	0.216	0.0006	3.47	6	3.236	6.056667	2.746	2.95
1.219	0.0006	1.219	0.0006	1.219	0.0006	3.64	6	3.264667	6.056667	3.206	2.95
1.219	0.0075	1.219	0.0075	1.219	0.0075	3.64	16.5	4.202333	16.67667	3.262	9.3
2.393	0.0075	2.393	0.0075	2.393	0.0075	3.85	16.5	3.666667	16.67667	3.356	9.3
2.393	0.037	2.393	0.037	2.393	0.037	3.85	35.2	4.322	29.13333	3.867	24.33
3.47	0.037	2.748	0.037	2.622	0.037			4.231333	29.13333	3.824	24.33
3.47	6	3.236	6.056667	2.746	2.95			5.064333	47.66	5.477	53.33
3.64	6	3.264667	6.056667	3.206	2.95						

3.64	16.5	4.202333	16.67667	3.262	9.3						
3.85	16.5	3.666667	16.67667	3.356	9.3						
3.85	35.2	4.322	29.13333	3.867	24.33						
		4.231333	29.13333	3.824	24.33						
		5.064333	47.66	5.477	53.33						
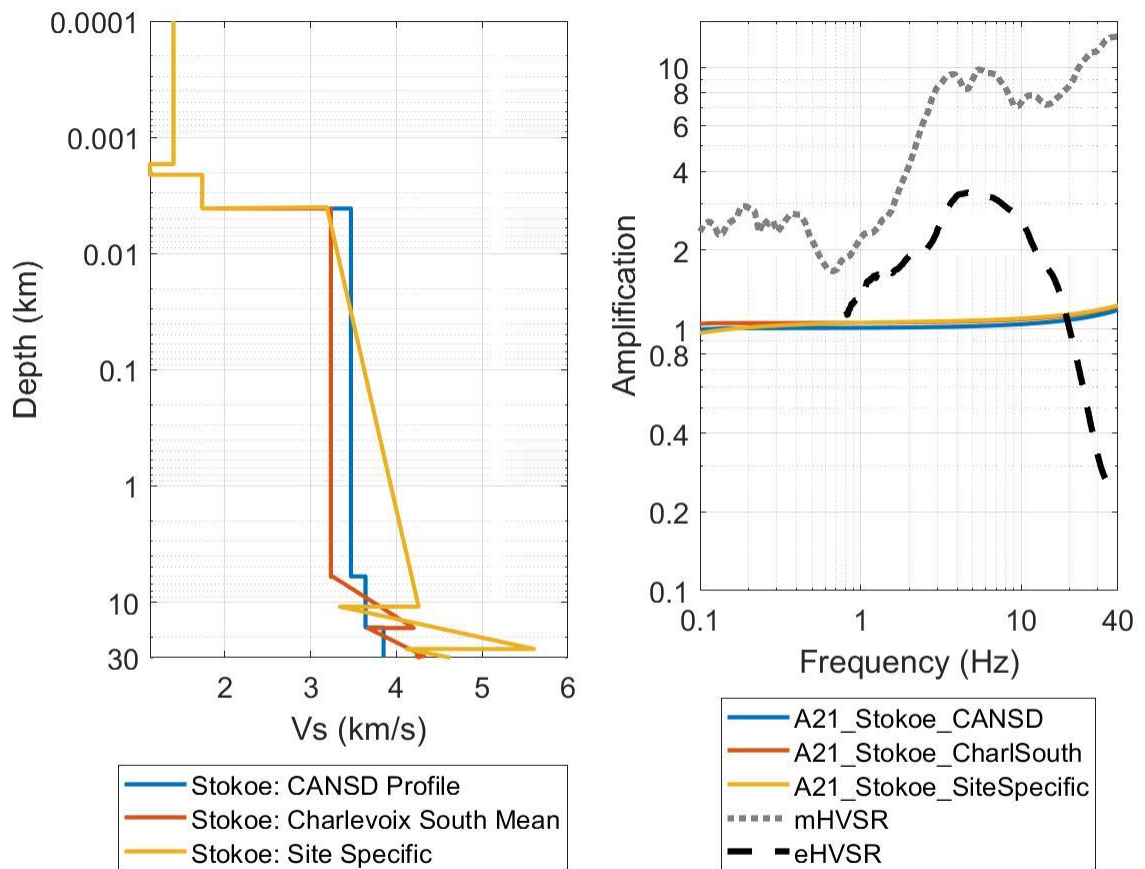
Figure A3: Station A21 velocity profile, on the left, and resultant amplification profile on the right for 3 different types of profiles – a region wide, a local profile, and a site-specific profile (solid lines) (Bent et al., 2019; personal communication Bent; Brune and Dorman, 1963; Stokoe et al, 2021) and the horizontal to vertical spectral ratio from earthquake (black dashed) and microtremor (grey dotted) (Ladak, 2020; Ladak et al., 2021) data.

Table A3: Station A21 combined velocity profiles (Bent et al., 2019; personal communication Bent; Brune and Dorman, 1963; Stokoe et al, 2021).

Stokoe: CANSD Profile		Stokoe: Charlevoix South Mean		Stokoe: Site-specific	
Vs (km/s)	Depth (km)	Vs (km/s)	Depth (km)	Vs (km/s)	Depth (km)
1.402	0	1.402	0	1.402	0
1.402	0.0001	1.402	0.0001	1.402	0.0001
1.402	0.0017	1.402	0.0017	1.402	0.0017
1.128	0.0017	1.128	0.0017	1.128	0.0017
1.128	0.0021	1.128	0.0021	1.128	0.0021
1.737	0.0021	1.737	0.0021	1.737	0.0021
1.737	0.0041	1.737	0.0041	1.737	0.0041
3.47	0.0041	3.236	0.0041	3.19	0.004
3.47	6	3.236	6.056667	4.259	10.91
3.64	6	3.264667	6.056667	3.339	10.91
3.64	16.5	4.202333	16.67667	5.604	25.24
3.85	16.5	3.666667	16.67667	4.121	25.24
3.85	35.2	4.322	29.13333	5.097	35.3
		4.231333	29.13333	4.693	35.3
		5.064333	47.66		
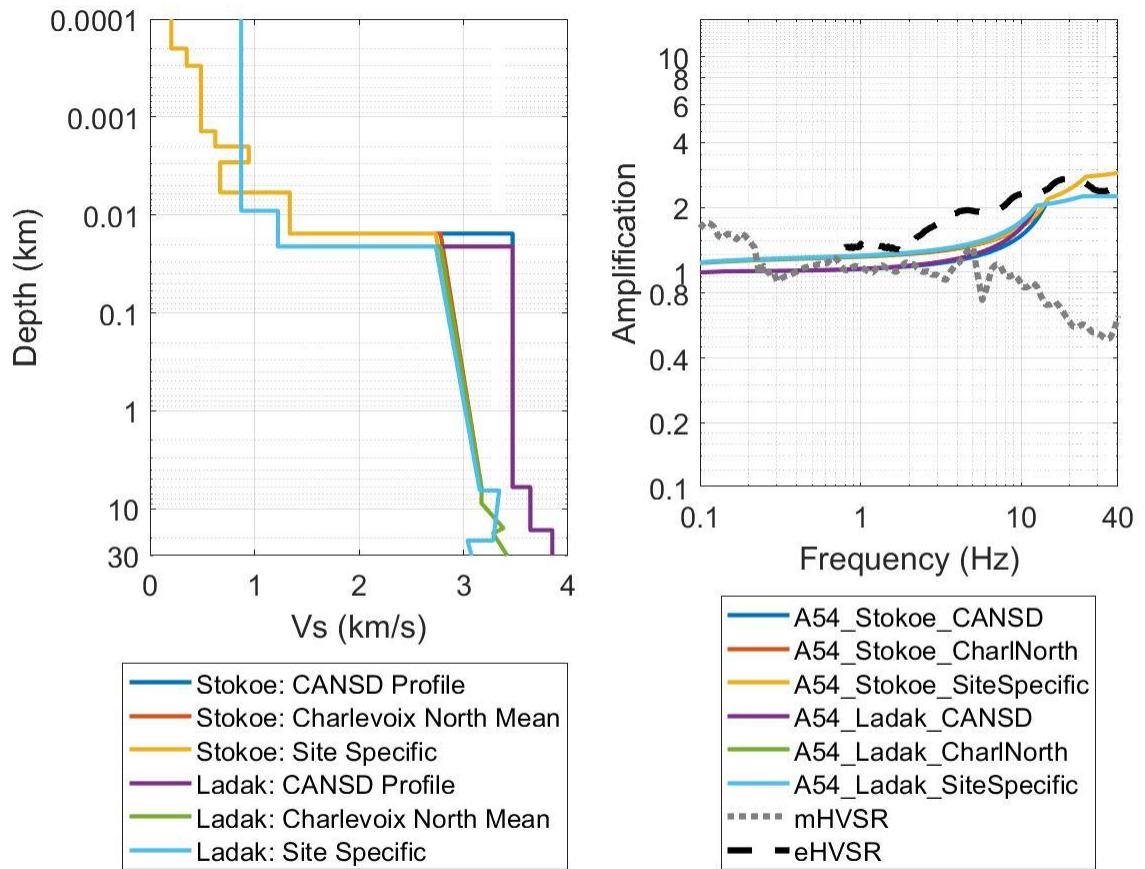
Figure A4: Station A54 velocity profile, on the left, and resultant amplification profile on the right for 3 different types of profiles – a region wide, a local profile, and a site-specific profile with two near-surface velocity profiles (solid lines) (Bent et al., 2019; personal communication Bent; Brune and Dorman, 1963; Ladak, 2020; Ladak et al., 2021; Stokoe et al, 2021) and the horizontal to vertical spectral ratio from earthquake (black dashed) and microtremor (grey dotted) (Ladak, 2020; Ladak et al., 2021) data.

Table A4: Station A54 combined velocity profiles (Bent et al., 2019; personal communication Bent; Brune and Dorman, 1963; Ladak, 2020; Ladak et al. 2021; Stokoe et al, 2021).

Stokoe: CANSD Profile		Stokoe: Charlevoix North Mean		Stokoe: Site-specific		Ladak: CANSD Profile		Ladak: Charlevoix North Mean		Ladak: Site-specific	
Vs (km/s)	Depth (km)	Vs (km/s)	Depth (km)	Vs (km/s)	Depth (km)	Vs (km/s)	Depth (km)	Vs (km/s)	Depth (km)	Vs (km/s)	Depth (km)
0.204	0	0.204	0	0.204	0	0.873	0	0.8729	0	0.8729	0
0.204	0.0001	0.204	0.0001	0.204	0.0001	0.873	0.0001	0.873	0.0001	0.873	0.0001
0.204	0.0002	0.204	0.0002	0.204	0.0002	0.873	0.00907	0.8729	0.00907	0.8729	0.00907
0.351	0.0002	0.351	0.0002	0.351	0.0002	1.224	0.00907	1.224	0.00907	1.224	0.00907
0.351	0.0003	0.351	0.0003	0.351	0.0003	1.224	0.021	1.224	0.021	1.224	0.021
0.488	0.0003	0.488	0.0003	0.488	0.0003	3.47	0.021	2.78075	0.021	2.734	0.021
0.488	0.0014	0.488	0.0014	0.488	0.0014	3.47	6	3.17375	6.135	3.156	6.49
0.625	0.0014	0.625	0.0014	0.625	0.0014	3.64	6	3.17175	8.76	3.342	6.49
0.625	0.002	0.625	0.002	0.625	0.002	3.64	16.5	3.38225	15.74	3.284	21.05
0.945	0.002	0.945	0.002	0.945	0.002	3.85	16.5	3.28275	17.74	3.039	21.05
0.945	0.0029	0.945	0.0029	0.945	0.0029	3.85	35.2	3.431	31.51	3.088	33.34
0.671	0.0029	0.671	0.0029	0.671	0.0029			3.89025	31.51	3.837	33.34

0.671	0.0059	0.671	0.0059	0.671	0.0059						
1.338	0.0059	1.338	0.0059	1.338	0.0059						
1.338	0.0155	1.338	0.0155	1.338	0.0155						
3.47	0.0155	2.78075	0.0155	2.734	0.0155						
3.47	6	3.17375	6.135	3.156	6.49						
3.64	6	3.17175	8.76	3.342	6.49						
3.64	16.5	3.38225	15.74	3.284	21.05						
3.85	16.5	3.28275	17.74	3.039	21.05						
3.85	35.2	3.431	31.51	3.088	33.34						
		3.89025	31.51	3.837	33.34						

Figure A5: Station A61 velocity profile, on the left, and resultant amplification profile on the right for 3 different types of profiles – a region wide, a local profile, and a site-specific profile with two near-surface velocity profiles (solid lines) (Bent et al., 2019; personal communication Bent; Brune and Dorman, 1963; Ladak, 2020; Ladak et al., 2021; Stokoe et al, 2021) and the horizontal to vertical spectral ratio from earthquake (black dashed) and microtremor (grey dotted) (Ladak, 2020; Ladak et al., 2021) data.

Table A5: Station A61 combined velocity profiles (Bent et al., 2019; personal communication Bent; Brune and Dorman, 1963; Ladak, 2020; Ladak et al. 2021; Stokoe et al, 2021).

Stokoe: CANSD Profile		Stokoe: Charlevoix North Mean		Stokoe: Site-specific		Ladak: CANSD Profile		Ladak: Charlevoix North Mean		Ladak: Site-specific	
Vs (km/s)	Depth (km)	Vs (km/s)	Depth (km)	Vs (km/s)	Depth (km)	Vs (km/s)	Depth (km)	Vs (km/s)	Depth (km)	Vs (km/s)	Depth (km)
0.109	0	0.109	0	0.109	0	1.915	0	1.915	0	1.915	0
0.109	0.0001	0.109	1.00E-04	0.109	1.00E-04	1.915	0.001	1.915	0.001	1.915	0.001
0.109	0.0005	0.109	0.0005	0.109	0.0005	1.915	0.03	1.915	0.03	1.915	0.03
0.424	0.0005	0.424	5.00E-04	0.424	5.00E-04	3.47	0.03	2.78075	0.03	3.022	0.03
0.424	0.002	0.424	0.002	0.424	0.002	3.47	6	3.17375	6.135	2.832	7.59
0.564	0.002	0.564	0.002	0.564	0.002	3.64	6	3.17175	8.76	3.055	7.59
0.564	0.0029	0.564	0.0029	0.564	0.0029	3.64	16.5	3.38225	15.74	3.524	16.6
0.725	0.0029	0.725	0.003	0.725	0.003	3.85	16.5	3.28275	17.74	3.678	16.6
0.725	0.0059	0.725	0.0059	0.725	0.0059	3.85	35.2	3.431	31.51	3.479	30.83
0.945	0.0059	0.945	0.006	0.945	0.006			3.89025	31.51	3.671	30.83
0.945	0.0151	0.945	0.0151	0.945	0.0151						
1.402	0.0151	1.402	0.015	1.402	0.015						

1.402	0.0295	1.402	0.03	1.402	0.03						
3.47	0.0295	2.78075	0.0295	3.022	0.03						
3.47	6	3.17375	6.135	2.832	7.59						
3.64	6	3.17175	8.76	3.055	7.59						
3.64	16.5	3.38225	15.74	3.524	16.6						
3.85	16.5	3.28275	17.74	3.678	16.6						
3.85	35.2	3.431	31.51	3.479	30.83						
		3.89025	31.51	3.671	30.83						

Figure A6: Station A64 velocity profile, on the left, and resultant amplification profile on the right for 3 different types of profiles – a region wide, a local profile, and a site-specific profile with two near-surface velocity profiles (solid lines) (Bent et al., 2019; personal communication Bent; Brune and Dorman, 1963; Ladak, 2020; Ladak et al., 2021; Stokoe et al, 2021) and the horizontal to vertical spectral ratio from earthquake (black dashed) and microtremor (grey dotted) (Ladak, 2020; Ladak et al., 2021) data.

Table A6: Station A64 combined velocity profiles (Bent et al., 2019; personal communication Bent; Brune and Dorman, 1963; Ladak, 2020; Ladak et al. 2021; Stokoe et al, 2021).

Stokoe: CANSD Profile		Stokoe: Charlevoix North Mean		Stokoe: Site-specific		Ladak: CANSD Profile		Ladak: Charlevoix North Mean		Ladak: Site-specific	
Vs (km/s)	Depth (km)	Vs (km/s)	Depth (km)	Vs (km/s)	Depth (km)	Vs (km/s)	Depth (km)	Vs (km/s)	Depth (km)	Vs (km/s)	Depth (km)
2.56	0	2.56	0	2.56	0	1.075	0	1.075	0	1.075	0
2.56	0.0001	2.56	0.0001	2.56	0.0001	1.075	1E-07	1.075	1E-07	1.075	1E-07
2.56	0.0009	2.56	0.0009	2.56	0.0009	1.075	6E-07	1.075	6E-07	1.075	6E-07
1.981	0.0009	1.981	0.0009	1.981	0.0009	1.075	6E-07	1.075	6E-07	1.075	6E-07
1.981	0.002	1.981	0.002	1.981	0.002	1.075	1.9E-06	1.075	1.9E-06	1.075	1.9E-06

3.018	0.002	3.018	0.002	3.018	0.002	1.0751	1.9E-06	1.0751	1.9E-06	1.0751	1.9E-06
3.018	0.0047	3.018	0.0047	3.018	0.0047	1.0751	4.4E-06	1.0751	4.4E-06	1.0751	4.4E-06
3.47	0.0047	2.78075	0.0047	3.467	0.0047	1.0751	4.4E-06	1.0751	4.4E-06	1.0751	4.4E-06
3.47	6	3.17375	6.135	3.807	8.96	1.0751	9.4E-06	1.0751	9.4E-06	1.0751	9.4E-06
3.64	6	3.17175	8.76	3.29	8.96	1.0752	9.4E-06	1.0752	9.4E-06	1.0752	9.4E-06
3.64	16.5	3.38225	15.74	3.521	13.31	1.0752	1.95E-05	1.0752	1.95E-05	1.0752	1.95E-05
3.85	16.5	3.28275	17.74	3.514	13.31	1.0754	1.95E-05	1.0754	1.95E-05	1.0754	1.95E-05
3.85	35.2	3.431	31.51	4.057	24.87	1.0754	3.96E-05	1.0754	3.96E-05	1.0754	3.96E-05
		3.89025	31.51	3.853	24.87	1.0758	3.96E-05	1.0758	3.96E-05	1.0758	3.96E-05
				4.376	44.23	1.0758	7.98E-05	1.0758	7.98E-05	1.0758	7.98E-05

						1.0766	7.98E-05	1.0766	7.98E-05	1.0766	7.98E-05
						1.0766	0.00016	1.0766	0.00016	1.0766	0.00016
						1.0781	0.00016	1.0781	0.00016	1.0781	0.00016
						1.0781	0.000321	1.0781	0.000321	1.0781	0.000321
						1.0806	0.000321	1.0806	0.000321	1.0806	0.000321
						1.0806	0.000643	1.0806	0.000643	1.0806	0.000643
						1.0846	0.000643	1.0846	0.000643	1.0846	0.000643
						1.0846	0.001286	1.0846	0.001286	1.0846	0.001286

						1.0904	0.001286	1.0904	0.001286	1.0904	0.001286
						1.0904	0.002573	1.0904	0.002573	1.0904	0.002573
						1.0977	0.002573	1.0977	0.002573	1.0977	0.002573
						1.0977	0.005148	1.0977	0.005148	1.0977	0.005148
						1.1062	0.005148	1.1062	0.005148	1.1062	0.005148
						1.1062	0.010296	1.1062	0.010296	1.1062	0.010296
						1.1154	0.010296	1.1154	0.010296	1.1154	0.010296

						1.1154	0.020592	1.1154	0.020592	1.1154	0.020592
						2.5758	0.020592	2.5758	0.020592	2.5758	0.020592
						2.5758	0.03	2.5758	0.03	2.5758	0.03
						3.47	0.03	2.78075	0.03	3.467	0.03
						3.47	6	3.17375	6.135	3.807	8.96
						3.64	6	3.17175	8.76	3.29	8.96
						3.64	16.5	3.38225	15.74	3.521	13.31
						3.85	16.5	3.28275	17.74	3.514	13.31
						3.85	35.2	3.431	31.51	4.057	24.87
								3.89025	31.51	3.853	24.87

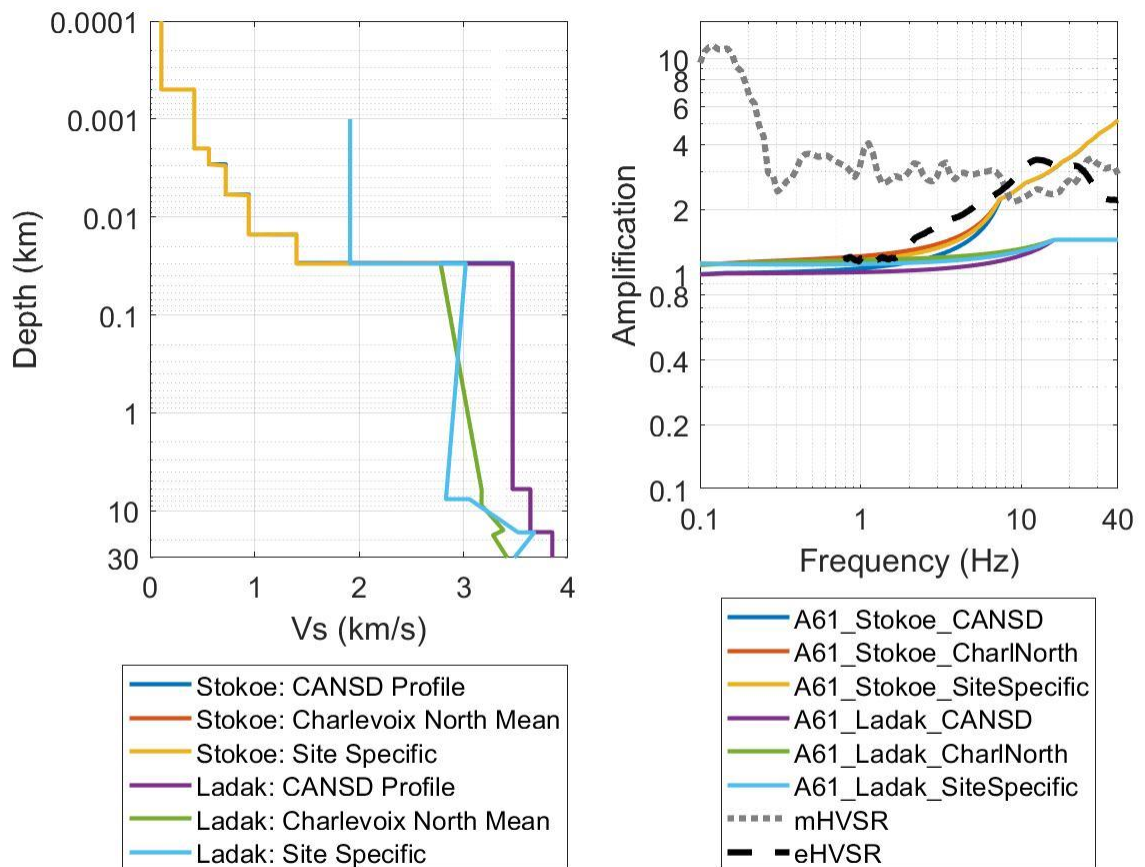|										4.376	44.23
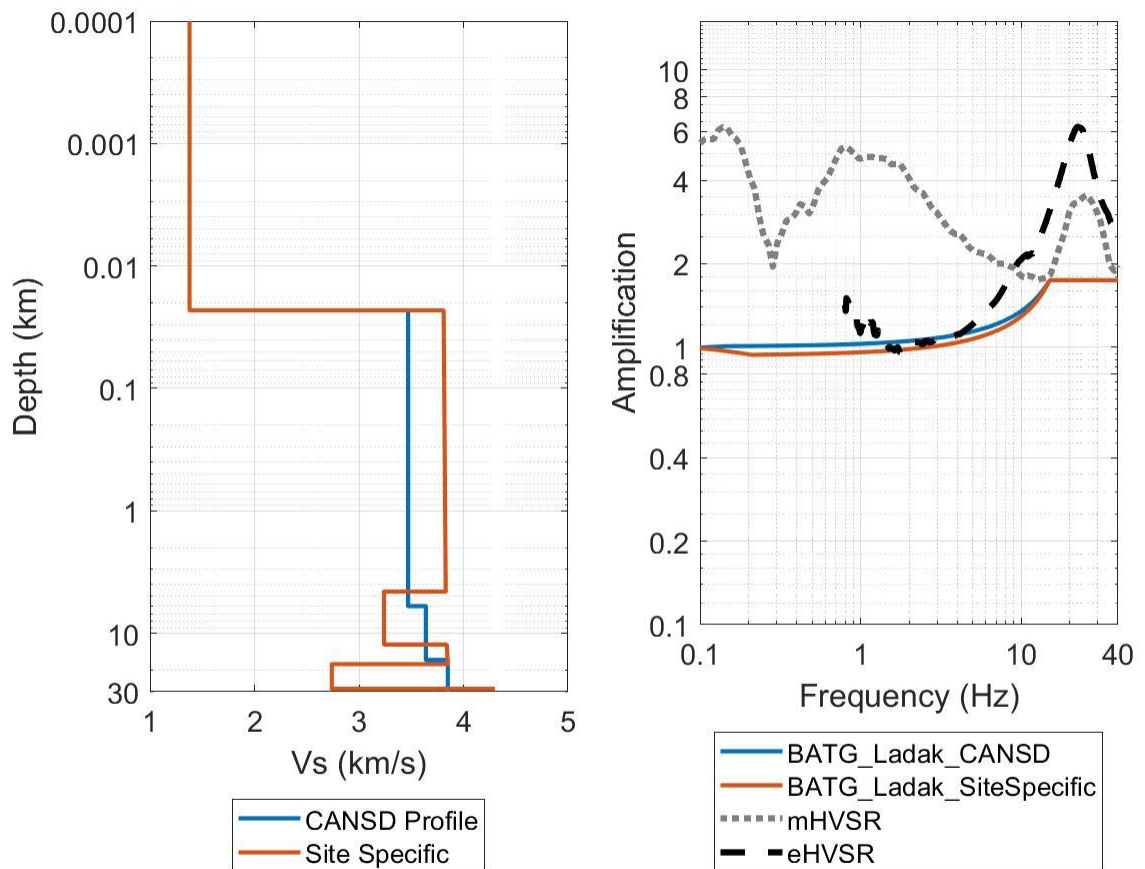
Figure A7: Station BATG velocity profile, on the left, and resultant amplification profile on the right for 2 different types of profiles – a region wide, and a site-specific profile (solid lines) (Kao et al., 2014; Brune and Dorman, 1963; Ladak, 2020; Ladak et al., 2021) and the horizontal to vertical spectral ratio from earthquake (black dashed) and microtremor (grey dotted) (Ladak, 2020; Ladak et al., 2021) data.

Table A7: Station BATG combined velocity profiles (Kao et al., 2014; Brune and Dorman, 1963; Ladak, 2020; Ladak et al. 2021).

CANSD Profile		Site-specific	
Vs (km/s)	Depth (km)	Vs (km/s)	Depth (km)
1.379	0	1.379	0
1.379	0.0001	1.379	0.0001
1.379	0.023	1.379	0.023
3.47	0.023	3.81	0.023
3.47	6	3.83	4.56
3.64	6	3.24	4.56
3.64	16.5	3.24	12.36
3.85	16.5	3.84	12.36
3.85	35.2	3.85	17.86
		2.74	17.86
		2.74	28.42
		4.3	28.42

Figure A8: Station BCLQ velocity profile, on the left, and resultant amplification profile on the right for 2 different types of profiles – a region wide, and a site-specific profile (solid lines) (Bent and Kao, 2015; Brune and Dorman, 1963; Ladak, 2020; Ladak et al., 2021) and the horizontal to vertical spectral ratio from earthquake (black dashed) and microtremor (grey dotted) (Ladak, 2020; Ladak et al., 2021) data.

Table A8: Station BCLQ combined velocity profiles

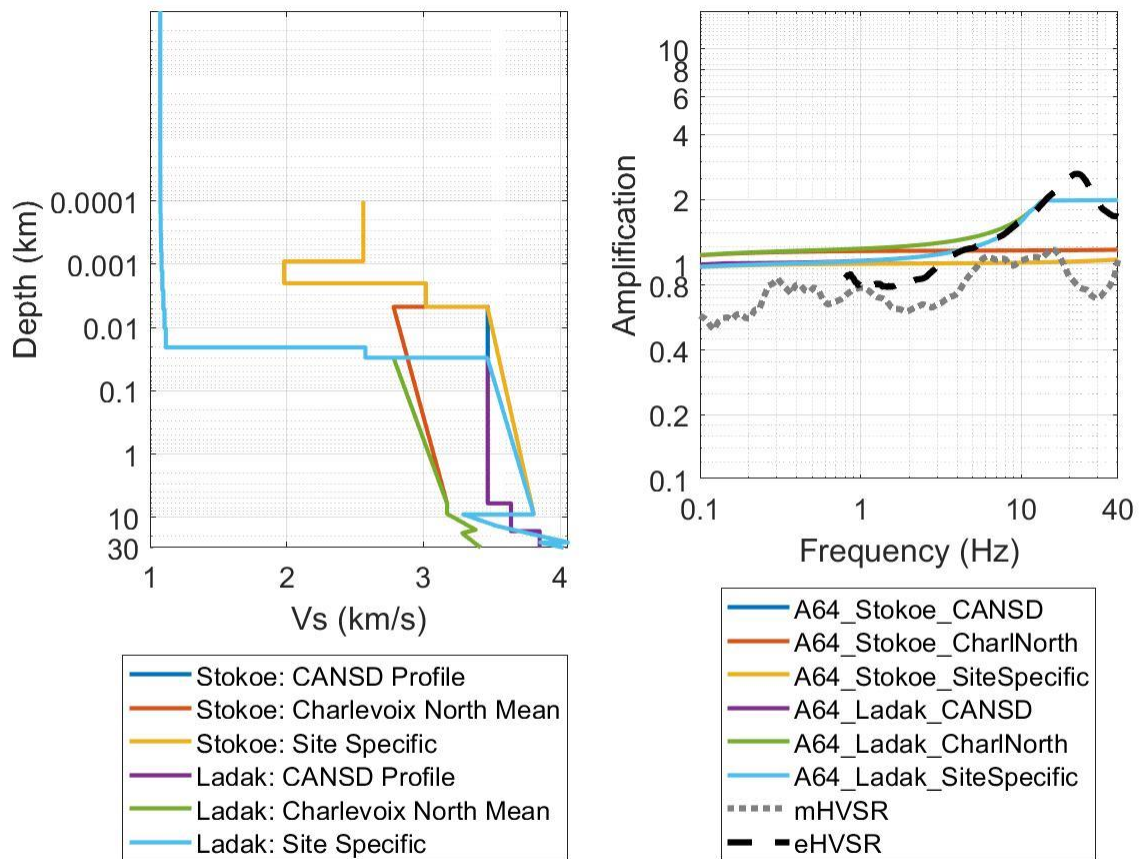| CANSD Profile		Site-specific	
Vs (km/s)	*Depth (km)*	*Vs (km/s)*	*Depth (km)*
1.339	0	1.339	0
1.339	0.001	1.339	0.001
1.339	0.016	1.339	0.016
3.47	0.016	2.691	0.016
3.47	6	4.76	8.12
3.64	6	3.466	8.12
3.64	16.5	3.4	9.27
3.85	16.5	3.538	9.27
3.85	35.2	4.406	17.77
		3.86	17.77
		4.568	29
		4.423	29
		4.794	41.78

Figure A9: Station CNQ velocity profile, on the left, and resultant amplification profile on the right for 2 different types of profiles – a region wide, and a site-specific profile (solid lines) (Brune and Dorman, 1963; Kuponiyi et al., 2016; Ladak, 2020; Ladak et al., 2021) and the horizontal to vertical spectral ratio from microtremor (grey dotted) (Ladak, 2020; Ladak et al., 2021) data.

Table A9: Station CNQ combined velocity profiles (Brune and Dorman, 1963; Kuponiyi et al., 2016; Ladak, 2020; Ladak et al. 2021).

CANSD Profile		Site-specific		Site-specific Cont'd	
Vs (km/s)	Depth (km)	Vs (km/s)	Depth (km)	Vs (km/s)	Depth (km)
1.935	0	1.935	0	3.7403	16.5
1.935	0.01	1.935	0.01	3.7105	17
1.935	0.03	1.935	0.03	3.6947	17.5
3.47	0.03	3.864	0.03	3.6965	18
3.47	6	3.8612	0.5	3.6823	18.5
3.64	6	3.8626	1	3.6733	19
3.64	16.5	3.8626	1.5	3.654	19.5
3.85	16.5	3.8615	2	3.6496	20
3.85	35.2	3.8626	2.5		
		3.8599	3		
		3.8626	3.5		
		3.8685	4		
		3.8689	4.5		
		3.8582	5		
		3.8381	5.5		
		3.8265	6		
		3.8381	6.5		
		3.8265	7		
		3.8132	7.5		
		3.8055	8		
		3.8034	8.5		
		3.8042	9		
		3.776	9.5		

		3.7695	10		
		3.7563	10.5		
		3.7673	11		
		3.7506	11.5		
		3.7374	12		
		3.738	12.5		
		3.7333	13		
		3.7266	13.5		
		3.7333	14		
		3.724	14.5		
		3.7551	15		
		3.7478	15.5		
		3.746	16		
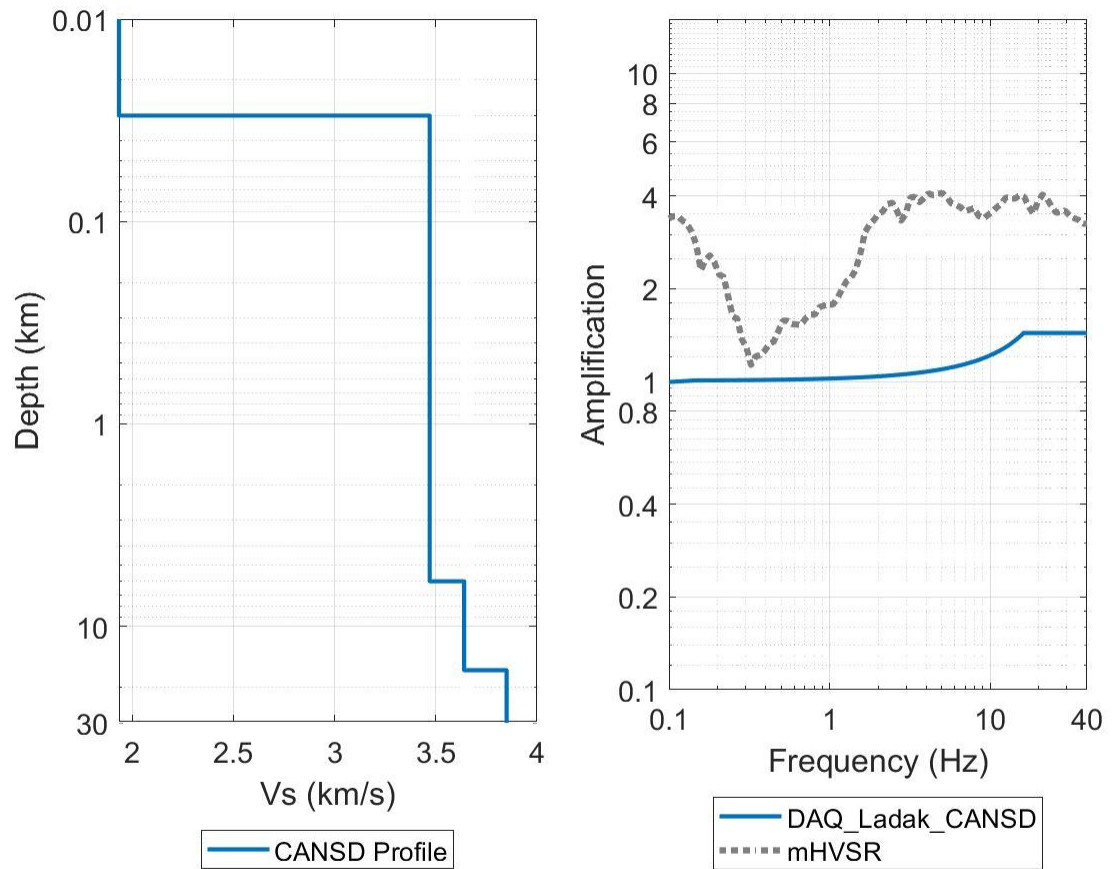
Figure A10: Station DAQ velocity profile, on the left, and resultant amplification profile on the right for 1 profile – a region wide profile (solid line) (Brune and Dorman, 1963; Ladak, 2020; Ladak et al., 2021) and the horizontal to vertical spectral ratio from microtremor (grey dotted) (Ladak, 2020; Ladak et al., 2021) data.

Table A10: Station DAQ combined velocity profile (Brune and Dorman, 1963; Ladak, 2020; Ladak et al. 2021).

CANSD Profile	
Vs (km/s)	*Depth (km)*
1.935	0
1.935	0.01
1.935	0.03
3.47	0.03
3.47	6
3.64	6
3.64	16.5
3.85	16.5
3.85	35.2

Figure A11: Station DPQ velocity profile, on the left, and resultant amplification profile on the right for 2 different types of profiles – a region wide, and a site-specific profile (solid lines) (Bent and Kao, 2015; Brune and Dorman, 1963; Ladak, 2020; Ladak et al., 2021) and the horizontal to vertical spectral ratio from earthquake (black dashed) and microtremor (grey dotted) (Ladak, 2020; Ladak et al., 2021) data.

Table A11: Station DPQ combined velocity profiles (Bent and Kao, 2015; Brune and Dorman, 1963; Ladak, 2020; Ladak et al. 2021).

CANSD Profile		Site-specific	
Vs (km/s)	*Depth (km)*	*Vs (km/s)*	*Depth (km)*
1.57	0	1.57	0
1.57	0.0001	1.57	0.0001
1.57	0.009	1.57	0.009
3.47	0.009	3.247	0.009
3.47	6	3.962	12.77
3.64	6	3.537	12.77
3.64	16.5	4.163	22.4
3.85	16.5	4.044	22.4
3.85	35.2	5.327	47.72

Figure A12: Station GAC velocity profile, on the left, and resultant amplification profile on the right for 2 different types of profiles – a region wide, and a site-specific profile (solid lines) (Brune and Dorman, 1963; Cassidy, 1995; Ladak, 2020; Ladak et al., 2021) and the horizontal to vertical spectral ratio from earthquake (black dashed) and microtremor (grey dotted) (Ladak, 2020; Ladak et al., 2021) data.

Table A12: Station GAC combined velocity profiles (Brune and Dorman, 1963; Cassidy, 1995; Ladak, 2020; Ladak et al. 2021).

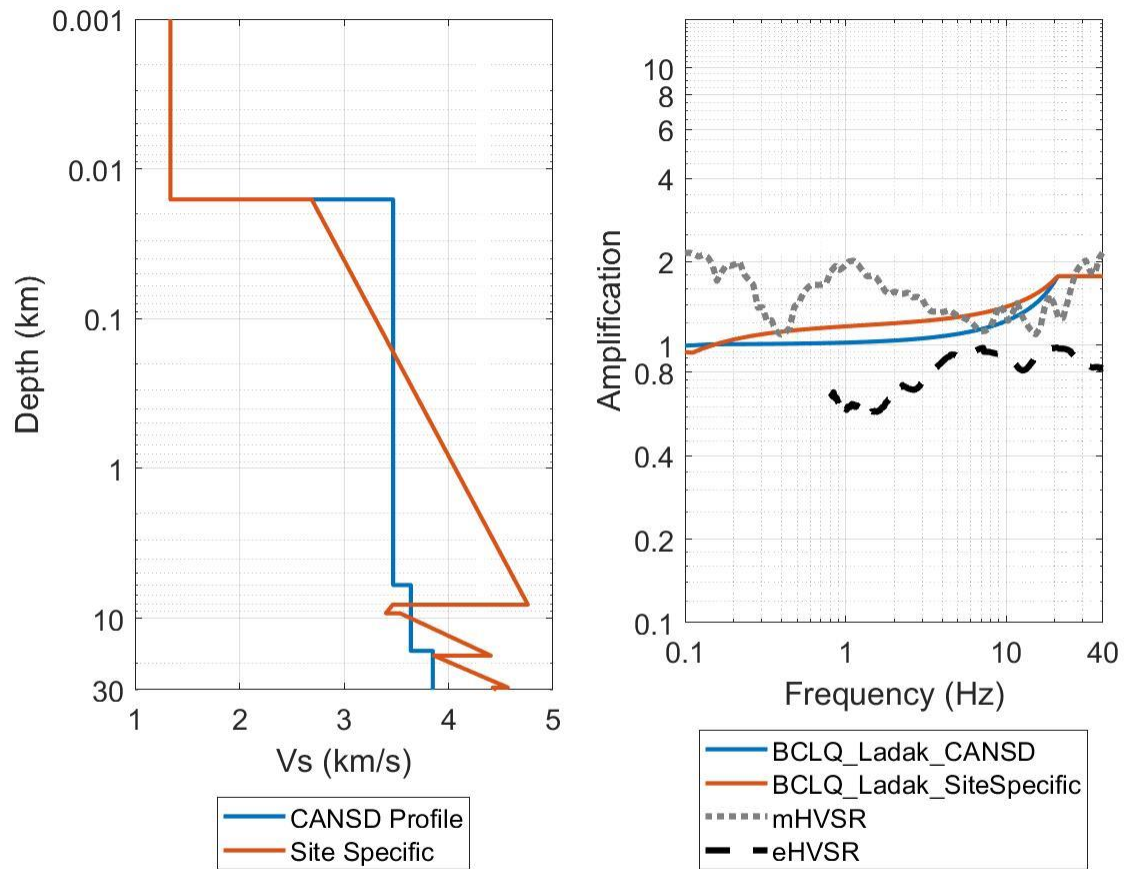| CANSD Profile		Site-specific	
Vs (km/s)	*Depth (km)*	*Vs (km/s)*	*Depth (km)*
1.339893	0	1.339893	0
1.339893	0.000001	1.339893	0.000001
1.339893	8.35E-05	1.339893	8.35E-05
1.342265	8.35E-05	1.342265	8.35E-05
1.342265	0.000251	1.342265	0.000251
1.346336	0.000251	1.346336	0.000251
1.346336	0.000585	1.346336	0.000585
1.352697	0.000585	1.352697	0.000585
1.352697	0.001253	1.352697	0.001253
1.361579	0.001253	1.361579	0.001253
1.361579	0.002589	1.361579	0.002589
3.300387	0.002589	3.300387	0.002589
3.300387	0.008	3.300387	0.008
3.47	0.008	3.1	0.008
3.47	6	3.1	0.5
3.64	6	3.5	0.5
3.64	16.5	3.5	3
3.85	16.5	3.7	3
3.85	35.2	3.7	18.6
		4	18.6
		4	40.6

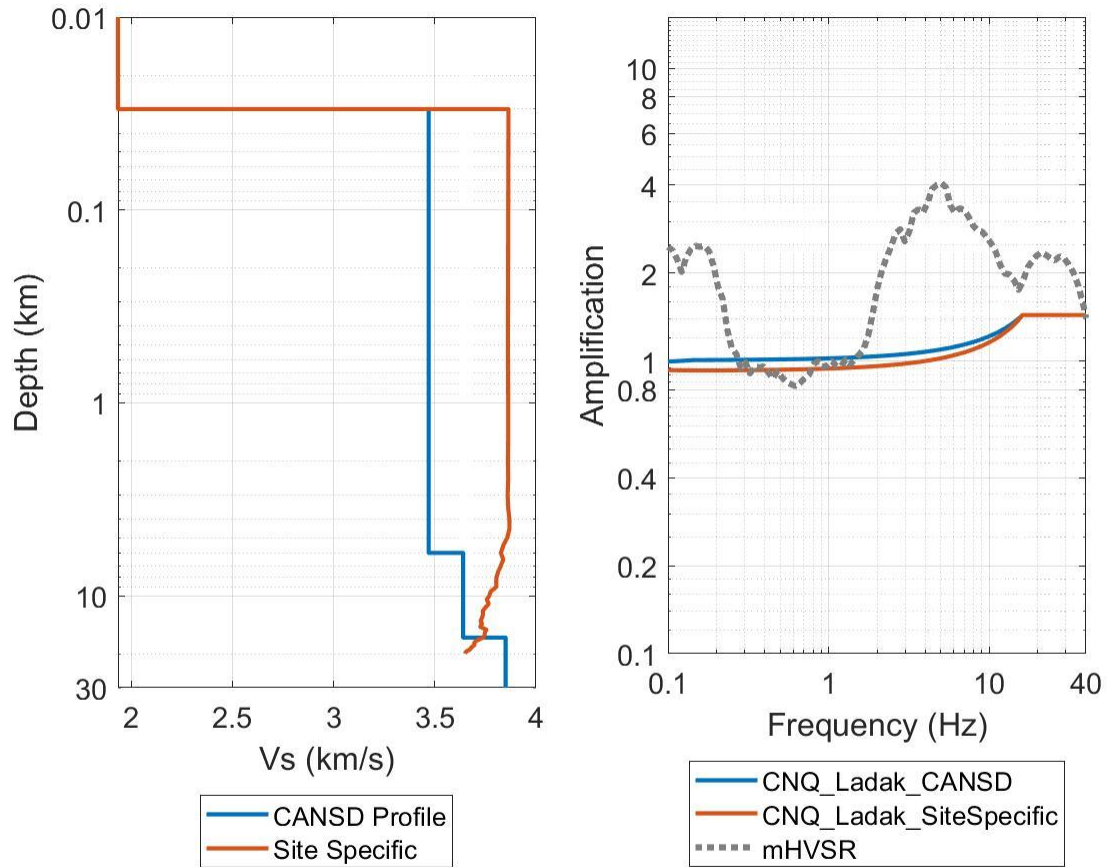**Figure A13: Station GBN velocity profile, on the left, and resultant amplification profile on the right for 2 different types of profiles – a region wide, and a site-specific profile (solid lines) (Brune and Dorman, 1963; Kuponiyi et al., 2016; Ladak, 2020; Ladak et al., 2021) and the horizontal to vertical spectral ratio from earthquake (black dashed) and microtremor (grey dotted) (Ladak, 2020; Ladak et al., 2021) data.**

Table A13: Station GBN combined velocity profiles (Brune and Dorman, 1963; Kuponiyi et al., 2016; Ladak, 2020; Ladak et al. 2021).

CANSD Profile		Site-specific		Site-specific Cont'd	
Vs (km/s)	Depth (km)	Vs (km/s)	Depth (km)	Vs (km/s)	Depth (km)
1.164	0	1.164	0	3.4163	15.5
1.164	0.0001	1.164	0.001	3.4181	16
1.164	0.02058	1.164	0.02058	3.4212	16.5
2.074	0.02058	2.074	0.02058	3.4227	17
2.074	0.029	2.074	0.029	3.4247	17.5
3.47	0.029	3.5468	0.029	3.4269	18
3.47	6	3.5685	0.5	3.4297	18.5
3.64	6	3.4315	1	3.4287	19
3.64	16.5	3.3387	1.5	3.4318	19.5
3.85	16.5	3.2601	2	3.4349	20
3.85	35.2	3.1856	2.5	3.8	20.6
		3.0952	3	3.96	20.6
		3.0449	3.5	3.92	26.17
		3.033	4	4.1	26.17
		3.0698	4.5	4.1	40.16
		3.1313	5	4.9	40.16
		3.209	5.5		
		3.2767	6		
		3.3216	6.5		
		3.3507	7		
		3.3708	7.5		
		3.3855	8		
		3.3955	8.5		

|		3.406	9		
		3.4088	9.5		
		3.4126	10		
		3.4169	10.5		
		3.4205	11		
		3.4217	11.5		
		3.419	12		
		3.4167	12.5		
		3.4151	13		
		3.4151	13.5		
		3.4142	14		
		3.4134	14.5		
		3.4135	15		
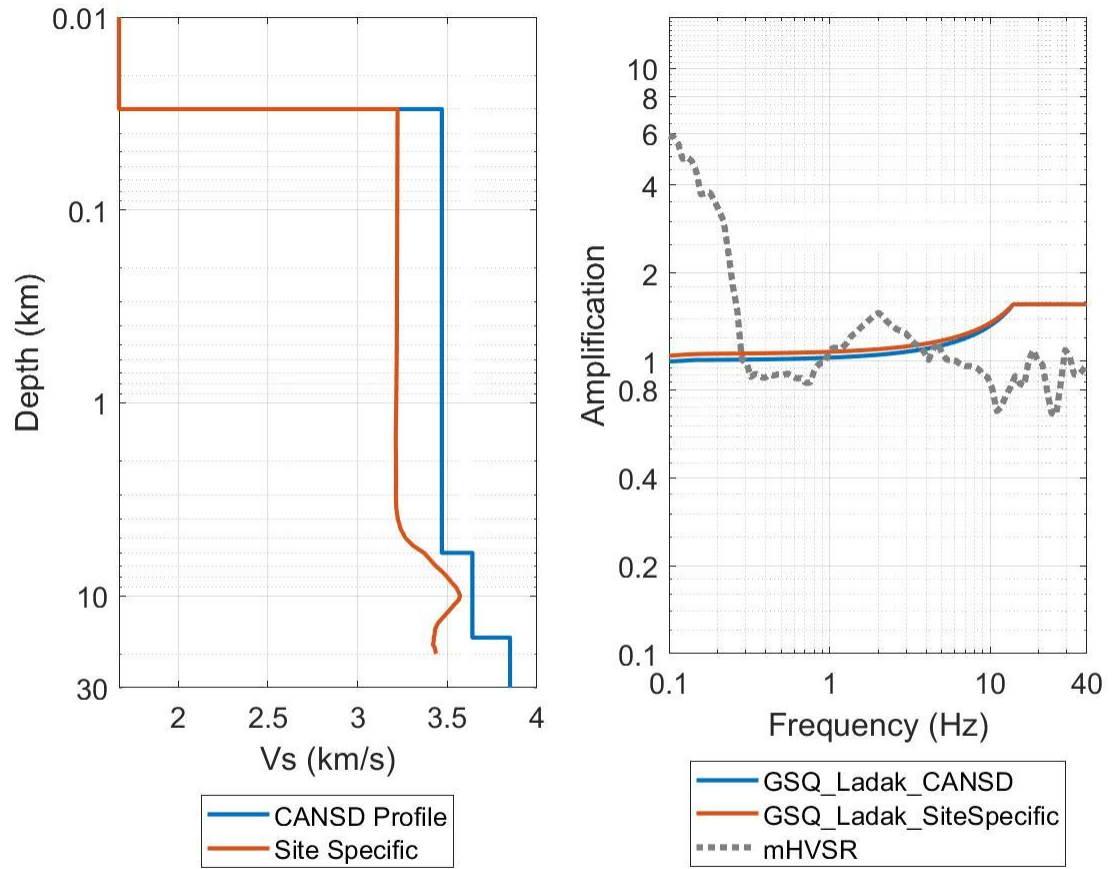
Figure A14: Station GSQ velocity profile, on the left, and resultant amplification profile on the right for 2 different types of profiles – a region wide, and a site-specific profile (solid lines) (Brune and Dorman, 1963; Kuponiyi et al., 2016; Ladak, 2020; Ladak et al., 2021) and the horizontal to vertical spectral ratio from microtremor (grey dotted) (Ladak, 2020; Ladak et al., 2021) data.

Table A14: Station GSQ combined velocity profiles (Brune and Dorman, 1963; Kuponiyi et al., 2016; Ladak, 2020; Ladak et al. 2021).

CANSD Profile		Site-specific		Site-specific Cont'd	
Vs (km/s)	Depth (km)	Vs (km/s)	Depth (km)	Vs (km/s)	Depth (km)
1.671	0	1.671	0	3.4244	16.5
1.671	0.01	1.671	0.01	3.4256	17
1.671	0.03	1.671	0.03	3.4228	17.5
3.47	0.03	3.2231	0.03	3.4208	18
3.47	6	3.2189	0.5	3.4291	18.5
3.64	6	3.2158	1	3.4329	19
3.64	16.5	3.2129	1.5	3.4343	19.5
3.85	16.5	3.2141	2	3.437	20
3.85	35.2	3.2146	2.5		
		3.2141	3		
		3.2158	3.5		
		3.2247	4		
		3.2401	4.5		
		3.2658	5		
		3.3095	5.5		
		3.3712	6		
		3.4046	6.5		
		3.4345	7		
		3.4716	7.5		
		3.5	8		
		3.5223	8.5		
		3.5472	9		
		3.5616	9.5		

		3.5716	10		
		3.5647	10.5		
		3.5438	11		
		3.5262	11.5		
		3.5089	12		
		3.4915	12.5		
		3.4755	13		
		3.4587	13.5		
		3.4457	14		
		3.4384	14.5		
		3.4317	15		
		3.4304	15.5		
		3.4295	16		
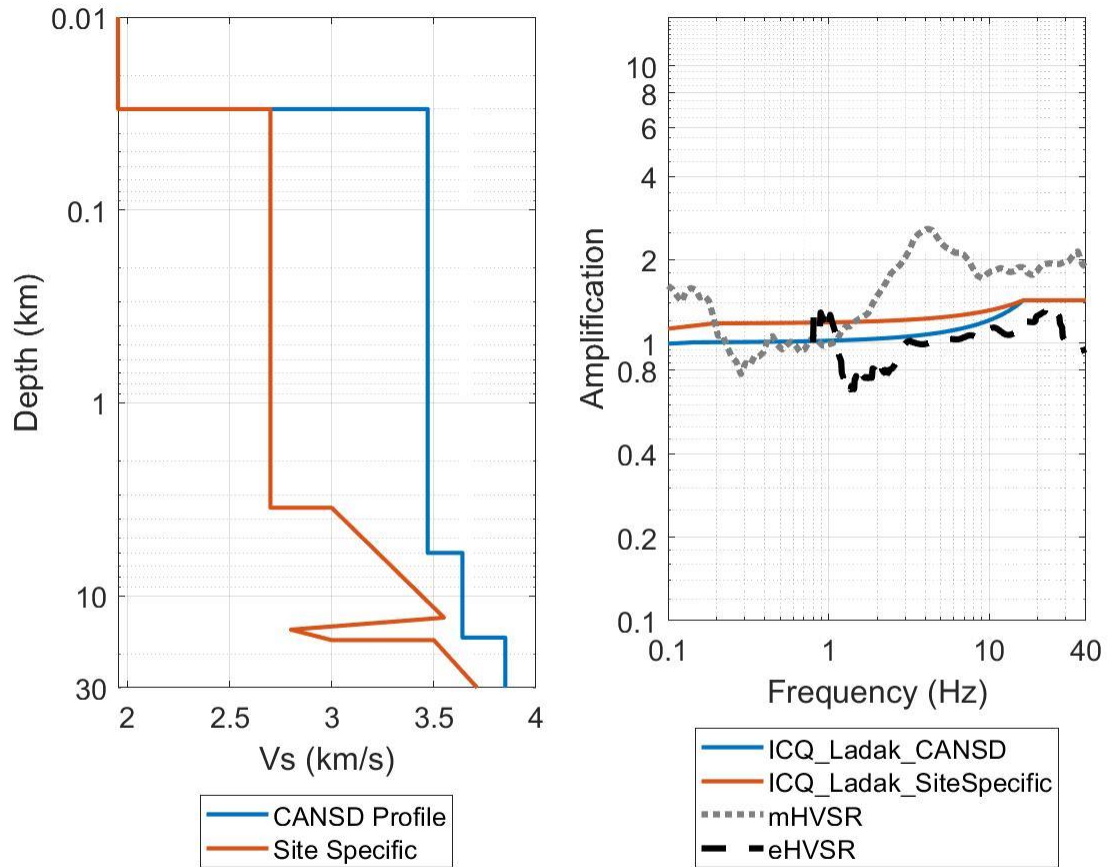
Figure A15: Station ICQ velocity profile, on the left, and resultant amplification profile on the right for 2 different types of profiles – a region wide, and a site-specific profile (solid lines) (Kao et al., 2014; Brune and Dorman, 1963; Ladak, 2020; Ladak et al., 2021) and the horizontal to vertical spectral ratio from earthquake (black dashed) and microtremor (grey dotted) (Ladak, 2020; Ladak et al., 2021) data.

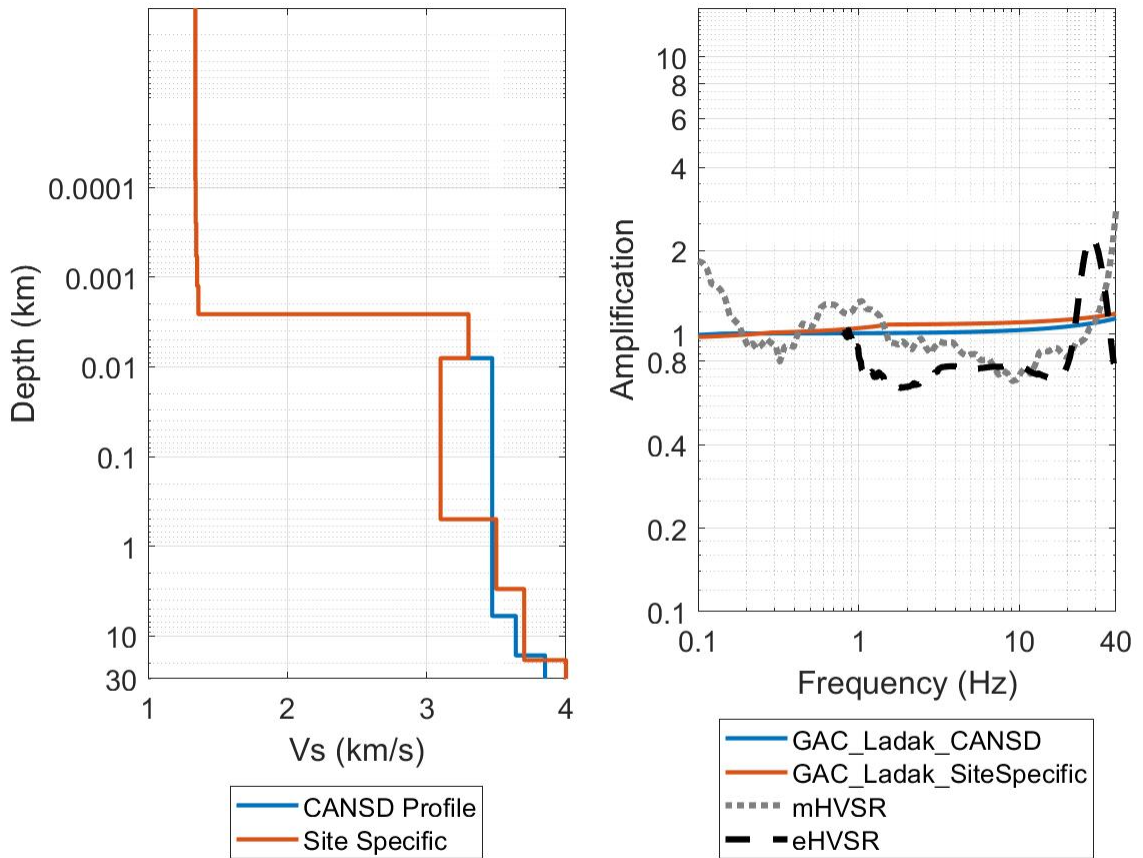**Table A15: Station ICQ combined velocity profiles (Kao et al., 2014; Brune and Dorman, 1963; Ladak, 2020; Ladak et al. 2021).**

CANSD Profile		Site-specific	
Vs (km/s)	*Depth (km)*	*Vs (km/s)*	*Depth (km)*
1.954	0	1.954	0
1.954	0.01	1.954	0.01
1.954	0.03	1.954	0.03
3.47	0.03	2.7	0.03
3.47	6	2.7	3.5
3.64	6	3	3.5
3.64	16.5	3.55	13
3.85	16.5	2.8	15
3.85	35.2	3	17
		3.5	17
		3.8	38

Figure A16: Station KGNO velocity profile, on the left, and resultant amplification profile on the right for 1 profile – a region wide profile (solid line) (Brune and Dorman, 1963; Ladak; 2020; Ladak et al., 2021) and the horizontal to vertical spectral ratio from earthquake (black dashed) data.

Table A16: Station KGNO combined velocity profile (Brune and Dorman, 1963; Ladak, 2020; Ladak et al. 2021).

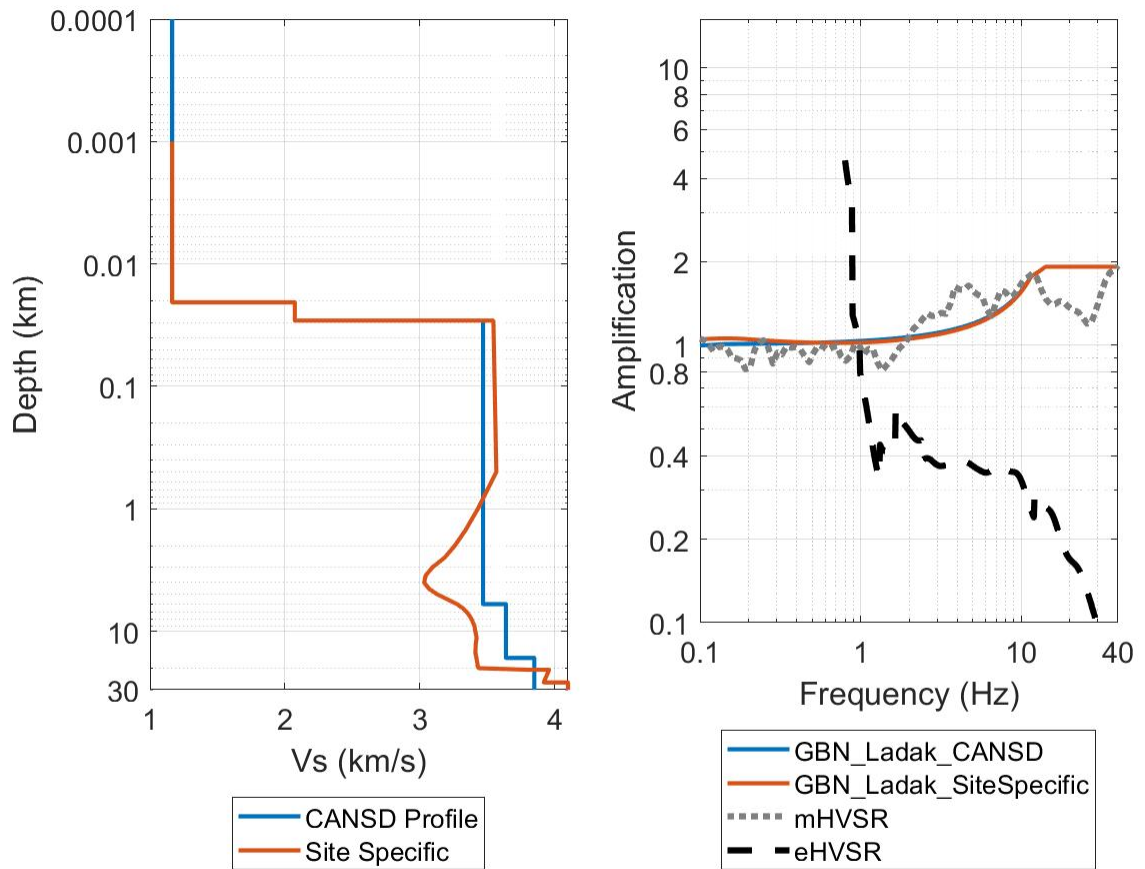| CANSD Profile	
Vs (km/s)	*Depth (km)*
1.86	0
1.86	0.0001
1.86	0.03
3.47	0.03
3.47	6
3.64	6
3.64	16.5
3.85	16.5
3.85	35.2
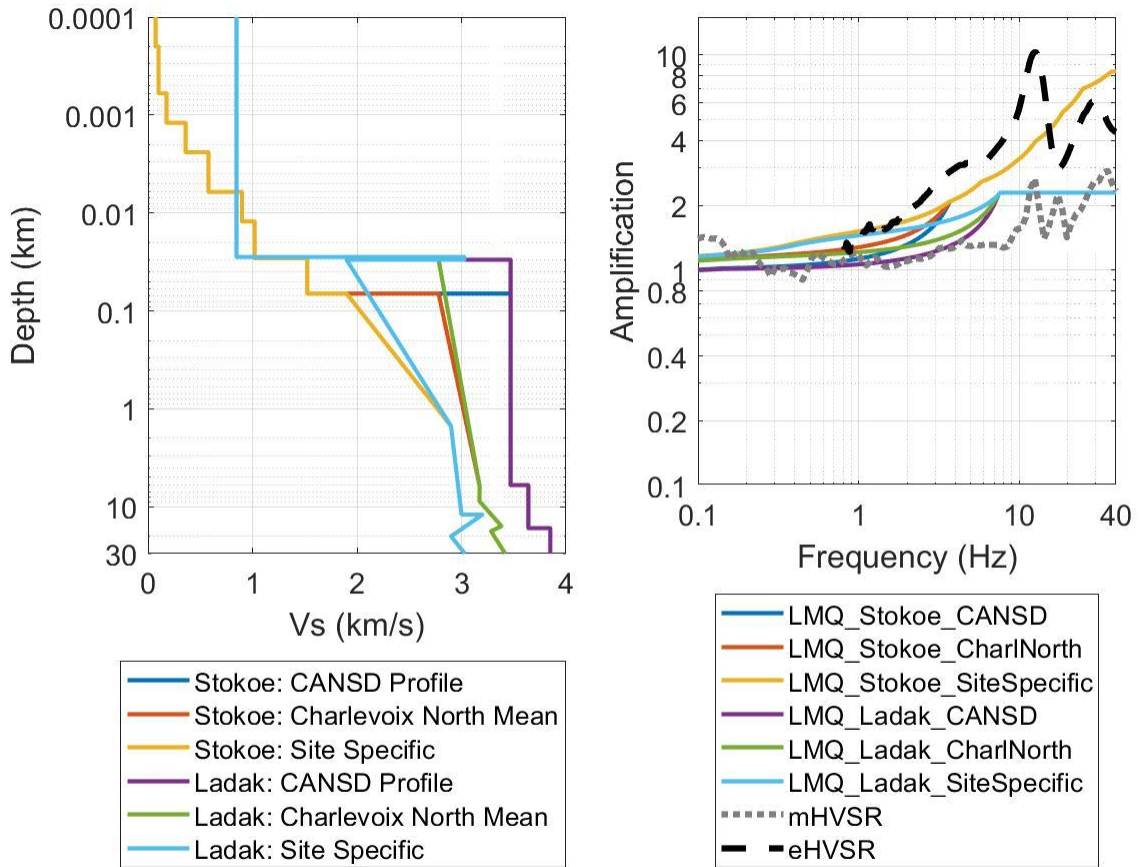
Figure A17: Station LMQ velocity profile, on the left, and resultant amplification profile on the right for 3 different types of profiles – a region wide, a local profile, and a site-specific profile with two near-surface velocity profiles (solid lines) (Bent and Kao, 2015; Brune and Dorman, 1963; Ladak, 2020; Ladak et al., 2021; Stokoe et al, 2021) and the horizontal to vertical spectral ratio from earthquake (black dashed) and microtremor (grey dotted) (Ladak, 2020; Ladak et al., 2021) data.

Table A17: Station LMQ combined velocity profiles (Bent and Kao, 2015; Brune and Dorman, 1963; Ladak, 2020; Ladak et al. 2021; Stokoe et al, 2021).

Stokoe: CANSD Profile		Stokoe: Charlevoix North Mean		Stokoe: Site-specific		Ladak: CANSD Profile		Ladak: Charlevoix North Mean		Ladak: Site-specific	
Vs (km/s)	Depth (km)	Vs (km/s)	Depth (km)	Vs (km/s)	Depth (km)	Vs (km/s)	Depth (km)	Vs (km/s)	Depth (km)	Vs (km/s)	Depth (km)
0.073	0	0.073	0	0.073	0	0.847	0	0.847	0	0.847	0
0.073	0.0001	0.073	0.0001	0.073	0.0001	0.847	0.0001	0.847	0.0001	0.847	0.0001
0.073	0.0002	0.073	0.0002	0.073	0.0002	0.847	0.02814	0.847	0.02814	0.847	0.02814
0.101	0.0002	0.101	0.0002	0.101	0.0002	3.027	0.02814	3.027	0.02814	3.027	0.02814
0.101	0.0006	0.101	0.0006	0.101	0.0006	3.027	0.03	3.027	0.03	3.027	0.03
0.177	0.0006	0.177	0.0006	0.177	0.0006	3.47	0.03	2.78075	0.03	1.9	0.03
0.177	0.0012	0.177	0.0012	0.177	0.0012	3.47	6	3.17375	6.135	2.9	1.5
0.36	0.0012	0.36	0.0012	0.36	0.0012	3.64	6	3.17175	8.76	3	12
0.36	0.0024	0.36	0.0024	0.36	0.0024	3.64	16.5	3.38225	15.74	3.2	12
0.579	0.0024	0.579	0.0024	0.579	0.0024	3.85	16.5	3.28275	17.74	2.9	20
0.579	0.0061	0.579	0.0061	0.579	0.0061	3.85	35.2	3.431	31.51	3.1	37

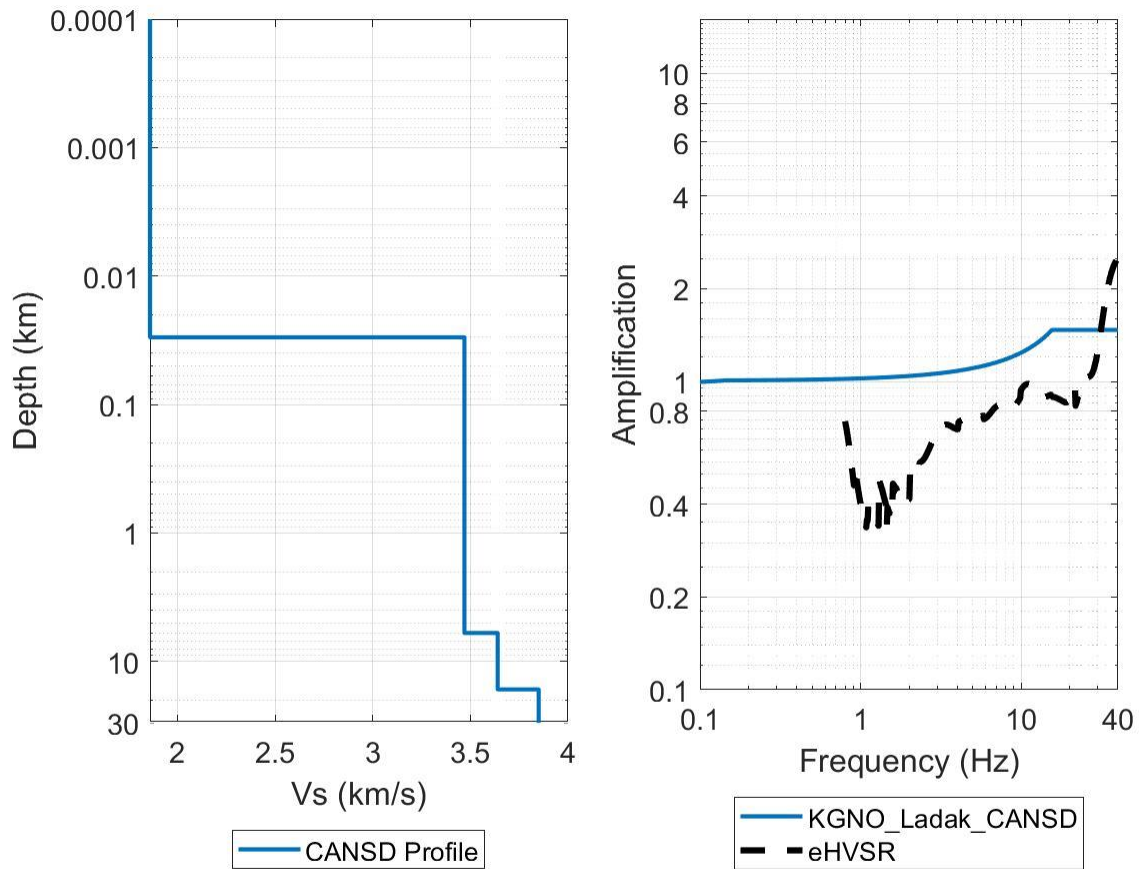|											
0.899	0.0061	0.899	0.0061	0.899	0.0061			3.89025	31.51		
0.899	0.0122	0.899	0.0122	0.899	0.0122						
1.021	0.0122	1.021	0.0122	1.021	0.0122						
1.021	0.029	1.021	0.029	1.021	0.029						
1.524	0.029	1.524	0.029	1.524	0.029						
1.524	0.0665	1.524	0.0665	1.524	0.0665						
3.47	0.0665	2.78075	0.0665	1.9	0.0665						
3.47	6	3.17375	6.135	2.9	1.5						
3.64	6	3.17175	8.76	3	12						
3.64	16.5	3.38225	15.74	3.2	12						
3.85	16.5	3.28275	17.74	2.9	20						
3.85	35.2	3.431	31.51	3.1	37						
		3.89025	31.51								
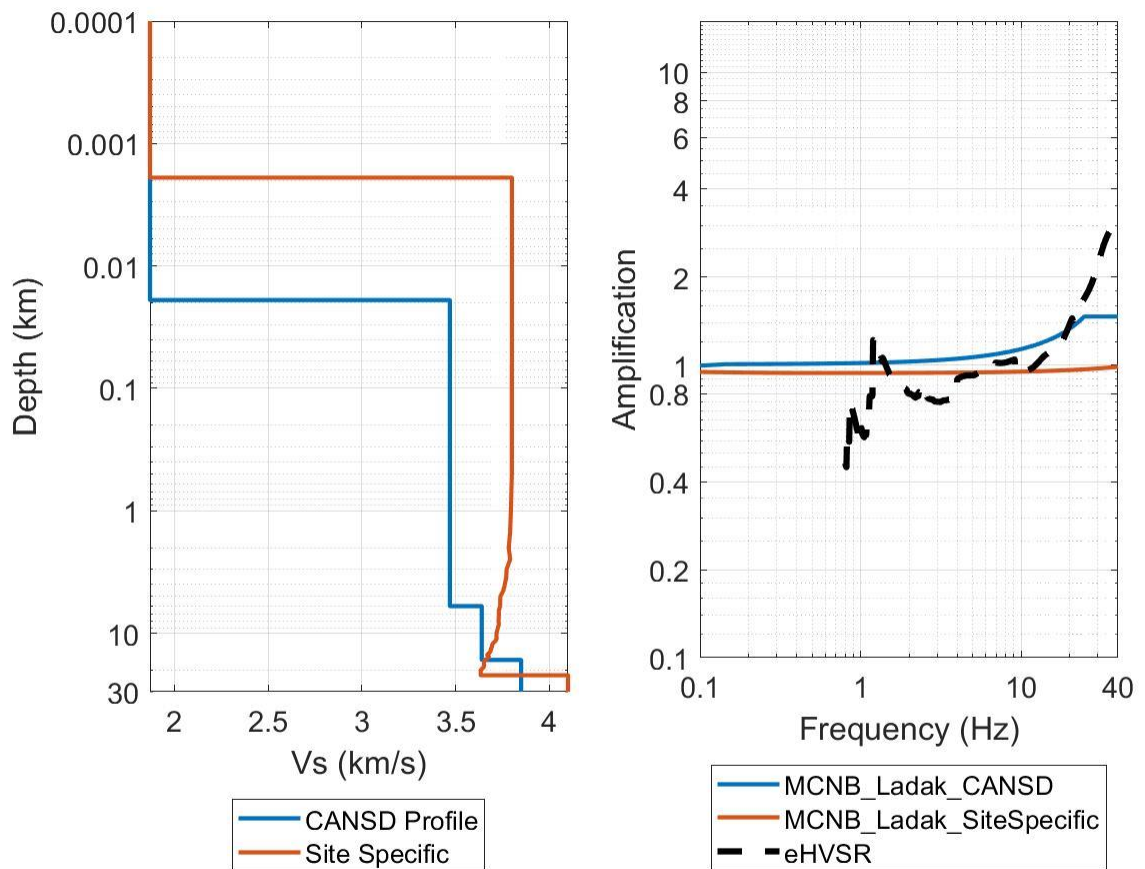
Figure A18: Station MCNB velocity profile, on the left, and resultant amplification profile on the right for 2 different types of profiles – a region wide, and a site-specific profile (solid lines) (Brune and Dorman, 1963; Kuponiyi et al., 2016; Ladak, 2020; Ladak et al., 2021) and the horizontal to vertical spectral ratio from earthquake (black dashed) data.

Table A18: Station MCNB combined velocity profiles (Brune and Dorman, 1963; Kuponiyi et al., 2016; Ladak, 2020; Ladak et al. 2021).

CANSD Profile		Site-specific		Site-specific Cont'd	
Vs (km/s)	Depth (km)	Vs (km/s)	Depth (km)	Vs (km/s)	Depth (km)
1.870467	0	1.870467	0	3.6598	16.5
1.870467	0.0001	1.870467	0.0001	3.6524	17
1.870467	0.019	1.870467	0.0019	3.6515	17.5
3.47	0.019	3.801	0.0019	3.652	18
3.47	6	3.8006	0.5	3.652	18.5
3.64	6	3.7954	1	3.6492	19
3.64	16.5	3.7912	1.5	3.6409	19.5
3.85	16.5	3.784	2	3.6345	20
3.85	35.2	3.7916	2.5	3.6345	22
		3.7725	3	4.1	22
		3.7707	3.5	4.1	43.3
		3.763	4	4.7	43.3
		3.7545	4.5		
		3.7392	5		
		3.7383	5.5		
		3.7383	6		
		3.7309	6.5		
		3.7314	7		
		3.7306	7.5		
		3.7295	8		
		3.7314	8.5		
		3.7258	9		
		3.7219	9.5		

		3.719	10		
		3.718	10.5		
		3.7196	11		
		3.7143	11.5		
		3.7013	12		
		3.6951	12.5		
		3.6939	13		
		3.6879	13.5		
		3.6879	14		
		3.6791	14.5		
		3.6686	15		
		3.6786	15.5		
		3.6702	16		
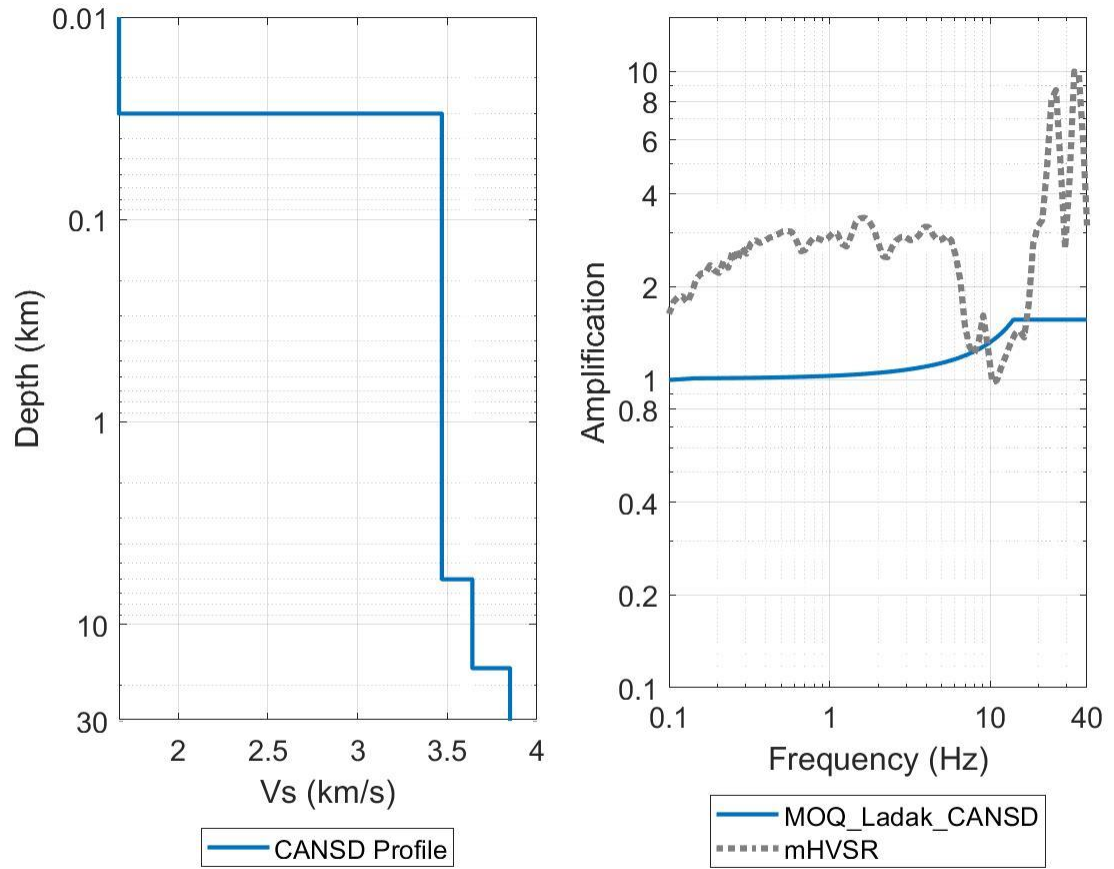
Figure A19: Station MOQ velocity profile, on the left, and resultant amplification profile on the right for 1 profile – a region wide profile (solid line) (Brune and Dorman, 1963; Ladak, 2020; Ladak et al., 2021) and the horizontal to vertical spectral ratio from earthquake (black dashed) and microtremor (grey dotted) (Ladak, 2020; Ladak et al., 2021) data.

**Table A19: Station MOQ combined velocity profile (Brune and Dorman, 1963; Ladak, 2020; Ladak et al. 2021).**

| CANSD Profile	
Vs (km/s)	*Depth (km)*
1.671	0
1.671	0.01
1.671	0.03
3.47	0.03
3.47	6
3.64	6
3.64	16.5
3.85	16.5
3.85	35.2
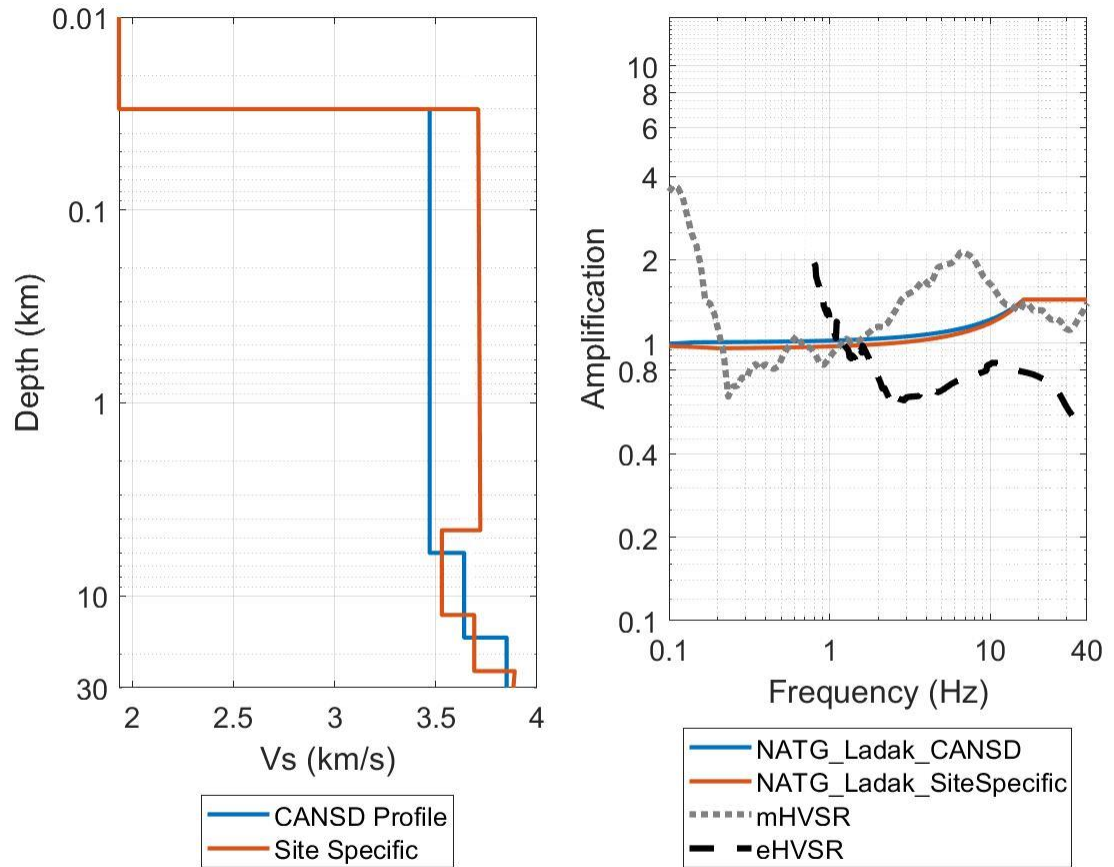
Figure A20: Station NATG velocity profile, on the left, and resultant amplification profile on the right for 2 different types of profiles – a region wide, and a site-specific profile (solid lines) (Kao et al, 2014; Brune and Dorman, 1963; Ladak, 2020; Ladak et al., 2021) and the horizontal to vertical spectral ratio from earthquake (black dashed) and microtremor (grey dotted) (Ladak, 2020; Ladak et al., 2021) data.

Table A20: Station NATG combined velocity profiles (Kao et al, 2014; Brune and Dorman, 1963; Ladak, 2020; Ladak et al. 2021).

CANSD Profile		Site-specific	
Vs (km/s)	Depth (km)	Vs (km/s)	Depth (km)
1.935	0	1.935	0
1.935	0.01	1.935	0.01
1.935	0.03	1.935	0.03
3.47	0.03	3.71	0.03
3.47	6	3.72	4.58
3.64	6	3.53	4.58
3.64	16.5	3.53	12.59
3.85	16.5	3.69	12.59
3.85	35.2	3.69	24.61
		3.89	24.61
		3.88	33.12
		3.75	33.12
		3.76	46.18
		4.5	46.18

Figure A21: Station ORIO velocity profile, on the left, and resultant amplification profile on the right for 1 profile – a region wide profile (solid line) (Brune and Dorman, 1963; Ladak, 2020; Ladak et al., 2021) and the horizontal to vertical spectral ratio from earthquake (black dashed) and microtremor (grey dotted) (Ladak, 2020; Ladak et al., 2021) data.

Table A21: Station ORIO combined velocity profile (Brune and Dorman, 1963; Ladak, 2020; Ladak et al. 2021).

CANSD Profile	
Vs (km/s)	*Depth (km)*
1.57	0
1.57	0.001
1.57	0.03
3.47	0.03
3.47	6
3.64	6
3.64	16.5
3.85	16.5
3.85	35.2
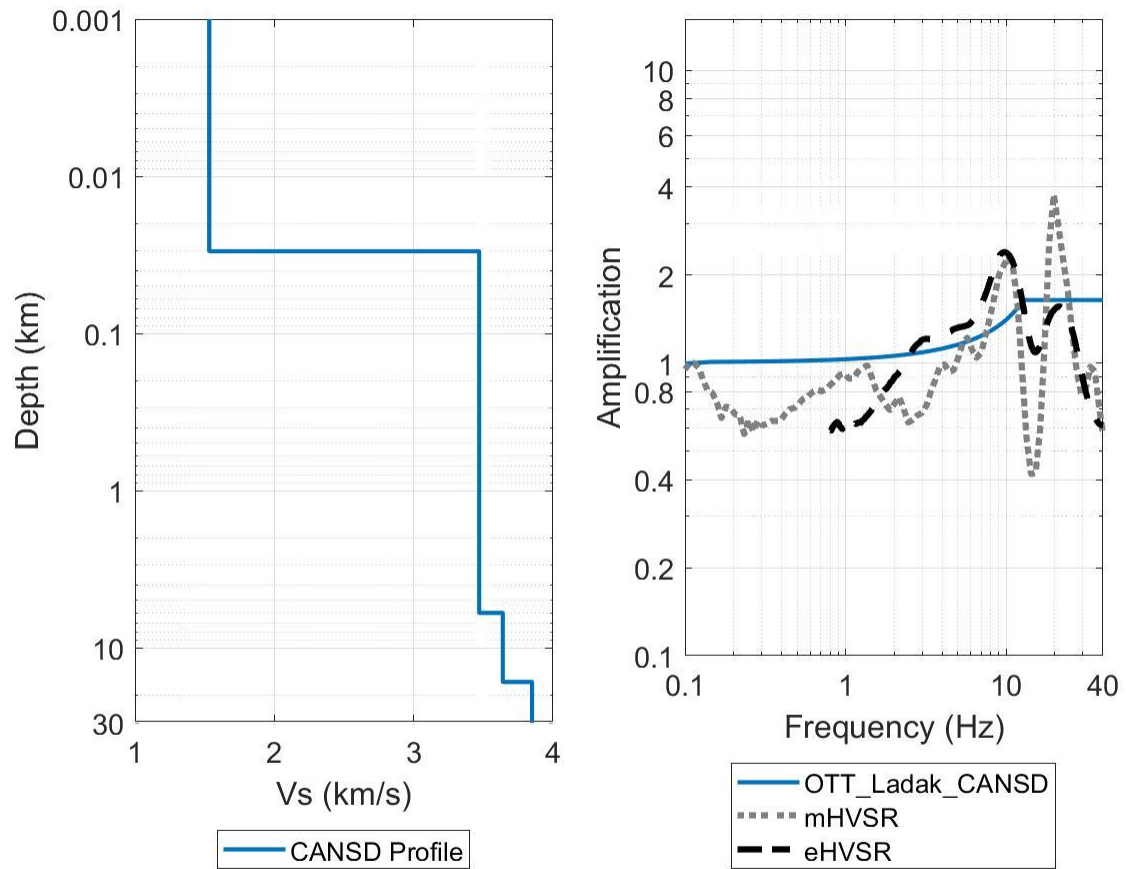
Figure A22: Station OTT velocity profile, on the left, and resultant amplification profile on the right for 1 profile – a region wide profile (solid line) (Brune and Dorman, 1963; Ladak, 2020; Ladak et al., 2021) and the horizontal to vertical spectral ratio from earthquake (black dashed) and microtremor (grey dotted) (Ladak, 2020; Ladak et al., 2021) data.

Table A22: Station OTT combined velocity profile (Brune and Dorman, 1963; Ladak, 2020; Ladak et al. 2021).

| CANSD Profile	
Vs (km/s)	*Depth (km)*
1.533	0
1.533	0.001
1.533	0.03
3.47	0.03
3.47	6
3.64	6
3.64	16.5
3.85	16.5
3.85	35.2
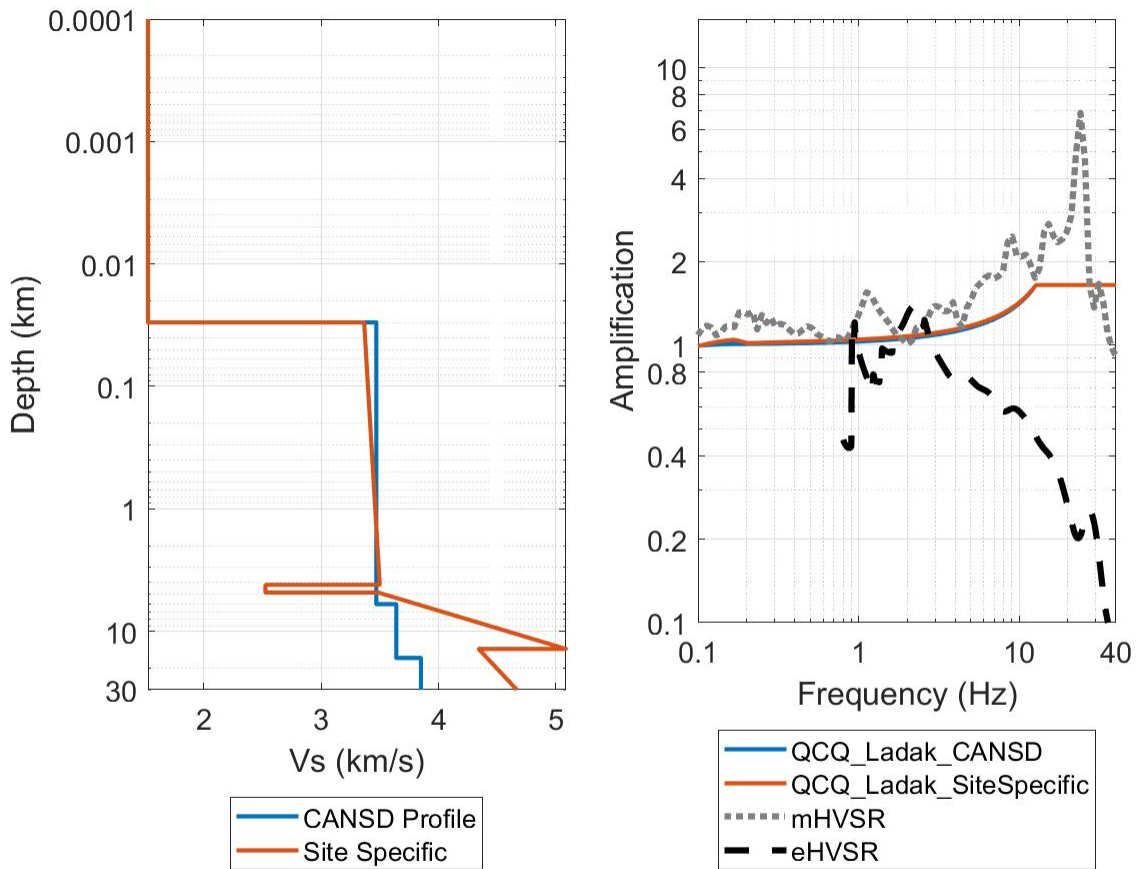
Figure A23: Station QCQ velocity profile, on the left, and resultant amplification profile on the right for 2 different types of profiles – a region wide, and a site-specific profile (solid lines) (Bent and Kao, 2015; Brune and Dorman, 1963; Ladak, 2020; Ladak et al., 2021) and the horizontal to vertical spectral ratio from earthquake (black dashed) and microtremor (grey dotted) (Ladak, 2020; Ladak et al., 2021) data.

Table A23: Station QCQ combined velocity profiles (Bent and Kao, 2015; Brune and Dorman, 1963; Ladak, 2020; Ladak et al. 2021).

CANSD Profile		Site-specific	
Vs (km/s)	Depth (km)	Vs (km/s)	Depth (km)
1.523	0	1.523	0
1.523	0.0001	1.523	0.0001
1.523	0.03	1.523	0.03
3.47	0.03	3.366	0.03
3.47	6	3.499	4.17
3.64	6	2.525	4.17
3.64	16.5	2.524	4.82
3.85	16.5	3.484	4.82
3.85	35.2	5.087	13.93
		4.342	13.93
		4.679	30.8
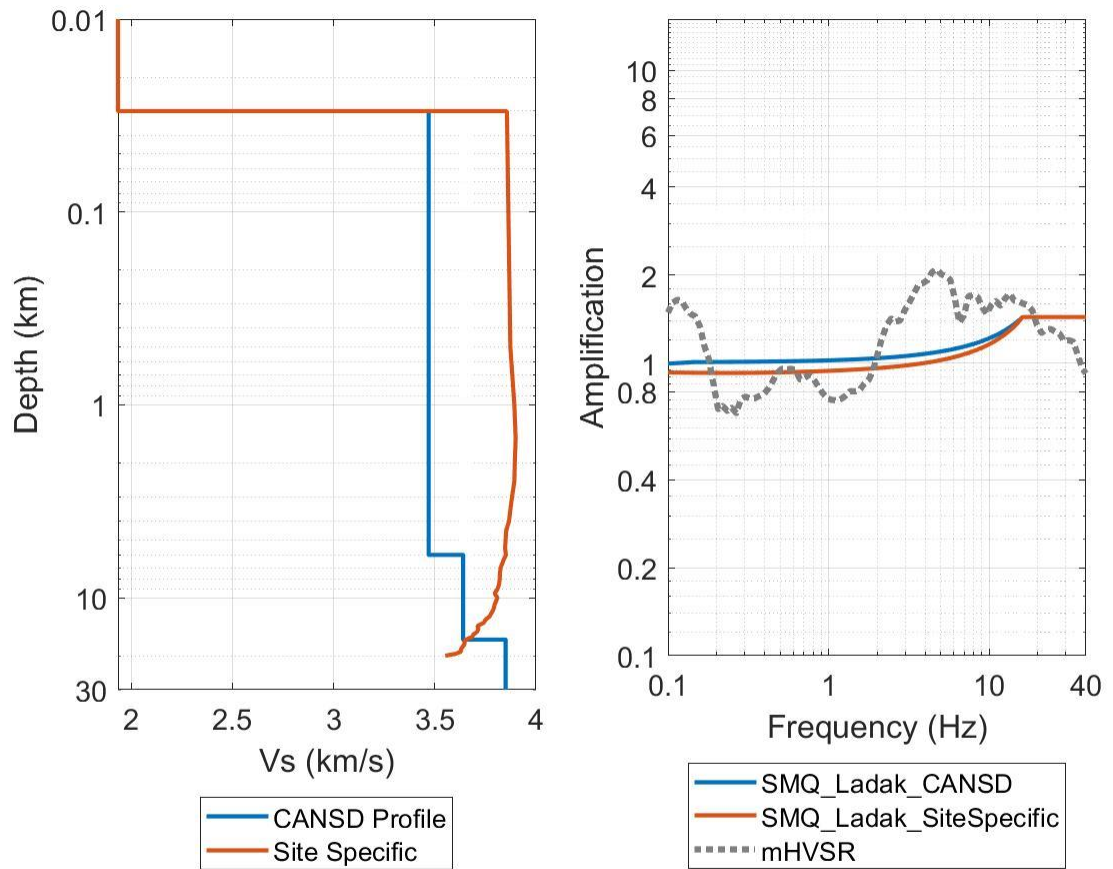
Figure A24: Station SMQ velocity profile, on the left, and resultant amplification profile on the right for 2 different types of profiles – a region wide, and a site-specific profile (solid lines) (Brune and Dorman, 1963; Kuponiyi et al., 2016; Ladak, 2020; Ladak et al., 2021) and the horizontal to vertical spectral ratio from microtremor (grey dotted) (Ladak, 2020; Ladak et al., 2021) data.

Table A24: Station SMQ combined velocity profiles (Brune and Dorman, 1963; Kuponiyi et al., 2016; Ladak, 2020; Ladak et al. 2021).
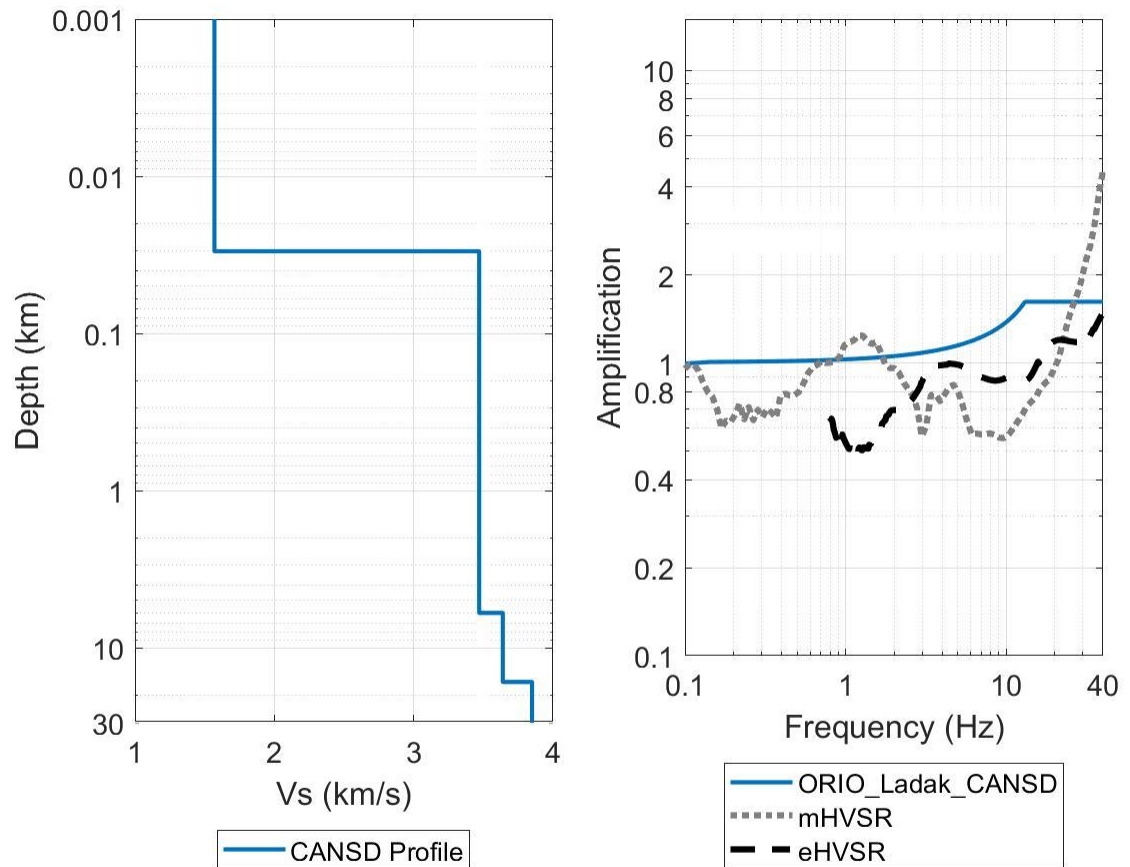
CANSD Profile		Site-specific		Site-specific Continued	
Vs (km/s)	*Depth (km)*	*Vs (km/s)*	*Depth (km)*	*Vs (km/s)*	*Depth (km)*
1.935	0	1.935	0	3.6832	16
1.935	0.01	1.935	0.01	3.6525	16.5
1.935	0.03	1.935	0.03	3.647	17
3.47	0.03	3.8563	0.03	3.646	17.5
3.47	6	3.8732	0.5	3.6366	18
3.64	6	3.8931	1	3.6296	18.5
3.64	16.5	3.8995	1.5	3.6296	19
3.85	16.5	3.8952	2	3.6057	19.5
3.85	35.2	3.8931	2.5	3.5517	20
		3.8816	3		
		3.8733	3.5		
		3.8669	4		
		3.8525	4.5		
		3.85	5		
		3.8472	5.5		
		3.8512	6		
		3.8366	6.5		
		3.8253	7		
		3.8216	7.5		
		3.821	8		
		3.8176	8.5		
		3.8105	9		
		3.7957	9.5		

		3.8098	10		
		3.8014	10.5		
		3.7939	11		
		3.7902	11.5		
		3.78	12		
		3.771	12.5		
		3.7507	13		
		3.7417	13.5		
		3.7111	14		
		3.7157	14.5		
		3.7093	15		
		3.6918	15.5		
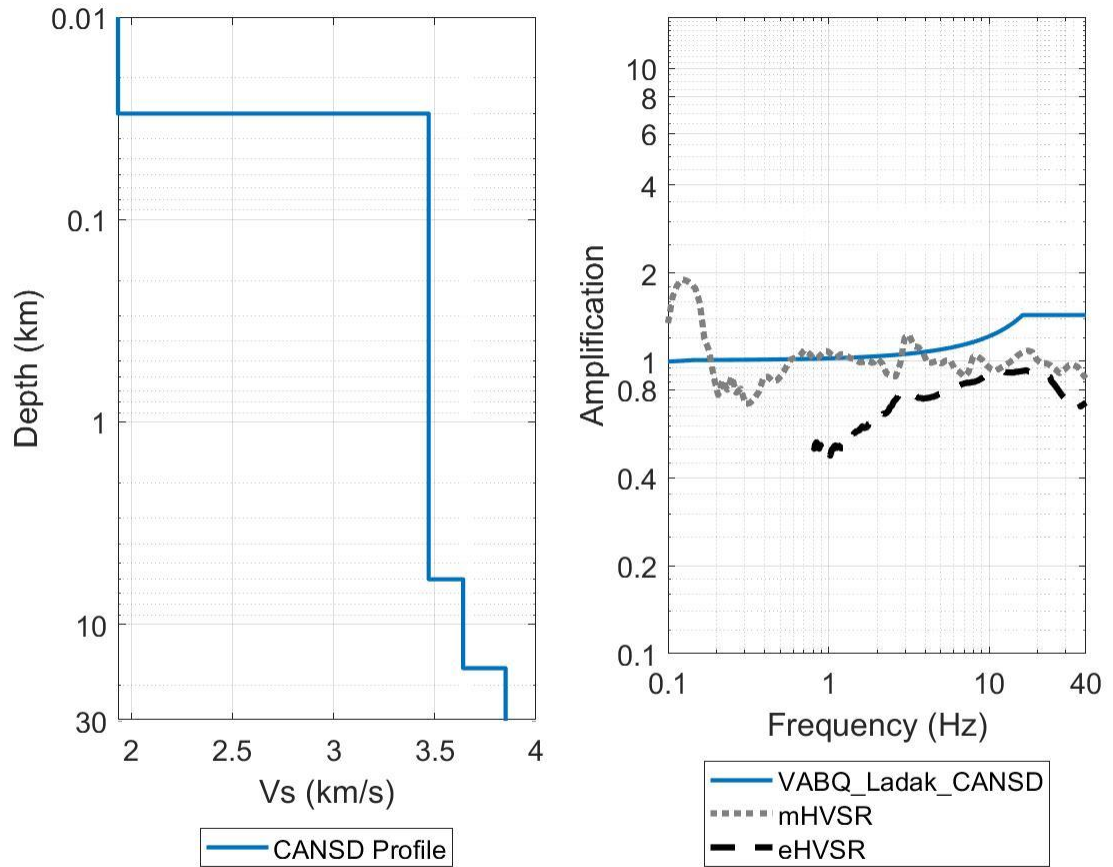
Figure A25: Station VABQ velocity profile, on the left, and resultant amplification profile on the right for 1 profile – a region wide profile (solid line) (Brune and Dorman, 1963; Ladak, 2020; Ladak et al., 2021) and the horizontal to vertical spectral ratio from earthquake (black dashed) and microtremor (grey dotted) (Ladak, 2020; Ladak et al., 2021) data.

Table A25: Station VABQ combined velocity profiles (Brune and Dorman, 1963; Ladak, 2020; Ladak et al. 2021).

| CANSD Profile	
Vs (km/s)	*Depth (km)*
1.935	0
1.935	0.01
1.935	0.03
3.47	0.03
3.47	6
3.64	6
3.64	16.5
3.85	16.5
3.85	35.2

Average regional profiles were generated in Charlevoix to examine any potential shift in kappa due to the lower crustal profiles.
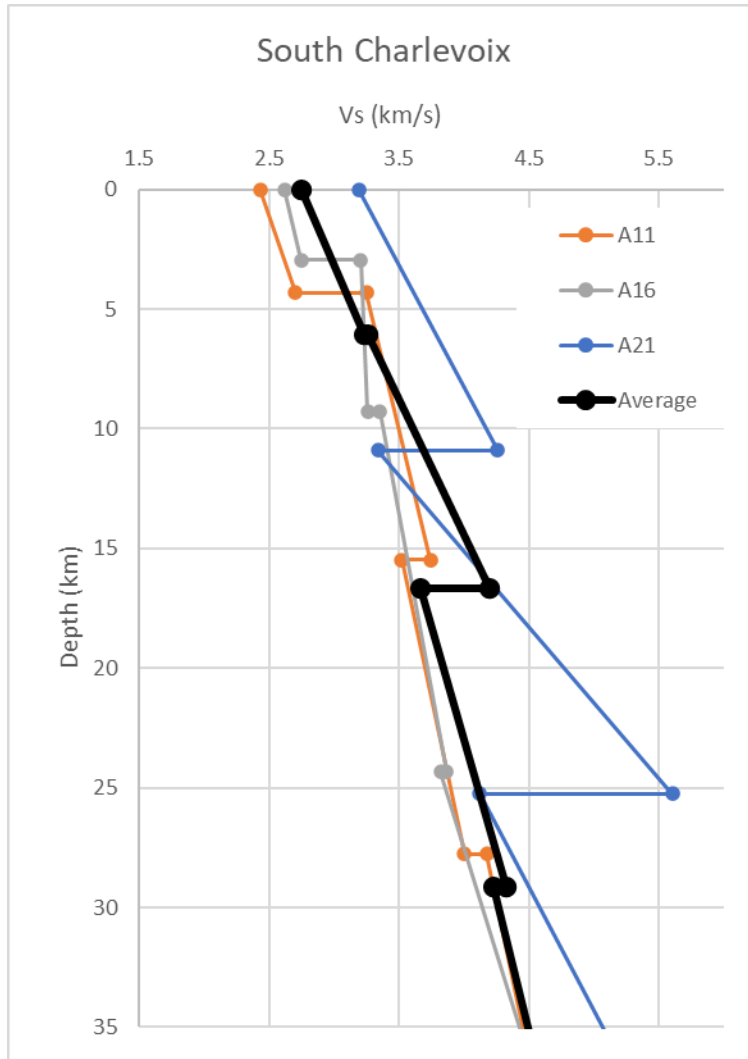
Figure A26: Average Palaeozoic Crustal Profile from Charlevoix Stations A11, A16 and A21 (generated from Bent and Kao (2015) profiles).

Table A26: Mean South Charlevoix Crustal Profile (Bent and Kao, 2015).

Mean South Charlevoix	
Depth (km)	*Vs (km/s)*
0	2.748
6.056667	3.236
6.056667	3.264667
16.67667	4.202333
16.67667	3.666667
29.13333	4.322
29.13333	4.231333
47.66	5.064333
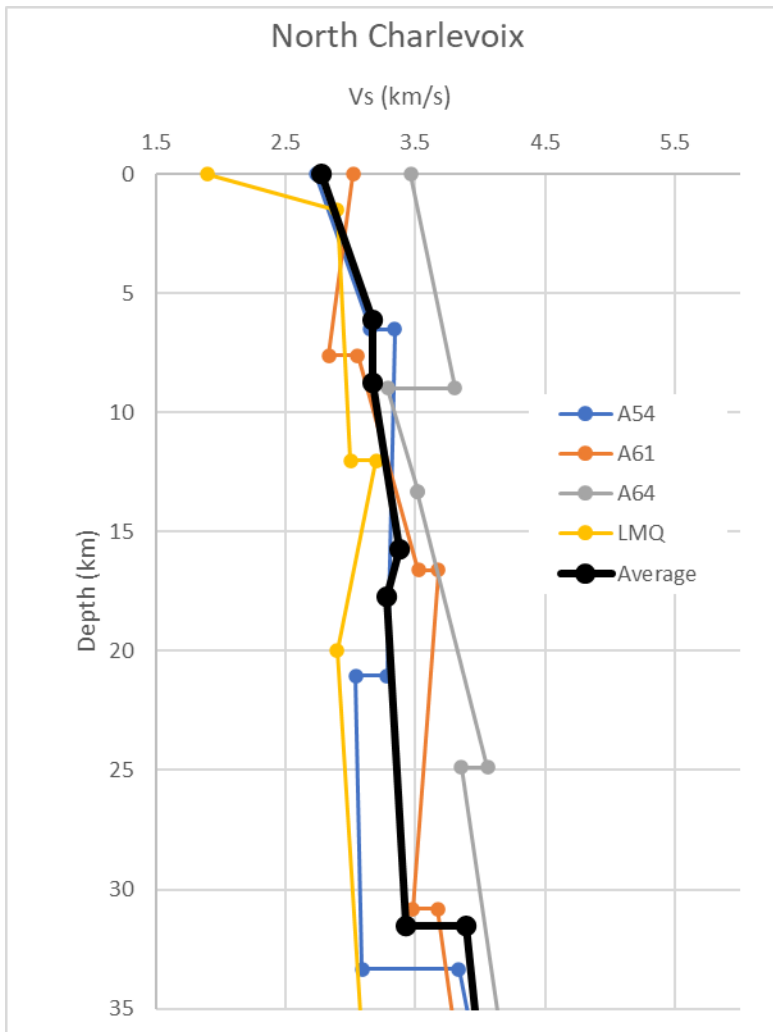
Figure A27: Average Precambrian Crustal Profile from Charlevoix Stations A54, A61, A64 and LMQ (generated from Bent et al. (2019) and personal communication with Bent profiles).

Table A27: Mean North Charlevoix Crustal Profile (Bent et al., 2019; personal communication Bent).

Mean North Charlevoix	
Depth (km)	*Vs (km/s)*
0	2.78075
6.135	3.17375
8.76	3.17175
15.74	3.38225
17.74	3.28275
31.51	3.431
31.51	3.89025
61.8675	4.47625

Table A28: Mean vertical component station-specific kappa using an inversion (κ) and an inversion followed by a constrained source parameter inversion (κ$_{con}$) with the associated standard deviation. Each section is headed with the deeper velocity profile provided by CANSD (Brune and Dorman, 1963) or Site-Specific models (Bent and Kao, 2015; Bent et al., 2019; personal communication Bent; Kao, 2014; Cassidy, 1995; Kuponiyi et al., 2016), then the shallow profile of either Stokoe (Stokoe et al., 2021) or Ladak (Ladak, 2020; Ladak et al. 2021) which is followed by the kappa results. N/A signifies there were either no records for the station, no velocity profile, or not a sufficient number of records to obtain a mean and standard deviation for kappa.

| | | | CANSD | | | | | | | |
| | | | Ladak | | | | Stokoe | | | |
Station	No. Rec	No. Rec Iteration	κ (ms)	κ^{std} (ms)	κ$_{con}$ (ms)	κ$_{con}^{std}$ (ms)	κ (ms)	κ^{std} (ms)	κ$_{con}$ (ms)	κ$_{con}^{std}$ (ms)
A11	724	719	N/A	N/A	N/A	N/A	-16.8	7.8	3.3	7.4
A16	820	817	-19.4	14.1	-7.0	8.2	-19.4	14.1	-8.3	8.5
A21	735	722	N/A	N/A	N/A	N/A	10.6	6.6	-1.1	11.2
A54	833	828	-11.0	12.3	-12.9	8.3	-11.0	12.3	-14.3	8.4
A61	822	817	-5.7	11.0	-0.1	8.6	-5.7	11.0	-1.3	9.1
A64	798	792	-9.5	11.6	-6.8	7.0	-9.5	11.6	-7.9	7.3
BATG	183	0	-27.7	10.4	N/A	N/A	N/A	N/A	N/A	N/A

BCLQ	303	294	-10.2	7.7	-3.5	8.6	N/A	N/A	N/A	N/A
CNQ	589	476	-4.7	6.2	-8.9	6.3	N/A	N/A	N/A	N/A
DAQ	593	574	-3.4	7.2	-10.2	6.7	N/A	N/A	N/A	N/A
DPQ	247	112	-8.6	8.5	-11.6	8.5	N/A	N/A	N/A	N/A
GAC	1019	218	5.3	13.7	2.7	12.7	N/A	N/A	N/A	N/A
GBN	8	0	-0.1	11.9	N/A	N/A	N/A	N/A	N/A	N/A
GSQ	566	438	-13.4	9.7	-0.1	5.8	N/A	N/A	N/A	N/A
ICQ	220	186	-5.7	8.5	-5.5	6.0	N/A	N/A	N/A	N/A
KGNO	12	7	-25.1	16.4	-14.9	16.4	N/A	N/A	N/A	N/A
LMQ	260	260	-1.7	7.9	-13.1	7.6	-1.7	7.9	-13.6	7.5
MCNB	55	0	-20.2	13.9	N/A	N/A	N/A	N/A	N/A	N/A
MOQ	232	63	-7.8	11.6	-2.6	8.0	N/A	N/A	N/A	N/A
NATG	57	0	-3.2	12.9	N/A	N/A	N/A	N/A	N/A	N/A
ORIO	98	75	-8.4	8.0	-7.5	7.1	N/A	N/A	N/A	N/A
OTT	550	190	-3.9	10.3	-11.0	10.8	N/A	N/A	N/A	N/A
QCQ	171	168	-9.3	16.3	6.7	9.1	N/A	N/A	N/A	N/A
SMQ	662	448	-7.5	7.3	-9.3	6.3	N/A	N/A	N/A	N/A
VABQ	294	137	-15.9	8.8	-8.4	7.9	N/A	N/A	N/A	N/A

Station	No. Rec	No. Rec Iteration	κ (ms)	κ^{std} (ms)	κ$_{con}$ (ms)	κ$_{con}^{std}$ (ms)	κ (ms)	κ^{std} (ms)	κ$_{con}$ (ms)	κ$_{con}^{std}$ (ms)
Charlevoix North										
			Ladak				**Stokoe**			
A54	833	751	-11.0	12.3	-12.0	9.3	-11.0	12.3	-12.0	9.3
A61	822	755	-5.7	11.0	0.7	8.4	-5.7	11.0	0.7	8.4
A64	798	748	-9.5	11.6	-5.9	8.2	-9.5	11.6	-5.9	8.2
LMQ	260	249	-1.7	7.9	-9.8	7.4	-1.7	7.9	-9.8	7.4
Charlevoix South										
			Ladak				**Stokoe**			
A11	724	615	N/A	N/A	N/A	N/A	-16.8	7.8	-1.2	9.0
A16	820	615	-19.4	14.1	N/A	N/A	-19.4	14.1	-13.0	9.6
A21	735	615	N/A	N/A	N/A	N/A	10.6	6.6	-6.5	9.4
Site-specific										
			Ladak				**Stokoe**			

		Iteration								
A11	724	719	N/A	N/A	N/A	N/A	-16.8	7.8	3.3	7.4
A16	820	817	-19.4	14.1	-8.5	8.8	-19.4	14.1	-8.3	8.5
A21	735	722	N/A	N/A	N/A	N/A	10.6	6.6	-1.1	11.2
A54	833	825	-11.0	12.3	-14.3	8.9	-11.0	12.3	-14.3	8.4
A61	822	815	-5.7	11.0	-1.6	8.6	-5.7	11.0	-1.3	9.1
A64	798	791	-9.5	11.6	-8.3	7.7	-9.5	11.6	-7.9	7.3
BATG	183	0	-27.7	10.4	N/A	N/A	N/A	N/A	N/A	N/A
BCLQ	303	284	-10.2	7.7	-4.4	8.8	N/A	N/A	N/A	N/A
CNQ	589	476	-4.7	6.2	-8.9	6.3	N/A	N/A	N/A	N/A
DPQ	247	64	-8.6	8.5	-12.2	8.1	N/A	N/A	N/A	N/A
GAC	1019	0	5.3	13.7	N/A	N/A	N/A	N/A	N/A	N/A
GBN	8	0	-0.1	11.9	N/A	N/A	N/A	N/A	N/A	N/A
GSQ	566	438	-13.4	9.7	-0.1	5.8	N/A	N/A	N/A	N/A
ICQ	220	186	-5.7	8.5	-5.5	6.0	N/A	N/A	N/A	N/A
LMQ	260	260	-1.7	7.9	-13.6	7.7	-1.7	7.9	-13.6	7.5
MCNB	55	0	-20.2	13.9	N/A	N/A	N/A	N/A	N/A	N/A
NATG	57	0	-3.2	12.9	N/A	N/A	N/A	N/A	N/A	N/A

| QCQ | 171 | 163 | -9.3 | 16.3 | 5.7 | 9.1 | N/A | N/A | N/A | N/A |
| SMQ | 662 | 448 | -7.5 | 7.3 | -9.3 | 6.3 | N/A | N/A | N/A | N/A |

Table A29: Mean horizontal (EAS) component station-specific kappa using an inversion (κ) and an inversion followed by a constrained source parameter inversion (κ$_{con}$) with the associated standard deviation. Each section is headed with the deeper velocity profile provided by CANSD (Brune and Dorman, 1963) or Site-specific models (Bent and Kao, 2015; Bent et al., 2019; personal communication Bent; Kao, 2014; Cassidy, 1995; Kuponiyi et al., 2016), then the shallow profile of either Stokoe (Stokoe et al., 2021) or Ladak (Ladak, 2020; Ladak et al. 2021) which is followed by the kappa results. N/A signifies there were either no records for the station or not a sufficient number of records to obtain a mean and standard deviation for kappa.

| | | | CANSD | | | | | | | |
| | | | Ladak | | | | Stokoe | | | |
Station	No. Rec	No. Rec Iteration	κ (ms)	κ^{std} (ms)	κ$_{con}$ (ms)	κ$_{con}$^{std} (ms)	κ (ms)	κ^{std} (ms)	κ$_{con}$ (ms)	κ$_{con}$^{std} (ms)
A11	724	718	N/A	N/A	N/A	N/A	-3.6	8.3	9.0	6.8
A16	821	818	-0.6	10.1	-1.8	6.8	3.3	10.6	7.4	7.4
A21	732	720	N/A	N/A	N/A	N/A	21.4	6.0	3.9	10.6
A54	828	817	-9.6	9.8	0.7	6.9	-4.8	9.3	3.6	7.0
A61	820	807	0.4	7.5	-3.4	7.5	6.5	11.0	11.3	7.1
A64	800	779	-1.3	10.9	-1.2	6.9	-3.2	7.7	-7.9	6.8
BATG	181	0	-6.9	9.6	N/A	N/A	N/A	N/A	N/A	N/A
BCLQ	306	276	-7.8	7.9	-3.8	6.7	N/A	N/A	N/A	N/A

CNQ	0	0	N/A	N/A	N/A	N/A	N/A	N/A	N/A	N/A
DAQ	0	0	N/A	N/A	N/A	N/A	N/A	N/A	N/A	N/A
DPQ	66	20	-12.8	9.2	-13.9	9.1	N/A	N/A	N/A	N/A
GAC	159	90	-17.0	15.3	-9.1	9.9	N/A	N/A	N/A	N/A
GBN	8	0	-0.5	4.8	N/A	N/A	N/A	N/A	N/A	N/A
GSQ	0	0	N/A	N/A	N/A	N/A	N/A	N/A	N/A	N/A
ICQ	43	0	-7.6	8.1	N/A	N/A	N/A	N/A	N/A	N/A
KGNO	18	8	-19.5	19.8	-7.8	19.6	N/A	N/A	N/A	N/A
LMQ	260	260	-9.3	9.2	-4.9	6.4	0.4	8.9	8.5	6.8
MCNB	56	0	-25.3	16.2	N/A	N/A	N/A	N/A	N/A	N/A
MOQ	0	0	N/A	N/A	N/A	N/A	N/A	N/A	N/A	N/A
NATG	57	0	-7.8	11.7	N/A	N/A	N/A	N/A	N/A	N/A
ORIO	101	79	-20.4	8.2	-7.4	8.0	N/A	N/A	N/A	N/A
OTT	450	87	1.8	8.8	-13.7	9.1	N/A	N/A	N/A	N/A
QCQ	9	7	10.0	14.7	9.3	9.1	N/A	N/A	N/A	N/A
SMQ	0	0	N/A	N/A	N/A	N/A	N/A	N/A	N/A	N/A
VABQ	294	37	-7.5	7.9	-2.5	7.7	N/A	N/A	N/A	N/A
			Charlevoix North							

			Ladak				Stokoe			
Station	No. Rec	No. Rec Iteration	κ (ms)	κ^{std} (ms)	κ_{con} (ms)	κ_{con}^{std} (ms)	κ (ms)	κ^{std} (ms)	κ_{con} (ms)	κ_{con}^{std} (ms)
A54	828	750	-8.7	10.3	0.1	6.7	-4.6	9.5	1.8	6.8
A61	820	754	-0.3	7.1	-4.1	6.8	7.3	10.0	9.0	6.7
A64	800	747	-1.0	9.8	-1.9	6.8	-3.5	7.7	-8.6	6.9
LMQ	260	249	-8.0	9.2	-5.4	6.2	0.9	8.4	6.7	6.7
			Charlevoix South							
			Ladak				**Stokoe**			
Station	No. Rec	No. Rec Iteration	κ (ms)	κ^{std} (ms)	κ_{con} (ms)	κ_{con}^{std} (ms)	κ (ms)	κ^{std} (ms)	κ_{con} (ms)	κ_{con}^{std} (ms)
A11	724	614	N/A	N/A	N/A	N/A	-3.9	8.3	12.2	7.2
A16	821	614	-0.6	10.1	N/A	N/A	4.6	10.2	8.7	7.6
A21	732	614	N/A	N/A	N/A	N/A	21.3	6.0	5.0	9.9
			Site-specific							
			Ladak				**Stokoe**			
Station	No. Rec	No. Rec Iteration	κ (ms)	κ^{std} (ms)	κ_{con} (ms)	κ_{con}^{std} (ms)	κ (ms)	κ^{std} (ms)	κ_{con} (ms)	κ_{con}^{std} (ms)

A11	724	718	N/A	N/A	N/A	N/A	-4.0	8.3	11.5	6.7
A16	821	818	-0.7	10.2	-0.1	6.7	4.8	10.0	7.4	7.3
A21	732	720	N/A	N/A	N/A	N/A	21.3	6.0	4.1	10.4
A54	828	817	-8.7	10.3	0.4	6.8	-4.6	9.6	3.7	6.8
A61	820	807	0.01	7.2	-3.9	7.3	7.1	10.5	11.0	7.0
A64	800	779	-1.3	10.9	-2.0	6.9	-3.2	7.7	-8.3	6.6
BATG	181	0	-6.3	9.6	N/A	N/A	N/A	N/A	N/A	N/A
BCLQ	306	276	-9.0	7.9	-3.8	6.7	N/A	N/A	N/A	N/A
DPQ	66	16	-13.1	9.3	-12.3	6.6	N/A	N/A	N/A	N/A
GAC	159	0	-17.3	15.3	N/A	N/A	N/A	N/A	N/A	N/A
GBN	8	0	-0.6	4.7	N/A	N/A	N/A	N/A	N/A	N/A
ICQ	43	0	-5.6	8.9	N/A	N/A	N/A	N/A	N/A	N/A
LMQ	260	260	-7.2	8.4	-5.0	6.3	1.5	7.9	8.4	6.6
MCNB	56	0	-28.1	16.0	N/A	N/A	N/A	N/A	N/A	N/A
NATG	57	0	-7.6	11.8	N/A	N/A	N/A	N/A	N/A	N/A
QCQ	9	7	9.9	14.6	7.7	9.2	N/A	N/A	N/A	N/A

Curriculum Vitae

Name:	Samantha Palmer
Post-secondary Education and Degrees:	University of Victoria Victoria, British Columbia, Canada 2010-2016 B.Sc. Combined Honours in Physic and Earth Science. The University of Western Ontario London, Ontario, Canada 2016-2022 Ph.D.
Honours and Awards:	Province of Ontario Graduate Scholarship 2018-2019, 2019-2020, 2020 - 2021 Western Graduate Research Scholarship 2016-2017, 2017-2018, 2018-2019, 2019-2020, 2020-2021 Seismological Society of America Student Presentation Award 2019-2020 Seismological Society of America 2019 Travel Grant 2019-2020 Robert W. Hodder Travel Bursary 2019-2020 Chevron Canada Outstanding Student Paper in Seismology 2018-2019
Related Work Experience	Teaching Assistant/Research Assistant The University of Western Ontario 2016-2022 Teaching Assistant University of Victoria 2015-2016 Seismic Analyst Natural Resources of Canada – Pacific Geoscience Center

2015, 2018

Publications:

Palmer, S.M. and G.M. Atkinson (XXXX) This high frequency spectral decay, kappa, in eastern Canada determined with a broadband inversion approach, Bull. Seismol. Soc. Am.

Palmer S.M., Atkinson G.M., Ladak, S., Molnar, S. and Ghofrani H. (XXXX) Earthquake ground motion and site characterization database for earthquakes in eastern Canada. Earthquake Spectra.

Palmer, S.M., G.M. Atkinson, S. Ladak, S. Molnar, and H. Ghofrani (2022) Eastern Canada earthquake ground motion and site characterization database. DesignSafe, doi: 10.17603/ds2-3b7s-yw72.

Palmer, S.M., G.M. Atkinson, S. Ladak, S. Molnar (2021) CNSC final project report: High frequency ground motion characteristics for rock site. Canadian Nuclear Safety Commission internal document report.

Ladak, S., S. Molnar, and **S.M. Palmer** (2021) Multimethod site characterization to verify the hard rock (site class A) assumption at 25 seismograph stations across eastern Canada, Earthquake Spectra 37, 1487–1515. doi: 10.1177/87552930211001076

Palmer, S.M. and G.M. Atkinson (2020) High frequency decay slope of spectra (kappa) for M≥3.5 earthquakes on rock sites in eastern and western Canada, Bull. Seism. Am. 110(2), 471-488. doi: 10.1785/0120190206

Palmer, S.M. (2016) Earthquakes in the Juan de Fuca Strait (2007-2015). University of Victoria Undergraduate Honours Thesis, Institutional B.Sc. Honours Thesis.

Conference Publications:

Palmer, S.M. and G.M. Atkinson (2021) Kappa on rock sites in eastern Canada. OECD NEA Kappa Workshop Videoconference via Zoom, May 25-28. Co-oral Presentation with Dr. Gail Atkinson.

Palmer, S.M. and G.M. Atkinson (2019) High-frequency ground motion effects for rock sites in Cascadia vs eastern Canada. PGC Site Characterization Workshop Sidney British Columbia Canada, October 1. Oral Presentation

Palmer, S.M. and G.M. Atkinson (2019) An overview of high frequency ground motion characteristics of rock sites in eastern Canada. Proceedings of SMIRT 25 Division IV Charlotte NC USA, August 4-9. Oral Presentation.

Ladak, S., S. Molnar, **S.M. Palmer**, and G.M. Atkinson (2019) Earthquake site characterization at seismograph stations in eastern Canada, Proceedings of the 12th Canadian Conference on Earthquake Engineering Quebec City Quebec Canada, June 17-20. Oral Presentation by Sameer Ladak.

Ladak, S., S. Molnar, **S.M. Palmer** and G.M. Atkinson (2018) Application of non-invasive active and passive methods for determining the shear wave velocity profile at hard rock sites in eastern Canada. 36th General Assembly of the European Seismological Commission Book of Abstracts. ESC2018-S30-339, 443-444. Oral Presentation by Dr. Sheri Molnar.

Palmer, S.M. and G.M. Atkinson (2018) Site conditions and kappa in eastern Canada, CGU 2018 Conference Niagara Falls Canada, June 10-14. Oral Presentation.

Ladak, S., S. Molnar, G.M. Atkinson, and **S. Palmer** (2018) Non-invasive methods for determining the shear wave velocity profile at hard rock sites in Eastern Canada., CGU 2018 Conference Niagara Falls Canada, June 10-14. Poster Presentation by Sameer Ladak

Palmer, S.M. and G.M. Atkinson (2018) Bedrock site conditions and kappa in Charlevoix, Quebec, Seismol. Res. Lett. 89(2B), 750 and 821. Poster Presentation.

Ladak, S., S. Molnar, G.M. Atkinson, and **S. Palmer** (2018) Application of active and passive seismic array techniques at hard rock sites in eastern Canada. Seismol. Res. Lett. 89(2B), 750 and 821. Poster Presentation by Sameer Ladak.

Palmer, S.M. and G.M. Atkinson (2017) The relationship between site conditions and kappa: some recent observations, Seismol. Res. Lett. 88(2B), 516 and 646-647. Poster Presentation.

Palmer, S.M. and G.M. Atkinson (2017) Improving earthquake catalog locations in the Western Canada Sedimentary Basin using the double-difference method, Seismol. Res. Lett. 88(2B), 515 and 627. Poster Presentation.